Cover Page

The handle holds various files of this Leiden University dissertation.

Author: Turner, Monica L.
Title: Metals in the diffuse gas around high-redshift galaxies
Issue Date: 2015-11-12

Metals in the diffuse gas around high-redshift galaxies

Proefschrift

ter verkrijging van
de graad van Doctor aan de Universiteit Leiden,
op gezag van Rector Magnificus prof. mr. C.J.J.M. Stolker,
volgens besluit van het College voor Promoties
te verdedigen op donderdag 12 november 2015
klokke 10:00 uur

door

Monica L. Turner
geboren te Oakville, Canada
in 1987

Promotiecommissie

Promotores: Prof. dr. J. Schaye
                  Prof. dr. C. Steidel   (California Institute of Technology)

Overige leden: Dr. R. A. Simcoe   (Massachusetts Institute of Technology)
                  Prof. dr. T. Theuns   (Durham University)
                  Dr. J. K. Werk   (University of California Santa Cruz)
                  Prof. dr. M. Franx
                  Prof. dr. H. Röttgering

To my family

Contents

1 Introduction

1.1 The intergalactic medium

In the early Universe, prior to the formation of galaxies and stars, all baryons were in a gaseous phase. This gas then cooled radiatively, accreted onto virialized dark matter haloes, and eventually formed the stars and galaxies that we see today. A significant fraction of the baryons in the Universe are still predicted to reside in the gas in and around galaxy haloes, which is known as the intergalactic medium (IGM). The gas in the IGM constantly interacts with the nearby galaxies, through continuous accretion as well as outflows generated by energetic events such as explosions from supernovae (SNe). Therefore, it is crucial to study the IGM to obtain a complete picture of how galaxies form and evolve.

The IGM consists of primarily diffuse gas with a density of $n_H \approx 10^{-5}$–10^{-3} cm^3, which makes it very difficult to observe in emission. Instead, we employ bright background sources known as quasars or quasi-stellar objects (QSOs), whose emission is powered by accretion onto the central supermassive black hole of a galaxy. As the light from the QSO travels towards the observer, it is continuously redshifted due to the expansion of the Universe, which allows signatures of intervening gas to be imprinted as individual absorption lines on the spectrum. Particularly at higher redshifts, the vast amount of neutral hydrogen in the Universe creates a dense series of absorption lines known as the Lyman α (Lyα) forest. In Fig. 1.1, we present the spectrum of a z = 3.7 QSO, where the Lyα forest is evident below $\lambda \sim 5700$ Å. Higher-order Lyman series transitions beginning with Lyβ are also present, and make identification of individual absorption lines in this region of the spectrum prohibitively difficult.

While it was first believed that the IGM is composed of discrete clouds, Bi et al. (1992) proposed that it takes the form of a smooth, diffuse medium, and that the Lyα forest can be reproduced by density fluctuations in this medium (see also Bi, 1993; Bi & Davidsen, 1997). This picture was found to be consistent with simulations (e.g., Cen et al., 1994; Miralda-Escudé et al., 1996; Theuns et al., 1998), as well as analytic models (Schaye, 2001), in which the IGM was also determined to be a good tracer of the underlying density (e.g., Tytler, 1987; Hernquist et al., 1996). This is an intuitive picture of the IGM, since baryons tend to follow the underlying dark matter, and hydrogen makes up the majority of baryons. As the gas collapses into dark matter haloes and eventually forms galaxies, the wide range of gas densities throughout this process can explain the strength of H I absorbers encountered in the Lyα forest. The strongest absorbers are thought to trace the areas closest to galaxies, while weaker absorbers probe the sheets and filaments in intergalactic regions.

In addition to hydrogen, absorption by heavy elements such as carbon, silicon, and oxygen are also seen in QSO absorption spectra, and commonly studied transitions are marked in Fig. 1.1. These elements are necessarily synthesized in stars found in galaxies, so their presence in the diffuse IGM can put constraints on the cycle of gas through the galaxy ecosystem. As metal-line absorption can span a vast range of transition energies, the presence (or paucity) of certain ions can provide clues about the physical state of the gas. In general, ions with lower ionization energies, such as Si II and C II, reside in cooler regions of higher H I column density where they can be shielded from photoionization. On the other hand, higher ions such as C IV and O VI can probe hotter, more diffuse gas phases. Of course, each ion can be present in gas with some range of temperature and densities, so detailed modelling of multiple ions is required to constrain the physical conditions in detail.

The IGM is ionized by two main processes, photoionization and collisional ionization. The dominant mechanism is thought to be photoionization, as the IGM is constantly subjected to background light emitted by QSOs and galaxies known as the UV background (UVB). Because the UVB has a very low surface brightness, its normalization and shape cannot be measured directly. Rather, the properties of the UVB can be inferred from indirect observations (e.g., Bechtold et al., 1987; Adams et al., 2011), or predicted using models of QSO and galaxy radiation (e.g., Faucher-Giguère et al., 2009; Haardt & Madau, 2012). Models of the UVB are subject to large uncertainties, such as the expected luminosities of QSOs and galaxies throughout cosmic time as well as photon escape fractions. Throughout this thesis, we use the UVB model of Haardt & Madau (2001).

At temperatures $\gtrsim 10^5$ K, collisions between atoms and electrons become energetic enough to liberate electrons, and collisional ionization begins to dominate. While such temperatures are not typical of the high-redshift IGM, at lower redshifts a large amount of gas is thought to be shock-heated through gravitational infall or galactic winds. This tenuous hot phase is predicted to carry the missing baryons required to bring the baryon budget of galaxies in line with the cosmological fraction (e.g., Shull et al., 2012). The study of metal ions with high ionization energies such as O VI and Ne VIII are of particular interest, as their ionization fractions peak at temperatures where collisional ionization dominates.

1.1.1 Pixel optical depth

Absorption lines from the intervening IGM can be well described by a Voigt profile, which consist of a convolution of natural or collisional broadening and thermal broadening. Fitting Voigt profiles to individual absorption lines can be a very powerful tool, as it allows the measurement of the redshift, velocity width and column density of the gas in question. However, the density of the Lyα forest makes this task very difficult at high redshift (but see e.g. Rudie et al. 2012b).

In this thesis, we use an alternative technique known as the pixel optical depth method (Cowie & Songaila, 1998; Ellison et al., 2000; Schaye et al., 2000a; Aguirre et al., 2002; Schaye et al., 2003), which is described in full detail in Chapter 2. Rather than attempting to decompose the spectrum into individual absorption lines, we use the rest wavelength of the transition in question to define the region in the spectrum where we would expect to find absorption due to the ion. In Fig. 1.1, we denote the areas of the spectrum where the absorption due to H I, O VI, C IV and Si IV are expected, at a redshift ranging from that of
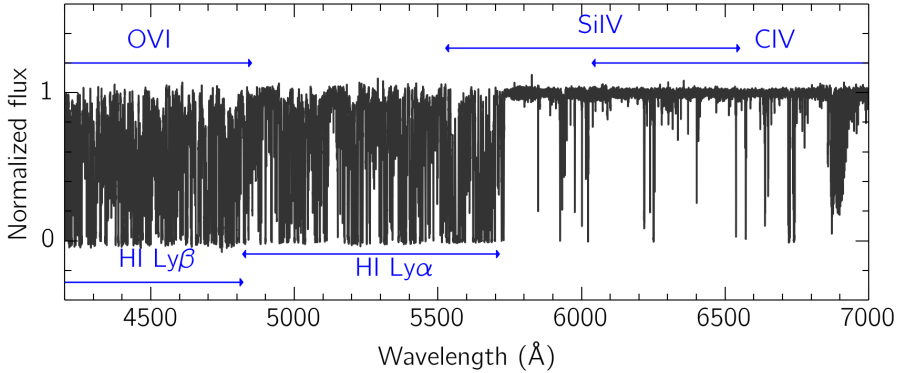
Figure 1.1: A $z = 3.7$ QSO spectrum whose continuum has been normalized. Blueward of the QSO Lyα emission (located at $\lambda \sim 5700$ Å), the dense collection of absorption lines forms the Lyα forest. The arrows indicate the regions which have the same redshift range as the portion of the Lyα forest before Lyβ begins. Ovi is coincident with the beginning the Lyβ absorption, and due to the superposition of numerous absorption lines from Hi, individual Ovi absorbers are nearly impossible to discern at this redshift. In contrast, Civ and Siiv are located primarily redward of the QSO Lyα emission, and suffer much less from contamination.

the QSO to where they Lyβ forest begins in Lyα. The wavelength of each binned spectral pixel is then converted to a redshift, the optical depth of each pixel is given to be $-\ln(F)$, where F is the normalized flux.

This method allows us to make corrections for saturation or contamination depending on the ion. For example, many Hi Lyα pixels will be saturated, so we can look to higher-order Hi transitions to search for unsaturated counterparts. Although Civ lies redwards of the Lyα forest and does not suffer from contamination by Hi, we still need to make corrections due to contamination by its own doublet. Importantly, this technique allows us probe ions such as Ovi, which are almost completely obscured by Hi. Since we know the Hi Lyα optical depths, we can subtract some of the expected contribution of Hi in the Ovi region.

In addition to the fact that the pixel optical depth method allows us to access particularly difficult ions at high redshift, its advantage lies in the fact that it is fast and objective, and can be applied uniformly to both observed and simulated spectra. Furthermore, it can be sensitive to weak metal-line absorption in low density gas, important for the study of the diffuse IGM. However, one shortcoming is that the interpretation is not always as straightforward as with individual absorption lines. For example, when averaging over large numbers of pixels, one is unable to differentiate between a contribution from many weak absorbers, or from few strong absorbers.

The pixel optical depth method has been used extensively to study the high redshift IGM. Schaye et al. (2003) found that the distribution of Civ in the IGM is spatially inhomogeneous, with a metallicity that depended strongly on the overdensity δ. At $\log_{10} \delta = -0.5$ the authors measured [C/H] $= -3.47^{+0.07}_{-0.06}$. Other work also demonstrated that the IGM was enriched early, with a significant fraction of all silicon in place by $z \sim 3$ (Aguirre et al., 2004). The dominant ionization mechanism for the ions with lower ionization energies was determined to be photoionization, while Ovi was found to potentially arise partly in

collisionally ionized gas (Aguirre et al., 2008).

1.1.2   Gas around galaxies

In addition to the study of gas in the IGM, the past decade has seen rapid growth of observations of the gas around galaxies, dubbed as the circumgalactic medium (CGM). Bahcall & Spitzer (1969) first proposed that the absorbers seen in the spectra of QSOs may originate from the gas in galaxy haloes. The first association between galaxies and metal-line absorbers using MgII was made some decades later (Bergeron & Boissé, 1991; Bergeron et al., 1992). Not soon after, an abundance of observations unearthed relationship between galaxies and metal-line absorption for ions spanning a wide range of ionization energies (e.g., Chen et al., 2001; Stocke et al., 2006; Chen & Mulchaey, 2009; Prochaska et al., 2011).

Indeed, it is not unexpected that metal-line absorption be associated with galaxies, since metals must be synthesized in stars. However, metal-rich gas can often be found at relatively large distances from the nearest known galaxy. This phenomenon is generally seen around star-forming galaxies, and is thought to be caused by the galaxies driving large-scale outflows, due to energetic processes such as SNe explosions. Such outflows are found to have velocities reaching 800–1000 km s^{-1}, and have been observed across numerous epochs, from the local M82 galaxy (e.g., Bland & Tully, 1988; Lehnert et al., 1999) to nearly $z \sim 5$ (e.g., Franx et al., 1997; Jones et al., 2012), as well as many redshifts in between (e.g., Heckman et al., 1990; Steidel et al., 1996, 1999; Pettini et al., 2000; Ajiki et al., 2002; Shapley et al., 2003; Rupke et al., 2005; Martin, 2005; Tremonti et al., 2007; Weiner et al., 2009; Quider et al., 2009; Steidel et al., 2010).

At low redshifts, most absorption lines are shifted too far into the UV to be observable from the ground (with the exception of MgII). However, the advent of the Cosmic Origins Spectrograph on the Hubble Space Telescope has brought in an unprecedented amount data on low redshift QSOs. Tumlinson et al. (2011) found OVI to be ubiquitous around star-forming L* galaxies. These same galaxies were also found to have significant reservoirs of cool, metal-enriched gas (Werk et al., 2014). Pushing to lower galaxy masses, metal-line absorption has also found to be common in the CGM of dwarf galaxies, with CIV being observed observed out to ≈ 0.5 R$_{vir}$ (Bordoloi et al., 2014).

At higher redshifts, while QSOs are more readily observable from the ground with UV spectrographs such as HIRES on Keck and UVES on the Very Large Telescope (VLT), galaxy spectroscopy is prohibitively expensive, making the association between absorbers and galaxies significantly more challenging. The observational data used in Chapters 2 and 3 of this thesis come from the Keck Baryonic Structure Survey (KBSS, Rudie et al., 2012b; Steidel et al., 2014), which is an ongoing galaxy survey in 15 QSO fields at $z \sim 2.5$. This epoch is of particular interest, as it is believed to be the peak of both inflows (Faucher-Giguère et al., 2011) and star formation (e.g., Madau et al., 1996; Reddy et al., 2008), which may have a powerful impact on the CGM.

The KBSS has already provided substantial insight into the gas around galaxies at high redshifts. For HI, Rakic et al. (2011) used the pixel optical depth technique to construct the first 2-dimensional maps of absorption around galaxies. Rudie et al. (2012b) fitted Voigt profiles to thousands of individual HI absorbers, and found that the strongest HI absorbers were located within $\lesssim 300$ pkpc and ± 300 km s^{-1} of galaxy positions. The catalogue of fitted HI absorbers was also used to study the temperature-density relation of the IGM (Rudie

et al., 2012a) and the column density distribution function (Rudie et al., 2013). Metal-line absorption was also examined by Adelberger et al. (2003) and Adelberger et al. (2005b), who found strong correlations between galaxies and C IV absorbers. Finally, Steidel et al. (2010) used down-the-barrel observations as well as galaxy pairs to characterize metal-line absorption in the inner CGM, from 0 to 125 proper kpc (pkpc), of the KBSS galaxies. In Chapters 2 and 3, we use the pixel optical depth technique to expand the study of metal-line absorption around the survey galaxies out to impact parameters of 2 proper Mpc (pMpc).

1.2   Cosmological simulations

Although dark matter and dark energy are far from being fundamentally understood, the cosmological parameters governing the large-scale structure of our Universe are constrained to high level of precision using numerous independent measurement techniques (see e.g., Planck Collaboration et al., 2013). Indeed, cosmological simulations are able to capture large-scale structure extremely well. However, the inclusion of baryonic processes in simulations is substantially more uncertain. The main issue resides in the fact that there are baryonic processes crucial to the formation of galaxies which are not resolved on the ~kpc scales probed by cosmological simulations, for example, the formation of individual stars from molecular clouds. Thus, simulations invoke subgrid recipes to couple such processes to the resolved scales.

The specific baryonic processes that have been subject to significant debate over the last decades are collectively known as energetic feedback, which refers to any mechanism that drives gas out of the galaxy. When the first cosmological simulations were run, it was apparent that without a way to constantly remove gas from galaxies, the gas would overcool and form far more stars than observed at a fixed halo mass. While the observed galaxy stellar mass function has a shallow low mass slope and exponential decline at high masses (Schechter, 1976), the first galaxy simulations produced galaxies with masses following the power-law halo mass relation instead. At lower galaxy masses, the evacuation of gas can be explained primarily by SNe explosions. Individual explosions can form hot bubbles of gas, and the combination of multiple explosions can form a hot superbubble driving an outflow (e.g., Weaver et al., 1977; Mac Low & Ferrara, 1999). Other processes may also be important, such as stellar winds or radiation pressure. At higher galaxy masses, feedback from the accretion of matter onto the galaxy central black hole becomes important for driving out the gas.

While there is observational evidence for both star-formation driven winds (see the discussion about outflows in § 1.1.2) and AGN feedback (see Fabian 2012 for a review), simulations are unable to resolve individual supernovae or black hole accretion disks. Furthermore, it is unclear whether the energy should be injected thermally or kinetically. It is also not apparent how much energy or momentum should be coupled to the gas, and how it should be distributed amongst nearby particles. However, the implementation of these processes is actually very crucial, as the final properties of galaxies depend very sensitively on the implementation (e.g., Haas et al., 2013a). Thus, the realization of feedback in simulations remains an open problem in the field of galaxy formation theory.

Recently, the EAGLE simulations (Schaye et al., 2015; Crain et al., 2015) have approached the issue by calibrating the feedback to a handful of robust observables: the galaxy stellar

mass function, the galaxy mass-central black hole mass relation, and galaxy disk sizes, all at $z \sim 0$. So far, these simulations have shown significant promise in reproducing numerous observables which were not used to calibrate the feedback, such as the Tully-Fisher relation (Schaye et al., 2015) and the evolution of the galaxy stellar mass function (Furlong et al., 2015). In Chapters 4 and 5, we compare our observations of the high-redshift CGM and IGM to these simulations.

1.2.1   Gas in simulations

Because the CGM encompasses the region where infalling gas and star-formation driven outflows cross paths, its properties are predicted to be very sensitive to feedback physics in simulations. In particular, observations of metal-line absorption could be used to put constraints on the physical conditions of the gas around galaxies. Some comparisons between the observed CGM and simulations are detailed below.

At high redshifts, some simulations were unable to reproduce observations of H I around massive galaxies and QSOs (Fumagalli et al., 2014; Faucher-Giguère et al., 2015). In contrast, Rakic et al. (2012) found good agreement between the H I pixel optical depths around galaxies and the OWLS simulations (Schaye et al., 2010), while Rahmati et al. (2015) was also able to reconcile the observations with the EAGLE simulations. The latter work attributed this success to a combination of efficient feedback in the simulations, and also taking care to carefully mimic the characteristics of the observations. For metal-line absorption, Shen et al. (2013) performed zoom-in simulations of a massive galaxy and reproduced observations by Steidel et al. (2010) characterizing the CGM around the KBSS galaxies. However, a separate study using cosmological simulations did not find high enough C IV column densities, even when extreme feedback models were invoked (Suresh et al., 2015).

At low-redshift, efficient feedback is essential to match observations of metal-line absorption in the CGM, particularly at distances beyond ~ 50 kpc Stinson et al. (2012); Hummels et al. (2013). However, even with efficient feedback, some simulations have difficulty reproducing observations of O VI, possibly due to a paucity of hot gas or poor metal mixing (Hummels et al., 2013; Ford et al., 2015). Recently, the CGM has been found to be an essential, complementary discriminator between different feedback models. Liang et al. (2015) studied a zoom-in simulation of a galaxy with a stellar to halo mass ratio, star formation history, and metallicity consistent with observations. However, in spite of the apparent agreement with observations, the column densities derived from metal-line absorption in the CGM were found to be well below observed values. The authors determined that increasing the SN energy or adding feedback from cosmic rays could bring the observations of the CGM and simulations into agreement.

1.3   This thesis

In this thesis we study H I and metal-line absorption in observations of the extended CGM of galaxies at $z \approx 2.5$ and the IGM at $z \approx 3.5$. We employ data from the KBSS, as well as archival and new observations of QSOs using the VLT/UVES spectrograph. The redshift range of 2.5–3.5 is of particular interest because it offers a glimpse into the Universe during the time when star formation was the most active. Furthermore, the UV and optical

features of galaxies are shifted into optical and IR wavelengths, respectively, making observations feasible from ground-based instruments. Using the pixel optical depth method, we are uniquely positioned to study the CGM and IGM at this crucial epoch.

In Chapter 2, we study metal absorption around 854 $z \approx 2.4$ star-forming from the KBSS. The KBSS galaxies lie in the fields of 15 hyper-luminous background QSOs, and have impact parameters that range from 35 pkpc to 2 pMpc. The galaxy redshifts have all been measured spectroscopically from either rest-frame UV features or nebular emission lines, which have associated measurement errors of ≈ 150 km s^{-1} and ≈ 18 km s^{-1}, respectively. We employ the pixel optical depth method to create the first galaxy-centred 2-dimensional maps of the median absorption by Ovɪ, Nv, Cɪv, Cɪɪɪ, and Siɪv, and update the results from Rakic et al. (2012) on Hɪ. We uncover a strong enhancement of the absorption relative to randomly located regions at small galactocentric distances, and find that this strong enhancement extends to at least 180 pkpc in the transverse direction, and ± 240 km s^{-1} along the line-of-sight (LOS, ~ 1 pMpc in the case of pure Hubble flow). A small but significant enhancement of absorption of Cɪv and Hɪ out to our maximum impact parameter of 2 pMpc in the transverse direction is also observed. We repeat the analysis using only the 340 galaxies with redshifts measured from nebular emission lines, and find no decrease in the extent of the enhancement along the LOS. This implies that that gas peculiar velocities from either infall, outflow, or virial motions, rather than redshift errors, are responsible for the redshift-space anisotropy.

In Chapter 3, we also utilize data from the KBSS to study the physical conditions of the circumgalactic gas. We find that at fixed Hɪ, Cɪv, and Siɪv, the Ovɪ absorption is strongly enhanced for impact parameters < 180 pkpc and LOS distances out to ~ 350 km s^{-1}. For pixels with $\tau_{\mathrm{Hɪ}} \gtrsim 10$, we invoke ionization models to demonstrate that the relation between Ovɪ and Hɪ absorption is consistent with enriched, photoionized gas. However, the same models would produce unrealistically high metallicities in underdense gas for pixels with $\tau_{\mathrm{Hɪ}} \lesssim 1$. We therefore conclude that the observations are consistent with a scenario where the gas at small galactocentric distances is collisionally ionized, with a metallicity $\gtrsim 10^{-1}$ of solar. The large velocity extent and high metallicity provide evidence that we may be probing hot, metal enriched outflows.

In Chapter 4, we compare the results of Hɪ, Cɪv and Siɪv absorption from Chapter 2 to the EAGLE simulations. Sightlines are extracted from the simulations, with properties chosen to match the resolution, pixel size, and signal-to-noise ratio of the observed spectra, and the observed distributions of galaxy impact parameters and redshift errors are also considered. We find excellent agreement between the observations and simulations, for both the high optical depths close to galaxies and the enhancement observed to 2 pMpc impact parameters. Furthermore, we detect redshift-space distortions similar to those observed, and confirm that they are caused by peculiar velocities. We consider a range of different minimum halo masses, and find the best match for $M_{\mathrm{halo}}^{\mathrm{min}} \sim 10^{12}$ M$_\odot$, which agrees with independent measurements from clustering. We examine different subgrid feedback models where the strength of the stellar feedback is increased and decreased by a factor of two, and do not see a significant change in the results. This indicates that the dominant contribution to the redshift-space distortions comes from infalling or rotating gas, rather than from outflows.

In Chapter 5, we turn to examining the IGM at $z \sim 3.5$. We study pixel optical depth relations from new, high-quality absorption spectra of eight QSOs with $\langle z_{\mathrm{QSO}} \rangle = 3.75$.

Strong correlations are found between Civ, Siiv, Ovi and Hi, between Ciii and Civ, and between Siiii and Siiv. We then compare these results with the EAGLE simulations, by generating mock spectra with properties similar to UVES observations. The simulations agree well with relations between Ovi and Hi, between Ciii and Civ, and between Siiii and Siiv. However, they fall short of the median observed Civ and Siiv optical depths when binned by Hi. At $\tau_{\mathrm{HI}} = 1$, the discrepancy is at most ~ 0.1 dex, and increases to up to ~ 1 dex at $\tau_{\mathrm{HI}} = 10^2$, where the Hi optical depths may be representative of dense regions close to galaxies. We consider different ionizing background models, and we find that the model which accounts for delayed Heii reionization by reducing the intensity above 4 Ryd agrees well with the observations, but only for $\tau_{\mathrm{HI}} \lesssim 10$. We explore the consequence of using a simulation with higher resolution, which would be able to resolve lower mass galaxies thought to be important for polluting the IGM, and although we do see an improvement, the tension is not fully resolved. Finally, because the relation between Ovi and Hi matches the observations and is insensitive to ionziation model, it is likely probing collisionally ionized gas. This means that while there is sufficient enriched hot gas in the simulation, there may be a dearth of cooler gas required to reproduce observations of Civ and Siiv.

2 Metal-line absorption around $z \approx 2.4$ star-forming galaxies in the Keck Baryonic Structure Survey

We study metal absorption around 854 $z \approx 2.4$ star-forming galaxies taken from the Keck Baryonic Structure Survey (KBSS). The galaxies examined in this work lie in the fields of 15 hyper-luminous background QSOs, with galaxy impact parameters ranging from 35 proper kpc (pkpc) to 2 proper Mpc (pMpc). Using the pixel optical depth technique, we present the first galaxy-centred 2-D maps of the median absorption by Ovi, Nv, Civ, Ciii, and Siiv, as well as updated results for Hi. At small galactocentric radii we detect a strong enhancement of the absorption relative to randomly located regions that extend out to at least 180 pkpc in the transverse direction, and ±240 km s^{-1} along the line-of-sight (LOS, ~ 1 pMpc in the case of pure Hubble flow) for all ions except Nv. For Civ (and Hi) we detect a significant enhancement of the absorption signal out to 2 pMpc in the transverse direction, corresponding to the maximum impact parameter in our sample. After normalising the median absorption profiles to account for variations in line strengths and detection limits, in the transverse direction we find no evidence for a sharp drop-off in metals distinct from that of Hi. We argue instead that non-detection of some metal line species in the extended circumgalactic medium is consistent with differences in the detection sensitivity. Along the LOS, the normalised profiles reveal that the enhancement in the absorption is more extended for Ovi, Civ, and Siiv than for Hi. We also present measurements of the scatter in the pixel optical depths, covering fractions, and equivalent widths as a function of projected galaxy distance. Limiting the sample to the 340 galaxies with redshifts measured from nebular emission lines does not decrease the extent of the enhancement along the LOS compared to that in the transverse direction. This rules out redshift errors as the source of the observed redshift-space anisotropy and thus implies that we have detected the signature of gas peculiar velocities from infall, outflows, or virial motions for Hi, Ovi, Civ, Ciii, and Siiv.

2.1 Introduction

The exchange of baryons between galaxies and their surroundings remains a poorly understood problem in galaxy formation theory. Currently, hydrodynamical cosmological simulations suffer from large uncertainties in their implementations of sub-grid physics, particularly those related to feedback from star formation and active galactic nuclei (AGN).

Variations within these recipes can create vast differences in the resulting galaxy properties (e.g., Haas et al., 2013a,b), which manifest themselves also in the distribution of cosmic metals (e.g., Wiersma et al., 2011). Metals in different ionisation states hold clues to the structure, kinematics, temperature, and composition of the gas in which they reside, and they are therefore an important observational tool for comparison with simulations.

Observations have shown that the movements of these metals through the circum-galactic and intergalactic medium (CGM and IGM, respectively) are influenced by galactic-scale outflows, which are commonly observed in star-forming galaxies at $z \sim$ 2–3 (e.g., Steidel et al., 1996; Pettini et al., 2000; Quider et al., 2009; Steidel et al., 2010); but also in nearby galaxies ($z < 2$) (e.g., Heckman et al., 1990, 2000; Martin, 2005; Rupke et al., 2005; Tremonti et al., 2007; Weiner et al., 2009) as well as in those at higher redshifts (e.g., Franx et al., 1997; Steidel et al., 1999; Ajiki et al., 2002; Shapley et al., 2003; Jones et al., 2012). These outflows are often metal-rich, with velocities of up to 800–1000 km s^{-1}.

Aguirre et al. (2001), Oppenheimer & Davé (2008), and Oppenheimer et al. (2010) studied such winds in cosmological simulations, and found that they are likely responsible for metal pollution in the IGM. Furthermore, Oppenheimer et al. (2010) determined that these outflows are often bound to the galaxies and fall back in, with most star forming gas at $z \sim 1$ coming from such recycled material. Simulations by Booth et al. (2012) suggest that galaxies residing in low-mass ($M_{\text{tot}} < 10^{10}$ M$_\odot$) haloes are required to account for the observed CIV absorption associated with relatively weak HI absorption (Schaye et al., 2003). However, Wiersma et al. (2010) found that only half of intergalactic metals originated from $M_{\text{tot}} \lesssim 10^{11}$ M$_\odot$ haloes. The authors also noted that in their simulations, half of the inter-galactic metals at $z = 2$ were ejected between $2 < z < 3$. This prediction is consistent with observations by Sicmoe (2011) that suggested that 50% of metals observed in the IGM at $z \sim 2.4$ have been there since $z \sim 4.3$ (1.3 Gyrs). In general, many questions still remain about the masses of the galaxies responsible for metal pollution, as well as the epoch(s) at which the bulk of it may have occurred.

To search for intergalactic metals, observations of absorption-line systems are often used. Bahcall & Spitzer (1969) first suggested that intervening absorbers could be associated with galaxy haloes; indeed, it has has been shown that MgII (e.g., Bergeron & Boissé, 1991; Zibetti et al., 2005; Nielsen et al., 2013), CIV (e.g., Chen et al., 2001), and OVI (e.g., Stocke et al., 2006; Chen & Mulchaey, 2009; Prochaska et al., 2011; Tumlinson et al., 2011) absorbers are found to occur near galaxies. Adelberger et al. (2003, 2005b) found evidence for metals out to 300 proper kpc using CIV-galaxy cross-correlation studies at $z \sim 3$, while Steidel et al. (2010) used galaxy pairs to observe the equivalent widths (EWs) of various ions near $\sim L_*$ galaxies at $z \sim$2–3, galaxies, and showed that these galaxies have metal-enriched gas out to $\sim$ 125 proper kpc.

Theoretical studies of metals around simulated galaxies have also been undertaken. For example, Ford et al. (2013) examined the distribution of the absorption of various ions around $z = 0.25$ galaxies with halo masses 10^{11}–10^{13} M$_\odot$, and found that all ions examined showed enhanced absorption near the galaxy centres, with lower ions arising in denser gas closer to the galaxies and higher ions found further away. A similar effect was seen by Shen et al. (2013), who analysed a zoom-in simulation of a $z \sim 3$, $\sim 10^{11}$M$_\odot$ galaxy. They found that low ions were predominantly tracing cool ($T < 10^5$ K) gas at radii less than the galaxy virial radius R$_{vir}$, while higher ions trace hotter gas out to beyond 2×R$_{vir}$.

In this work, we study the distribution of metals around galaxies using data from the

Keck Baryonic Structure Survey (KBSS, Rudie et al., 2012b; Steidel et al., 2014). This survey consists of a combination of high-quality quasi-stellar object (QSO) spectra, and a survey focused on redshifts below those of the QSOs. We combine these two components in order to use a galaxy-centred approach to study metals in the CGM, by examining metal optical depths and EWs in the QSO spectra as a function of galaxy impact parameter and line-of-sight (LOS) distances. The metal ions examined here are, ordered by decreasing ionisation energy, O VI, N V, C IV, C III, and Si IV. Additionally, we revisit the results for H I previously examined in Rakic et al. (2012) using the updated KBSS galaxy sample. Thanks to observations with MOSFIRE (McLean et al., 2012), not only has the total sub-sample size grown from 679 to 854 galaxies, but both the fraction and total number of galaxies with redshifts measured using nebular emission lines have increased substantially from 10% (71 galaxies) to 45% (381 galaxies).

The structure of the paper is as follows: we first describe our galaxy and QSO samples in § 2.2, while in § 2.3 we discuss the pixel optical depth recovery for the various ions. The results are presented in § 2.4, where in particular we examine optical depth maps in § 2.4.1; cuts through these maps in § 2.4.2; optical depths as a function of 3-dimensional (3-D) Hubble distance in § 2.4.3; the optical depth distributions in § 2.4.5; EWs in § 2.4.6; covering fractions in § 2.4.4; and the effects of the galaxy redshift measurement errors in § 2.4.7. Finally, we present our conclusions in § 2.5. Throughout the paper, we quote proper rather than comoving units (denoted as pkpc and pMpc), and have used cosmological parameters determined from the Planck mission (Planck Collaboration et al., 2013), i.e. $H_0 = 67.1$ km s^{-1} Mpc^{-1}, $\Omega_m = 0.318$, and $\Omega_\Lambda = 0.683$.

The sample of galaxies used in this work comes from a subset of the KBSS, which consists of ~ 2550 $\langle z \rangle \sim 2.3$ galaxies selected to lie in the fields of 15 hyper-luminous ($L_{bol} \gtrsim 10^{14} L_\odot$) redshift 2.5–2.85 QSOs which all have extremely high-quality, i.e., high resolution and signal-to-noise (S/N) Keck/HIRES spectra. The galaxies in each QSO field were chosen primarily using ultraviolet (UV) colour selection techniques (Steidel et al., 2003, 2004; Adelberger et al., 2004) with the purpose of tuning the galaxy redshift selection functions to optimise overlap with the range probed by the QSO spectra. Galaxies with apparent magnitude $m_R \leq 25.5$ were then followed up spectroscopically using Keck/LRIS, NIRSPEC, and/or MOSFIRE, with priority given to those likely to have redshifts in the QSO Lyα forest and those near the QSO sightline. For more details on the observations, see § 2.1 of Rudie et al. (2012b).

Typically, the galaxies in the full survey sample have dynamical masses of $\sim 7 \times 10^{10}$ M$_\odot$ (Erb et al., 2006c), and reside in halos with masses $\sim 10^{12}$ M$_\odot$ (Adelberger et al., 2005b; Conroy et al., 2008; Trainor & Steidel, 2012; Rakic et al., 2013). This corresponds to virial radii and circular velocities of ≈ 90 pkpc and ≈ 217 km s^{-1}, respectively. They tend to have median star formation rates ~ 25 M$_\odot$ yr^{-1} (Erb et al., 2006b; Steidel et al., 2014), gas-phase metallicites $\sim 0.5 Z_\odot$ (Erb et al., 2006a) and stellar ages ~ 0.7 Gyr (Erb et al., 2006c).

The sub-sample that we use satisfies two constraints. Firstly, we require that the galaxies have impact parameters ≤ 2 pMpc (or $\simeq 4'$ at $z \sim 2.4$), so that the range in common is covered in all 15 KBSS fields. Secondly, we only use galaxies that have a redshift within the range of the Lyα forest, since our pixel optical depth recovery is limited to this region (see
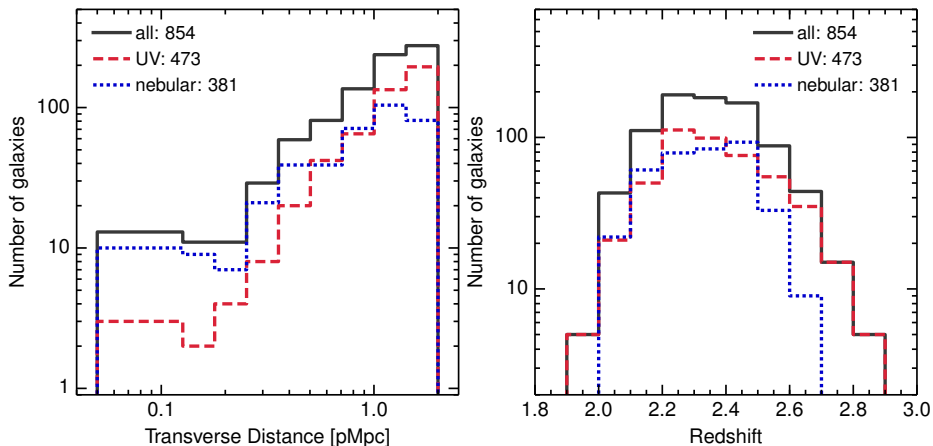
Figure 2.1: Histograms of the sub-sample of KBSS galaxies used in this work, selected to have redshifts in the Lyα forest and impact parameters ≤ 2 pMpc. The left panel shows the distribution as a function of impact parameter, and the right as a function of galaxy redshift. The values for the impact parameter histogram are given in Table 2.1.

2.2 Galaxy Sample

§ 2.3). We define the redshift of the Lyα forest as follows:

$$(1 + z_{\mathrm{qso}}) \frac{\lambda_{\mathrm{Ly}\beta}}{\lambda_{\mathrm{Ly}\alpha}} - 1 \leq z \leq z_{\mathrm{qso}} - (1 + z_{\mathrm{qso}}) \frac{3000 \,\mathrm{km\ s^{-1}}}{c} \tag{2.1}$$

where $\lambda_{\mathrm{Ly}\alpha}$ = 1215.7 Å and $\lambda_{\mathrm{Ly}\beta}$ = 1025.7 Å are the H I Lyα and Lyβ rest wavelengths, respectively. The lower limit on the galaxy redshifts is set by the beginning of the Lyβ forest in H I, and a cut is made 3000 km s^{-1} bluewards of the redshift z_{qso} to avoid proximity effects (i.e., these regions can be affected by ejecta and/or the ionising radiation field originating from the QSO). We note that in our analysis (§ 2.4), we search for absorption within ±1350 km s^{-1} of galaxies. Therefore, in practice, our sample contains galaxies that have redshifts extending 1350 km s^{-1} above or below the Lyα forest limits given above.

Fig. 2.1 shows histograms of the galaxy impact parameters (left panel) and redshifts (right panel) for the 854 galaxies that satisfy the above constraints. We also show the distributions separately for the galaxies whose redshifts were measured from rest-frame UV features (using LRIS; 473 galaxies) and from rest-frame optical nebular emission lines (using NIRSPEC and MOSFIRE; 381 galaxies). Since the impact parameter binning shown in this figure is used throughout this paper, we have included the bin edge values as well as the number of galaxies in each bin in Table 2.1. The two smallest impact parameter bins exhibit the strongest optical depth enhancement for the metals studied in this work, so many of our results are based on the nearest 24 galaxies, of which 19 have nebular redshifts. As the volume sampled in these inner bins is comparably small, the number of galaxies at small impact parameters is somewhat reduced compared to the larger bins. The median redshifts of the three galaxy samples shown (all galaxies, UV-only, and nebular-only) are $\langle z \rangle$ = 2.34,

Table 2.1: Number of galaxies per impact parameter bin. Except for the innermost bin (which has been extended in order to include the smallest impact parameter galaxies), the bins are spaced logarithmically and are 0.15 dex in size.

Bin #	Lower edge (pMpc)	Upper edge (pMpc)	Total # of galaxies	# with nebular z
1	0.04	0.13	13	10
2	0.13	0.18	11	9
3	0.18	0.25	11	7
4	0.25	0.36	29	21
5	0.36	0.50	59	39
6	0.50	0.71	81	39
7	0.71	1.00	136	71
8	1.00	1.42	238	104
9	1.42	2.00	276	81

2.35, and 2.33, respectively.

2.2.1 QSO Spectra

The 15 quasars that are part of the KBSS were all observed with Keck/HIRES, and their spectra have a typical resolution of $R \approx 36000$. A detailed description of the data is given in Rudie et al. (2012b); briefly, the spectra were reduced using T. Barlow's MAKEE package where each spectral order was continuum normalised using low-order spline interpolation, and the final spectra were rebinned to pixels of 2.8 km s^{-1}. The final continua were fitted by hand, with an automated iterative correction procedure applied redwards of the quasar's Lyα emission line (described in Appendix 2.A). Based on tests done in Aguirre et al. (2002), we expect the errors induced due to continuum fits to be $\lesssim 1\%$. We also test the effects of the automated continuum fit that we apply redwards of Lyα in Appendix 2.B.

Six of the spectra contain damped Lyα systems (DLAs) in the Lyα forest region, which have been fitted with Voigt profiles and had their damping wings divided out (as described in Rudie et al. 2012b). The saturated portions of the six Lyα forest region DLAs were masked and not used for the recovery of optical depths for ions in this region (our masking procedure is described more fully in Appendix 2.A). For more information about the QSOs, see Table 1 of Rakic et al. (2012) and also Trainor & Steidel (2012).

2.2.2 Galaxy Redshifts

Redshifts for KBSS galaxies are measured from features in their rest-frame far-UV and optical spectra. The strongest features in the rest-frame UV spectra of these galaxies are the H I Lyα emission line (when present) and a series of metallic interstellar absorption lines. All of these strong features have been empirically determined to lie at significant velocity offsets with respect to the systemic velocity of the galaxy (Shapley et al., 2003; Adelberger et al., 2003; Steidel et al., 2010; Rakic et al., 2012) which is generally interpreted as evidence for strong mass outflows from such systems. The rest-frame optical spectra of KBSS galaxies consist primarily of nebular emission lines which arise in H II regions within galaxies and therefore trace the systemic velocity of the system to much higher fidelity. For this reason, we prefer redshifts measured from nebular emission lines, when

they are available.

Many galaxies in the KBSS have been observed with the near-IR Keck instruments NIRSPEC and MOSFIRE which have spectral resolutions $R \approx 1200$ and ≈ 3600, respectively. Such observations allowed measurement of galaxy redshifts using their nebular emission lines Hα, Hβ, and [O$_{\text{III}}$] $\lambda\lambda 4959, 5007$ for 381 galaxies in our KBSS subsample. Since the nebular emission lines are good tracers of the systemic galaxy velocity, for those galaxies with nebular redshifts we take $z_{\text{gal}} = z_{\text{neb}}$. The measurement uncertainties for the two instruments, which were estimated by comparing multiple observations of the same galaxy either on two separate occasions or in two different bands, are determined to be $\approx \pm 60$ km s^{-1} and $\approx \pm 18$ km s^{-1}, respectively We emphasise that most of the galaxies in the three smallest impact parameter bins have nebular redshifts (see Table 2.1).

The remaining 473 galaxies in our KBSS subsample lack rest-frame optical spectra and therefore have redshifts measured from rest-frame UV lines observed with Keck/LRIS ($R \approx 800$–1300). To account for the offset of rest-frame UV features from the systemic galaxy velocity, we apply a correction to those galaxy redshifts estimated from interstellar absorption lines, z_{ISM}, and Lyα emission lines, $z_{\text{Ly}\alpha}$.

Rakic et al. (2011) used the fact that the mean foreground galaxy Lyα absorption profiles seen in QSO spectra should be symmetric around the true galaxy redshift to determine the corrections needed to infer the systemic galaxy redshifts. Another approach, which is the one that we use in this work, was first applied by Adelberger et al. (2005a) and Steidel et al. (2010). They used a sample of galaxies having redshifts measured from both rest-frame UV and nebular emission lines to estimate the typical offset between the two measurement techniques.

To calculate the velocity offset values, we use all galaxies with $2 < z_{\text{neb}} < 3$ that have both rest-frame UV and optical spectra, where the errors on the mean have been determined from bootstrap resampling the galaxies 1000 times with replacement, and taking the 1σ confidence intervals. The resulting offset values are implemented as follows:

- For galaxies with only Lyα emission lines detected (50 galaxies),

$$z_{\text{gal,Ly}\alpha} = z_{\text{Ly}\alpha} - 220^{+30}_{-29}\text{km s}^{-1}. \tag{2.2}$$

- For galaxies with only interstellar absorption lines (244 galaxies),

$$z_{\text{gal,ISM}} = z_{\text{ISM}} + 110^{+19}_{-16}\text{km s}^{-1}. \tag{2.3}$$

- For galaxies with both Lyα emission and interstellar absorption (179 galaxies), first the following corrections are made to the measured redshifts:

$$z_{\text{gal,Ly}\alpha} = z_{\text{Ly}\alpha} - 370^{+17}_{-16}\text{km s}^{-1}.$$
$$z_{\text{gal,ISM}} = z_{\text{ISM}} + 200^{+18}_{-16}\text{km s}^{-1}. \tag{2.4}$$

The arithmetic mean of the corrected redshifts,

$$z_{\text{gal}} = \frac{z_{\text{gal,Ly}\alpha} + z_{\text{gal,ISM}}}{2}, \tag{2.5}$$

is then used as the final corrected value, unless it does not satisfy

$$z_{\text{ISM}} < z_{\text{gal}} < z_{\text{Ly}\alpha}, \tag{2.6}$$

in which case we use the arithmetic mean of the uncorrected values,

$$z_{\text{gal}} = \frac{z_{\text{Ly}\alpha} + z_{\text{ISM}}}{2}. \tag{2.7}$$

Based on the sample of 238 galaxies with both nebular and UV redshift estimates, we find that the rest-frame UV redshifts exhibit a 1-σ scatter of ± 150 km s^{-1}. This value corresponds to the error for individual systemic redshift estimates, rather than the error on the mean velocity offset.

2.3   Optical depth recovery

To study the absorption of metals in the vicinity of galaxies, we have used the pixel optical depth method (Cowie & Songaila, 1998; Songaila, 1998; Ellison et al., 2000; Schaye et al., 2000a; Aguirre et al., 2002; Schaye et al., 2003) rather than the complementary technique of fitting Voigt profiles to absorption lines. The pixel optical depth approach is advantageous in the sense that it allows one to quickly and objectively measure absorption strengths in a statistical sense, even for weak signals in highly contaminated regions. On the other hand, with the standard pixel optical depth method, information about line widths is lost, and the interpretation of optical depths is not always as straightforward as that of column densities. In this section, we give a brief description of our specific implementation which is taken largely from Aguirre et al. (2002) with some minor improvements; more details can be found in Appendix 2.A.
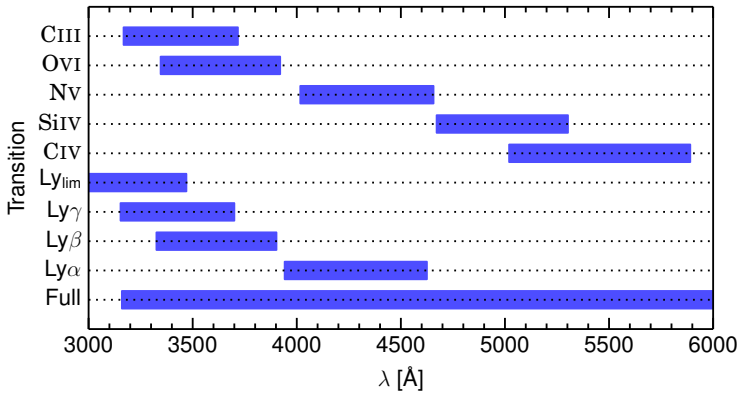
2.3.1   Redshift ranges

For each metal transition, the so-called fiducial redshift range that we use for the recovery is first set by that of the Lyα forest, which was described in § 2.2 and is given by Equation 2.1. As for H$\textsc{i}$, for all ions considered we set the upper limit to be $z_{\text{qso}} - 3000$ km s^{-1} to avoid proximity effects. Additional redshift range modifications are made based on the transition in question, the reasons for which can be seen more clearly by examining Fig. 2.2.

Firstly, the O$\textsc{vi}$ region overlaps mainly with the Lyβ forest, but extends marginally into the Lyα forest since its rest wavelength is slightly higher than that of Lyβ. In an effort to make the contamination across the recovery area uniform, we limit O$\textsc{vi}$ to overlap only with the Lyβ forest, and take $z_{\text{max}} = (1 + z_{\text{qso}})\lambda_{\text{HI,Ly}\beta}/\lambda_{\text{OVI,2}} - 1$ where $\lambda_{Z,k}$ is the rest wavelength of multiplet component k of the ion Z.

The N$\textsc{v}$ doublet ($\lambda_{\text{rest}} = [1238.8, 1242.8]$ Å) has rest-wavelengths which are slightly above that of H$\textsc{i}$ Lyα ($\lambda_{\text{rest}} = 1215.8$Å), and therefore the recovery region of this species lies mainly in the Lyα forest. Although no correction is done for contamination by Lyα, to keep the level of contamination in the recovery region uniform, we impose the constraint that the recovered optical depth region must not extend to redshifts outside of the Lyα forest, namely $z_{\text{max}} = (1 + z_{\text{qso}})\lambda_{\text{Ly}\alpha}/\lambda_{\text{Nv}} - 1$.

The recovery regions of C$\textsc{iv}$ ($\lambda_{\text{rest}} = [1548.2, 1550.8]$ Å) and Si$\textsc{iv}$ ($\lambda_{\text{rest}} = [1393.8, 1402.8]$ Å) both lie mainly redwards of the Lyα forest. In the case of Si$\textsc{iv}$, we avoid any contamination from Lyα by excluding wavelengths bluewards of the quasar's Lyα emission, corresponding to a minimum redshift of $z_{\text{min}} = (1 + z_{\text{qso}})\lambda_{\text{Ly}\alpha}/\lambda_{\text{SiIV}} - 1$. For C$\textsc{iv}$, the limits given in

Figure 2.2: Wavelength ranges of various transitions in one of our QSOs (Q1549+1933, z_{qso} = 2.8443), when their redshifts are restricted to that of the H I Lyα forest (z = 2.24–2.81) plus the additional ion-dependent constraints outlined in § 2.3. The bottom row (marked "Full") shows the wavelength range covered by the observed spectrum.

Table 2.2: Rest wavelengths of both strong and weak components and their separation (if applicable), as well as the pixel optical depth recovery implementation, for the different metal ions studied in this work.

Metal ion	λ_{rest}(Å) strong	weak	Δv (km s^{-1})	Subtr. higher-order H I	Doublet min.	Self-contam.
O VI	1031.927	1037.616	1650	✓	✓	
N V	1238.821	1242.804	962		✓	
C IV	1548.195	1550.770	498			✓
C III	977.020	…	…	✓		
Si IV	1393.755	1402.770	1930		✓	

Equation 2.1 are used; however, it is possible to expand the range to lower redshifts until the quasar's Lyα emission limit is reached ($z_{min} = [1+z_{qso}]\lambda_{Ly\alpha}/\lambda_{C IV} - 1$), which can significantly increase the number of galaxies in the sample. We experiment with this modification in Appendix 2.B.4.

2.3.2 Corrections for contamination

Below we briefly outline the optical depth recovery method used (see Appendix 2.A for the full description). A summary of the metal ion rest wavelengths, the doublet separation in km s^{-1} (if applicable), and pixel optical depth implementations (to be explained below) is given in Table 2.2. Here we also note that the separation between the strong O VI transition (λ_{rest} = 1031.927 Å) and H I Lyβ (λ_{rest} = 1025.7223 Å) is 1810 km s^{-1}. It is important to keep the above transition separations in mind when examining the optical depths, since contamination can be expected on these characteristic scales. To visualise the corrections for contamination, in Fig. 2.3 we have plotted ±500 km s^{-1} regions of the spectrum around the galaxy Q1549-D15, for each of the ions studied. The black lines denote the original

flux, while the red lines are calculated from the recovered optical depths derived using the following procedure.

Implementing the above redshift ranges, we define the optical depth for each ion Z and multiplet component k as $\tau_{Z,k}(z) = -\ln(F)$, where $F(\lambda)$ is the normalised flux at $\lambda = \lambda_k(1+z)$. Beginning with H I Lyα, the main source of error is the saturation of the absorption; to account for this, for every saturated pixel we search for unsaturated higher-order lines at the same redshift and take the minimum of the optical depths (corrected for differences in oscillator strengths and rest-frame wavelengths, and accounting for noise). An example of a saturated region with corresponding unsaturated higher-order lines can be seen in panels (a)–(c) of Fig. 2.3. We also use the higher-order transitions to search for and flag Lyα pixels contaminated by metal line absorption, something which was not implemented in Aguirre et al. (2002).

The recovered H I optical depths are then used to clean the C III and O VI regions by subtracting the optical depths of five higher order H I lines starting from Lyβ. In both Aguirre et al. (2002) and this work, the H I subtraction is performed on all unsaturated metal ion pixels. However, the subtraction cannot be done reliably for saturated metal ion pixels since their optical depths are not well defined. In Aguirre et al. (2002), such pixels remain unchanged by the subtraction procedure, which could result in recovered optical depths being biased high. To combat this, we have made another addition to the recovery method, where for saturated metal line pixels we sum the optical depths from the higher-order H I components. If this value is consistent with saturation, we flag the pixel as contaminated and discard it. Panel (d) of Fig. 2.3 shows the effect of H I subtraction on the C III region, where any absorption that is seen in the black spectrum but not in the red is due to known higher-order H I lines.

Furthermore, since O VI is a doublet, we perform the H I subtraction on both doublet components and further correct for contamination by taking the minimum of the optical depths between the two components at each redshift, taking into account relative oscillator strengths and rest wavelengths. This doublet minimum correction is also made for N V and Si IV, which are mainly contaminated by H I Lyα and C IV, respectively. We note that for metals that have a doublet component, we always scale the weaker transition optical depths to the strongest transition (in this work, all doublets considered have an optical depth ratio of 2). Unlike in Aguirre et al. (2002), we allow pixels from the weaker transition to be used in the doublet minimum correction even if they have been flagged as having flux > 1 (or a negative optical depth). Panels (g)–(h) (N V) and (k)–(l) (Si IV) of Fig. 2.3 demonstrate how this technique can remove contaminating absorption lines.

Finally, C IV shows relatively strong absorption with a recovery region that lies redwards of the Lyα forest; this means that the main source of contamination comes from its own doublet. To correct for this, we iteratively subtract the expected optical depth of the contaminating doublet from each pixel. The result of doing so is shown in panels (i)–(j) of Fig. 2.3.

How important is it to correct for contamination? In Appendix 2.B we examine the recovery of each metal ion in turn to see how the above procedure affects our final result. In general, we find that performing the correction increases the dynamic range of recovered optical depths and decreases the scatter when they are binned as a function of galactocentric distance. However, we note that even without any corrections, the main conclusions of this work still hold.
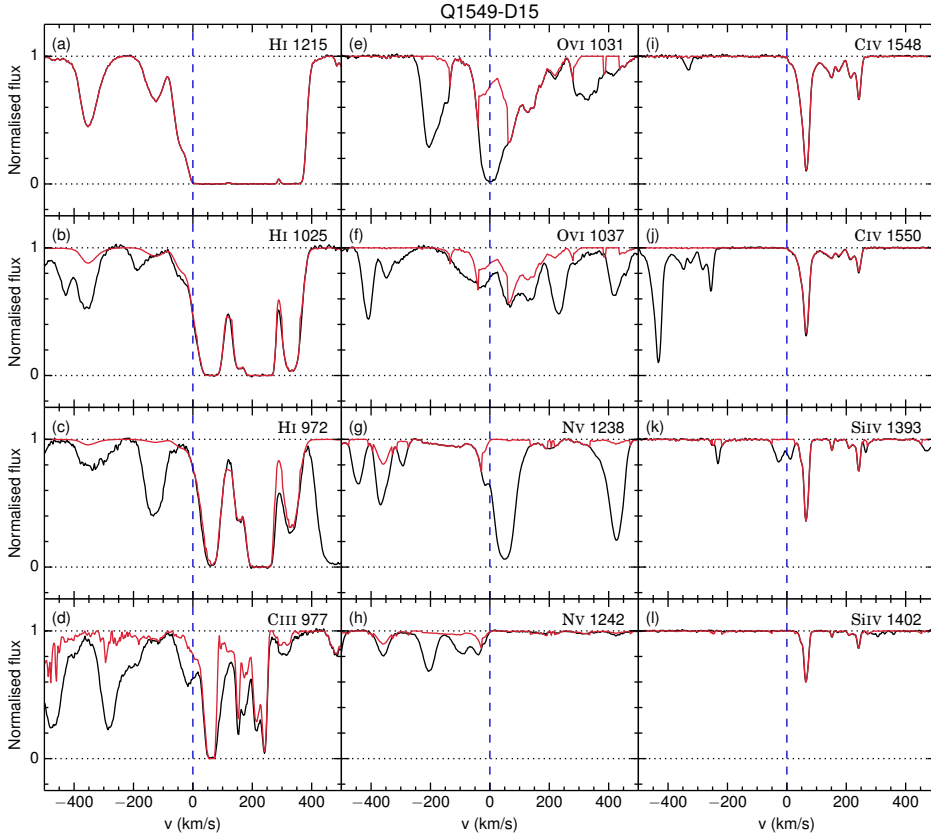
Figure 2.3: Normalised flux (black lines) and recovered optical depths converted to normalised flux (red lines) for regions ± 500 km s^{-1} around the ions studied in this work at the redshift of the galaxy Q1549-D15, which has an impact parameter of 58 pkpc. $v = 0$ km s^{-1} corresponds to the galaxy redshift, and is marked by the vertical dashed blue line. We stress here that, particularly for those metal ions bluewards of Lyα (Ovi, Nv, and Ciii), the derived optical depths are *apparent* rather than true optical depths, since we have no way of fully correcting for all possible contamination. Panels (a), (b) and (c) show Lyα, Lyβ and Lyγ, respectively, and demonstrate how higher-order Hi components often have unsaturated pixels which can be used to correct pixels which are saturated in Lyα (such as in the region shown here from 0–400 km s^{-1}). Panel (d) makes clear that much of the absorption in the Ciii region can be attributed to higher order Hi absorption, and is at least partially corrected for in the Hi subtraction procedure. We note that the noise from the subtracted Hi is responsible for the fine structure seen at negative velocities for Ciii. Both Nv (panels (g) and (h)) and Siiv (panels (k) and (l)) have their optical depths corrected for contamination by taking the minimum optical depth between the two double components. This procedure allowed us to identify and correct for the contaminating absorption systems located at ~ 50 and ~ 450 km s^{-1} for Nv (panel (g)), and at ~ -250 and ~ 0 km s^{-1} for Siiv (panel (k)). The recovery procedure for the Ovi doublet, shown in panels (e) and (f), uses both Hi subtraction as well as taking the minimum optical depth value between the two doublet components. Finally, the ~ -350 km s^{-1} absorption line in panel (i) was identified and removed by the Civ self-contamination correction.

It is important to note that the corrections for contamination are not perfect. For example, because we can only reliably recover H I Lyα in the range of the Lyα forest, we cannot correct contamination of O VI and C III (which lie in the Lyβ forest) by Lyα. Hence, the optical depths quoted should not be taken at face value. This is particularly relevant for C III, N V and O VI, which all suffer from substantial residual contamination from H I. However, because the contamination is due to gas at very different redshifts, it does not vary systematically with the distance to galaxies will therefore not give rise to spurious trends of absorption strength with separation from galaxies. It can only compromise our ability to detect such a trend.

2.4   Results

We can now use the recovered optical depths from § 2.3 and combine them with the redshifts and impact parameters of the galaxies from § 2.2 to investigate how H I and metal ions are distributed around galaxies. In § 2.4.1, we bin the pixel optical depths by galaxy impact parameter and along the LOS to create 2-dimensional (2-D) optical depth maps, while in § 2.4.2 we make the cuts through these maps to look for redshift space distortions in order to compare the optical depth distributions for different ions. We bin the pixels by their 3-D distance to the galaxy in § 2.4.3, where distances are estimated assuming pure Hubble flow, and in § 2.4.5 we show how the distribution of optical depths for each ion varies as a function of impact parameter. Covering fractions are examined in § 2.4.4, and lastly we explore the effect of galaxy redshift errors on our results in § 2.4.7. Unless specified otherwise, all errors are calculated by bootstrap resampling (with replacement) the galaxy sample 1000 times within each impact parameter bin, and taking the 1σ confidence intervals.

2.4.1   2-D Optical depth maps

For each ion we have constructed a galaxy-centred map of the median optical depth as a function of the transverse and LOS separation from the galaxies. The maps extend 2 pMpc in the transverse direction and 5.64 pMpc along the LOS (i.e. ±1350 km s^{-1}), where velocity differences were converted into proper distances given each galaxy's redshift and assuming pure Hubble flow. The pixels contributing to the maps were binned logarithmically in the LOS and transverse directions, where the first bin runs from 0.04–0.13 pMpc and subsequent bins are 0.15 dex wide. We note that each bin contains pixels coming from several different galaxy sightlines, where the number of contributing galaxies depends on the impact parameter (see Table 2.1). The median pixel optical depth in each bin was then taken to construct Fig. 2.4, where the images were smoothed by a Gaussian with a σ equal to the bin size. The right y-axis indicates the LOS velocity difference assuming the median redshift of the galaxies in our sample, $z = 2.34$. The (unsmoothed) optical depth values in each bin, plus their 1σ errors, are given in Table 2.3.

We note that the optical depth scales on the maps presented in Fig. 2.4 run from the median optical depth of all pixels in the redshift range considered for the particular ion and recovery method (which we denote as $\tau_{Z,\text{rnd}}$ for each ion Z), up to the maximum value of all smoothed pixels in the image, in order to maximise the dynamic range. It is therefore
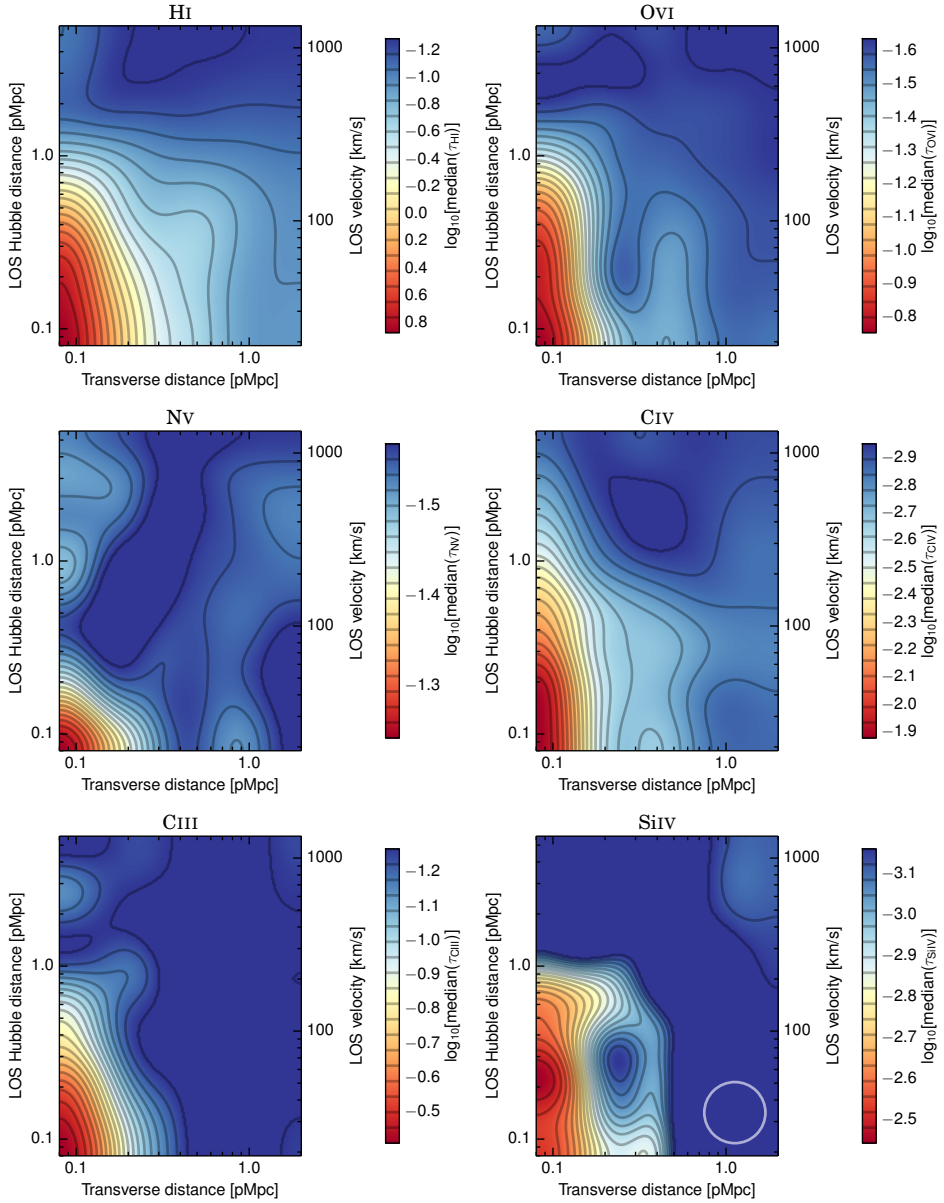
Figure 2.4: 2-D optical depth maps constructed by binning the galaxy impact parameters and LOS distance (assuming pure Hubble flow) logarithmically, taking the absolute LOS distance, and calculating the median optical depth in each bin. The bins are 0.15 dex wide except for the innermost bin, which runs from 0 to 130 pkpc. The maps have been smoothed using a Gaussian that has σ equal to the bin size, and the FWHM of the smoothing kernel is indicated by open the white circle in the bottom right corner of the Si IV map. For each ion, the range of optical depths is set to run from the median of all pixels in the considered redshift range to the maximum value in the smoothed image. Note that the minimum optical depth shown typically reflects the median level of noise and contamination rather than the detection of true metal absorption. The ions considered and their rest frame wavelengths are, from left to right: H I (1215.7 Å), O VI (1031.9 Å), N V (1238.8 Å), C IV (1548.2 Å), C III (977.0 Å), and Si IV (1393.8 Å). In every case, there is a region of very strongly enhanced absorption at impact parameters of $\lesssim$ 2 pkpc, which is smeared along the LOS direction. This elongation likely originates primarily from gas peculiar velocities, as discussed in § 2.4.7.

Table 2.3: The median $\log_{10} r_{\mathrm{H\,I}}$ and 1σ errors as a function of impact parameter (rows) and distance along the LOS (columns), used to construct Fig. 2.4. The values from the innermost transverse and LOS distance bins are plotted in Fig. 2.5. Tables for O VI, N V, C IV, C III, and Si IV are available online at http://www.strw.leidenuniv.nl/~turnerm/kbss_metals_table.pdf.

D (pMpc)	0.04–0.13	0.13–0.18	0.18–0.25	0.25–0.36	0.36–0.50	0.50–0.71	0.71–1.00	1.00–1.42	1.42–2.00
0.00–0.13	$1.06^{+0.94}_{-0.29}$	$0.13^{+0.25}_{-0.37}$	$0.08^{+0.39}_{-1.37}$	$-0.83^{+0.29}_{-0.14}$	$-0.28^{+0.15}_{-0.17}$	$-0.78^{+0.18}_{-0.17}$	$-0.98^{+0.09}_{-0.09}$	$-0.97^{+0.08}_{-0.08}$	$-0.92^{+0.09}_{-0.08}$
0.13–0.18	$0.95^{+0.32}_{-0.31}$	$-0.12^{+0.18}_{-0.24}$	$0.11^{+0.24}_{-0.99}$	$-0.94^{+0.27}_{-0.21}$	$-0.40^{+0.12}_{-0.17}$	$-0.81^{+0.11}_{-0.15}$	$-0.95^{+0.12}_{-0.11}$	$-0.98^{+0.08}_{-0.09}$	$-0.92^{+0.10}_{-0.09}$
0.18–0.25	$0.99^{+0.17}_{-0.21}$	$-0.40^{+0.63}_{-0.11}$	$-0.01^{+0.23}_{-0.65}$	$-0.90^{+0.42}_{-0.27}$	$-0.49^{+0.15}_{-0.14}$	$-0.72^{+0.13}_{-0.15}$	$-1.00^{+0.12}_{-0.07}$	$-0.93^{+0.08}_{-0.07}$	$-0.97^{+0.09}_{-0.08}$
0.25–0.36	$0.96^{+0.20}_{-0.70}$	$-0.31^{+0.28}_{-0.51}$	$-0.55^{+0.25}_{-0.16}$	$-0.71^{+0.21}_{-0.38}$	$-0.50^{+0.12}_{-0.16}$	$-0.55^{+0.09}_{-0.13}$	$-0.96^{+0.08}_{-0.07}$	$-0.95^{+0.09}_{-0.07}$	$-0.96^{+0.06}_{-0.07}$
0.36–0.50	$0.43^{+0.43}_{-0.72}$	$-0.68^{+0.76}_{-0.25}$	$-0.65^{+0.17}_{-0.10}$	$-0.91^{+0.24}_{-0.20}$	$-0.52^{+0.16}_{-0.18}$	$-0.63^{+0.11}_{-0.09}$	$-0.86^{+0.11}_{-0.09}$	$-0.98^{+0.06}_{-0.06}$	$-0.96^{+0.07}_{-0.06}$
0.50–0.71	$0.05^{+0.37}_{-0.47}$	$-0.53^{+0.79}_{-0.41}$	$-0.88^{+0.32}_{-0.22}$	$-0.87^{+0.24}_{-0.28}$	$-0.75^{+0.24}_{-0.19}$	$-0.70^{+0.07}_{-0.10}$	$-0.85^{+0.11}_{-0.08}$	$-0.93^{+0.06}_{-0.06}$	$-0.99^{+0.06}_{-0.07}$
0.71–1.00	$-0.51^{+0.09}_{-0.12}$	$-0.57^{+0.32}_{-0.23}$	$-0.68^{+0.27}_{-0.29}$	$-0.98^{+0.17}_{-0.18}$	$-0.79^{+0.12}_{-0.13}$	$-0.96^{+0.10}_{-0.08}$	$-0.92^{+0.06}_{-0.08}$	$-1.00^{+0.05}_{-0.06}$	$-1.02^{+0.05}_{-0.05}$
1.00–1.42	$-0.81^{+0.18}_{-0.22}$	$-0.89^{+0.13}_{-0.11}$	$-0.94^{+0.47}_{-0.19}$	$-1.09^{+0.14}_{-0.12}$	$-1.04^{+0.10}_{-0.11}$	$-1.13^{+0.09}_{-0.09}$	$-1.06^{+0.07}_{-0.06}$	$-1.09^{+0.05}_{-0.05}$	$-1.10^{+0.05}_{-0.05}$
1.42–2.00	$-1.36^{+0.19}_{-0.14}$	$-1.45^{+0.23}_{-0.18}$	$-1.04^{+0.33}_{-0.27}$	$-1.14^{+0.09}_{-0.11}$	$-1.26^{+0.07}_{-0.07}$	$-1.17^{+0.08}_{-0.08}$	$-1.09^{+0.07}_{-0.06}$	$-1.16^{+0.04}_{-0.04}$	$-1.16^{+0.04}_{-0.04}$
2.00–2.83	$-0.98^{+0.27}_{-0.22}$	$-1.43^{+0.11}_{-0.15}$	$-1.32^{+0.09}_{-0.10}$	$-1.39^{+0.13}_{-0.13}$	$-1.36^{+0.07}_{-0.08}$	$-1.16^{+0.06}_{-0.06}$	$-1.29^{+0.04}_{-0.04}$	$-1.17^{+0.03}_{-0.04}$	$-1.25^{+0.04}_{-0.04}$
2.83–3.99	$-1.01^{+0.12}_{-0.14}$	$-1.34^{+0.10}_{-0.09}$	$-1.43^{+0.21}_{-0.14}$	$-1.24^{+0.09}_{-0.09}$	$-1.27^{+0.06}_{-0.07}$	$-1.28^{+0.05}_{-0.05}$	$-1.33^{+0.05}_{-0.05}$	$-1.22^{+0.03}_{-0.03}$	$-1.28^{+0.03}_{-0.03}$
3.99–5.64	$-1.02^{+0.12}_{-0.14}$	$-1.20^{+0.11}_{-0.12}$	$-1.38^{+0.17}_{-0.12}$	$-1.21^{+0.10}_{-0.10}$	$-1.34^{+0.06}_{-0.06}$	$-1.38^{+0.05}_{-0.06}$	$-1.27^{+0.04}_{-0.04}$	$-1.29^{+0.03}_{-0.02}$	$-1.28^{+0.03}_{-0.03}$

advised that care be taken in the interpretation of these maps, as the true dynamic range of any one species may not be properly captured since the minimum of the range (set by $\tau_{Z,\mathrm{rnd}}$) is set by the contamination and/or shot noise. We list $\tau_{Z,\mathrm{rnd}}$ (as well as the median S/N for all considered pixels) for each ion in Table 2.4.

One should also keep in mind that although these maps are constructed by situating the galaxies at the origin, at large distances the median absorption is likely affected by gas near neighbouring galaxies, most of which will be undetected. These maps should be interpreted as the average properties of gas around galaxies, which include the effects of clustering. We elaborate further on this point in § 2.4.4.

Before further discussing Fig. 2.4, we first summarise the results from a similar analysis of H I from Rakic et al. (2012), using an earlier sample from the KBSS (see also Rudie et al. 2012b). We note that the 2-D H I median optical depth map presented in Fig. 6 of Rakic et al. (2012) is analogous to the top left panel of Fig. 2.4 in this work (but created with a slightly different galaxy sample). As described in Rakic et al. (2012), the first point to note from these figures is the strongly enhanced absorption extending $\sim 10^2$ pkpc in the transverse direction and ~ 1 pMpc (~ 240 km s^{-1}) along the LOS. They concluded that this redshift space distortion, often called the "finger of God" effect, could have two origins. Firstly, the redshift estimates of the galaxies have associated errors that smear the signal along the LOS. Specifically, the errors are roughly $\Delta v \approx 150$ km s^{-1} for LRIS, $\Delta v \approx 60$ km s^{-1} for NIRSPEC, and $\Delta v \approx 18$ km s^{-1} for MOSFIRE redshifts. Additionally, peculiar velocities of the gas arising from infall, outflows or virial motions may be responsible for this effect, particularly because the extent of the elongation is greater than that which one may expect purely from redshift errors.

The second main result from the 2-D H I median optical depth map studied in Rakic et al. (2012) (again, see their Fig. 6 or the top left panel of our Fig. 2.4) was the presence of an anisotropy on large scales. They noticed that while H I absorption was enhanced out to the maximum considered impact parameter of 2 pMpc, along the LOS it already dropped off at ≈ 1.5 pMpc (≈ 300 km s^{-1}). Such a feature could be attributed to the Kaiser (1987) effect, originally defined as Doppler shifts in galaxy redshifts caused by the large-scale co-herent motions of the galaxies towards cluster centres, which manifest as LOS distortions. Although in this work we are not specifically looking at clusters, any large-scale coherent motions should produce a similar effect. In the case of Rakic et al. (2012), since one would expect redshift space distortions caused by measurement errors to elongate the signal, the observed compression is likely due to peculiar velocities of infalling gas. Indeed, Rakic et al. (2013) used simulations to show that the observed anisotropy is consistent with being due to the Kaiser effect. However, we note that a similar study at $z \sim 3$ by Tummuangpak et al. (2014) examining the Lyα-galaxy correlation function found the observed infall to be smaller than would be predicted by simulations.

We emphasise here that the typical galaxy redshift error of our sample has changed sub-stantially since Rakic et al. (2012). Most galaxies in the innermost bins now have redshifts measured using nebular lines, while the converse was true for Rakic et al. (2012, see their Fig. 1). However, as we show in Appendix 2.D, the extent of the elongation of the optical depth signal along the LOS direction has not changed significantly between the two sam-ples, even though the redshift errors are now considerably smaller. This suggests that the main origin of the small-scale anisotropy is gas peculiar velocities (see § 2.4.7 for further discussion). Note also that the large-scale anisotropy detected by Rakic et al. (2012) is also

Table 2.4: The log of the median optical depth, and the median continuum S/N of all pixels (with normalized flux > 0.7) in the redshift range considered for the particular ion and recovery method.

Ion	$\log_{10}\tau_{Z,\mathrm{rnd}}$	$\mathrm{S/N}_{\mathrm{med}}$
H I	−1.29	70.1
O VI	−1.64	45.7
N V	−1.57	72.4
C IV	−2.95	83.6
C III	−1.27	37.8
Si IV	−3.16	84.4

present here, as can be seen most clearly from the top left panel of Fig. 2.5 (compare the last red point with the black point at the same distance).

While the goal of Rakic et al. (2012) was to study H I, in this work we are extending the analysis to metal ions. In Fig. 2.4 we compare the 2-D H I optical depth distribution to those of the metals. In all cases we see a strong central enhancement of absorption, which is elongated along the LOS. For a more quantitative picture, we have made "cuts" through the maps, and plotted the (unsmoothed) optical depth values from the nearest LOS bin (red squares) and the innermost transverse distance bin (black circles) for each ion in Fig. 2.5 (see also Table 2.3). Note that the first bin is identical for the transverse and LOS directions. For every ion except for N V (and one data point in Si IV), the optical depths of the data points in the LOS direction are greater than those in the transverse direction (i.e., the black points are above the red points) for bins 2–7, or out to ~ 1 pMpc.

The discrepancy between N V and the other ions is likely due to the fact that N V is both relatively weak and has H I contamination that is difficult to correct for, and not necessarily due to intrinsically different redshift-space structure. This is supported by the fact that the dynamic range of optical depths probed for N V is much smaller than those for the other ions.

In Fig. 2.5 we show the median optical depth of a random region (horizontal dashed line) as well as the 1σ scatter (horizontal dotted line). From this, it is clear that the scatter is quite large relative to many of the detected optical depth enhancements. The full distribution of pixel optical depths is discussed in more detail in § 2.4.5.

We estimate the confidence levels associated with these measurements by bootstrap resampling the galaxies in each impact parameter bin. In each bootstrap realisation we randomise the galaxy redshifts and compute the median optical depth as a function of transverse or LOS distance for both the original and randomised galaxy redshifts. Then, in each transverse or LOS distance bin, we calculate the fraction of bootstrap realisations for which the median optical depth computed using galaxies with randomised redshifts is higher than the median optical depth computed using the original galaxy redshifts. From this, we determine that for N V, only in the innermost bin is the optical depth enhancement detected with a confidence level ≥ 68% (1σ).

In Fig. 2.6 (Table 2.5) we now make larger cuts through the maps from Fig. 2.4, and divide the results for each ion by $\tau_{Z,\mathrm{rnd}}$ in order to compare the ions with each other in the same figure. Since the innermost impact parameter bin contains only 13 galaxies, and because we see an enhanced optical depth signal out to larger distances, for the cut along the LOS direction we combine the two innermost impact parameter bins to create a single bin
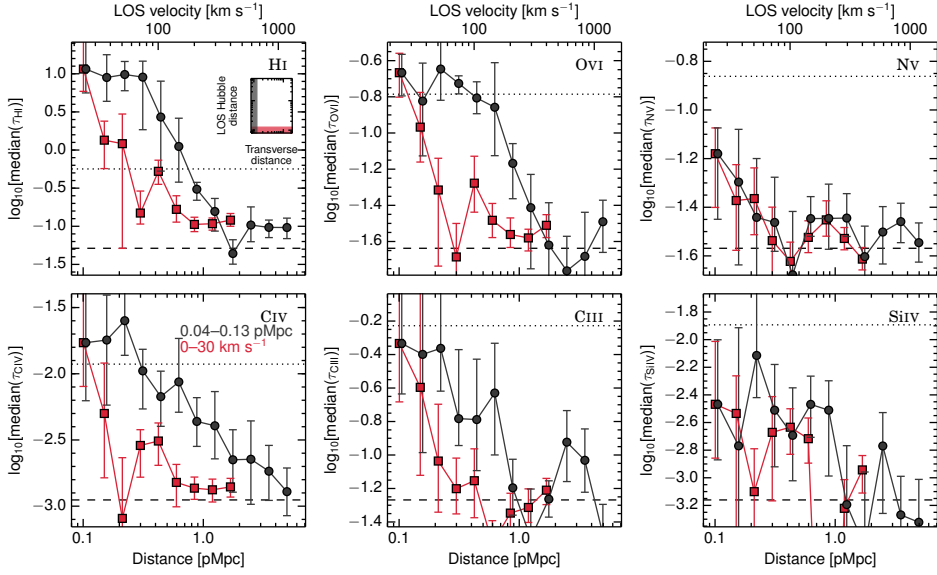
Figure 2.5: Cuts through the median optical depth maps shown in Fig. 2.4 along the innermost LOS and transverse distance bins, where each panel represents a different ion. Contrary to Fig. 2.4, the data have not been smoothed. The black circles run along the LOS and are taken from a 0.04–0.13 pMpc cut in impact parameter, while the red squares run along the transverse direction using a a ± 30.0 km s^{-1} LOS cut size, which corresponds to 0.13 pMpc at $z = 2.34$ in the case of pure Hubble flow. The insets show the scaled down areas plotted in Fig. 2.4, where the coloured strips denote the cut sizes. The horizontal dashed lines represent the median optical depths of all pixels in the redshift range considered for each ion, while the horizontal dotted line shows the 1σ scatter. In every case except for Nv, the median optical depth values along the LOS are greater than than those in the transverse direction for bins 2–7 (i.e. out to ~ 1 pMpc or 240 km s^{-1}).
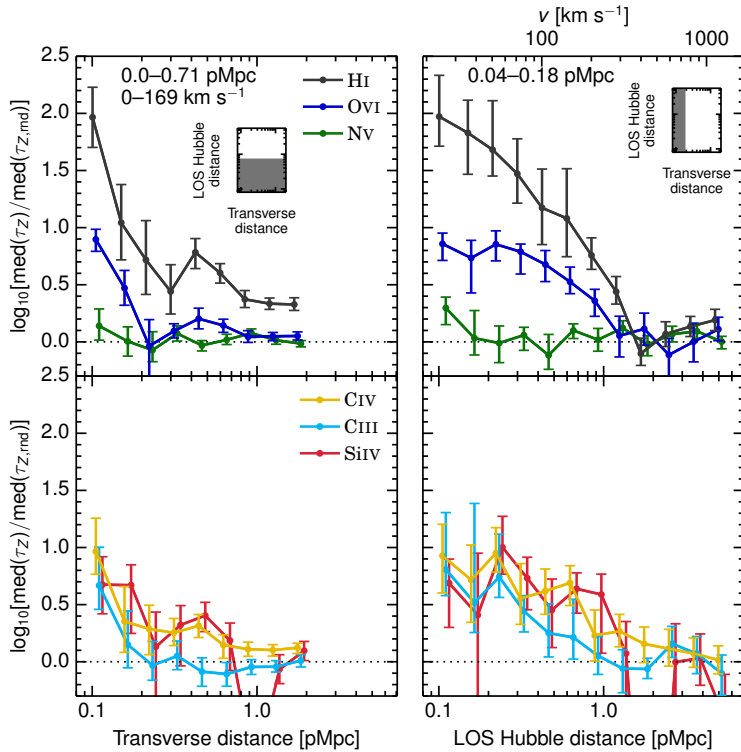
Figure 2.6: Cuts through the (unsmoothed) median optical depth maps from Fig. 2.4 along the transverse (left) and LOS (right) directions. All optical depths were divided by their corresponding $\tau_{Z,\mathrm{rnd}}$ so that the medians of all ions are aligned, and denoted by the horizontal dotted black line. For clarity, the different ions have been divided between the top and bottom panels, and the points have been offset from each other horizontally by 0.02 dex. The shaded strip in the inset shows the region included in each cut. Except for NV, the optical depths of all ions are enhanced out to at least 180 pkpc in the transverse direction and ~ 1 pMpc (~ 240 km s^{-1}) along the LOS. Like HI, the optical depth of CIV is significantly enhanced along the entire extent of the transverse direction (bottom left panel).

Table 2.5: The median $\log_{10} \tau_Z$ and 1σ errors determined by taking cuts through Fig. 2.4. Unlike in Fig. 2.5, bins have have now been combined in order to reduce the amount of noise and facilitate comparisons between different ions, and the results are plotted in Fig. 2.6. Specifically, the values along the transverse direction (top portion of the table) are measured from a 170 km s^{-1} (0.71 pMpc, or combining the first six bins) cut along the LOS, while the values along the LOS (bottom portion of the table) are calculated from a 0.18 pMpc (combining the first two bins) transverse direction cut. For comparison, the bottom row of the table lists the median optical depths measured over the full redshift range of each ion ($\tau_{Z,\mathrm{rnd}}$). We note that $\log_{10} \tau_{\mathrm{SiIV}} = -6.00$ is a flag value which indicate that the median optical depth in that bin is negative.

D_{trans} (pMpc)	H I	O VI	N V	C IV	C III	Si IV
0.04–0.13	$0.68^{+0.26}_{-0.26}$	$-0.74^{+0.09}_{-0.10}$	$-1.43^{+0.15}_{-0.13}$	$-1.99^{+0.29}_{-0.29}$	$-0.60^{+0.34}_{-0.21}$	$-2.49^{+0.24}_{-0.26}$
0.13–0.18	$-0.25^{+0.36}_{-0.33}$	$-1.17^{+0.15}_{-0.15}$	$-1.56^{+0.13}_{-0.13}$	$-2.60^{+0.21}_{-0.21}$	$-1.12^{+0.30}_{-0.21}$	$-2.49^{+0.18}_{-0.30}$
0.18–0.25	$-0.57^{+0.34}_{-0.30}$	$-1.67^{+0.23}_{-0.34}$	$-1.64^{+0.16}_{-0.19}$	$-2.67^{+0.21}_{-0.23}$	$-1.30^{+0.21}_{-0.13}$	$-3.03^{+0.30}_{-0.51}$
0.25–0.36	$-0.85^{+0.23}_{-0.12}$	$-1.54^{+0.06}_{-0.09}$	$-1.50^{+0.07}_{-0.07}$	$-2.70^{+0.13}_{-0.11}$	$-1.22^{+0.13}_{-0.12}$	$-2.84^{+0.17}_{-0.36}$
0.36–0.50	$-0.51^{+0.20}_{-0.14}$	$-1.44^{+0.09}_{-0.09}$	$-1.60^{+0.06}_{-0.05}$	$-2.64^{+0.10}_{-0.10}$	$-1.35^{+0.12}_{-0.13}$	$-2.76^{+0.12}_{-0.14}$
0.50–0.71	$-0.69^{+0.08}_{-0.09}$	$-1.49^{+0.05}_{-0.05}$	$-1.55^{+0.05}_{-0.05}$	$-2.81^{+0.09}_{-0.12}$	$-1.38^{+0.10}_{-0.10}$	$-2.98^{+0.15}_{-0.26}$
0.71–1.00	$-0.92^{+0.08}_{-0.07}$	$-1.59^{+0.05}_{-0.05}$	$-1.49^{+0.04}_{-0.03}$	$-2.84^{+0.06}_{-0.06}$	$-1.31^{+0.06}_{-0.06}$	$-4.13^{+0.35}_{-1.87}$
1.00–1.42	$-0.95^{+0.05}_{-0.05}$	$-1.59^{+0.04}_{-0.04}$	$-1.55^{+0.04}_{-0.03}$	$-2.85^{+0.05}_{-0.05}$	$-1.31^{+0.05}_{-0.05}$	$-3.23^{+0.13}_{-0.12}$
1.42–2.00	$-0.96^{+0.05}_{-0.05}$	$-1.59^{+0.04}_{-0.04}$	$-1.58^{+0.03}_{-0.03}$	$-2.83^{+0.04}_{-0.05}$	$-1.26^{+0.06}_{-0.06}$	$-3.06^{+0.08}_{-0.09}$

D_{LOS} (pMpc)	v_{LOS} (km s^{-1})	H I	O VI	N V	C IV	C III	Si IV
0.00–0.13	0–30	$0.68^{+0.36}_{-0.26}$	$-0.78^{+0.09}_{-0.15}$	$-1.27^{+0.10}_{-0.15}$	$-2.03^{+0.28}_{-0.33}$	$-0.46^{+0.50}_{-0.23}$	$-2.47^{+0.21}_{-0.39}$
0.13–0.18	30–42	$0.54^{+0.29}_{-0.29}$	$-0.90^{+0.15}_{-0.31}$	$-1.54^{+0.24}_{-0.24}$	$-2.24^{+0.31}_{-0.31}$	$-0.75^{+0.87}_{-0.25}$	$-2.75^{+0.54}_{-0.54}$
0.18–0.25	42–60	$0.39^{+0.43}_{-0.43}$	$-0.78^{+0.12}_{-0.12}$	$-1.58^{+0.15}_{-0.15}$	$-2.00^{+0.22}_{-0.22}$	$-0.53^{+0.39}_{-0.36}$	$-2.16^{+0.25}_{-0.27}$
0.25–0.36	60–84	$0.18^{+0.31}_{-0.26}$	$-0.85^{+0.07}_{-0.07}$	$-1.51^{+0.07}_{-0.13}$	$-2.40^{+0.31}_{-0.16}$	$-0.83^{+0.14}_{-0.18}$	$-2.43^{+0.18}_{-0.28}$
0.36–0.50	84–119	$-0.12^{+0.34}_{-0.35}$	$-0.96^{+0.20}_{-0.12}$	$-1.69^{+0.18}_{-0.12}$	$-2.33^{+0.23}_{-0.23}$	$-1.02^{+0.26}_{-0.21}$	$-2.71^{+0.27}_{-0.33}$
0.50–0.71	119–169	$-0.21^{+0.43}_{-0.34}$	$-1.11^{+0.10}_{-0.10}$	$-1.47^{+0.07}_{-0.06}$	$-2.26^{+0.15}_{-0.20}$	$-1.06^{+0.19}_{-0.33}$	$-2.52^{+0.14}_{-0.21}$
0.71–1.00	169–238	$-0.53^{+0.15}_{-0.12}$	$-1.28^{+0.14}_{-0.14}$	$-1.55^{+0.10}_{-0.10}$	$-2.72^{+0.22}_{-0.22}$	$-1.22^{+0.17}_{-0.16}$	$-2.57^{+0.18}_{-0.51}$
1.00–1.42	238–336	$-0.85^{+0.13}_{-0.17}$	$-1.58^{+0.17}_{-0.19}$	$-1.45^{+0.06}_{-0.06}$	$-2.69^{+0.15}_{-0.15}$	$-1.33^{+0.17}_{-0.17}$	$-3.09^{+0.28}_{-0.72}$
1.42–2.00	336–475	$-1.39^{+0.13}_{-0.13}$	$-1.52^{+0.14}_{-0.14}$	$-1.59^{+0.10}_{-0.08}$	$-2.80^{+0.15}_{-0.16}$	$-1.33^{+0.21}_{-0.09}$	$-6.00^{+2.41}_{-0.00}$
2.00–2.83	475–671	$-1.22^{+0.11}_{-0.11}$	$-1.75^{+0.14}_{-0.21}$	$-1.50^{+0.07}_{-0.07}$	$-2.84^{+0.17}_{-0.17}$	$-1.11^{+0.15}_{-0.15}$	$-3.16^{+0.34}_{-1.35}$
2.83–3.99	671–948	$-1.15^{+0.09}_{-0.11}$	$-1.64^{+0.16}_{-0.26}$	$-1.48^{+0.07}_{-0.07}$	$-2.88^{+0.14}_{-0.15}$	$-1.20^{+0.12}_{-0.12}$	$-3.13^{+0.35}_{-0.24}$
3.99–5.64	948–1339	$-1.10^{+0.09}_{-0.09}$	$-1.53^{+0.10}_{-0.10}$	$-1.57^{+0.05}_{-0.06}$	$-2.94^{+0.17}_{-0.12}$	$-1.37^{+0.16}_{-0.19}$	$-3.67^{+0.40}_{-2.33}$
$\log_{10}(\tau_{Z,\mathrm{rnd}})$		-1.29	-1.64	-1.57	-2.95	-1.27	-3.16

out to 0.18 pMpc. In the transverse direction, we combine the six smallest bins, which leads to a cut size of ±170 km s^{-1} (or 0.71 pMpc). A similar bin size was previously motivated by Rakic et al. (2011)[1] because it is the scale over which τ_{HI} is smooth in the LOS direction, and because they found errors between points along LOS direction (but not in the transverse direction) to be correlated on smaller scales (i.e. for separations $\lesssim$ 100 km s^{-1}; see Appendix B of Rakic et al. 2012). We note that the conclusions from this section are not affected by the precise size of the cut.

From the right panels of Fig. 2.6 we can see that in general, along the LOS, the optical depth enhancement is very small or undetectable beyond ~ 240 km s^{-1} (~ 1 pMpc) for both H$\textsc{i}$ and the metals. In the transverse direction only H$\textsc{i}$ and C$\textsc{iv}$ remain significantly enhanced above the noise level for all impact parameters. Calculating confidence intervals as before, we find a $\geq$ 84% confidence level for H$\textsc{i}$ in every bin, and a $\geq$ 68% (i.e., 1σ) confidence level for C$\textsc{iv}$ at every point except for the sixth bin (0.50–0.71 pMpc) which has a confidence level of 55%.

It is important to mention that the non-detection of this large-scale enhancement for the other the metal ions may be due to sensitivity limits rather than a true paucity of these species at larger impact parameters. Due either to contamination (for ions with rest wavelengths shortward of Lyα) or shot noise and continuum fitting errors (for Si$\textsc{iv}$), we are likely unable to probe optical depths down to the true median level for these ions.

2.4.2 Rescaled profiles

Next we consider the distribution of the metals presented in our optical depth maps and compare them to H$\textsc{i}$ and to each other, in an effort to explore whether the measured absorption signals trace the same gaseous structure. Of course, the metal optical depths are set not only by the metal abundance, but are also determined by the varying degree of ionisation and hence by the density and temperature of the gas in which they reside.

With this point in mind, we explore whether the optical depth profiles of the different ions arise from the same intrinsic functional form, i.e. whether their spatial (in the transverse direction) or kinematic (in the LOS direction) profiles have the same shape. However, as Figs. 2.4, 2.5, and 2.6 suggest, the comparison is not straightforward, as some metals have a very small dynamic range where the median optical depth (set by the detection limit) lies close to the maximum binned optical depth value. We therefore propose a method to normalise the curves to alleviate this problem.

If all ions follow the same intrinsic profile, but appear to vary because the transitions through which they are observed have different strengths and because they suffer from different levels of contamination and noise, then for each ion Z, the median optical depth profile can be written as

$$f_Z(x) = a_Z f(x) + \text{med}_Z \tag{2.8}$$

where $f_Z(x)$ is the observed, apparent optical depth of species Z, $f(x)$ is the intrinsic profile (which varies from $\max(f)$ at $x = 0$ to 0 as $x \to \infty$), a_Z is a scale factor that sets the relative strengths of different transitions, and med_Z is the median optical depth to which the curve asymptotes (i.e. the detection limit set by noise and contamination). For C$\textsc{iv}$ and Si$\textsc{iv}$, this

---

[1]Due to a slightly different cosmology and median galaxy redshift used in Rakic et al. (2012), the velocity interval corresponding to 0.71 pMpc was closer to ±165 km s^{-1}.
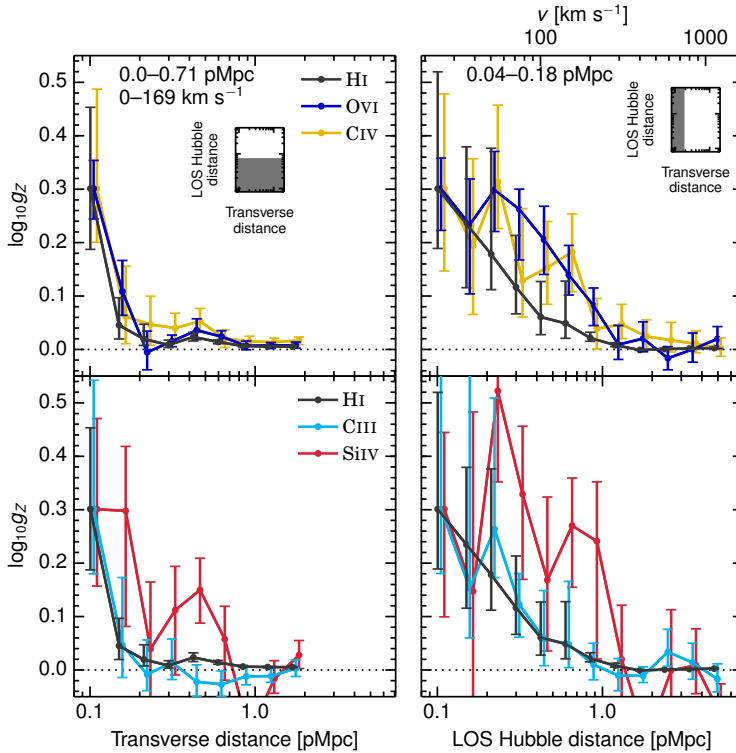
Figure 2.7: The same as Fig. 2.6, but after re-scaling the optical depths using Equation 2.9 to account for differences in transition strengths and detection limits. Note that Hɪ is shown in both the top and bottom panels, while Nv has been removed. In general, the shapes of the rescaled metal optical depth profiles appear similar to that of Hɪ, although Ovɪ, Cɪv and Siɪv are somewhat enhanced relative to Hɪ along the LOS direction.

value is set mostly by shot noise and continuum fitting errors, while for the other transitions it is mainly unrelated absorption (i.e. contamination).

Although the values of a_Z and med_Z will certainly depend on the ion in question, it is possible that the intrinsic profile $f(x)$ does not vary between different ions. To examine this, we can try and normalise the curves such that, if indeed $f(x)$ does not depend on the ion Z, then the normalised curves should also be equivalent for different ions. This can be achieved using the following transformation:

$$g_Z(x) = \frac{f_Z(x) - \text{med}_Z}{\text{max}_Z - \text{med}_Z} + 1 \qquad (2.9)$$

where $\text{max}_Z = f_Z(x_{\text{max}})$ and x_{max} is the value of x at which the maximum value of $f_Z(x)$ occurs. For the optical depth profiles, x_{max} is usually the innermost transverse or LOS distance bin. Combining Equations 2.8 and 2.9, we obtain the expression $g_Z(x) = f(x)/f(x_{\text{max}}) + 1$, which is independent of Z and varies between 1 and 2. In summary, if the observed spatial and/or kinematic optical depth profiles of different ions are all the same apart from

a multiplicative factor reflecting the strength of the transition and an additional constant reflecting the levels of contamination and noise, then by using the transformation in Equation 2.9, the resulting curves should all overlap each other.

We implemented the above by taking med_k to be $\tau_{Z,\mathrm{rnd}}$, and max_k to be the optical depth of the innermost point of the curve in question (the values differ along the LOS and transverse directions, due to the different cut sizes taken). The resulting curves are shown in Fig. 2.7. Note that the normalisation method will amplify any small point-to-point variations inversely with dynamic range. Since Nv has a relatively small dynamic range, variations which appear small in the top left panel (particularly the first few points along the transverse direction) of Fig. 2.6 manifest themselves as large deviations compared to the other curves, and for this reason we have chosen to omit Nv from Fig. 2.7.

The curves resulting from cuts along the transverse direction (left panels of Fig. 2.7) appear quite similar for all species observed. In every case (including Hɪ), the optical depth drops sharply after the first impact parameter bin, and quickly asymptotes to the median. The plateau in the absorption at impact parameters 180 pkpc–2 pMpc that was clearly detected for Hɪ and Cɪv in Figs. 2.4 and 2.6 may therefore also be present for the other species, but cannot be detected due to the smaller dynamic range in their recovered optical depths. Along the LOS (right panels of Fig. 2.7), the situation is less uniform. While Cɪɪɪ tends to trace the Hɪ profile, Ovɪ, Cɪv and Siɪv appear to be *more enhanced* than Hɪ out to ~ 1 pMpc or 240 km s^{-1}. This result suggests that we might be seeing two different gas phases, i.e. a relatively compact one traced mainly by Hɪ and Cɪɪɪ, and a phase that is more extented in real and/or velocity space and that is traced by Ovɪ, Cɪv and Siɪv.

We again point out that any fluctuations in the normalised optical depth values for the metal ions are magnified in these figures, due to the lower dynamic range of optical depths. Although this makes it difficult to draw secure conclusions about any observed differences in the distributions of the metals with respect to each other and to Hɪ, we can at least say that the strong Hɪ enhancement seen along the LOS direction is also present for the metal ions Ovɪ, Cɪv, Cɪɪɪ and Siɪv.

2.4.3   3-D Hubble distance

If we assume that the velocity differences between galaxies and the nearby absorption regions in the quasar are due only to Hubble flow, then we can calculate the 3-D Hubble distance as $\sqrt{b^2 + (H(z)\Delta v)^2}$, where b is the galaxy impact parameter, $H(z)$ is the Hubble parameter, and Δv is the LOS separation between the absorber and the galaxy. We have computed the 3-D Hubble distance for every galaxy-pixel pair, divided them into 0.15 dex distance bins as in Fig. 2.4, and taken the median optical depth in every bin. The result is plotted in Fig. 2.8, and the data are given in Table 2.6. We stress that this metric is a poor approximation for distances $\lesssim$ 1 pMpc since Fig. 2.5 revealed strong anisotropies along the LOS on this scale, and we have shaded the poor-approximation region grey in Fig. 2.8.

Although using the Hubble distance results in the loss of some important information, by using this projection we are able to achieve higher S/N ratios because each 3-D bin contains many more pixels than those constructed from cuts through the median optical depth maps. Specifically, we are able see a significant enhancement of optical depth above the median for Hɪ out to ~ 2.8 pMpc (99.5% confidence) and for Cɪv out to ~ 4.0 pMpc
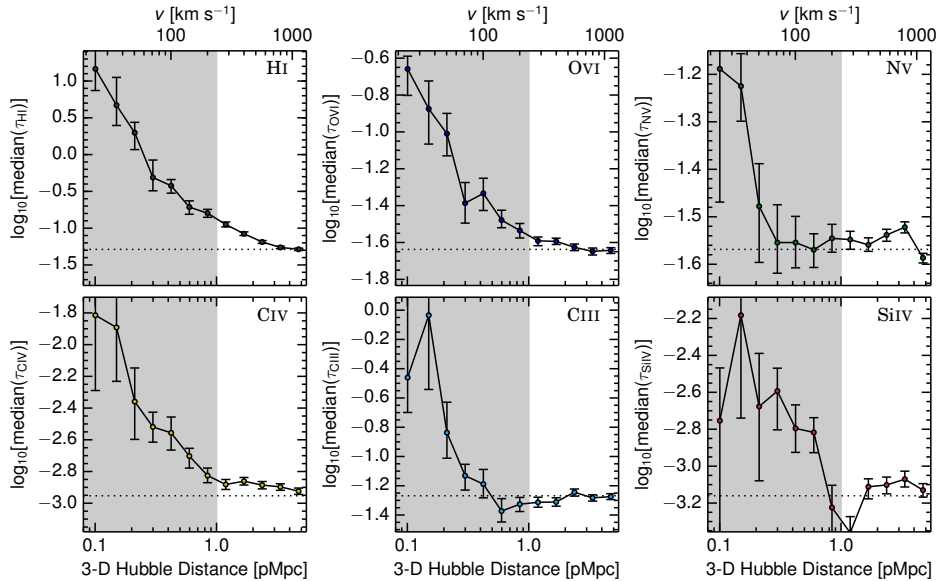
Figure 2.8: The median optical depth as a function of 3-D Hubble distance for all galaxies in our sample, assuming that velocity differences between the galaxies and associated absorption regions are purely due to Hubble flow. This assumption is certainly incorrect for $\lesssim 1$ pMpc, and we have therefore greyed out the regions that we believe are effected by redshift-space distortions. The horizontal dotted black lines indicate the median optical depth for all pixels of the ion shown. One advantage of examining 3-D Hubble distance is that it allows us to decrease the noise by combining large numbers of pixels, particularly at large distances. As a result, the enhancement in the median optical depth of C IV can now be detected out to ~ 4 pMpc.

Table 2.6: The median $\log_{10}\tau_Z$ and 1σ errors as a function of 3-D Hubble distance (left column). Columns 2–7 display values for the different ions Z studied in this work, and the data are plotted in Fig. 2.8. For comparison, the bottom row of the table lists the median optical depths measured over the full redshift range of each ion ($\tau_{Z,\mathrm{rnd}}$).

v_{Hubble} (km s^{-1})	D_{Hubble} (pMpc)	H I	O VI	N V	C IV	C III	Si IV
0–30	0.00–0.13	$1.16^{+1.39}_{-0.29}$	$-0.66^{+0.07}_{-0.14}$	$-1.19^{+0.11}_{-0.28}$	$-1.81^{+0.63}_{-0.47}$	$-0.46^{+4.46}_{-0.24}$	$-2.75^{+0.29}_{-3.25}$
30–42	0.13–0.18	$0.67^{+0.38}_{-0.29}$	$-0.88^{+0.15}_{-0.19}$	$-1.22^{+0.07}_{-0.07}$	$-1.89^{+0.26}_{-0.34}$	$-0.03^{+0.38}_{-0.51}$	$-2.18^{+0.30}_{-0.56}$
42–60	0.18–0.25	$0.30^{+0.14}_{-0.23}$	$-1.01^{+0.11}_{-0.12}$	$-1.48^{+0.09}_{-0.07}$	$-2.36^{+0.21}_{-0.24}$	$-0.84^{+0.21}_{-0.17}$	$-2.68^{+0.29}_{-0.40}$
60–84	0.25–0.36	$-0.31^{+0.24}_{-0.18}$	$-1.39^{+0.11}_{-0.11}$	$-1.55^{+0.08}_{-0.06}$	$-2.52^{+0.09}_{-0.10}$	$-1.13^{+0.08}_{-0.10}$	$-2.59^{+0.12}_{-0.21}$
84–119	0.36–0.50	$-0.42^{+0.08}_{-0.10}$	$-1.33^{+0.08}_{-0.09}$	$-1.55^{+0.06}_{-0.05}$	$-2.56^{+0.10}_{-0.11}$	$-1.19^{+0.10}_{-0.09}$	$-2.80^{+0.13}_{-0.13}$
119–169	0.50–0.71	$-0.71^{+0.08}_{-0.10}$	$-1.48^{+0.05}_{-0.04}$	$-1.57^{+0.03}_{-0.04}$	$-2.70^{+0.05}_{-0.08}$	$-1.37^{+0.09}_{-0.07}$	$-2.82^{+0.08}_{-0.11}$
169–238	0.71–1.00	$-0.80^{+0.05}_{-0.06}$	$-1.53^{+0.04}_{-0.04}$	$-1.55^{+0.03}_{-0.03}$	$-2.83^{+0.05}_{-0.05}$	$-1.33^{+0.05}_{-0.05}$	$-3.22^{+0.12}_{-0.17}$
238–336	1.00–1.42	$-0.95^{+0.03}_{-0.03}$	$-1.59^{+0.02}_{-0.03}$	$-1.55^{+0.02}_{-0.02}$	$-2.88^{+0.03}_{-0.03}$	$-1.31^{+0.03}_{-0.03}$	$-3.36^{+0.09}_{-0.17}$
336–475	1.42–2.00	$-1.08^{+0.03}_{-0.02}$	$-1.59^{+0.02}_{-0.02}$	$-1.56^{+0.01}_{-0.01}$	$-2.86^{+0.02}_{-0.02}$	$-1.31^{+0.03}_{-0.03}$	$-3.11^{+0.04}_{-0.07}$
475–671	2.00–2.83	$-1.19^{+0.02}_{-0.02}$	$-1.63^{+0.02}_{-0.02}$	$-1.54^{+0.01}_{-0.01}$	$-2.89^{+0.02}_{-0.02}$	$-1.24^{+0.02}_{-0.03}$	$-3.10^{+0.04}_{-0.05}$
671–948	2.83–3.99	$-1.26^{+0.02}_{-0.02}$	$-1.65^{+0.02}_{-0.02}$	$-1.52^{+0.01}_{-0.01}$	$-2.90^{+0.02}_{-0.02}$	$-1.28^{+0.02}_{-0.02}$	$-3.07^{+0.04}_{-0.04}$
948–1339	3.99–5.64	$-1.29^{+0.02}_{-0.02}$	$-1.64^{+0.01}_{-0.02}$	$-1.59^{+0.01}_{-0.01}$	$-2.92^{+0.02}_{-0.02}$	$-1.27^{+0.02}_{-0.02}$	$-3.13^{+0.04}_{-0.04}$
	$\log_{10}(\tau_{Z,\mathrm{rnd}})$	-1.29	-1.64	-1.57	-2.95	-1.27	-3.16

(90% confidence)[2]. The latter result suggests that the enhancement of CIV above the median seen throughout the 2-D map in Fig. 2.4 is a real effect. We note that for NV, the enhancement seen at ~ 900 km s^{-1} is likely due to residual contamination from its own doublet.

2.4.4   Covering fraction

The results from § 2.4.1 tell us about the median optical depths as a function of distance from galaxies. However, we are also interested in the rate of occurrence of relatively high optical depth (and hence more rare) systems. To quantify this, we use the covering fraction, which we define as the fraction of galaxies in a particular impact parameter bin for which the median pixel optical depth within ±170 km s^{-1} of the galaxy exceeds some threshold value $\tau_{Z,\text{thresh}}$. We have checked that the results remain unchanged using a larger velocity interval of ±300 km s^{-1}.

To see which values of $\tau_{Z,\text{thresh}}$ may be informative, for each ion Z we calculate the median optical depth for 1000 random ±170 km s^{-1} regions selected from the full recovered redshift range, which are taken to represent typical IGM values. We then select the $\tau_{Z,\text{thresh}}$ values for which the covering fractions of the 1000 random regions are 0.25, 0.05, and 0.01 (the exact values of $\tau_{Z,\text{thresh}}$ for each ion are displayed in Fig. 2.9). In Appendix 2.C we instead use an EW threshold and find that our conclusions still hold. The covering fractions for HI and each metal, as a function of impact parameter and for different values of $\tau_{Z,\text{thresh}}$ are shown in Fig. 2.9 and Table 2.7, with the associated random region covering fraction denoted by the horizontal dashed lines.

First we examine values of $\tau_{Z,\text{thresh}}$ for which the IGM covering fraction is 0.25 and 0.05 (red circles and blue diamonds respectively). In every case except for NV, we observe elevated covering fractions within the two smallest impact parameter bins. For larger impact parameters, the HI covering fraction is higher than the IGM value out to 2 pMpc, which is in agreement with § 5 of Rudie et al. (2012b). Additionally, OVI and in particular CIV both have covering fractions significantly above that of the IGM along the full range of impact parameters. This is consistent with the finding that we are able to detect levels of CIV optical depth enhancement above the median IGM value at all impact parameters probed (Figs. 2.4 and 2.6). Again, the fact that for impact parameters ≳ 180 pkpc we only see significantly enhanced covering fractions for HI, OVI, and CIV does not necessarily mean that the other metal ions are not present, but could rather be due to contamination and noise preventing us from probing low enough optical depths, and could also be due to changes in the ionisation level of the gas.

Finally, turning our attention to the values of $\tau_{Z,\text{thresh}}$ for which the IGM covering fraction is 0.01 (yellow squares), only HI, CIV, and SiIV show significant enhancement at small impact parameters. This suggests that for the ions bluewards of Lyα, the highest optical depth values are largely the result of contamination. Furthermore, HI and CIV no longer have enhanced covering fractions at large impact parameters, which suggests that the rare, high optical depth systems are preferentially located very near galaxies.

Here we address the two major transverse direction enhancement extents seen in HI and the metal ions: a strong enhancement (out to ≈ 180 pkpc) and a weak enhancement

---

[2]We note that in the eighth 3-D Hubble distance bin, which runs from 1.0–1.4 pMpc, we only detect the CIV enhancement with a confidence level of 80%.
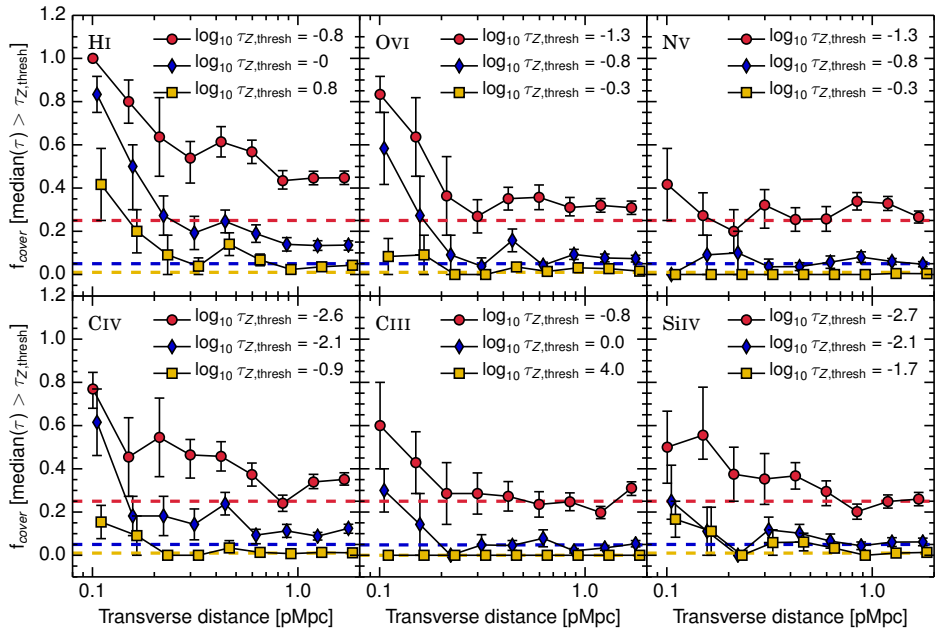
Figure 2.9: Covering fraction for each ion, defined as the fraction of galaxies within some impact parameter bin that have a median optical depth within ±170 km s^{-1} above some threshold value. These values are chosen to be the optical depths for which the covering fraction computed for 1000 random regions in the IGM is equal to 0.25 (red circles), 0.05 (blue diamonds), and 0.01 (yellow squares). The IGM covering fraction values are indicated by the horizontal dashed lines of corresponding colour. Points determined using different $\tau_{Z,\text{thresh}}$ values have been offset horizontally by 0.02 dex for clarity. We note that points where the covering fraction is 0 or 1 have no errorbar because bootstrapping galaxies from the same sample cannot change the covering fraction within that particular impact parameter bin.

Table 2.7: Covering fraction and 1σ errors as a function of transverse distance (top row), which is defined as the fraction of galaxies in each impact parameter bin that have a median optical depth within $\pm 170\ \mathrm{km\,s^{-1}}$ above some threshold value. The threshold values are set by the optical depth at which the covering fraction of 1000 random $\pm 170\ \mathrm{km\,s^{-1}}$ regions, f_{GM}, are equal to 0.25, 0.05, and 0.01 (second column), and the results are plotted in Fig. 2.9.

Ion	D_{trans} (pMpc) f_{GM}	0.04–0.13	0.13–0.18	0.18–0.25	0.25–0.36	0.36–0.50	0.50–0.71	0.71–1.00	1.00–1.42	1.42–2.00
Hɪ	0.25	$1.00^{+0.00}_{-0.00}$	$0.80^{+0.10}_{-0.10}$	$0.64^{+0.18}_{-0.18}$	$0.54^{+0.08}_{-0.12}$	$0.61^{+0.07}_{-0.07}$	$0.57^{+0.05}_{-0.05}$	$0.43^{+0.05}_{-0.04}$	$0.45^{+0.03}_{-0.03}$	$0.45^{+0.03}_{-0.03}$
	0.05	$0.83^{+0.08}_{-0.08}$	$0.50^{+0.10}_{-0.20}$	$0.27^{+0.09}_{-0.09}$	$0.19^{+0.08}_{-0.08}$	$0.25^{+0.05}_{-0.05}$	$0.19^{+0.04}_{-0.04}$	$0.14^{+0.03}_{-0.03}$	$0.13^{+0.02}_{-0.02}$	$0.14^{+0.02}_{-0.02}$
	0.01	$0.42^{+0.17}_{-0.17}$	$0.20^{+0.10}_{-0.10}$	$0.09^{+0.09}_{-0.09}$	$0.04^{+0.04}_{-0.04}$	$0.14^{+0.05}_{-0.05}$	$0.07^{+0.03}_{-0.03}$	$0.02^{+0.02}_{-0.02}$	$0.04^{+0.01}_{-0.01}$	$0.04^{+0.01}_{-0.01}$
Oᴠɪ	0.25	$0.83^{+0.08}_{-0.08}$	$0.64^{+0.18}_{-0.18}$	$0.36^{+0.18}_{-0.18}$	$0.27^{+0.08}_{-0.08}$	$0.35^{+0.05}_{-0.06}$	$0.36^{+0.06}_{-0.06}$	$0.31^{+0.05}_{-0.04}$	$0.32^{+0.03}_{-0.03}$	$0.31^{+0.03}_{-0.03}$
	0.05	$0.58^{+0.17}_{-0.17}$	$0.27^{+0.18}_{-0.18}$	$0.09^{+0.09}_{-0.09}$	$0.04^{+0.04}_{-0.04}$	$0.16^{+0.05}_{-0.05}$	$0.04^{+0.01}_{-0.03}$	$0.09^{+0.02}_{-0.02}$	$0.08^{+0.02}_{-0.02}$	$0.07^{+0.02}_{-0.02}$
	0.01	$0.08^{+0.08}_{-0.08}$	$0.09^{+0.09}_{-0.09}$	$0.00^{+0.00}_{-0.00}$	$0.00^{+0.00}_{-0.00}$	$0.04^{+0.02}_{-0.02}$	$0.01^{+0.01}_{-0.01}$	$0.03^{+0.02}_{-0.02}$	$0.03^{+0.01}_{-0.01}$	$0.02^{+0.01}_{-0.01}$
Nᴠ	0.25	$0.42^{+0.17}_{-0.17}$	$0.27^{+0.1}_{-0.09}$	$0.20^{+0.10}_{-0.10}$	$0.32^{+0.07}_{-0.11}$	$0.25^{+0.05}_{-0.05}$	$0.26^{+0.06}_{-0.06}$	$0.34^{+0.04}_{-0.04}$	$0.33^{+0.03}_{-0.03}$	$0.27^{+0.03}_{-0.03}$
	0.05	$0.00^{+0.00}_{-0.00}$	$0.09^{+0.09}_{-0.09}$	$0.10^{+0.10}_{-0.10}$	$0.04^{+0.04}_{-0.04}$	$0.04^{+0.02}_{-0.02}$	$0.06^{+0.03}_{-0.03}$	$0.08^{+0.02}_{-0.02}$	$0.06^{+0.01}_{-0.01}$	$0.05^{+0.01}_{-0.01}$
	0.01	$0.00^{+0.00}_{-0.00}$	$0.00^{+0.00}_{-0.00}$	$0.00^{+0.00}_{-0.00}$	$0.00^{+0.00}_{-0.00}$	$0.00^{+0.00}_{-0.00}$	$0.00^{+0.00}_{-0.00}$	$0.00^{+0.00}_{-0.00}$	$0.00^{+0.00}_{-0.00}$	$0.00^{+0.00}_{-0.00}$
Cɪᴠ	0.25	$0.77^{+0.08}_{-0.09}$	$0.45^{+0.18}_{-0.18}$	$0.55^{+0.18}_{-0.18}$	$0.46^{+0.07}_{-0.11}$	$0.46^{+0.07}_{-0.07}$	$0.37^{+0.05}_{-0.05}$	$0.24^{+0.04}_{-0.04}$	$0.34^{+0.04}_{-0.03}$	$0.35^{+0.03}_{-0.03}$
	0.05	$0.62^{+0.15}_{-0.15}$	$0.18^{+0.09}_{-0.09}$	$0.18^{+0.09}_{-0.09}$	$0.14^{+0.07}_{-0.07}$	$0.24^{+0.05}_{-0.05}$	$0.09^{+0.03}_{-0.04}$	$0.11^{+0.03}_{-0.03}$	$0.09^{+0.02}_{-0.02}$	$0.12^{+0.02}_{-0.02}$
	0.01	$0.15^{+0.08}_{-0.08}$	$0.09^{+0.09}_{-0.09}$	$0.00^{+0.00}_{-0.00}$	$0.00^{+0.00}_{-0.00}$	$0.03^{+0.02}_{-0.02}$	$0.01^{+0.01}_{-0.01}$	$0.01^{+0.01}_{-0.01}$	$0.01^{+0.01}_{-0.01}$	$0.01^{+0.01}_{-0.01}$
Cɪɪɪ	0.25	$0.60^{+0.20}_{-0.20}$	$0.43^{+0.14}_{-0.14}$	$0.29^{+0.14}_{-0.14}$	$0.29^{+0.10}_{-0.10}$	$0.27^{+0.07}_{-0.07}$	$0.24^{+0.06}_{-0.06}$	$0.25^{+0.04}_{-0.04}$	$0.20^{+0.03}_{-0.03}$	$0.31^{+0.03}_{-0.03}$
	0.05	$0.30^{+0.10}_{-0.10}$	$0.14^{+0.14}_{-0.14}$	$0.00^{+0.00}_{-0.00}$	$0.05^{+0.05}_{-0.05}$	$0.05^{+0.02}_{-0.02}$	$0.08^{+0.04}_{-0.04}$	$0.02^{+0.01}_{-0.01}$	$0.03^{+0.01}_{-0.01}$	$0.05^{+0.01}_{-0.01}$
	0.01	$0.00^{+0.00}_{-0.00}$	$0.00^{+0.00}_{-0.00}$	$0.00^{+0.00}_{-0.00}$	$0.00^{+0.00}_{-0.00}$	$0.00^{+0.00}_{-0.00}$	$0.00^{+0.00}_{-0.00}$	$0.00^{+0.00}_{-0.00}$	$0.00^{+0.00}_{-0.00}$	$0.00^{+0.00}_{-0.00}$
Siɪᴠ	0.25	$0.50^{+0.17}_{-0.17}$	$0.56^{+0.22}_{-0.11}$	$0.38^{+0.12}_{-0.12}$	$0.35^{+0.12}_{-0.12}$	$0.37^{+0.06}_{-0.07}$	$0.30^{+0.05}_{-0.07}$	$0.20^{+0.04}_{-0.04}$	$0.25^{+0.03}_{-0.03}$	$0.26^{+0.03}_{-0.03}$
	0.05	$0.25^{+0.17}_{-0.08}$	$0.11^{+0.11}_{-0.11}$	$0.00^{+0.00}_{-0.00}$	$0.12^{+0.06}_{-0.06}$	$0.10^{+0.04}_{-0.04}$	$0.07^{+0.03}_{-0.03}$	$0.04^{+0.02}_{-0.02}$	$0.06^{+0.02}_{-0.02}$	$0.06^{+0.02}_{-0.02}$
	0.01	$0.17^{+0.08}_{-0.08}$	$0.11^{+0.11}_{-0.11}$	$0.00^{+0.00}_{-0.00}$	$0.06^{+0.06}_{-0.06}$	$0.06^{+0.04}_{-0.04}$	$0.03^{+0.02}_{-0.02}$	$0.00^{+0.00}_{-0.00}$	$0.01^{+0.01}_{-0.01}$	$0.01^{+0.01}_{-0.01}$

(out to $\approx$ 2 pMpc). We have observed the strong enhancement for all ions studied out to $\approx$ 180 pkpc, in both the transverse cuts (left panels of Fig. 2.6) and the covering fraction (Fig. 2.9). To put this distance into context, we take the comoving number density of identically selected galaxies in this survey from Reddy et al. (2008), which is $\Phi = 3.7 \times 10^{-3}$ cMpc^{-3} (for $\mathcal{R} \leq 25.5$). From this, we can infer that the regions within 180 pkpc around galaxies comprise only $\sim$ 0.4% of the total volume of the universe. In spite of being present in a very small volume, the high optical depths and covering fractions within this distance indicate that these regions contain substantial amounts of H I and metals ions.

The second, weaker enhancement out to $\approx$ 2 pMpc can be seen for H I and C IV (and marginally for O VI) in the transverse-direction cuts (left panels of Fig. 2.6), 3-D Hubble distance (Fig. 2.8), and covering fraction (Fig. 2.9).

Although the enhanced absorption observed on these scales is statistically significant, we note that 2 pMpc corresponds to $\sim$ 20$\times$ the virial radii of the galaxies in our sample, far beyond the physical sphere of influence of the galaxies centred at the origins of these figures. Performing the same calculation as above, to determine the fraction of the volume of the Universe within 2 pMpc of these galaxies results in a value that exceeds unity – i.e., if these galaxies were uniformly distributed, all of space would lie within 2 pMpc of a galaxies that meets these selection criteria. However, it is well established that galaxies are clustered (e.g., Adelberger et al., 2005b), so we would expect many of the "spheres" from our simple calculation to be overlapping.

Indeed, Rudie et al. (2012b) noted that the galaxy-galaxy autocorrelation scale-length for this same sample of galaxies has been measured to be $\approx$ 2.8 pMpc (Trainor & Steidel, 2012), which certainly suggests that the 2-halo term plays a role in the enhancement at large scales. Another possibility is that we are seeing metals in the IGM; in reality we are likely observing a combination of both CGM metals from other clustered galaxies, as well as some truly intergalactic metals.

Studies by Adelberger et al. (2003) at $z \sim 3$ and Adelberger et al. (2005a) at $z \sim 2.5$, using decrements in transmitted flux, found evidence for elevated (with respect to random IGM positions) H I absorption out to impact parameters of $\sim$ 2 pMpc. The authors also measured a strong correlation between the positions of C IV absorbers and galaxies, with the strength of the correlation increasing with absorber strength. Furthermore, at $z \sim 0.5$ Zhu et al. (2014) found Mg II absorber and galaxy positions to be correlated out to $\sim$ 20 pMpc. The above results are certainly consistent with the fact that we are finding enhanced covering fractions for H I and C IV out to impact parameters of 2 pMpc.

2.4.5 Optical depth distributions

Up until this point we have only considered median optical depths. To acquire a sense of how individual pixel optical depth values are distributed, we have plotted their probability density functions (PDFs) for ±170 km s^{-1} regions around galaxies in Fig. 2.10, where each panel shows a different ion. The galaxies are divided into the usual impact parameter bins (coloured lines), except for the final six bins which have been combined into three (with sizes of 0.30 dex for clarity). The values marked "sat." are for pixels which we found to be saturated, and, in the case of H I, whose optical depths could not be recovered from higher order Lyman series lines. We set the optical depth values of such pixels to 10^4. We have also determined the PDFs for 1000 random regions in the IGM, which are shown by the black
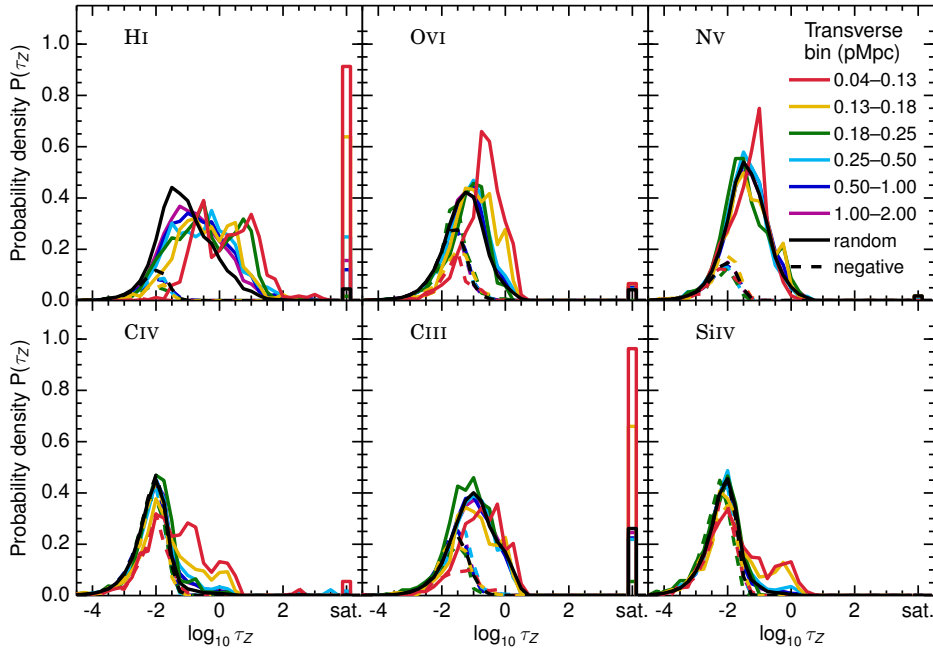
Figure 2.10: Pixel optical depth PDFs within ± 170 km s^{-1} of galaxies divided by impact parameter bin (coloured lines), where each panel displays a different ion. We have used the usual binning scheme, but combined the last six bins to create three in order to reduce the number of lines plotted. The black line shows the PDF for 1000 random ± 170 km s^{-1} regions within the full redshift range corresponding to each ion. The portion marked "sat" represents pixels that were found to be saturated, and for which the optical depth could not be recovered. The dashed lines show the PDFs for pixels which had negative optical depths, where we have taken the log of their absolute values. Except for Nv, the PDFs for the two smallest impact parameter bins (and more for Hi) tend to higher optical depth values compared to the PDF of random regions.

lines. Finally, for pixels which have negative optical depths, we have taken the log of their absolute values and plotted their PDFs using dashed lines.

First we consider the source of the positive optical depths, by comparing their distributions (solid lines) to those of negative optical depths (dashed lines), which we expect to reflect the level of shot-noise in the spectrum. Aside from the bins with impact parameters < 0.18 pMpc, for Civ and Siiv the distributions of positive and negative optical depths are similar to each other, suggesting that most of the positive optical depths arise from shot noise around the level of the continuum. This is not surprising for ions with restframe wavelengths redwards of the QSO Lyα emission, i.e. regions that do not suffer from Hi contamination. On the other hand, for the remaining ions, the negative optical depths contribute minimally to the full distribution, which means that the positive optical depths should primarily reflect real absorption (including contamination).

Fig. 2.10 demonstrates that the scatter in optical depths is quite large. Even for regions at small galactocentric distances, many optical depths reach values typical of random IGM regions (which may of course be close to undetected galaxies). However, except perhaps for Nv, the optical depth PDFs of the 2 or 3 smallest impact parameter bins for each ion

appear substantially different from the random region PDF, and in particular tend towards higher optical depth values.[3]

2.4.6 Equivalent widths

In studies where individual absorption lines are examined, EW is often used to parametrise their strength independently of the line shapes, and can also be computed using spectral stacking. Another advantage of employing EW as a metric is that it can be applied to spectra with low S/N or resolution. In particular, to measure absorption at very small impact parameters (i.e., less than our smallest value of 35 pkpc), the usage of QSO-galaxy pairs is currently not viable, and instead galaxy-galaxy pairs (with much lower resolution spectra) must be used. By stacking such spectra to create mean flux profiles, Steidel et al. (2010) measured EW as a function of galaxy impact parameter (see their Fig. 21 and their Table 4). We have plotted their results for the ions which are also in our sample (H I, C IV, and Si IV) in Fig. 2.11. In addition to measuring EWs for small impact parameters by using galaxy-galaxy pairs, they also used galaxy-quasar pairs to calculate H I EWs for impact parameters of 128–280 pkpc, which we denote by the large black open circles. We note that the galaxy-quasar sample from Steidel et al. (2010) is comprised of the same QSOs and mostly the same galaxies as the sample used in this work.

We calculate typical EWs as a function of galaxy impact parameter by shifting the absorption spectrum (i.e. the associated region of the intervening QSO) of every galaxy to the rest-frame wavelength of the ion in question and computing the mean spectrum within the transverse distance bin. To simulate the effect of a suppressed continuum, as appropriate for the low-resolution spectra used in Steidel et al. (2010), we follow Rakic et al. (2012) and calculate the mean flux level of all pixels in all spectra within the wavelength region probed for a particular ion. We then divide the mean flux profile by this value before integrating the flux decrement over ± 500 km s^{-1} to compute the EW. The results are given in Table 2.8 and Fig. 2.11. We have verified that the conclusions presented here hold if we use 150, 300 and 600 km s^{-1} intervals instead.

For overlapping impact parameter bins, we see good agreement between the two samples for H I and Si IV. Additionally, C IV shows good agreement when we compare the outer transverse distance bin of Steidel et al. (2010) with our second-smallest bin. The models from Steidel et al. (2010) predict that when one extrapolates EWs to larger impact parameters, there is sharp drop in EW around impact parameters of $\sim 10^2$ pkpc for the metal ions and around ~ 200 pkpc for H I. We do not see such an effect in our data, where the EW values drop off relatively slowly with increasing transverse distance. However, the models were only intended to explain the behaviour of the EWs down to 0.1 Å, and were insensitive to any plateau at smaller EW values. On the other hand, we find good agreement between both sets of measured H I EW values at large impact parameters, in spite of the differences in the galaxy sample, bin size, and EW measurement technique.

To ease comparison with other studies, we convert EW to column density as in Savage

---

[3]Unfortunately, because of spatial correlations between the optical depth pixels, the use of the Kolmogorov-Smirnov test to compare the PDFs is not appropriate for this data.
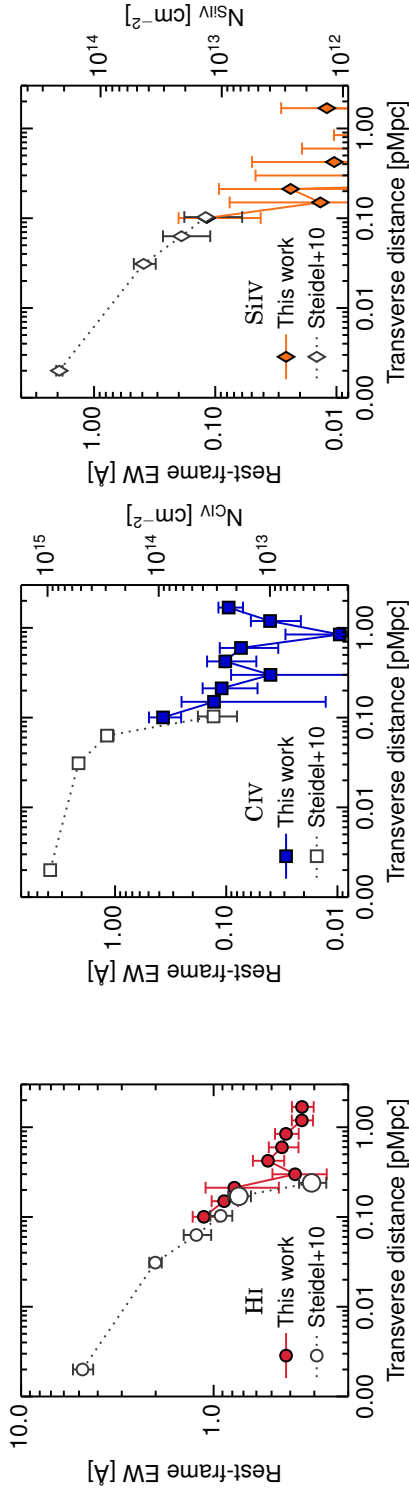
Figure 2.11: Rest-frame EW calculated using the mean spectrum within each galaxy impact parameter bin (filled points), where each panel shows a different ion. Here, the average spectrum was divided by the mean flux of all spectral pixels and the flux decrement was integrated over ±500 km s^{-1}. Also plotted are EWs calculated using galaxy pairs from low-resolution spectra (open points) as well as H$_I$ EWs from galaxy-QSO pairs (left panel, large open circles at 128–280 pkpc) taken from Steidel et al. (2010). Note that for clarity, each panel has a different range along the y-axis. EWs were also calculated for an average spectrum created from 1000 random ±500 km s^{-1} regions, and the result was negative for all three ions. For reference, on the right-hand y-axis of the two rightmost panels we show the corresponding column density calculated from Equation 2.10, which assumes that the absorbers are on the linear portion of the curve-of-growth. At the point of overlap, $\sim 10^2$ pkpc, our points agree with Steidel et al. (2010), and although we do not see the sharp drop off at larger impact parameters predicted by their models, we do find consensus in the measured H$_I$ EWs at large impact parameters.

Table 2.8: Median EWs and 1σ errors (in Å) calculated by integrating the normalised flux decrement over a ± 500 km s^{-1} region as a function of transverse distance for H I, C IV and Si IV. These values are plotted in Fig. 2.11. We also show two different column density estimates, $\log_{10} N^{EW}$ and $\log_{10} N^{EW}_{rec}$, where N is in cm^{-2}. N^{EW} was computed by applying Equation 2.10 to the EWs from the row above. N^{EW}_{rec} was measured by performing the EW integration on the recovered optical depths converted back to flux, rather than on the observed flux as was done for N^{EW}, and then applying Equation 2.10. Empty values correspond to negative column densities (due to negative EWs), and u.l. denotes 1σ upper limits.

Ion	D_{trans} (pMpc)	0.04–0.13	0.13–0.18	0.18–0.25	0.25–0.36	0.36–0.50	0.50–0.71	0.71–1.00	1.00–1.42	1.42–2.00
H I	EW	$1.12^{+0.16}_{-0.17}$	$0.88^{+0.14}_{-0.14}$	$0.78^{+0.32}_{-0.32}$	$0.38^{+0.12}_{-0.12}$	$0.52^{+0.10}_{-0.09}$	$0.44^{+0.08}_{-0.08}$	$0.42^{+0.06}_{-0.06}$	$0.35^{+0.04}_{-0.04}$	$0.35^{+0.04}_{-0.05}$
C IV	EW	$0.37^{+0.13}_{-0.12}$	$0.13^{+0.12}_{-0.12}$	$0.11^{+0.05}_{-0.06}$	$0.04^{+0.05}_{-0.05}$	$0.10^{+0.05}_{-0.05}$	$0.07^{+0.04}_{-0.04}$	$0.01^{+0.02}_{-0.02}$	$0.04^{+0.02}_{-0.02}$	$0.10^{+0.02}_{-0.02}$
	$\log_{10} N^{EW}$	$13.62^{+0.12}_{-0.18}$	$13.16^{+0.28}_{-1.38}$	$13.09^{+0.18}_{-0.29}$	$12.66^{+0.36}_{-\infty}$	$13.06^{+0.17}_{-0.27}$	$12.92^{+0.19}_{-0.35}$	$12.03^{+0.49}_{-\infty}$	$12.66^{+0.17}_{-0.29}$	$13.03^{+0.10}_{-0.12}$
	$\log_{10} N^{EW}_{rec}$	$13.55^{+0.11}_{-0.17}$	$12.66^{+0.46}_{-\infty}$	$12.66^{+0.30}_{-0.97}$	$12.80^{+0.29}_{-1.37}$	$12.70^{+0.25}_{-0.61}$	12.28 (u.l.)	...	...	$12.40^{+0.23}_{-0.42}$
Si IV	EW	$0.12^{+0.08}_{-0.08}$	$0.01^{+0.06}_{-0.07}$	$0.02^{+0.07}_{-0.06}$	$-0.01^{+0.05}_{-0.05}$	$0.01^{+0.04}_{-0.04}$	$-0.01^{+0.02}_{-0.03}$	$-0.01^{+0.02}_{-0.02}$	$-0.02^{+0.01}_{-0.01}$	$0.01^{+0.02}_{-0.02}$
	$\log_{10} N^{EW}$	$13.12^{+0.22}_{-0.53}$	$12.19^{+0.77}_{-\infty}$	$12.43^{+0.57}_{-\infty}$	12.71 (u.l.)	$12.07^{+0.67}_{-\infty}$	12.28 (u.l.)	12.09 (u.l.)	...	$12.13^{+0.38}_{-\infty}$
	$\log_{10} N^{EW}_{rec}$	$12.83^{+0.33}_{-\infty}$	12.62 (u.l.)	...	...	...	...	...	...	...

& Sembach (1991), assuming the linear curve-of-growth regime (i.e. $\tau < 1$):

$$N = 4\pi\varepsilon_0 \frac{m_e c^2}{\pi e^2} \frac{EW}{f_{Z,k}\lambda_{Z,k}^2}$$

$$= 1.13 \times 10^{20} \frac{1}{f_{Z,k}} \left(\frac{1\text{Å}}{\lambda_{Z,k}}\right)^2 \left(\frac{EW}{1\text{Å}}\right) \text{cm}^{-2} \tag{2.10}$$

where ε_0 is the permittivity of free space, m_e is the electron mass, e is the electric charge, c is the speed of light, and $\lambda_{Z,k}$ and $f_{Z,k}$ are the rest-frame wavelength and oscillator strength of the kth transition of ion Z. Fig. 2.10 demonstrates that the linear regime is not a valid assumption for H I since a substantial number of pixels have $\tau > 1$, however, we can still apply Equation 2.10 to C IV and Si IV.[4] We show this conversion as a secondary vertical axis in Fig. 2.11. In addition, in Table 2.8 we give the column densities computed from Equation 2.10 applied to the given EWs (N^{EW}). Furthermore, instead of calculating EW directly from the observed spectrum, we convert the recovered optical depths back to flux values, and integrate over those to determine column densities, which are also presented in Table 2.8 (N_{rec}^{EW}).

2.4.7 Galaxy redshift measurements

As discussed earlier, the various nebular and rest-frame UV-based galaxy redshifts suffer from different levels of uncertainty. In general, there is significantly more uncertainty associated with those redshifts determined from interstellar absorption or Lyα emission lines than with nebular redshifts measured by NIRSPEC or MOSFIRE. Since the elongation of the absorption enhancement along the LOS could be caused at least in part by redshift errors (e.g., Rakic et al. 2013), reducing them helps disentangle this effect from that of peculiar velocities. Currently, our galaxy sample has 381 galaxies with redshifts measured from nebular emission lines, and 340 of those are derived from MOSFIRE observations, which we estimate have errors of $\Delta v \approx 18$ km s^{-1} (compared to 41 galaxies with NIRSPEC measured redshifts that have an estimated error of $\Delta v \approx 60$ km s^{-1}). The measurement errors from these instruments are much smaller than the ~ 240 km s^{-1} extent of elongation seen along the LOS.

Therefore, we experiment with using different subsamples of KBSS galaxies. In Fig. 2.12, we again show the (unsmoothed) median optical depths from cuts taken along the maps in Fig. 2.4, using the innermost bins and plotting points along the transverse direction (left columns) and LOS direction (right columns). The blue circles show the cuts constructed using the full galaxy sample and are identical to the points in Fig. 2.6. We also consider the results when only galaxies whose redshifts were measured from nebular emission lines using NIRSPEC or MOSFIRE are used (381 galaxies or 45% of the full sample for H I, orange squares).

In general, we do not see any significant differences between the cuts taken from the fiducial sample and the one using only nebular redshifts. For the points along the trans-

---

[4] Examining the curve-of-growth and assuming a Doppler parameter $b_D = 10$ km s^{-1}, we find that the linear regime is valid for $N_{CIV} \lesssim 8 \times 10^{13}$ cm^{-2} and $N_{SiIV} \lesssim 3 \times 10^{13}$ cm^{-2}. Furthermore, from visual inspection we conclude that the spectral regions around the 30 smallest impact parameter galaxies show no evidence for saturation in C IV and Si IV.
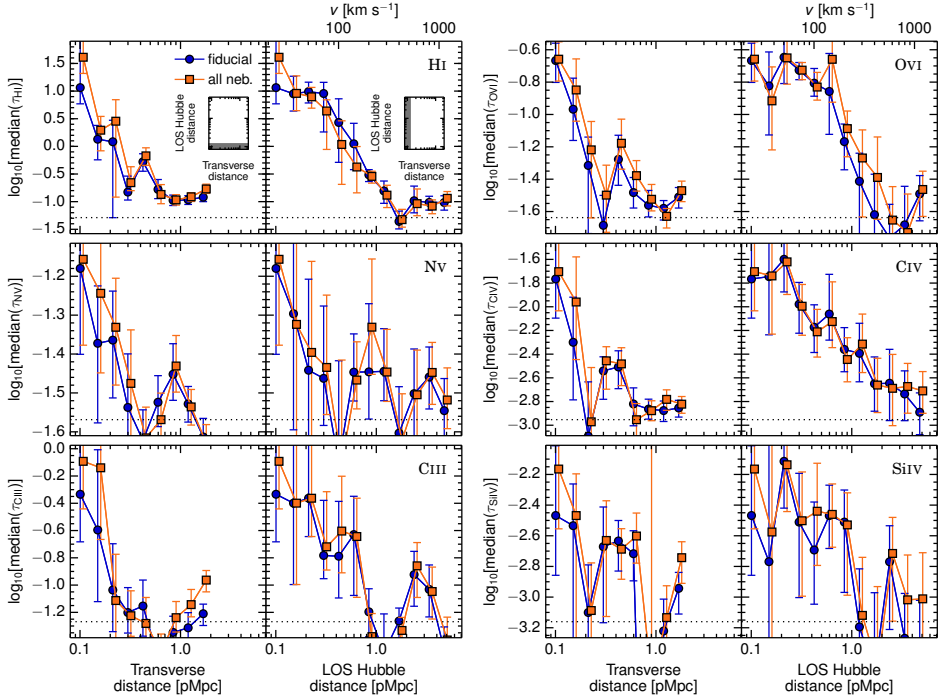
Figure 2.12: The median log optical depth $\tau_{Z,\mathrm{rnd}}$ where each set of two horizontal panels shows a different ion. The left and right panels in each set of two show points along the transverse and LOS directions, respectively. The cut sizes, shown in the insets, are the same as in Fig. 2.6, i.e., 0–30 km s^{-1} and 0.04–0.18 pMpc for the points along the transverse and LOS directions, respectively. The results from the fiducial sample used throughout this work, which consists of galaxy redshifts measured using a mix of rest-frame UV lines and nebular emission lines, are shown by the blue circles (835 galaxies), while the orange squares indicate the medians from all galaxies that have their redshift measured using nebular emission lines (354 galaxies). Points have been offset horizontally by 0.03 dex for clarity. The elongation of the optical depth enhancement along the LOS does not decrease when the sample only contains galaxies with nebular redshifts, which indicates that redshift measurement errors do not contribute significantly to this effect.

verse direction, one might expect that more accurate redshift measurements would result in an increase in the observed absorption. Although a small effect can be seen, that is, in most cases along the transverse direction the orange squares are at slightly higher optical depths than the blue circles, the result is not significant for any fixed transverse distance (although the increase in optical depths could be significant if integrated over the full impact parameter range).

We note that discrepancies between the two samples may be due to the different galaxies used to construct each optical depth profile. To test this, in Appendix 2.D we take the 238 galaxies that have had *both* their nebular and rest-frame UV redshifts measured, and show the results determined using only one type of redshift measurement at a time in Fig. 2.23. The slight enhancement along the transverse direction is no longer apparent in this comparison, so it may be a consequence of the different galaxies used in the nebular-only sample. However, it is important to note that in Fig. 2.23 the number of galaxies in the sample is

relatively small and hence that subtle differences may be hidden in the noise. Furthermore, in Fig. 2.24 we directly plot our results against those from Rakic et al. (2012), where only 10% of the galaxy sample had redshifts measured from nebular emission lines. We find that the H I optical depths along the LOS agree between the two sample for the innermost bin, although the redshift error effects become apparent in larger impact parameter bins.

The most striking result from Fig. 2.12 is that we do not observe significant differences between the LOS-direction optical depth profiles of the two galaxy samples. The lack of change in the extent of the optical depth enhancement when galaxy redshift errors are reduced from ~ 150 to ~ 10 km s^{-1} implies that the small-scale anisotropy detected for H I by Rakic et al. (2012) and Rudie et al. (2012b), and for H I and metals in this work, originates from gas peculiar velocities rather than from redshift errors.

Finally, as in Rudie et al. (2012b), we would like to extract the peculiar velocity field by subtracting the redshift errors (≈ 18 km s^{-1}) and transverse extent of the absorption (180 pkpc or ≈ 42 km s^{-1}) in quadrature from the observed velocity enhancement; doing so results in $\sim \pm 240$ km s^{-1}, and is in good agreement with the peculiar velocities measured in Rudie et al. (2012b) of $\sim \pm 260$ km s^{-1}. The magnitudes of the peculiar velocities we observe are consistent with what would be expected from infall, outflows, and virial velocities, so although it is currently difficult to disentangle the exact nature of their origin, it is likely that we are detecting motions of the gas around LBGs.

2.5   Summary And Conclusions

We have studied metals in the CGM around 854 $z \approx 2$–2.8 galaxies taken from the KBSS. The sample contains 381 galaxies that have been observed with NIRSPEC and/or MOS-FIRE, allowing us to measure their redshifts using nebular emission lines with estimated errors of only $\Delta v \approx 60$ km s^{-1} and $\Delta v \approx 18$ km s^{-1} for the two instruments, respectively. The galaxies studied lie in the fields of 15 hyper-luminous QSOs for which high-quality Keck spectra are available, with galaxy impact parameters ranging from 35 pkpc to 2 pMpc. Using the QSO spectra, the optical depth at each pixel in the Lyα forest redshift range was recovered for H I as well as for five metal ions (O VI, N V, C IV, C III, and Si IV). This was done using a slightly modified version of the pixel optical depth technique of Aguirre et al. (2002), which corrects the optical depths for saturation and various forms of contamination.

The main results are summarised below:

1. We have presented 2-D maps of the median absorption around galaxies in H I (first shown for a smaller sample by Rakic et al. 2012), as well as the first maps of O VI, N V, C IV, C III, and Si IV. These maps were created by taking the medians of the binned pixel optical depths as a function of the LOS and transverse distances from the galaxies in our sample (Fig. 2.4, § 2.4.1).

2. For every ion studied except perhaps for N V, we measure an enhancement of the absorption at small galactocentric radii, out to ~ 180 pkpc in the transverse direction and $\sim \pm 240$ km s^{-1} along the LOS (~ 1 pMpc assuming pure Hubble flow). Inside this region the median optical depth is typically enhanced above that of random regions

by about one order of magnitude for the metals and by two order of magnitude for HI (Figs. 2.4 and 2.5, § 2.4.1).

3. In the transverse direction, HI and CIV show a slight enhancement out to the maximum impact parameter covered by the survey (2 pMpc). The non-detection of an enhancement in the other ions at such large impact parameters does not necessarily imply that these ions are not present; rather, it may reflect differences in detection limits (Fig. 2.6, § 2.4.1).

4. The visual impression from the maps is that the enhancement of the HI is more extended in the transverse direction than that of the metals. However, normalising the optical depth profiles such that they all have the same maximum and asymptote, the metal ions do not show a significantly different profile shape (i.e. drop-off of optical depth values) with increasing transverse distance compared to HI. In the LOS direction, CIII traces the normalised HI profile, while OVI, CIV and SiIV show evidence for more extended absorption (Fig. 2.7, § 2.4.2).

5. Comparing cuts through the median optical depth maps in the transverse direction to those in the LOS direction, for all ions except NV the optical depths are higher in the LOS than in the transverse direction out to distances of ~ 1 pMpc (i.e. $240 \, \text{km s}^{-1}$) (Fig. 2.5, § 2.4.1).

6. We examined the median optical depth as a function of 3-D Hubble distance, which allows us to reduce the noise by combining pixels from both the LOS and transverse directions. Focusing on larger distance scales which should be minimally affected by redshift-space distortions (i.e. $\gtrsim 1$ pMpc), we find the CIV optical depth to be slightly enhanced out to ~ 4 pMpc. (Fig. 2.8, § 2.4.3).

7. The pixel optical depth PDFs at all impact parameters and for random regions all show similar amounts of scatter. However, at small impact parameters, particularly in the two innermost bins (i.e. < 180 pkpc), the distributions of optical depths are typically skewed to higher values (Fig. 2.10, § 2.4.5).

8. Comparison to the EWs from Steidel et al. (2010), which were calculated using galaxy pairs and probe smaller impact parameters than in this work, yields agreement for the overlapping impact parameter bins (Fig. 2.11, § 2.4.6).

9. The value of the covering fraction, defined as the fraction of galaxies for which the median optical depth within $\pm 170 \, \text{km s}^{-1}$ exceeds specific values, was found to be greater than the covering fraction at a random location for galaxy impact parameters below ~ 180 pkpc, for all ions (Fig. 2.9, § 2.4.4).

10. For HI, CIV, and in some cases OVI, the covering fraction is elevated with respect to the IGM for all impact parameters probed, which is consistent with the optical depth enhancement seen along the transverse distance cuts. However, for high optical depth threshold values, corresponding to the top 1% of random regions, the enhancement is only seen at impact parameters < 0.13 pMpc, which suggests that high optical depth systems are preferentially found at very small galactocentric distances (Fig. 2.9, § 2.4.4).

11. Limiting the sample to galaxies with nebular redshifts does not impart any significant change to the observed median optical depths as a function of transverse and LOS distance from the galaxies, even when the same sample of galaxies is used to compare the measurement techniques. This implies that the elongation of the optical depth enhancement along the LOS direction is due to gas peculiar velocities rather than redshift errors (Fig. 2.12, § 2.4.7).

Thanks to our unique sample, and particularly due to its unprecedented combination of size and data quality, we were able to study the 2-D metal distribution around galaxies in a way that has not been possible until now. We have presented the first 2-D maps of metal absorption around galaxies and we have quantified the enhancement in the absorption signal near $z \approx 2.4$ star-forming galaxies for 5 different metal ions, as well as for neutral hydrogen. Observations with MOSFIRE have allowed us to significantly reduce the errors on galaxy redshift measurements, to the point where we now have compelling evidence that the redshift-space distortions seen in the 2-D H I and metal ion optical depth distributions (i.e. the Finger-of-God effect seen in the LOS direction) is caused by peculiar motions of the gas.

As MOSFIRE observations proceed and the KBSS galaxy sample continues to grow, improvements in the data will allow us to split the sample according to various galaxy properties (e.g., mass, SFR, etc.) and to study how these characteristics affect the CGM. Additionally, we plan to examine the ratios between different metal ions and between metal ions and H I, and also to compare the results from this work to simulations.

Acknowledgements

2.A   The pixel optical depth method

In this appendix, we describe our implementation of the pixel optical depth technique. Our version is based on Aguirre et al. (2002), which was itself based on Cowie & Songaila (1998); Ellison et al. (2000); Schaye et al. (2000a), and we will point out where our method differs from that of Aguirre et al. (2002).

Using the redshift ranges given in § 2.3, we calculate the optical depth for each species Z and each multiplet component k (if applicable) as:

$$\tau_{Z,k}(z) \equiv -\ln[F_{Z,k}(z)] \qquad (2.11)$$

where $F_{Z,k}(z)$ is the normalised flux at redshift z, obtained from

$$F_{Z,k}(z) \equiv F(\lambda = \lambda_{Z,k}[1+z]) \qquad (2.12)$$

where $\lambda_{Z,k}$ is the transition's rest wavelength. For all optical depths other than $\tau_{\mathrm{HI,Ly\alpha}}(z)$, linear interpolation of the flux is used so that all discrete z values are the same as for $\tau_{\mathrm{HI,Ly\alpha}}(z)$. Before beginning the correction, we search for saturated pixels, defined as those pixels satisfying $F(\lambda) \leq N_\sigma \sigma(\lambda)$, where $\sigma(\lambda)$ is the normalised noise array, and we set $N_\sigma = 3$. Since the optical depths of the saturated pixels are not reliable, but will be high compared to the unsaturated pixels, we set their values to $\tau_{Z,k}(z) = 10^6$. Using such an extreme optical depth to flag the saturated pixels will not skew our results provided median statistics are used throughout the analysis.

First we perform the recovery for HI, since we will need the recovered optical depths to correct metals which are contaminated by higher order Lyman lines. For HI, the main source of error comes from the saturation of the Lyα lines. Therefore, for all Lyα pixels previously flagged as saturated, we look to all available higher order Lyman lines (in practice we have used $N = 16$ higher order components). We only use higher order pixels which satisfy $N_\sigma \sigma(\lambda) \leq F(\lambda) \leq 1 - N_\sigma \sigma(\lambda)$ at $\lambda = \lambda_{\mathrm{HI,Lyn}}[1+z]$, to ensure that they are not poorly detected. Scaling the higher order optical depths to the Lyα component strength, we set the recovered Lyα optical depth, $\tau_{\mathrm{HI,Ly\alpha}}^{\mathrm{rec}}(z)$ to be the minimum of all well-detected higher order pixels:

$$\tau_{\mathrm{HI,Ly\alpha}}^{\mathrm{rec}}(z) \equiv \min\left[\frac{\tau_{\mathrm{HI,Lyn}}(z) g_{\mathrm{HI,Ly\alpha}}}{g_{\mathrm{HI,Lyn}}}\right]. \qquad (2.13)$$

Here, $g_{\mathrm{HI,Lyn}} \equiv f_{\mathrm{HI,Lyn}} \lambda_{\mathrm{HI,Lyn}}$ where $f_{\mathrm{HI,Lyn}}$ is the oscillator strength.

In addition to the above correction for saturated pixels which is identical to the one used in Ellison et al. (2000) and Aguirre et al. (2002), we implement a procedure to search for and flag contaminated Lyα pixels. We consider a Lyα pixel to be contaminated if

$$F_{\mathrm{HI,Lyn}}(z) - N_\sigma \sigma(\lambda = \lambda_{\mathrm{HI,Lyn}}[1+z]) > $$
$$\max\left[F_{\mathrm{HI,Ly\alpha}}(z), N_\sigma \sigma(\lambda_{\mathrm{HI,Ly\alpha}}[1+z])\right]^{g_{\mathrm{HI,Lyn}}/g_{\mathrm{HI,Ly\alpha}}}. \qquad (2.14)$$

Specifically, for unsaturated Lyα pixels, we scale the Lyα flux to obtain the flux expected at higher-order transition n; if the observed flux at transition n is significantly greater than would be expected from the Lyα flux, the Lyα pixel is likely contaminated. In order to apply this algorithm to saturated Lyα pixels (for which the flux estimate is likely to be unreliable), we instead use the Lyα noise array to set the Lyα flux. All Lyα pixels found to be contaminated in this way are flagged and discarded for the remainder of the analysis.

The recovered HI Lyα optical depths are then used to correct unsaturated pixels of metals contaminated by Lyman series lines. For the recovery of OVI and CIII, which are located in the Lyβ forest, the procedure involves the subtraction of the Lyman lines starting with Lyβ (i.e., $n = 2$):

$$\tau_{Z,k}(z) := \tau_{Z,k}(z) - \sum_{n=2}^{N} \frac{g_{\mathrm{HI,Lyn}}}{g_{\mathrm{HI,Ly\alpha}}} \tau_{\mathrm{HI,Ly\alpha}}^{\mathrm{rec}}\left(\frac{\lambda \lambda_{\mathrm{HI,Ly\alpha}}}{\lambda_{\mathrm{HI,Lyn}}}\right) \qquad (2.15)$$

where $\lambda = \lambda_{Z,k}[1 + z]$ and we take $N = 5$ (the effects of varying N are explored in Appendix 2.B.2). For Ovɪ, the Hɪ optical depth subtraction procedure is performed for both multiplet components k.

Something else that we have implemented in the Hɪ subtraction procedure which was not done in Aguirre et al. (2002), is the treatment of saturated metal pixels. More specifically, since the true optical depth of saturated pixels cannot be measured accurately in the presence of noise, we cannot make a reliable Hɪ subtraction. Hence, we do not apply Equation 2.15 to pixels for which $F(\lambda) \leq N_\sigma \sigma(\lambda)$. Rather, if the sum of contaminating Hɪ optical depths is sufficient to saturate the absorption, i.e. if

$$\exp\left[-\sum_{n=2}^{N} \frac{g_{\text{Hɪ,Lyn}}}{g_{\text{Hɪ,Lyα}}} \tau_{\text{Hɪ,Lyα}}^{\text{rec}}\left(\frac{\lambda \lambda_{\text{Hɪ,Lyα}}}{\lambda_{\text{Hɪ,Lyn}}}\right)\right] < N_\sigma \sigma(\lambda), \tag{2.16}$$

then the pixel cannot be used to estimate the metal optical depth. For Cɪɪɪ, this pixel is discarded immediately. Since Ovɪ is a doublet and we are able to compare the two components in the next contamination correction step, it is not as crucial to discard all contaminated pixels right away. Instead, we perform this flagging procedure on each of the doublet components and only discard those redshifts for which both components are contaminated.

As mentioned above, the next step is to correct the optical depths of metals which have two multiplet components k (Ovɪ, Nv, and Sɪɪv) by taking the minimum of the the optical depths, where the optical depth of the weaker component is scaled to match that of the stronger one. Specifically, we take:

$$\tau_{Z,1}^{\text{rec}}(z) = \min\left[\tau_{Z,1}(z), \frac{g_{Z,1}}{g_{Z,2}} \tau_{Z,2}(z)\right]. \tag{2.17}$$

However, it may not be a good idea to use the minimum optical depth at every pixel. This is because, particularly in the case where both pixels are not contaminated, doing so will result in an optical depth value that is biased low. To combat this, Aguirre et al. (2002) would only take the optical depth of the weaker component if it were positive, i.e. $\tau_{Z,2}(z) > 0$. Here we use a different approach, where we take the noise level into account, and only use the optical depth of the weaker component if:

$$\left[\exp[-\tau_{Z,2}(z)] - N_\sigma \sigma(\lambda = \lambda_{Z,2}[1 + z])\right]^{\frac{g_{Z,1}}{g_{Z,2}}} > $$
$$\exp[-\tau_{Z,1}(z)] + N_\sigma \sigma(\lambda = \lambda_{Z,1}[1 + z]). \tag{2.18}$$

The left hand side of this condition contains the optical depth of the weaker component expressed in terms of flux, with the noise term subtracted, and then scaled to match the strength of the stronger component optical depth, which is on the right-hand side. This condition states that the scaled optical depth of the weaker component must be *significantly* lower than that of the stronger one in order that it be used for the recovered optical depth value.

Finally, the rest wavelength of Cɪv puts the recovery region redwards of the Lyα forest, and the majority of the contamination therefore consists of self-contamination from its own doublet. We correct for this self-contamination as follows Aguirre et al. (2002). First, every pixel is checked for contamination from other ions, which is done by testing to see if its optical depth is higher than what would be expected from self-contamination alone.

Specifically, we define $\tau_{\mathrm{CIV},1}(\lambda)$ as $\tau_{\mathrm{CIV},1}(z)$ where $z = \lambda/\lambda_{\mathrm{CIV},1} - 1$. If the optical depth at wavelength λ comes from the weaker component, we want to know the optical depth at the location of the strong component $\lambda_s = [\lambda_{\mathrm{CIV},1}/\lambda_{\mathrm{CIV},2}]\lambda$. We also want to consider the case where the optical depth at λ comes from the strong component, and therefore need the optical depth at the wavelength of the weak component, $\lambda_w = \lambda_{\mathrm{CIV},2}[1 + z]$. We then scale these optical depths to test if the optical depth at λ is higher than expected from self-contamination, which gives the condition:

$$
\begin{aligned}
&\exp\left[-\tau_{\mathrm{CIV},1}(\lambda)\right] + N_\sigma \bar{\sigma}(\lambda) < \\
&\exp\left[-\frac{g_{\mathrm{CIV},2}}{g_{\mathrm{CIV},1}}\tau_{\mathrm{CIV},1}(\lambda_s) - \frac{g_{\mathrm{CIV},1}}{g_{\mathrm{CIV},2}}\tau_{\mathrm{CIV},1}(\lambda_w)\right]
\end{aligned}
\tag{2.19}
$$

where $\bar{\sigma}^2(\lambda) = \sigma^2(\lambda) + \sigma^2(\lambda_s) + \sigma^2(\lambda_w)$; pixels meeting this condition are probably contaminated with absorption from other ions, and are therefore not used for the correction or any subsequent analysis. Then, an iterative doublet subtraction algorithm is used to remove self-contamination, where the scaled optical depth of the strong component at λ_s is subtracted from the optical depth at λ. Before doing this, for those pixels with $\tau_{\mathrm{CIV},1}(z) < 0$, we set $\tau_{\mathrm{CIV},1}(z) = 10^{-4}$ so that negative optical depth values won't affect the subtraction procedure. After first setting $\tau_{\mathrm{CIV},1}^{\mathrm{rec}}(\lambda) = \tau_{\mathrm{CIV},1}(\lambda)$, the following is repeated until convergence occurs (about 5 iterations):

$$
\tau_{\mathrm{CIV},1}^{\mathrm{rec}}(\lambda) := \tau_{\mathrm{CIV},1}(\lambda) - \frac{g_{\mathrm{CIV},2}}{g_{\mathrm{CIV},1}}\tau_{\mathrm{CIV},1}^{\mathrm{rec}}(\lambda_s).
\tag{2.20}
$$

Here we note the implementation of an automated continuum fitting procedure which we apply to the spectral regions with wavelengths greater than that of their quasar's Lyα emission. The purpose of this is to homogenise the continuum fitting errors, and it is performed as follows. This region of each spectrum is divided into bins of size $\Delta\lambda$ in the rest-frame, each with central wavelength λ_i and median flux $\bar{f}_i$. We then interpolate a B-spline through $\bar{f}_k$ and discard any pixels with flux values that are $N_\sigma^{cf} \times \sigma$ below the interpolated flux values. $\bar{f}_k$ is recalculated without the discarded pixels, and the procedure is repeated until convergence is reached. In our implementation, we use $N_\sigma^{cf} = 2$ and $\Delta\lambda = 20$ Å as in Schaye et al. (2003).

Finally, we discuss our masking procedure. As mentioned in § 2.2, six of the QSOs have DLAs located in their Lyα forest regions. For the recovery of HI and Nv, we use the spectra that have had the damping wings of these DLAs fitted out and the saturated region masked. However, for the recovery of Ovi and Ciii, we want to subtract as much HI contamination as possible. Therefore, we also perform an HI recovery without the Lyα forest region DLAs fitted out and masked, and use these values for the subtraction of contamination from the Ovi and Ciii regions. We found that the results for Ovi and Ciii obtained from using the unmasked DLA HI recovery are similar to those obtained from masking out the higher order components of the DLA by hand. Lastly, for all recoveries we have masked out two more DLAs which are bluewards of their QSO's Lyα forest region, i.e. saturated Lyman continuum absorption associated with strong HI absorbers, and we have also masked out all Lyman break regions, which occurs for three of our QSOs.
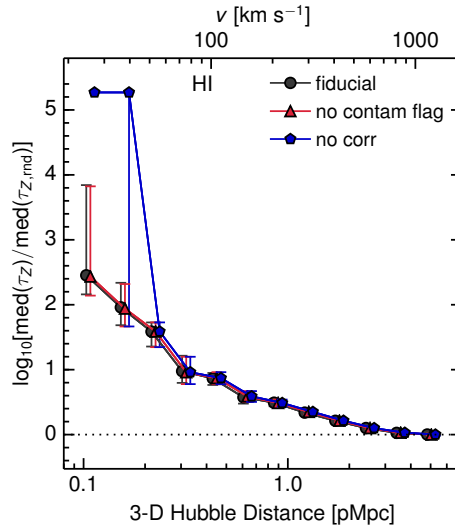
Figure 2.13: Similar to Fig. 2.8, but only for H$\textsc{i}$, dividing by $\tau_{Z,\text{rnd}}$, and modifying the optical depth recovery method. The modifications are: not flagging pixels determined to be contaminated from their higher-order H$\textsc{i}$ flux ("*no contam flag*"), and doing no correction at all (i.e. not using higher-order H$\textsc{i}$ lines to correct saturated H$\textsc{i}$ Lyα pixels, "*no corr*"). The points are offset horizontally by 0.02 dex for clarity.

2.B   Variation in pixel optical depth recovery

In this section we explore the sensitivity of our results to variations in the method used to recover the pixel optical depths. For this purpose we will compare the enhancement in the median optical depth relative to a random location as a function of 3-D Hubble distance. Note that corrections may change the median $\tau_{Z,\text{rnd}}$ even if they do not change the median $\tau_Z/\tau_{Z,\text{rnd}}$ plotted in this section. As we will demonstrate, our results are not particularly sensitive to any of the corrections that we apply in the recovery of pixel optical depths.

2.B.1   H$\textsc{i}$

We begin by examining one of the changes made to the H$\textsc{i}$ Lyα recovery algorithm with respect to that used in Aguirre et al. (2002), which is the use of higher-order H$\textsc{i}$ flux to flag contaminated H$\textsc{i}$ Lyα pixels. We show the resulting median optical depth divided by $\tau_{Z,\text{rnd}}$ as a function of Hubble distance in Fig. 2.13 for the fiducial H$\textsc{i}$ recovery as well as one performed without flagging contaminated pixels, and we can see that this change in the algorithm has almost no impact on the results. We have also plotted the median optical depths obtained when no H$\textsc{i}$ correction is done (i.e. saturated H$\textsc{i}$ Lyα pixels are not corrected using higher-order H$\textsc{i}$ components). This correction is most important for small galactocentric distances, where the median optical depths actually reach the optical depth value used to flag saturated pixels. However, the absence of this correction would not affect our overall conclusions.
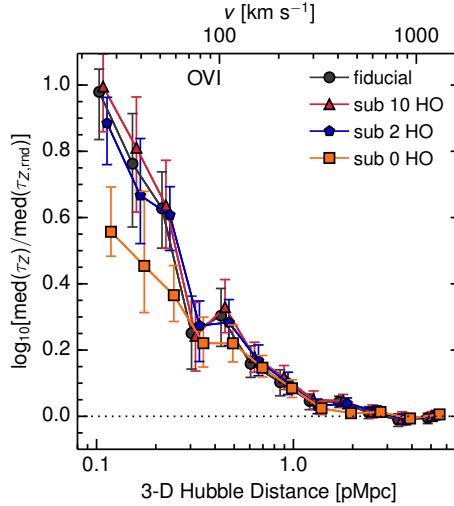
Figure 2.14: Similar to Fig. 2.13, but for Ovɪ, and modifying the optical depth recovery method with respect to the fiducial one (which invokes the subtraction of five higher order Hɪ lines). The modifications are: subtracting 10, 2, and 0 higher-order (HO) Hɪ lines, where the doublet minimum is taken in every case.
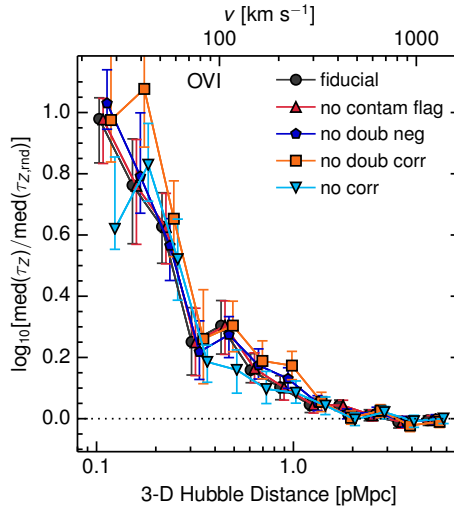
Figure 2.15: Similar to Fig. 2.13, but for the following modifications with respect to the fiducial optical depth recovery: pixels determined to be saturated with contaminating Hɪ are not flagged ("*no contam flag*"); the weaker doublet component is not considered if it has a negative optical depth ("*no doub neg*"); no doublet minimum taken ("*no doub corr*"); and no correction at all (i.e., neither Hɪ subtraction nor doublet minimum, "*no corr*").

2.B.2 OVI

For OVI, we first vary the number of higher order HI Lyman lines that are subtracted from the OVI region. The fiducial number that we use is five, and we have also tried subtracting ten, two, and zero higher order HI lines, the outcomes of which are shown in Fig. 2.14. In the recoveries where at least two higher-order HI lines are subtracted, the curves are almost identical. The main difference (which cannot be seen from this figure) is that the median optical depth in random locations ($\tau_{Z,\mathrm{rnd}}$) increases as fewer HI lines are subtracted.

Next we investigate the effects of the pixel optical depth recovery modifications with respect to Aguirre et al. (2002). Specifically, in Fig. 2.15, we show the median optical depth that results from not discarding pixels for which the contaminating HI absorption is thought to be saturated based on the sum of corresponding higher-order HI optical depths; and also using the doublet minimum condition from Aguirre et al. (2002): that is, instead of using Equation 2.18, the doublet minimum is taken for every pixel, except for pixels where the weaker component has a negative optical depth. Neither of these changes has any impact on the resulting median optical depth. In Fig. 2.15, we also look at the median optical depth from recoveries where we did not perform the doublet correction (that is, we still subtract five higher order HI lines, but then do not take the minimum of the OVI doublet at each redshift); finally where we did not perform any correction at all. Although not taking the doublet minimum does not have a significant affect on the outcome, not performing any correction at all does reduce the dynamic range with respect to the fiducial case.

Another technique which can be applied to the OVI recovery is to make redshift cuts such that those wavelength ranges contaminated by more higher order HI lines are removed from the analysis. For example, one can choose to limit the recovery to the region in the spectrum where only three HI lines (Lyα, Lyβ, Lyγ, and no further higher order lines) are present. In the top row Fig. 2.16 we show the result of limiting the spectral region to that contaminated by all, seven, and five higher order HI lines, respectively. For the five higher order HI line limit, there are so few galaxies in the innermost impact parameter bins (lower right panel of Fig. 2.16) that the error bars are likely not reliable. In general, we find these cuts slightly increase the dynamic range of the optical depths, but for up to 3 higher order lines, i.e. our most restrictive cut, the dynamic range in τ_{OVI} is significantly smaller. Given the low number of galaxies at the smallest impact parameters where the optical depth is enhanced with respect to the median (and the even lower numbers resulting from reducing the sample size), such differences are probably due to small number statistics.

Additionally, one could optimise the OVI recovery by making cuts in the S/N of the HIRES spectra, since it is at the lowest wavelengths of Keck (those of the OVI region) where the S/N declines quite rapidly. We try excluding individual regions with S/N less than 10 and 20 (using a higher S/N cut results in < 10 galaxies in the smallest impact parameter bin), and show the results in the top row of Fig. 2.17. Indeed, such cuts do appear to enhance the median central absorption relative to that in a random location. However, as was the case for the higher order HI line cuts, this could certainly be due to the varying and small number of galaxies in the smallest impact parameter bins (see the histograms in the bottom row of Fig. 2.17).
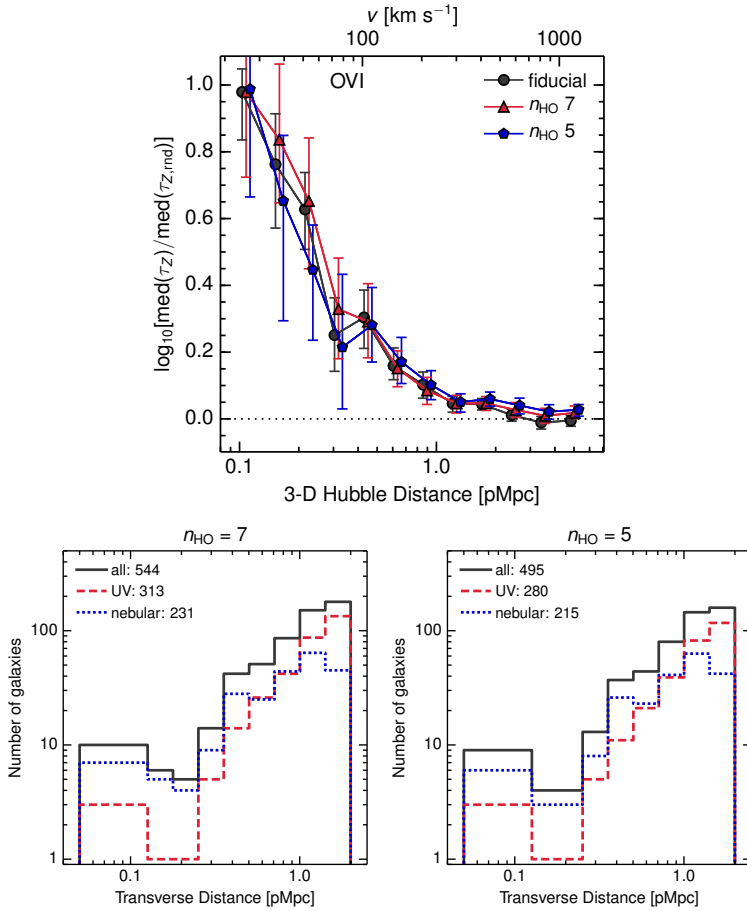
Figure 2.16: *Top*: Similar to Fig. 2.13, but limiting the spectral region to that contaminated by: any number (fiducial), seven and five higher order H I lines. *Bottom*: Histograms of the number of galaxies per impact parameter bin for each of the spectral region cuts shown above. For reference, the fiducial number of galaxies in each bin is 854 galaxies in total, with 473 and 381 having their redshifts measured from rest-frame UV features and nebular emission lines, respectively.
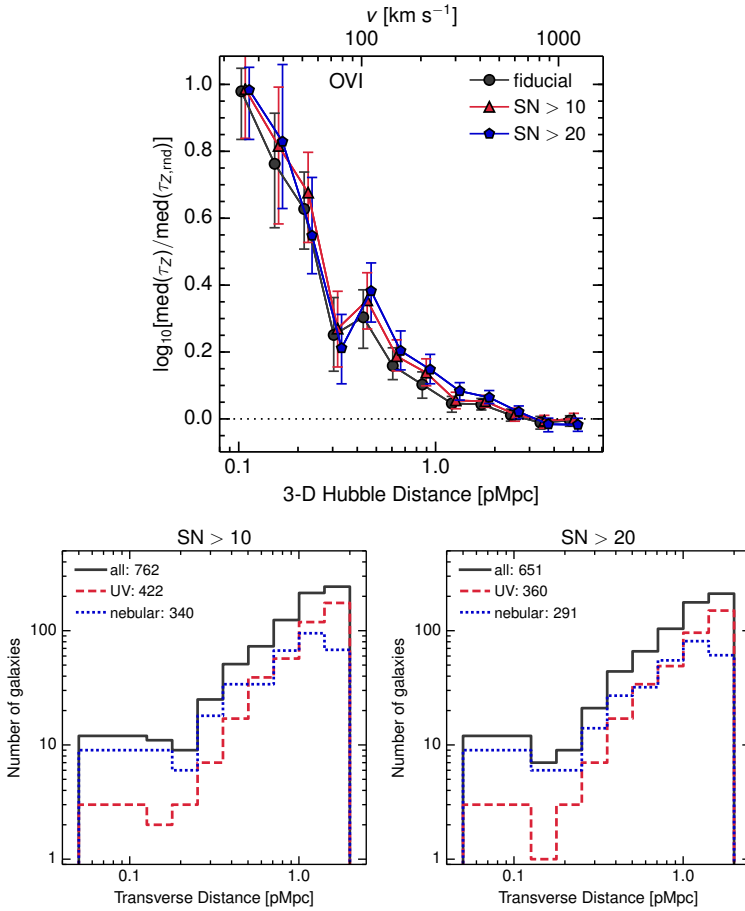
Figure 2.17: *Top*: Similar to Fig. 2.13, but limiting the used spectral region to that having S/N greater than 0 (fiducial), 10 and 20. *Bottom*: Histograms of the number of galaxies per impact parameter bin for each of the spectral region S/N cuts shown above. For reference, the fiducial number of galaxies in each bin is 854 galaxies in total, with 473 and 381 having their redshifts measured from rest-frame UV features and nebular emission lines, respectively.
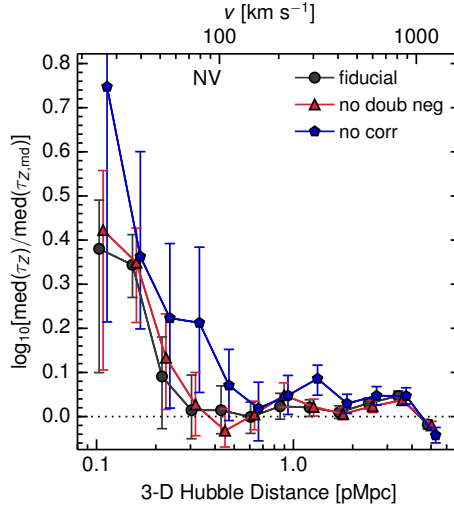
Figure 2.18: Similar to Fig. 2.13, but for Nv and comparing the use of the fiducial optical depth recovery method (taking the doublet minimum) to recoveries where the weaker doublet component is not considered if it has a negative optical depth ("*no doub neg*"), and where no correction is done at all ("*no corr*").

2.B.3 NV

The optical depth correction for Nv consists only of examining both doublet components at each redshift and taking the minimum of the two optical depths. In Fig. 2.18, we compare the 3-D-Hubble distance curves determined both with and without this correction, as well the curve resulting from using the doublet minimum condition from Aguirre et al. (2002) (where instead of using Equation 2.18, the doublet minimum is taken for all pixels except those where the weaker component has a negative optical depth). Neither of these changes have a significant impact on the resulting median optical depth. Not using the doublet correction yields a larger dynamic range; however, the errors become much larger. Hence, the significance with which the enhancement is detected is typically smaller without the correction. We also note that since the points here are correlated, the fact that the first five green points are above the black ones may not be a significant effect. Indeed, the differences between the two recovery methods is no longer seen when we use cuts along the transverse direction of the 2-D optical depth maps (where the points are independent) instead of the 3-D Hubble distances.

2.B.4 CIV

As described in § 2.3, we normally perform an automated continuum fit to any regions in the spectrum redwards of the Lyα emission. However, we find that this only slightly boosts the dynamic range in the recovered median optical depths, as can be seen in Fig. 2.19.

We have also examined the effect of not applying the self-contamination correction, but rather taking the doublet minimum, as well as not doing any correction at all. In both instances, the dynamic range probed is actually larger than in the self-contamination correc-
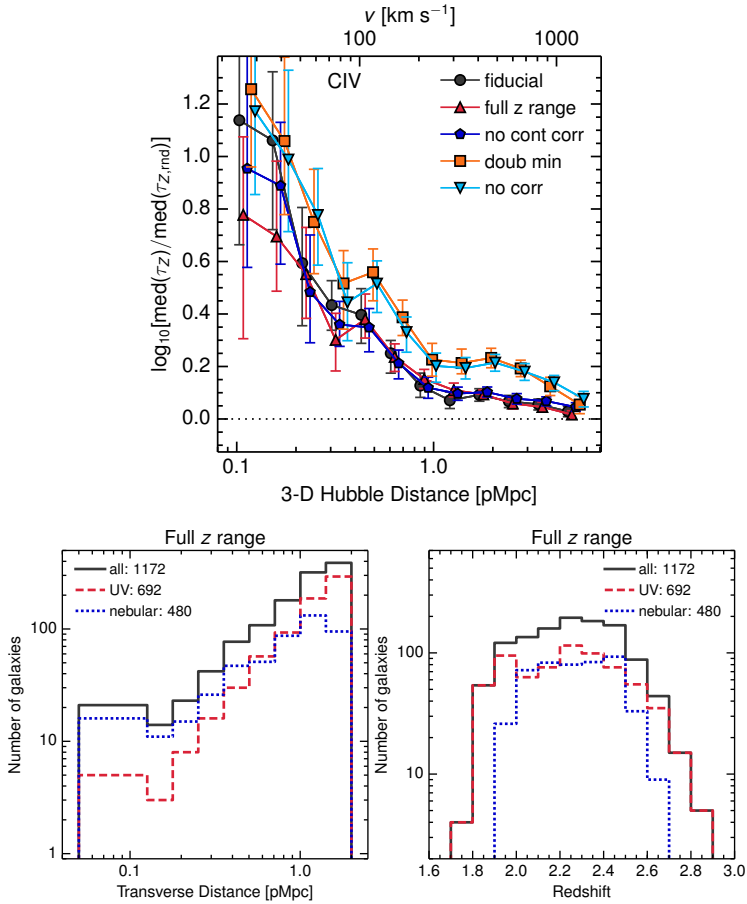
Figure 2.19: *Top*: Similar to Fig. 2.13, but plotting different C IV recoveries. These are: self-contamination correction ("*fiducial*"); using the full redshift range("*full z range*"); without the automatic continuum correction ("*no cont corr*"); taking the doublet minimum instead of the self-contamination correction ("*doub min*"); and without any correction ("*no corr*"). *Bottom*: The histograms show the number of galaxies per impact parameter (left) and redshift bin (right) obtained when the full C IV redshift range is used. For reference, the fiducial number of galaxies in each bin is 854 galaxies in total, with 473 and 381 having their redshifts measured from rest-frame UV features and nebular emission lines, respectively.
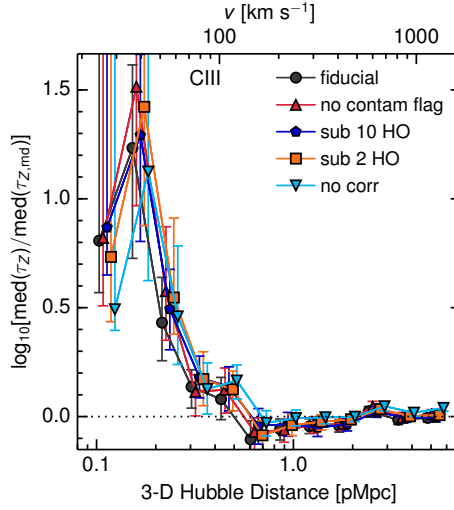
Figure 2.20: Similar to Fig. 2.13, but for CIII and modifying the optical depth recovery method with respect to the fiducial one (which invokes the subtraction of five higher order HI lines). The modifications are: not flagging pixels determined to be contaminated from their higher-order HI flux ("*no contam flag*"); and subtracting 10 ("*sub 10 HO*"), 2 ("*sub 2 HO*"), and 0 ("*no corr*") higher-order HI lines.

tion case. However, this increase in dynamic range is probably due to self-contamination. The CIV doublet separation is ~ 500 km s^{-1}. As this is smaller than the scale over which the absorption is enhanced, self-contamination will boost the enhancement in the apparent CIV absorption near galaxies.

Finally, our fiducial CIV recovery only uses pixels within the redshift range of the Lyα forest of the quasar, i.e. down to the redshift for which Lyα absorption coincides with the Lyβ emission line. However, the region where CIV can be recovered accurately (i.e., redwards of the QSO Lyα emission) extends to lower redshifts than this range, and so we experiment with performing the recovery down to the redshift for which CIV absorption coincides with the quasar's Lyα emission line.

The result is shown as the red points Fig. 2.19. Extending the recovered redshift range increases the number of galaxies that fall within the spectral coverage range (see the galaxy histograms in the right two panels of Fig. 2.19). However, the signal is slightly reduced, although the difference is not significant. The galaxy sample now contains, and the median redshift is now 2.27 instead of 2.34 for the fiducial sample. This could skew the sample to lower masses, since at lower redshift these galaxies are more easily observed. Alternatively, the small decrease in the enhancement may reflect small number statistics since it is not significant.

2.B.5 CIII

Since the correction for CIII involves the subtraction of higher-order contaminating HI lines, we repeat the procedure done for OVI where we test the effect of removing different numbers of higher order HI lines (the fiducial number being 5). In Fig. 2.20 we show the
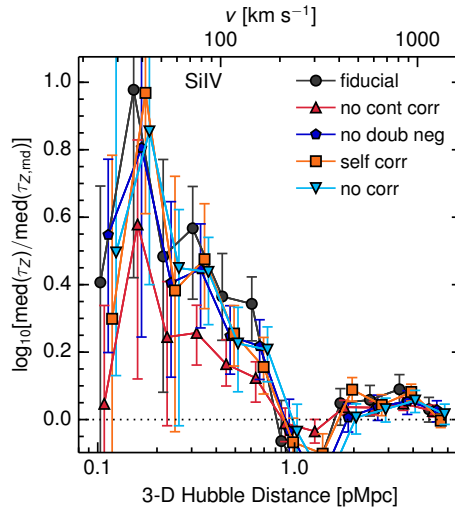
Figure 2.21: Similar to Fig. 2.13, but only for Siɪᴠ and for different optical depth recovery methods. These are: taking the doublet minimum ("*fiducial*"); without the automatic continuum correction ("*no cont corr*"); the weaker doublet component is not considered if it has a negative optical depth ("*no doub neg*"); performing a self-contamination correction instead of taking the doublet minimum ("*self corr*"); and without any correction ("*no corr*").

result of removing 10, 5, 2, and no higher order lines (no correction). We also show the effect of not flagging pixels determined to be saturated due to Hɪ contamination. We find almost no change except for the case of no correction, where the optical depth dynamic range is slightly reduced.

2.B.6   SiIV

In Fig. 2.21, we find that for Siɪᴠ (unlike for Cɪᴠ) the automated correction to the continuum fit substantially increases the dynamic range probed. Since Siɪᴠ is a relatively weak transition and its optical depths are very close to the noise level, it is likely quite sensitive to the continuum fit.

Using the doublet minimum condition from Aguirre et al. (2002) (where instead of using Equation 2.18, the doublet minimum is taken for all pixels except those where the weaker component has a negative optical depth), employing the self-contamination correction instead of the doublet minimum, or doing no correction at all does not significantly alter the dynamic range of the recovered optical depths, although we note that using the self-contamination correction results in larger errors. This may be due to the fact that Siɪᴠ is a relatively weak line (compared to Cɪᴠ) and the greatest source of contamination likely comes from Cɪᴠ rather than from its own doublet.
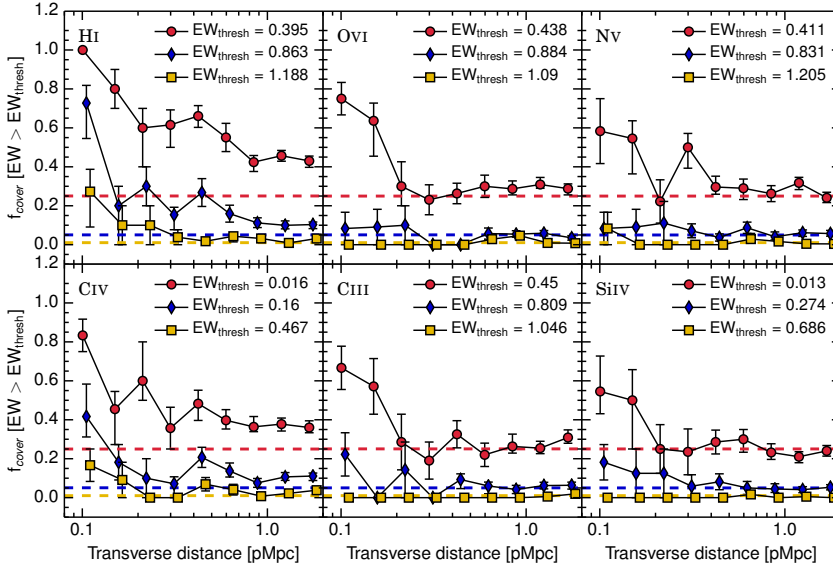
Figure 2.22: Covering fraction for each ion, defined as the fraction of galaxies within some impact parameter bin (plotted along the y-axis) that have an EW, calculated by integrating the flux decrement over ± 170 km s^{-1}, above some threshold value (in Å). These threshold values are set by some multiple of the median EW for 1000 randomly drawn regions integrated over ± 170 km s^{-1}. These regions are then used to determine the covering fraction of the EW$_{Z,\text{thresh}}$ values, which are denoted by the dotted horizontal lines. Points determined using different $\tau_{Z,\text{thresh}}$ values have been offset horizontally by 0.2 dex for clarity.

2.C   Covering fraction for EW thresholds

Here we investigate the outcome of using an alternate threshold for the covering fraction, where we use the EW (rather than the median optical depth) within ± 170 km s^{-1} of every galaxy, to facilitate comparison with low-quality data. The EW within ± 170 km s^{-1} is also computed for 1000 random regions within the spectra. We define the covering fraction as the fraction of galaxies within an impact parameter bin with an EW above EW$_{Z,\text{thresh}}$, where we take EW$_{Z,\text{thresh}}$ values as those where the covering fractions for random regions are 0.25, 0.05 and 0.01. The results are shown in Fig. 2.22 and Table 2.9.

In general, the results are similar to those obtained using our first covering fraction definition: for H$\textsc{i}$, the covering fraction is above that for random regions out to the largest impact parameter in our sample (2 pMpc), while for metals the covering fraction is only elevated for the smallest transverse distance bins. One difference to note is that for the EW thresholds, a signal is seen for the covering fraction of N$\textsc{v}$ (which was not the case using median optical depth thresholds).

Table 2.9: Covering fraction and 1-σ errors as a function of transverse distance (top row), which is defined as the fraction of galaxies in each impact parameter bin that have an EW within $\pm170\ \mathrm{km\ s^{-1}}$ above some threshold value. The threshold values are set by the EWs at which the covering fraction of 1000 random $\pm170\ \mathrm{km\ s^{-1}}$ regions, f_{GM}, are equal to 0.25, 0.05, and 0.01 (second column), and the results are plotted in Fig. 2.22.

Ion	D_{trans} (pMpc) f_{GM}	0.04–0.13	0.13–0.18	0.18–0.25	0.25–0.36	0.36–0.50	0.50–0.71	0.71–1.00	1.00–1.42	1.42–2.00
Hı	0.25	$1.00^{+0.00}_{-0.08}$	$0.80^{+0.10}_{-0.10}$	$0.60^{+0.10}_{-0.20}$	$0.62^{+0.08}_{-0.12}$	$0.66^{+0.05}_{-0.06}$	$0.55^{+0.07}_{-0.07}$	$0.42^{+0.03}_{-0.05}$	$0.46^{+0.03}_{-0.03}$	$0.43^{+0.02}_{-0.03}$
	0.05	$0.73^{+0.09}_{-0.18}$	$0.20^{+0.10}_{-0.20}$	$0.30^{+0.10}_{-0.10}$	$0.15^{+0.04}_{-0.08}$	$0.27^{+0.07}_{-0.07}$	$0.16^{+0.04}_{-0.04}$	$0.11^{+0.03}_{-0.02}$	$0.10^{+0.02}_{-0.02}$	$0.10^{+0.01}_{-0.02}$
	0.01	$0.27^{+0.11}_{-0.18}$	$0.10^{+0.10}_{-0.10}$	$0.10^{+0.10}_{-0.10}$	$0.04^{+0.04}_{-0.04}$	$0.02^{+0.02}_{-0.02}$	$0.04^{+0.01}_{-0.03}$	$0.03^{+0.02}_{-0.02}$	$0.01^{+0.01}_{-0.00}$	$0.03^{+0.01}_{-0.01}$
Ovı	0.25	$0.75^{+0.08}_{-0.18}$	$0.64^{+0.09}_{-0.09}$	$0.30^{+0.10}_{-0.13}$	$0.23^{+0.08}_{-0.08}$	$0.26^{+0.05}_{-0.05}$	$0.30^{+0.06}_{-0.06}$	$0.29^{+0.04}_{-0.03}$	$0.31^{+0.04}_{-0.02}$	$0.29^{+0.02}_{-0.03}$
	0.05	$0.08^{+0.08}_{-0.08}$	$0.09^{+0.09}_{-0.09}$	$0.10^{+0.10}_{-0.10}$	$0.00^{+0.00}_{-0.00}$	$0.00^{+0.00}_{-0.00}$	$0.06^{+0.03}_{-0.03}$	$0.05^{+0.02}_{-0.02}$	$0.06^{+0.01}_{-0.01}$	$0.04^{+0.01}_{-0.01}$
	0.01	$0.00^{+0.00}_{-0.00}$	$0.00^{+0.00}_{-0.00}$	$0.00^{+0.00}_{-0.00}$	$0.00^{+0.00}_{-0.00}$	$0.00^{+0.00}_{-0.00}$	$0.03^{+0.01}_{-0.01}$	$0.05^{+0.02}_{-0.02}$	$0.01^{+0.00}_{-0.00}$	$0.01^{+0.00}_{-0.00}$
Nv	0.25	$0.58^{+0.17}_{-0.17}$	$0.55^{+0.09}_{-0.18}$	$0.22^{+0.11}_{-0.11}$	$0.50^{+0.07}_{-0.11}$	$0.30^{+0.06}_{-0.04}$	$0.29^{+0.05}_{-0.06}$	$0.26^{+0.04}_{-0.04}$	$0.32^{+0.03}_{-0.03}$	$0.24^{+0.03}_{-0.02}$
	0.05	$0.08^{+0.08}_{-0.08}$	$0.09^{+0.09}_{-0.09}$	$0.11^{+0.01}_{-0.11}$	$0.07^{+0.04}_{-0.04}$	$0.04^{+0.04}_{-0.02}$	$0.09^{+0.03}_{-0.03}$	$0.04^{+0.02}_{-0.02}$	$0.06^{+0.01}_{-0.02}$	$0.06^{+0.02}_{-0.01}$
	0.01	$0.08^{+0.08}_{-0.08}$	$0.00^{+0.00}_{-0.00}$	$0.00^{+0.00}_{-0.00}$	$0.00^{+0.00}_{-0.00}$	$0.00^{+0.00}_{-0.00}$	$0.03^{+0.03}_{-0.01}$	$0.02^{+0.01}_{-0.02}$	$0.00^{+0.00}_{-0.00}$	$0.00^{+0.00}_{-0.00}$
Cıv	0.25	$0.83^{+0.08}_{-0.08}$	$0.45^{+0.09}_{-0.18}$	$0.60^{+0.10}_{-0.20}$	$0.36^{+0.11}_{-0.11}$	$0.48^{+0.07}_{-0.09}$	$0.40^{+0.05}_{-0.04}$	$0.36^{+0.05}_{-0.02}$	$0.38^{+0.03}_{-0.04}$	$0.36^{+0.03}_{-0.03}$
	0.05	$0.42^{+0.17}_{-0.10}$	$0.18^{+0.09}_{-0.09}$	$0.10^{+0.10}_{-0.10}$	$0.07^{+0.04}_{-0.07}$	$0.21^{+0.05}_{-0.05}$	$0.14^{+0.04}_{-0.03}$	$0.08^{+0.02}_{-0.02}$	$0.11^{+0.02}_{-0.02}$	$0.11^{+0.02}_{-0.02}$
	0.01	$0.17^{+0.08}_{-0.08}$	$0.09^{+0.09}_{-0.09}$	$0.00^{+0.00}_{-0.00}$	$0.00^{+0.00}_{-0.00}$	$0.07^{+0.03}_{-0.03}$	$0.04^{+0.03}_{-0.03}$	$0.01^{+0.01}_{-0.01}$	$0.02^{+0.01}_{-0.01}$	$0.04^{+0.01}_{-0.01}$
Cııı	0.25	$0.67^{+0.11}_{-0.11}$	$0.57^{+0.14}_{-0.14}$	$0.29^{+0.14}_{-0.14}$	$0.19^{+0.10}_{-0.10}$	$0.33^{+0.07}_{-0.07}$	$0.22^{+0.06}_{-0.06}$	$0.26^{+0.06}_{-0.03}$	$0.25^{+0.04}_{-0.03}$	$0.31^{+0.04}_{-0.03}$
	0.05	$0.22^{+0.11}_{-0.11}$	$0.00^{+0.00}_{-0.00}$	$0.14^{+0.14}_{-0.14}$	$0.00^{+0.00}_{-0.00}$	$0.09^{+0.03}_{-0.05}$	$0.06^{+0.02}_{-0.04}$	$0.04^{+0.02}_{-0.02}$	$0.06^{+0.02}_{-0.02}$	$0.06^{+0.02}_{-0.02}$
	0.01	$0.00^{+0.00}_{-0.00}$	$0.00^{+0.00}_{-0.00}$	$0.00^{+0.00}_{-0.00}$	$0.00^{+0.00}_{-0.00}$	$0.00^{+0.00}_{-0.00}$	$0.00^{+0.00}_{-0.00}$	$0.00^{+0.00}_{-0.00}$	$0.01^{+0.00}_{-0.01}$	$0.02^{+0.01}_{-0.01}$
Siıv	0.25	$0.55^{+0.18}_{-0.11}$	$0.50^{+0.16}_{-0.25}$	$0.25^{+0.12}_{-0.12}$	$0.24^{+0.12}_{-0.12}$	$0.29^{+0.06}_{-0.06}$	$0.30^{+0.05}_{-0.07}$	$0.23^{+0.04}_{-0.04}$	$0.21^{+0.03}_{-0.03}$	$0.24^{+0.03}_{-0.03}$
	0.05	$0.18^{+0.09}_{-0.09}$	$0.12^{+0.12}_{-0.12}$	$0.12^{+0.12}_{-0.12}$	$0.06^{+0.06}_{-0.06}$	$0.08^{+0.04}_{-0.04}$	$0.05^{+0.03}_{-0.03}$	$0.04^{+0.03}_{-0.02}$	$0.04^{+0.02}_{-0.02}$	$0.05^{+0.01}_{-0.01}$
	0.01	$0.00^{+0.00}_{-0.00}$	$0.00^{+0.00}_{-0.00}$	$0.00^{+0.00}_{-0.00}$	$0.00^{+0.00}_{-0.00}$	$0.00^{+0.00}_{-0.00}$	$0.02^{+0.02}_{-0.02}$	$0.00^{+0.00}_{-0.00}$	$0.01^{+0.01}_{-0.01}$	$0.00^{+0.00}_{-0.00}$

2.D   Galaxy redshift measurements

Fig. 2.12 investigated if there are any differences in the absorption profiles using the full galaxy sample (which contains galaxy redshifts measured from a mix of rest-frame UV features and nebular emission lines) to a sample of galaxies with redshifts measured only using nebular emission lines. However, the comparison was complicated by the fact that these two samples contain different galaxies (and also that the latter group has less than half as many galaxies as the former).

To remove galaxy sample effects, we now use only the 238 galaxies that have redshifts measured using both techniques, and directly compare the results in Fig. 2.23. The slight enhancement at large LOS distances in the optical depth of the nebular only sample that was visible in Fig. 2.12 for Ovɪ and Cɪv is less apparent here. Overall there is only one significant difference between the two samples, for the smallest impact parameter / LOS bin, the nebular-only optical depths are consistently lower than those measured from rest-frame UV features. This may suggest that the peak in the absorption is systematically offest from the galaxy's systemic redshift.

Furthermore, our galaxy sample has changed significantly from that of Rakic et al. (2012). Particularly in the innermost impact parameter bins, many more galaxies now have redshifts measured using MOSFIRE. This presents a problem: since the redshift errors in Rakic et al. (2012) were so large, then would we not expect to see a difference in the LOS extent of Hɪ optical depths between the two samples? Specifically, the results from Rakic et al. (2012) should essentially show the effect of being smoothed on 150 km s^{-1} scales with respect to the current data.

To explore this, we show our median Hɪ optical depth results (yellow circles) alongside those from Rakic et al. (2012, grey points) in Fig. 2.24. Specifically, we plot the unsmoothed data taken from cuts along the LOS through the Hɪ map in our Fig. 2.4 and Fig. 5 of Rakic et al. (2012). We also show how the current data look when smoothed with a σ = 150 km s^{-1} Gaussian as the magenta line. Naively, we would expect the points from Rakic et al. (2012) to be consistent with this curve, and indeed, except for the smallest transverse cut (upper left panel), they are in relatively good agreement.

As for the innermost transverse distance bin, it is still curious that Hɪ optical depths from this work and Rakic et al. (2012) are in near perfect agreement. A possible explanation comes from the fact that galaxies with low impact parameters were preferentially targeted with NIRSPEC – already in Rakic et al. (2012), 25% of galaxies with impact parameters less than 250 kpc had nebular redshifts (compared to 9% for the remainder of the sample), reducing the amount of change we would expect to see between this study and the previous one.

It is worth mentioning that the latest data resolve some tensions with theory. Fig. 7 of Rakic et al. (2013) demonstrates that the observed LOS optical depth values tend to be lower then those seen in simulations for impact parameters 0.013-0.25 pMpc, which is no longer the case with the updated KBSS galaxy sample.
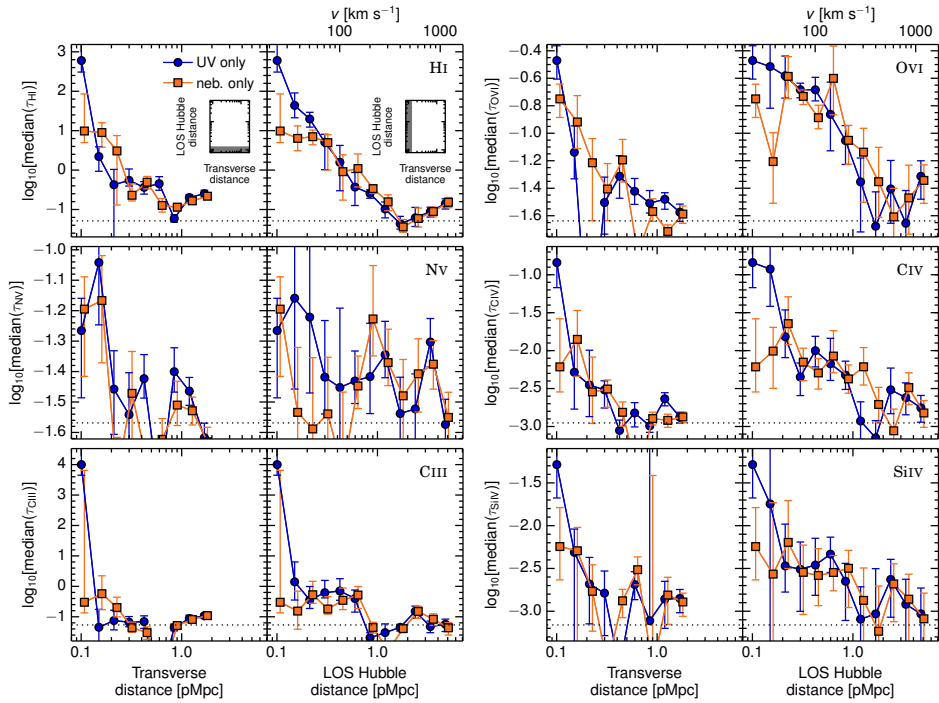
Figure 2.23: As Fig. 2.12, but for the same 238 galaxies, using either their redshifts measured from rest-frame UV features (blue circles) or from nebular emission lines (orange squares). Except for the first bin of CIV, there are no significant differences between the results based on nebular and rest-frame UV redshifts.
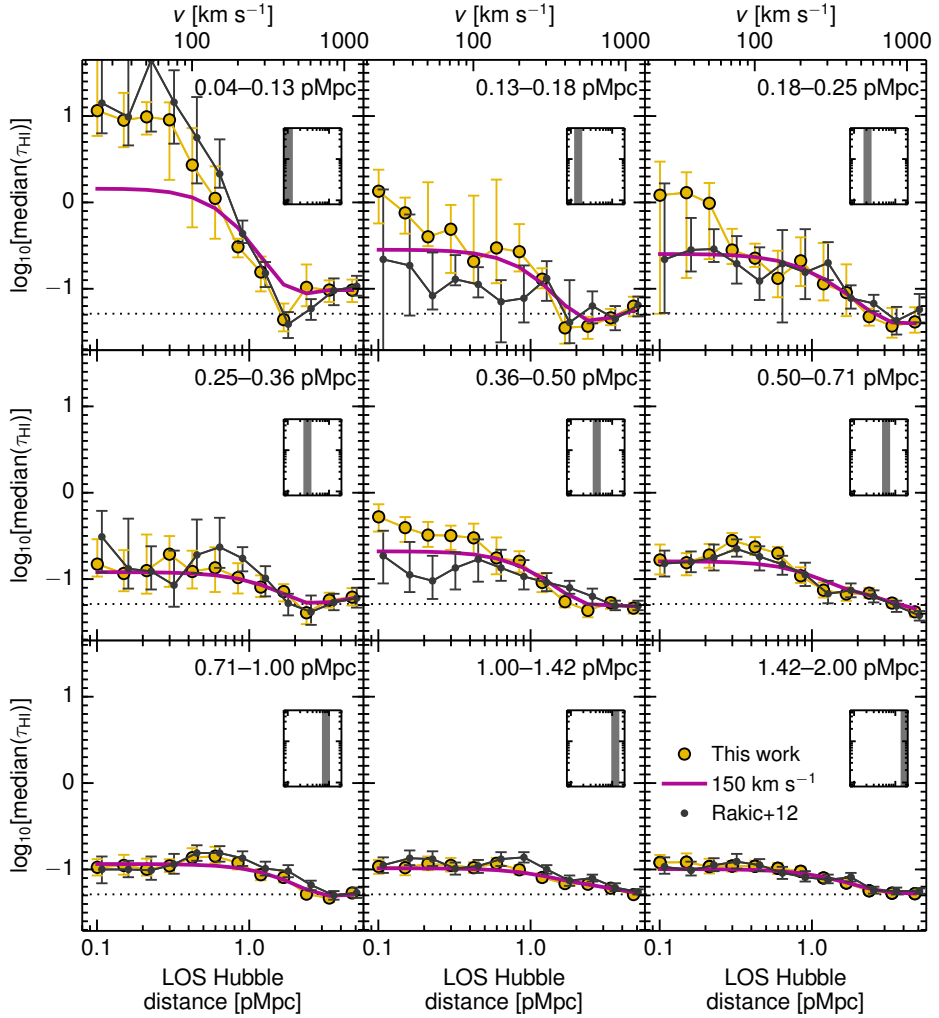
Figure 2.24: Cuts along the LOS through the unsmoothed H I map from Fig. 2.4 (using the values from Table 2.5), where each panel shows a different transverse distance bin as denoted by the label and shown by the inset. The yellow circles show the data from this work, and the magenta lines give the values after smoothing with a $\sigma = 150$ km s^{-1} Gaussian, to mimic the effect of larger redshift errors. For comparison, we display the points from Fig. 6 and Table 2 of Rakic et al. (2012), whose galaxy sample only had 10% nebular redshifts. Although we find no difference between the two data sets in the first panel (0.04–0.13 pMpc), the second and third panels (0.13–0.18 and 0.18–0.25 pMpc) show that the results from Rakic et al. (2012) are consistent with the current data after convolution with 150 km s^{-1} redshift errors.

3 Detection of hot, metal-enriched outflowing gas around $z \approx 2.3$ star-forming galaxies in the Keck Baryonic Structure Survey

We use quasar absorption lines to study the physical conditions in the circumgalactic medium of redshift $z \approx 2.3$ star-forming galaxies taken from the Keck Baryonic Structure Survey (KBSS). In Turner et al. (2014) we used the pixel optical depth technique to show that absorption by H I and the metal ions O VI, N V, C IV, C III and Si IV is strongly enhanced within $|\Delta v| \lesssim 170$ km s^{-1} and projected distances $|d| \lesssim 180$ proper kpc from sightlines to the background quasars. Here we demonstrate that the O VI absorption is also strongly enhanced at fixed H I, C IV, and Si IV optical depths, and that this enhancement extends out to ~ 350 km s^{-1}. At fixed H I the increase in the median O VI optical depth near galaxies is 0.3–0.7 dex and is detected at 2–3-σ confidence for all seven H I bins that have $\log_{10} \tau_{\rm H I} \geq -1.5$. We use ionization models to show that the observed strength of O VI as a function of H I is consistent with enriched, photoionized gas for pixels with $\tau_{\rm H I} \gtrsim 10$. However, for pixels with $\tau_{\rm H I} \lesssim 1$ this would lead to implausibly high metallicities at low densities if the gas were photoionized by the background radiation. This indicates that the galaxies are surrounded by gas that is sufficiently hot to be collisionally ionized ($T > 10^5$ K) and that a substantial fraction of the hot gas has a metallicity $\gtrsim 10^{-1}$ of solar. Given the high metallicity and large velocity extent (out to $\sim 1.5 \times v_{\rm circ}$) of this gas, we conclude that we have detected hot, metal enriched outflows arising from star-forming galaxies.

3.1 Introduction

Galaxy formation models predict that massive galaxies are surrounded by haloes of hot, chemically enriched gas, which may be penetrated by accreting streams of cold and largely metal-poor gas (e.g. Kereš et al., 2005; Dekel et al., 2009; van de Voort et al., 2011; van de Voort & Schaye, 2012). The hot component is heated through shocks associated with galactic winds and gas accretion, while the cold component is photo-heated to temperatures of $T \sim 10^4$ K. The circumgalactic medium thus results from the inflow of gas into the potential well set by the dark matter halo, and the outflows driven by feedback from star formation and/or active galactic nuclei (AGN). Hence, the gas around galaxies holds valuable clues to the fuelling and feedback processes that currently limit our understanding of galaxy

evolution.

This circumgalactic gas is very diffuse, making it difficult to detect in emission. Instead, the gas can be studied in absorption using high-quality spectra of background quasars. However, the low number density of bright quasars and the difficulty of obtaining accurate galaxy redshifts make it challenging to apply this technique to systematic surveys of the circumgalactic medium.

The advent of the Cosmic Origin Spectrograph on the Hubble Space Telescope and the MOSFIRE spectrograph on the Keck telescope have recently improved the situation by significantly increasing the quality of low-redshift quasar spectra and the accuracy with which redshifts can be measured for high-redshift galaxies, respectively. In particular, Tumlinson et al. (2011) found Ovɪ to be ubiquitous within 150 proper kiloparsec (pkpc) of z = 0.10–0.36 star-forming galaxies with median halo masses $\approx 1.6 \times 10^{12}$ M$_\odot$ (Werk et al., 2014). At $z \approx 2.4$, Turner et al. (2014) found strong enhancements of Ovɪ, Nv, Cɪv, Cɪɪɪ, Sɪɪv, and Hɪ within 180 pkpc and 240 km s^{-1} of star-forming galaxies that are also thought to be hosted by haloes with masses $\sim 10^{12}$ M$_\odot$. These studies confirmed and extended earlier work on the association between galaxies and absorbers.

The ion Ovɪ is of particular interest, because its absorption is relatively strong and because it can trace gas at $T \sim 10^5$–10^6 K, similar to the temperatures to which the gas is expected to be heated in shocks associated with winds and accretion events. Furthermore, it is the temperature range for which gas cooling from much higher temperatures is most likely to be detectable. Indeed, a number of simulations predict the presence of large amounts of Ovɪ around $M_{\mathrm{halo}} > 10^{11}$ M$_\odot$ galaxies (e.g. Stinson et al., 2012; Ford et al., 2013; Shen et al., 2013). In general, these studies find that Ovɪ resides in a collisionally ionized gas phase for impact parameters < 100 pkpc, outside of which Ovɪ tends to be found in a cooler, photoionized gas. Tepper-García et al. (2011) estimate that two-thirds of Ovɪ absorbers at z = 0.25 in their simulations trace gas with $T > 10^5$ K (see also Oppenheimer et al. 2012).

At low redshifts, many observational programmes have found that Ovɪ absorbers tend to be located within 300 pkpc of galaxy positions (e.g. Stocke et al., 2006; Chen & Mulchaey, 2009; Prochaska et al., 2011; Tumlinson et al., 2011). Although the presence of Ovɪ around galaxies is well established, the properties of the gas that it traces are still under debate, as Ovɪ systems are observed to arise in both photoionized and collisionally ionized phases (e.g, Danforth & Shull, 2008; Savage et al., 2014). While some studies find that Ovɪ in galaxy haloes is consistent with being photoionized (e.g. Prochaska et al., 2011), many circumgalactic Ovɪ absorbers are thought to be in a phase distinct from that of both Hɪ and lower ions at $T < 10^5$ K, due to their often complex and differing kinematic structures (e.g. Tripp et al., 2008) and/or inferences from ionization modelling (e.g. Werk et al., 2013). Using Hɪ Lyα absorber stacking[1] Pieri et al. (2014) found that for high ionization lines including Ovɪ, their observations were most consistent with $T = 10^4$–$10^{4.5}$ K, with a possible contribution from warmer $T \sim 10^{5.5}$ K gas (inferred from N/O measurements) .

---

[1]Although this work does not use direct galaxy detections, the authors inferred that their strongest absorber sample probes regions defined as circumgalactic in Rudie et al. (2012b) in $\approx$ 60 percent of cases. This was determined by using high-resolution QSO spectra from fields where the redshifts of Lyman break galaxies with impact parameters < 300 kpc are already known. The QSO spectra were degraded to match the resolution of the spectra used in Pieri et al. (2014), and a correction for the expected volume density of Lyman break galaxies from Reddy et al. (2008) was applied.

Because of its near-coincidence with the H I Lyβ forest, studying O VI absorption using line-fitting techniques becomes progressively more difficult with increasing redshift, although individual line fitting is still possible and has been done extensively at $z > 2$ (e.g. Bergeron et al., 2002; Carswell et al., 2002; Simcoe et al., 2002, 2004, 2006; Lopez et al., 2007; Schaye et al., 2007; Fox et al., 2008). Rather than looking by eye for individual O VI absorption lines, O VI has also been studied using the automatic pixel optical depth technique to correlate the absorption from O VI with that of other ions (Cowie & Songaila, 1998; Schaye et al., 2000a; Aguirre et al., 2008; Pieri et al., 2010), optionally correcting for much of the contamination by H I Lyman series lines (Aguirre et al., 2002, 2008; Turner et al., 2014).

Aracil et al. (2004) divided a sample of pixel optical depths into those near and far from strong H I Lyα absorption. They found that for gas at the same H I optical depth, the amount of O VI was enhanced near strong H I Lyα absorption for $2.1 < z < 3.2$. A similar study was then undertaken by Pieri et al. (2006) for the quasar Q1422 + 231 ($z = 3.62$). Motivated by the very strong correlation between galaxies and strong C IV absorbers found by Adelberger et al. (2003, 2005a), they used C IV optical depth as a galaxy proxy, and found enhancements in both C IV and O VI at fixed H I close to galaxy positions.

In this work we extend the technique used in Pieri et al. (2006) and apply it to a much larger sample of 15 quasars and 854 spectroscopically confirmed galaxies (with impact parameters as small as 40 pkpc) taken from the Keck Baryonic Structure Survey (KBSS, Steidel et al. 2014). Rakic et al. (2012) and Rudie et al. (2012b) have already used an earlier version of the survey to study the distribution of neutral hydrogen around the galaxies, while Turner et al. (2014) measured the distribution of metal ions using the same data as is analysed here. Using a galactocentric approach and the pixel optical depth technique, Turner et al. (2014) found metal-line absorption to be strongly enhanced with respect to random regions for impact parameters $\lesssim 180$ pkpc and line of sight (LOS) distances within ± 240 km s^{-1} of the galaxy positions (or ~1 pMpc in the case of pure Hubble flow). Furthermore, thanks to observations using MOSFIRE, the elongation of enhancement along the LOS was determined to be largely caused by gas peculiar velocities (rather than redshift errors).

While Turner et al. (2014) studied optical depth as a function of galaxy distance, here we will measure the enhancement of metal-line absorption at fixed H I optical depth. This enables us to tell whether the enhancement in metal absorption near galaxies found by Turner et al. (2014) merely reflects the higher gas densities implied by the observed increase in H I absorption, or whether it indicates that the circumgalactic gas has a higher metallicity or a different temperature compared to random regions with the same H I optical depth.

This paper is organized as follows. In Section 3.2 we briefly review the properties of the galaxy and quasar samples, the galaxy redshifts, and the pixel optical depth technique. In Section 3.3 we present the principal observational results of this paper, which is that we find a strong and significant enhancement of O VI at fixed H I, C IV and Si IV for impact parameters < 180 pkpc and velocities $\lesssim 350$ km s^{-1}. In section 3.4 we consider whether the observational result can be explained (1) if the gas near galaxies is photoionized and metal rich, (2) if the gas is photoionized by radiation from stars in the nearby galaxies, or (3) if the enriched gas is collisionally ionized. We find that small galactocentric distance pixels with $\tau_{\rm H I} \gtrsim 10$ are in agreement with scenarios (1) and (3), while for those that have $\tau_{\rm H I} \lesssim 1$, only scenario (3), i.e. the presence of hot, collisionally ionized gas, provides a consistent

explanation. Finally, in Section 3.5 we summarize and discuss our main results.

Throughout the paper, we use proper rather than comoving units (denoted as pkpc and pMpc), and employ cosmological parameters as measured from the Planck mission (Planck Collaboration et al., 2013), i.e. $H_0 = 67.1$ km s^{-1} Mpc^{-1}, $\Omega_m = 0.318$, $\Omega_\Lambda = 0.683$, and $\Omega_b h^2 = 0.0221$.

3.2   Observations and method

This work makes use of procedures that were detailed in Turner et al. (2014), which we will briefly outline here.

3.2.1   Galaxy & QSO samples

The KBSS is centred around the fields of 15 hyper-luminous QSOs, all of which have been observed extensively with Keck/HIRES and therefore have very high quality spectra. Details about the QSO reduction and analysis, including the fitting out of DLA wings, are described in Rudie et al. (2012b). The HIRES spectra typically have $R \simeq 45000$ (which corresponds to a FWHM $\simeq 7$ km s^{-1}), and S/N ranging from ~ 50 to 200 pixel^{-1} (we give the median S/N for the spectral regions covered by each ion in Table 3.1).

The survey focuses on obtaining spectroscopic redshifts for the galaxies in the above QSO fields. The full sample currently consists of ≈ 2550 galaxies at $\langle z \rangle \approx 2.3$, that were chosen to have redshifts in the range probed by the QSO spectra using UV-colour selection techniques from Steidel et al. (2003, 2004) and Adelberger et al. (2004). Spectroscopic follow-up using the instruments LRIS, NIRSPEC and/or MOSFIRE was then performed on galaxies with apparent magnitudes $m_\mathcal{R} \leq 25.5$ (see Rudie et al. 2012b for more information about the galaxy follow-up strategy). The above selection typically results in galaxies with halo masses $\sim 10^{12}$ M$_\odot$(Adelberger et al., 2005b; Conroy et al., 2008; Trainor & Steidel, 2012; Rakic et al., 2013), which corresponds to virial radii and circular velocities of ≈ 90 pkpc and ≈ 217 km s^{-1}, respectively. Furthermore, these galaxies tend to have dynamical masses $\approx 7 \times 10^{10}$ M$_\odot$(Erb et al., 2006c), median star formation rates ≈ 25 M$_\odot$ yr^{-1} (Erb et al., 2006b; Steidel et al., 2014), gas-phase metallicities ≈ 0.4 Z$_\odot$ (Steidel et al., 2014), and stellar ages ≈ 0.7 Gyr (Erb et al., 2006c).

In this work, we focus on the subset of 21 KBSS galaxies that satisfy the following two constraints. First, we limit the sample to galaxies with impact parameters < 180 pkpc. Although we also considered galaxies with impact parameters up to 2 pMpc as was done in Turner et al. (2014), we did not find any differences in the results from using impact parameter bins > 180 pkpc compared to those from random regions. The choice of 180 pkpc can be further motivated by the fact that Turner et al. (2014) found a strong metal optical depth enhancement above the median value for random regions up to the same impact parameter values.

The second constraint concerns the velocity direction, where we consider only galaxies that lie within the Lyα forest of the background QSO, defined as:

$$(1 + z_{\mathrm{qso}}) \frac{\lambda_{\mathrm{Ly}\beta}}{\lambda_{\mathrm{Ly}\alpha}} - 1 \leq z \leq z_{\mathrm{qso}} - (1 + z_{\mathrm{qso}}) \frac{3000 \, \mathrm{km \, s}^{-1}}{c}. \tag{3.1}$$

Table 3.1: The log of the median optical depth, and the median continuum S/N of all pixels (with normalized flux > 0.7) in the redshift range considered for the particular ion and recovery method.

Ion	$\log_{10}\tau_{Z,\mathrm{rnd}}$	$\mathrm{S/N_{med}}$
H$\textsc{i}$	−1.29	70.1
O$\textsc{vi}$	−1.64	45.7
C$\textsc{iv}$	−2.95	83.6
Si$\textsc{iv}$	−3.16	84.4

The left-hand side corresponds to the beginning of the Lyβ forest, while the right-hand side is set by the QSO emission redshift less an offset factor to avoid proximity effects. This second criterion is required so that the pixel optical depth analysis (as described in § 3.2.3) can be applied to the same redshift range for different ions.

3.2.2 Galaxy redshifts

NIRSPEC and MOSFIRE are both near-IR spectrographs, with galaxy redshift measurement uncertainties estimated to be $\Delta v \approx 60$ and 18 km s^{-1}, respectively. With these instruments, we are able to probe the rest-frame optical wavelengths for the galaxies in this sample, and to observe the nebular emission lines Hα, Hβ, and [O$\textsc{iii}$] $\lambda\lambda$4959,5007. Since these lines arise in H$\textsc{ii}$ regions of galaxies and, unlike Lyα, are not subject to significant resonant scattering, they are thought to be robust tracers of the systemic redshift, and for our analysis we therefore take the galaxy redshift to be equal to that of the nebular emission lines, $z_{\mathrm{gal}} = z_{\mathrm{neb}}$.

Although we are continuously working to increase the number of galaxies that have MOSFIRE observations, currently 4 out of the 21 galaxies in our sub-sample have been observed only with LRIS, which probes the rest-frame UV. From these data, we can measure the galaxy redshifts from either interstellar absorption lines (z_{ISM}) or Lyα emission lines ($z_{\mathrm{Ly}\alpha}$). However, these lines tend to be systematically offset from the systemic galaxy redshifts (Shapley et al., 2003; Adelberger et al., 2003; Steidel et al., 2010; Rakic et al., 2011). To correct for this, we consider the galaxies that have both a nebular and rest-frame UV redshift measurement, and use the average difference between z_{ISM} or $z_{\mathrm{Ly}\alpha}$ and z_{neb} to determine a bulk correction value. The specifics of the correction implementation, as well as the latest offset values, can be found in § 2.2 of Turner et al. (2014). Our final sample of 21 galaxies contains 17 and 4 galaxies with redshifts measured from nebular and rest-frame UV features, respectively. Their minimum, median, and maximum impact parameters are 35, 118, and 177 pkpc, respectively.

3.2.3 Pixel optical depths

In this work, we use the pixel optical depth method (Cowie & Songaila, 1998; Ellison et al., 2000; Schaye et al., 2000a; Aguirre et al., 2002; Schaye et al., 2003; Turner et al., 2014) to study how absorption varies with galaxy proximity. Because of the statistical nature of our approach, we lose information about individual systems. However, by studying correlations between the pixel optical depths of different transitions, we are able to probe gas to

lower densities, even in the presence of strong contamination, in a fast and fully automated manner.

A complete description of the method used is given in § 3 and Appendix A of Turner et al. (2014); here we give a short summary. We initially define the optical depth for ion Z and multiplet component k as

$$\tau_{Z,k}(z) \equiv -\ln[F_{Z,k}(z)] \tag{3.2}$$

where $F_{Z,k}(z)$ is the normalized flux at the pixel with a wavelength given by $\lambda = \lambda_{Z,k}[1 + z]$ where $\lambda_{Z,k}$ is the rest-wavelength of the kth transition of ion Z.

Next, we correct the absorption by each ion for saturation and for possible sources of contamination. Beginning with H I, if Lyα is saturated, we use the optical depths of higher-order transitions (Lyβ, Lyγ etc.) at the same redshift. Of all the higher-order pixels at a single redshift, we take the minimum of the optical depths that are not saturated (if there are any), scaled to the Lyα transition, and use it to replace the saturated Lyα value.

The recovered H I Lyα is then used to subtract 5 orders of the Lyman series of H I (starting from Lyβ) from the optical depths of ions that have rest-wavelengths in the Lyβ forest: O VI $\lambda\lambda 1032, 1038$ and C III 977. We note that for the recovery of ions that require H I subtraction, we do not mask the DLAs or fit out the wings for the H I recovery (see Turner et al. 2014).

For ions that have a closely-spaced doublet (O VI $\lambda\lambda 1032, 1038$ and Si IV $\lambda\lambda 1394, 1403$) we use the relative oscillator strengths to scale the optical depth of the weaker component to that of the stronger one, and take the minimum of the two optical depths at every redshift in order to correct for contamination.

Although C IV $\lambda\lambda 1548, 1551$ also has a closely-spaced doublet, due to its strength and the fact that it is located redwards of the Lyα forest, most contamination comes from other C IV systems. We therefore use a procedure where we iteratively subtract the optical depth of the weaker component at the position of the stronger component.

Although we attempt to correct for contamination, these corrections will generally not be perfect. In particular, we cannot correct for contamination of O VI by H I Lyα, which will cause our measurements of the O VI optical depth to be overestimates (however, on average it will affect all pixels in the forest equally). This contaminating Lyα absorption, as well as residual absorption from other contaminating lines, set the limit down to which we can detect enhancements in the O VI optical depth.

3.3   Results

The first step in our analysis is to compute the median $\tau_{\rm OVI}$ as a function of $\tau_{\rm HI}$, which we will often denote O VI(H I) for brevity. To do this, we take pixel pairs of $\tau_{\rm OVI}$ and $\tau_{\rm HI}$ at each redshift z, divide the pixels into 0.5 dex sized bins of $\log_{10} \tau_{\rm HI}$, and compute the median of $\tau_{\rm OVI}$ in each bin. We do this for both the full pixel sample (i.e. every pixel pair available from all 15 QSOs in the redshift range given by eq. 3.1, irrespective of the locations of the galaxies), and for pixels known to be located at small galactocentric distances, defined as those within[2] ± 170 km s^{-1} of the redshifts of galaxies with impact parameters < 180 pkpc.

---

[2]This velocity interval was chosen because (as explained in more detail in Rakic et al. 2012 and Turner et al. 2014) it is the scale over which the optical depths are smooth in the LOS direction.

To avoid effects due to small number statistics, we do the following. For the full pixel sample, we divide the spectra into chunks of 5Å. We then compute the number of chunks that are sampled by each $\log_{10} \tau_{HI}$ bin, and discard any bins that draw from fewer than five different chunks. For the small galactocentric distance pixel sample, we remove bins that do not have pixel contributions from at least five different galaxies. Finally, for both pixel samples we discard any bins containing fewer than 25 pixels in total.

The derived $O_{VI}(H_I)$ relations are shown in the left panel of Fig. 3.1, where the black points and red stars indicate the relations for the full pixel sample and the small galactocentric distance sample, respectively. We also provide the data values shown in this figure in Table 3.2. The behaviour of the $O_{VI}(H_I)$ relation for the full pixel sample is consistent with previous measurements (e.g. Schaye et al., 2000a; Aguirre et al., 2008) and we briefly explain the observed characteristics here.

Focusing on the black circles, there are two distinct regions in H_I optical depth, separated by[3] $\tau_{HI,cut} \sim 0.1$. For $\tau_{HI} > \tau_{HI,cut}$, τ_{OVI} increases with τ_{HI}. This relation arises because a large number of these pixel pairs are probing regions which have been enriched by oxygen, and the value at each pixel is set by the median number density ratio of O_{VI} to H_I.

For lower values of τ_{HI} (below $\tau_{HI,cut}$), τ_{OVI} stays approximately constant, which indicates that the measured value is determined by residual contamination or noise and that the true, median value of τ_{OVI} is below this detection limit. In general, this asymptotic value of τ_{OVI} is slightly less than the median O_{VI} optical depth of the full sample of pixels (the value is given in Table 3.1, and is indicated by the horizontal dotted black line in Fig. 3.1). We attempt to measure the constant value to which the O_{VI} pixel optical depths asymptote, which we call the O_{VI} flat level. As in Aguirre et al. (2008), we take this flat level to be the median of all τ_{OVI} pixels associated with $\tau_{HI} < \tau_{HI,cut}$.

Furthermore, we estimate a 1-σ error on this quantity by dividing each spectrum into 5 Å chunks and creating 1000 bootstrap resampled spectra. The flat level and the associated 1σ error are denoted by the black dashed line and grey region, respectively. It is difficult to probe O_{VI} optical depths below the flat level, as one becomes limited by contamination. Specifically, absorption from ions with rest wavelength less than that of H_I Lyα are found bluewards of the QSO Lyα emission line, and their recovery is limited by contamination from H_I and other metal lines. These metal transitions are less affected by the quality (S/N) of the spectra and are more sensitive to the method of recovery. On the other hand, for ions redwards of the QSO's Lyα emission, the median pixel optical depths are set mainly by the S/N and/or shot-noise, since the majority of pixels do not have detectable metal absorption. The two right panels of Figs. 4 and 5 in Aguirre et al. (2002) show the changes on the median levels for different recovery methods and S/N ratios for O_{VI} (bluewards of the QSO Lyα emission) and C_{IV} (redwards of the QSO Lyα emission) using simulated spectra. These figures clearly demonstrate how the median level for O_{VI} is more sensitive to recovery method while for C_{IV} changing the S/N has a greater effect.

Turning next to the red stars in the left panel of Fig. 3.1, we see a significant enhancement of τ_{OVI} at fixed τ_{HI} for the small galactocentric distance pixels compared to the full pixel sample. Such a difference is not present if we consider larger impact parameter bins

---

[3]As noted in Aguirre et al. (2008), because the O_{VI} pixel relations are not as strong as for C_{IV}, we fix the value of τ_{cut} by hand rather than using functional fits. We use the same values as in Aguirre et al. (2008) of τ_{cut} = 0.1 when pixel pairs are binned based on the optical depths of transitions that fall blueward of the QSO's Lyα emission (O_{VI}, H_I) and 0.01 for those falling redward (C_{IV}, Si_{IV}).
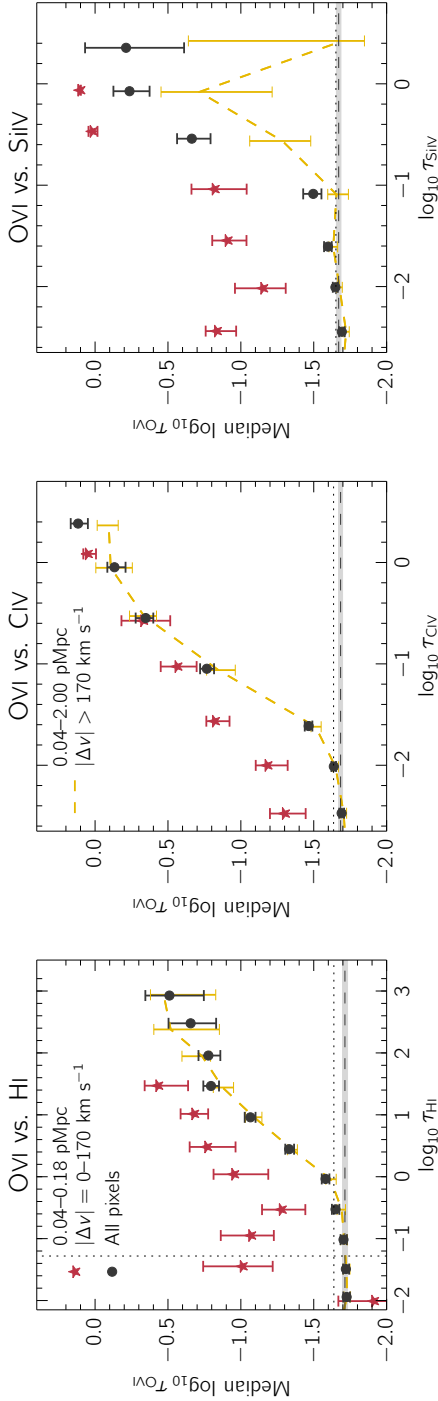
Figure 3.1: *Left panel*: The Ovɪ(Hɪ) relation for the full sample of pixels (black circles) and for pixels located at small galactocentric distances (red stars). Error bars indicate the 1σ uncertainty determined by bootstrap resampling the galaxies. The median values for the full sample are denoted by the horizontal and vertical dotted black lines. The Ovɪ flat level, defined as the median value for all Ovɪ pixels that have associated $\tau_{HI} < \tau_{HI,cut} = 0.1$, is represented by the horizontal dashed grey line, and the shaded region shows its 1-σ error. The dashed line shows the optical depth relation for the full pixel sample after masking out regions within ±170 km s^{-1} of known galaxy redshifts, where we have considered galaxies with impact parameters of up to 2 pMpc. For a given Hɪ optical depth, we find a strong enhancement for the median Ovɪ optical depth for pixels at small galactocentric distances. *Centre and right panels*: The same as the left panel except for Ovɪ(Cɪv) and Ovɪ(Sɪɪv). The fact that we observe the same trend when binning by different ions along the x-axis provides additional evidence that the effect we are seeing is real.

(not shown). We emphasize that although the full pixel sample is representative of random regions, it is composed of pixels both near and far from galaxies (and many of these galaxies are likely not detected in our survey). To demonstrate this, we examine the effect of masking out the regions in the spectra that are known to be near galaxies. We consider all galaxies in our sample with impact parameters ≤ 2 pMpc and with redshifts satisfying eq. 3.1, and mask out regions of ±170 km s^{-1} around these redshifts in all 15 of our QSO spectra. The resulting optical depth relation is shown as the dashed line in the left panel of Fig. 3.1, and we conclude that the full pixel sample relation is largely independent of the presence of regions proximate to detected galaxies.

Next, we vary the ion plotted along the x-axis. In the centre and right panels of Fig. 3.1, we show the relations for Ovi(Civ) and Ovi(Siiv), respectively (the values are also given in Table 3.2). Just as for Ovi(Hi), we observe significantly enhanced Ovi optical depths at both fixed τ_{CIV} and fixed τ_{SiIV}. The persistent enhancement of OVI absorption at fixed optical depth of three distinct ions (Hi, Civ and Siiv) makes the individual detections with respect to each ion still more significant. Here we note that although the Ovi(Hi) and Ovi(Civ) optical depth relations for which the galaxy positions have been masked out of the spectra show significant signal, this is not the case for Ovi(Siiv). This suggests that strong Siiv absorption arises primarily near galaxies.

It is instructive to assess how sensitive the enhancement is to the chosen velocity range. We have examined the Ovi(Hi) relation for velocity bins starting with $|\Delta v|$ = 0–170 km s^{-1} and increasing both velocity limits by increments of 10 km s^{-1}(such that each cut spanned the same total velocity range of 340 km s^{-1}). We found that for optical depth bins with $\tau_{\mathrm{HI}} \lesssim 1$, the enhancement is present up to a velocity range of $|\Delta v|$ = 270–440 km s^{-1}, and we take the midpoint of this bin, ~ 350 km s^{-1}, as an upper limit to the extent of the Ovi enhancement. In Fig. 3.2 we show the relation for the $|\Delta v|$ = 270–440 km s^{-1} velocity bin (central panel), as well as higher and lower velocity cuts (right and left panels, respectively). For most of the optical depth bins with $\tau_{\mathrm{HI}} > 1$, the enhancement in Ovi is only significant for velocities within ±170 km s^{-1} of the galaxy positions.

Although for the remainder of the analysis we will continue using the smallest velocity cut of $|\Delta v|$ = 0–170 km s^{-1} we emphasize that for the lowest Hi optical depth bins, Ovi is enhanced out to velocities of ~ 350 km s^{-1}, corresponding to $\gtrsim$ 1.5 times the typical circular velocities of the galaxies in our sample. While simulations predict that absorbers from galaxies below the detection limit can be projected to such velocities around their more massive counterparts (e.g., Rahmati & Schaye, 2014), in § 3.4 we determine that only a hot, collisionally ionized gas phase is observed out to these large velocities, which is certainly suggestive of outflows. Further comparisons with simulations will be required to fully disentangle outflow and clustering effects.

3.3.1   Are the observed differences in optical depth ratios real?

Fig. 3.1 suggests that the gas near the sample galaxies has properties different from that in random regions with the same strength of Hi, Civ, or Siiv optical depth. However, it is important to verify that the difference between the two pixel samples is not driven primarily by chance or systematic errors. In particular, limiting ourselves to only a few regions of the spectra could skew the results if, for example, these regions have different S/N, or inconsistent contamination levels due to being located at different redshifts.

Table 3.2: The median pixel optical depth values plotted in Fig. 3.1.

All pixels		0.04–0.18 pMpc $\Delta v = \pm 170$ km s^{-1}	
$\log_{10} \tau_{\mathrm{HI}}$	$\log_{10} \tau_{\mathrm{OVI}}$	$\log_{10} \tau_{\mathrm{HI}}$	$\log_{10} \tau_{\mathrm{OVI}}$
-1.94	$-1.73^{+0.02}_{-0.02}$	-2.01	$-1.91^{+0.24}_{-4.09}$
-1.49	$-1.72^{+0.02}_{-0.02}$	-1.45	$-1.01^{+0.27}_{-0.21}$
-1.02	$-1.70^{+0.02}_{-0.02}$	-0.95	$-1.07^{+0.21}_{-0.16}$
-0.53	$-1.65^{+0.02}_{-0.03}$	-0.53	$-1.28^{+0.13}_{-0.16}$
-0.04	$-1.58^{+0.03}_{-0.03}$	0.04	$-0.95^{+0.14}_{-0.24}$
0.44	$-1.33^{+0.03}_{-0.03}$	0.48	$-0.77^{+0.12}_{-0.20}$
0.96	$-1.07^{+0.04}_{-0.04}$	1.02	$-0.68^{+0.09}_{-0.10}$
1.47	$-0.80^{+0.05}_{-0.06}$	1.47	$-0.43^{+0.09}_{-0.21}$
1.96	$-0.78^{+0.07}_{-0.08}$		
2.48	$-0.66^{+0.15}_{-0.17}$		
$\log_{10} \tau_{\mathrm{CIV}}$	$\log_{10} \tau_{\mathrm{OVI}}$	$\log_{10} \tau_{\mathrm{CIV}}$	$\log_{10} \tau_{\mathrm{OVI}}$
-2.47	$-1.69^{+0.02}_{-0.02}$	-2.48	$-1.30^{+0.10}_{-0.15}$
-2.01	$-1.64^{+0.02}_{-0.02}$	-2.00	$-1.18^{+0.08}_{-0.14}$
-1.61	$-1.46^{+0.03}_{-0.03}$	-1.57	$-0.82^{+0.06}_{-0.10}$
-1.05	$-0.77^{+0.05}_{-0.05}$	-1.03	$-0.56^{+0.11}_{-0.13}$
-0.55	$-0.35^{+0.07}_{-0.05}$	-0.57	$-0.33^{+0.15}_{-0.19}$
-0.05	$-0.13^{+0.05}_{-0.08}$	0.08	$0.05^{+0.03}_{-0.06}$
0.38	$0.12^{+0.05}_{-0.07}$		
$\log_{10} \tau_{\mathrm{SiIV}}$	$\log_{10} \tau_{\mathrm{OVI}}$	$\log_{10} \tau_{\mathrm{SiIV}}$	$\log_{10} \tau_{\mathrm{OVI}}$
-2.45	$-1.69^{+0.02}_{-0.02}$	-2.44	$-0.83^{+0.07}_{-0.13}$
-2.01	$-1.65^{+0.02}_{-0.02}$	-2.02	$-1.15^{+0.19}_{-0.16}$
-1.61	$-1.60^{+0.03}_{-0.03}$	-1.55	$-0.91^{+0.10}_{-0.13}$
-1.09	$-1.50^{+0.07}_{-0.06}$	-1.04	$-0.82^{+0.16}_{-0.22}$
-0.54	$-0.66^{+0.10}_{-0.13}$	-0.47	$0.02^{+0.03}_{-0.04}$
-0.07	$-0.24^{+0.11}_{-0.14}$	-0.06	$0.10^{+0.01}_{-0.01}$
0.36	$-0.21^{+0.28}_{-0.40}$		
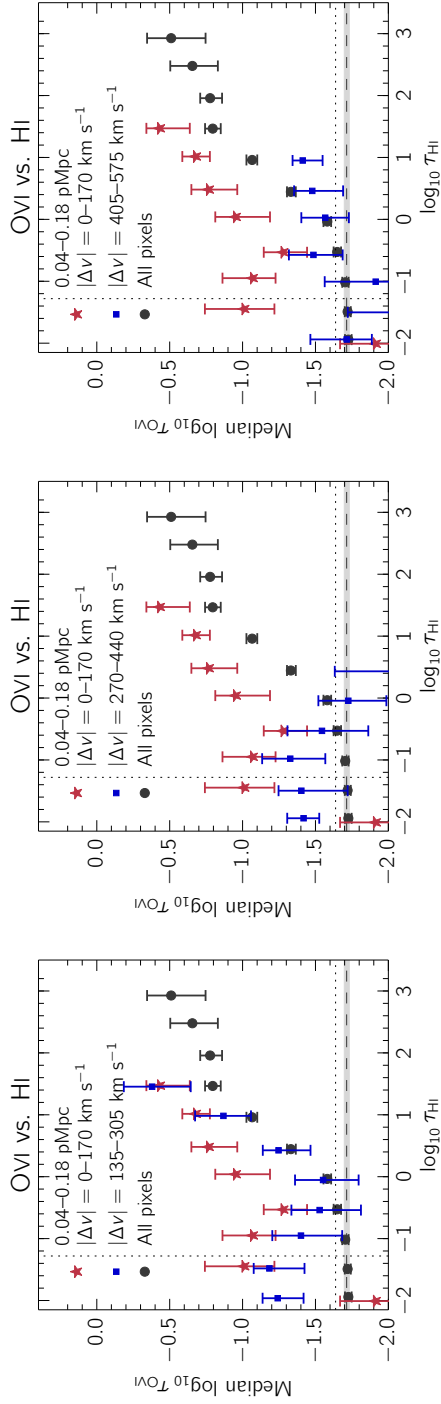
Figure 3.2: The same as Fig. 3.1 but we have overplotted the result of taking different velocity cuts when considering the small galactocentric distance points (blue squares). We have chosen velocity bins such that each cut spans the same velocity range of 340 km s^{-1}, and find that the enhancement of OVI at fixed τ_{HI} is present for $\tau_{\mathrm{HI}} \lesssim 0.1$ out to the $|\Delta v| = 270\text{--}440$ km s^{-1} velocity cut. Using the central value of this velocity range as our upper limit, we conclude that the enhancement persists out to ~ 350 km s^{-1}, which is $\gtrsim 1.5$ times the typical circular velocities of the galaxies in our sample.
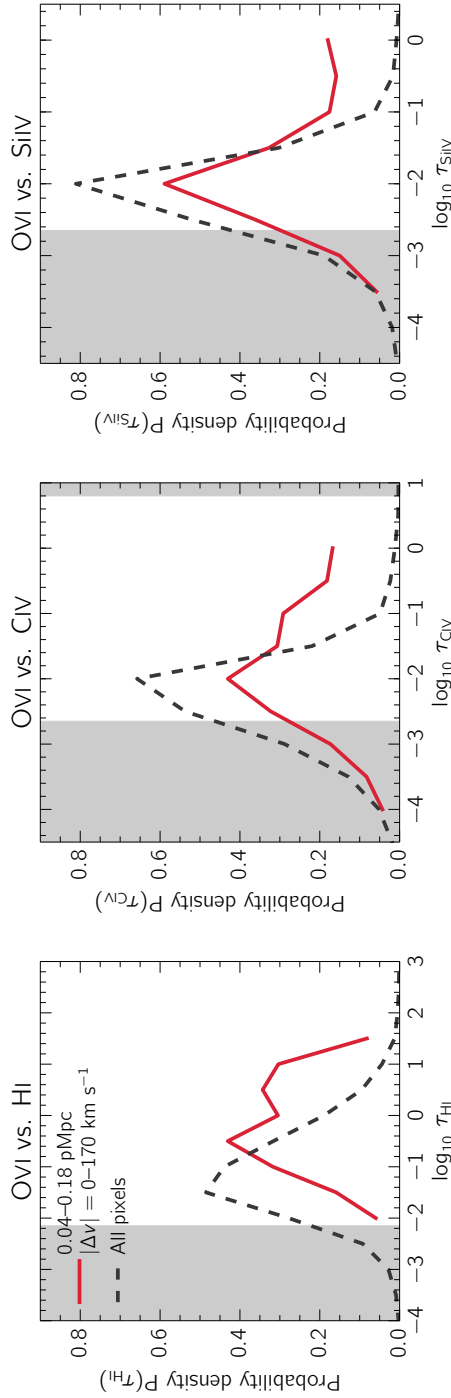
Figure 3.3: The probability density function of H I (left), C IV (centre) and Si IV (right) pixel optical depths for both the small galactocentric distance sample (red) and the full sample (black). For ease of comparison, we have shaded regions along the x-axis that are not included in the previous figures.
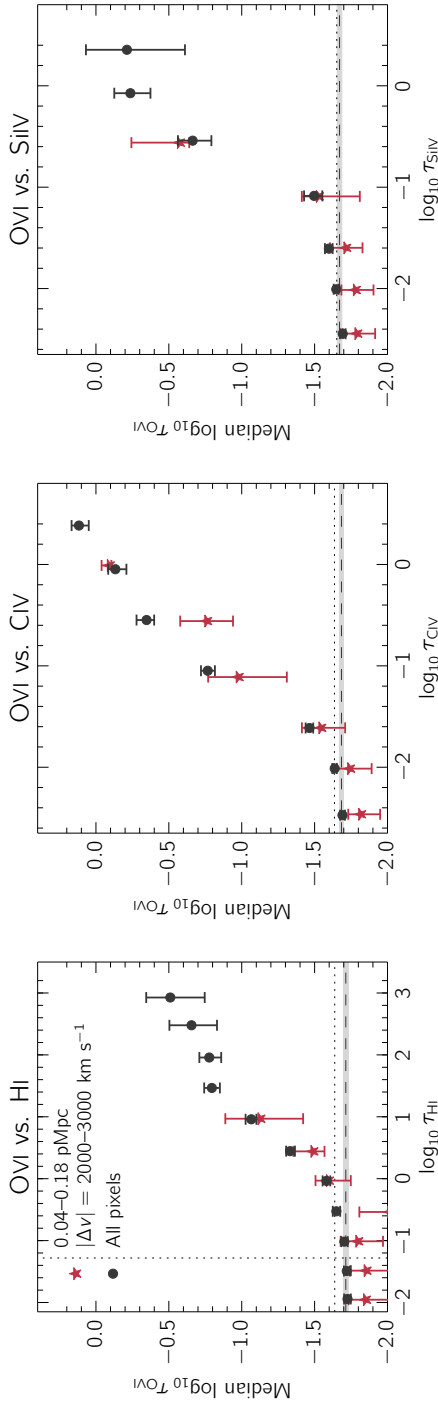
Figure 3.4: The same as Fig. 3.1 but instead of taking pixels within ±170 km s^{-1} of the galaxy redshifts, the red stars show the effect of choosing regions within $|\Delta v|$ = 2000–3000 km s^{-1} of the galaxy redshifts. By excluding the positions directly around the galaxies, but still using pixels within ~ 10³ km s^{-1} of the galaxy redshifts, we remove physical effects caused by the presence of the galaxy while probing the same spectral properties such as S/N, resolution, and distance from the QSO. Contrary to Fig. 3.1, the O VI absorption is not enhanced for the small galactocentric distance sample, which implies that the enhancement visible in that figure is not due to systematic differences in the spectral properties between the two samples.
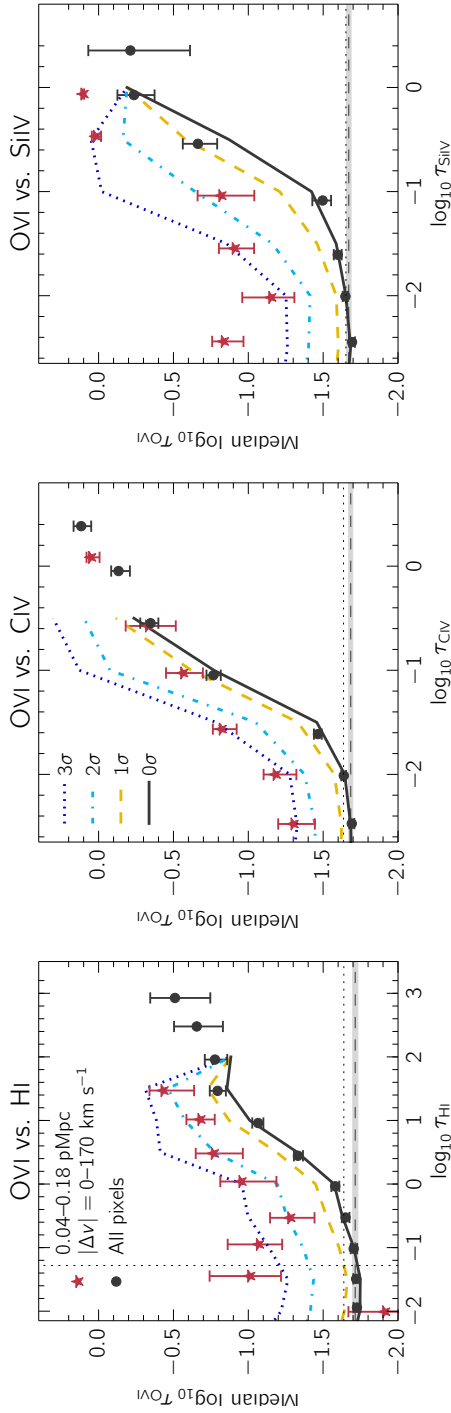
Figure 3.5: The same as Fig. 3.1, except that we have overplotted the results of randomising the redshifts of the small galactocentric distance galaxies 1000 times. For each of these randomizations, we recompute O$\textsc{vi}$(H$\textsc{i}$), O$\textsc{vi}$(C$\textsc{iv}$) and O$\textsc{vi}$(S$\textsc{iiv}$), and in this figure we show the median, and the 84.1, 98.7, and 99.8 percentiles (corresponding to 0, 1, 2, and 3σ, respectively) from the full distribution of realizations. We find that the enhancement of O$\textsc{vi}$ for fixed $\tau_{\text{O}\textsc{vi}}$, $\tau_{\text{C}\textsc{iv}}$ and $\tau_{\text{S}\textsc{iiv}}$ is approximately a 2–3-σ effect per bin.

First, we would like to be sure that the enhancement in the median O$\scriptsize VI$ optical depths is not due to a small number of pixels. In Fig. 3.3 we show the pixel optical depth probability density functions (PDFs) for H$\scriptsize I$, C$\scriptsize IV$ and Si$\scriptsize IV$, for both the small galactocentric distance and the full pixel samples (note that the x-axis ranges are larger than those shown in Fig. 3.1). Focusing on the small galactocentric distance pixels (red lines), one sees that the bins with enhanced median O$\scriptsize VI$ ($\log_{10} \tau_{\rm HI} \gtrsim -1$; $\log_{10} \tau_{\rm CIV}$ and $\log_{10} \tau_{\rm SiIV} \gtrsim -2$) comprise the majority of the pixels. Thus, the enhancement in the median O$\scriptsize VI$ optical depth cannot be attributed to a small number of pixels.

As a further test, in Fig. 3.4 we plot $\tau_{\rm OVI}$ versus $\tau_{\rm x}$ for the same $\tau_{\rm x}$ shown in Fig. 3.1, but instead of using pixels within $\Delta v = \pm170$ km s^{-1} of the galaxy redshifts, we look at regions further away, i.e. $|\Delta v| = 2000\text{--}3000$ km s^{-1}. This velocity cut is near enough to the galaxy redshifts that within each impact parameter bin we are still looking at areas of the spectra with the same S/N and contamination characteristics, but far enough to avoid regions that may be associated with the galaxies. If the enhancement of the O$\scriptsize VI$ optical depth at fixed H$\scriptsize I$, C$\scriptsize IV$, or Si$\scriptsize IV$ that we detect near galaxies were caused by systematic differences in the spectral properties of the two samples, then we would expect to see the enhancement to a similar significance in these figures. However, in every case where we previously saw an enhancement in the median O$\scriptsize VI$ optical depth for the pixels at small galactocentric distance, the effect is completely removed in Fig. 3.4.

Next, we examine whether the optical depth differences are consistent with random fluctuations. To do this, we take the galaxies from the small galactocentric distance sample, randomize their redshifts 1000 times, and calculate O$\scriptsize VI$(H$\scriptsize I$), O$\scriptsize VI$(C$\scriptsize IV$) and O$\scriptsize VI$(Si$\scriptsize IV$) for every random realization. In Fig. 3.5 we show the one-, two-, and three-σ percentiles that result from this procedure. From this, we measure the enhancements seen in O$\scriptsize VI$(H$\scriptsize I$), O$\scriptsize VI$(C$\scriptsize IV$), and O$\scriptsize VI$(Si$\scriptsize IV$) to be approximately a 2–3-σ effect per bin.

Additionally, because we do not observe differences in the O$\scriptsize VI$(H$\scriptsize I$), O$\scriptsize VI$(C$\scriptsize IV$) and O$\scriptsize VI$(Si$\scriptsize IV$) relations for galaxies with impact parameters > 180 pkpc and the full pixel sample, here we check whether the O$\scriptsize VI$ enhancement for the galaxies with impact parameters < 180 pkpc can be attributed to properties other than the galaxy distance to the QSO sightline. We directly test whether the following three characteristics in every impact parameter bins are consistent with the full sample: (1) the galaxy redshifts (lower galaxy redshifts mean that O$\scriptsize VI$ is more contaminated by H$\scriptsize I$), (2) the galaxy velocity distance from the QSO Lyα emission (to rule out QSO proximity effects) and (3) the S/N of the spectral regions (smaller S/N will bias the optical depth estimation high).

We have measured the *p*-values resulting from a 2-sample Kolmogorov-Smirnoff test, comparing the galaxy redshift, median S/N within ±170 km s^{-1} from the redshift of the galaxy, and redshift difference between the galaxy and the QSO, between the galaxies in the small galactocentric distance sample and the full galaxy sample. In every instance we find *p*-values greater than 0.1, which is consistent with the null hypothesis that the two samples are drawn from the same distribution.

Finally, in Appendix 3.A we have tested how the O$\scriptsize VI$ contamination correction affects our results. We determined that although the inferred values of the O$\scriptsize VI$ optical depths are sensitive to changes in the correction procedure, the enhancement of O$\scriptsize VI$ optical depths at fixed H$\scriptsize I$ the O$\scriptsize VI$ for pixels at small galactocentric distances compared to random regions is unchanged, and remains significant irrespective of the contamination correction details. Thus, we conclude that the observed optical depth differences are neither due to chance nor
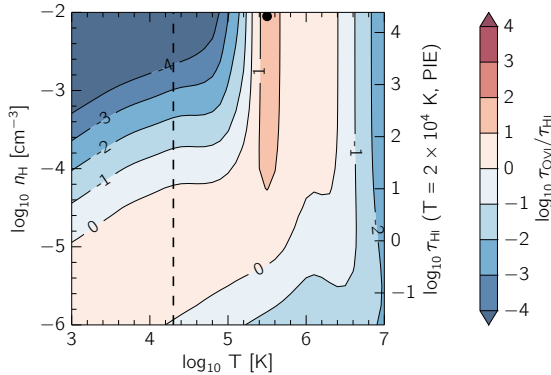
Figure 3.6: Theoretical optical depth ratios ($\log_{10} \tau_{OVI}/\tau_{HI}$) as a function of temperature and hydrogen density from CLOUDY modelling. For this figure we have assumed [O/H] = 0.0, however we allow this value to vary according to eq. 3.3 when comparing with the observations. The vertical dashed line denotes $T = 2 \times 10^4$ K, which is the temperature that we assume in the case of PIE. Furthermore, under the assumption of PIE we can convert hydrogen number densities to HI optical depths with eq. 3.5, and we show corresponding τ_{HI} values on the right-hand y-axis. For CIE, we set can use the ratios to set lower limits on the metallicity by using the maximum ratio from this temperature-density plane. This maximum occurs at $T = 3 \times 10^5$ K and is marked by the small black circle at $n_H = -2$.

to systematic variations in the spectral characteristics in either the QSOs or the galaxies.

3.4   Ionization models

In this section, we will investigate the physical origin of the difference in OVI observed between regions near our galaxies and in random locations. We focus on OVI(HI) because binning by τ_{HI} enables a more straightforward physical interpretation than binning by metal ion optical depth, due to the tight correlation between HI absorption and gas density in photoionized gas. We consider three possible scenarios and examine their plausibilities. The first hypothesis we consider is enriched photoionized ($T \sim 10^4$ K) gas, where the enhanced OVI(HI) near galaxies might be explained by higher gas metallicities. Second, we test the idea that ionizing radiation from the nearby galaxy could be responsible for the increase in OVI(HI). Finally, we consider whether our observations can be explained by a hot, collisionally ionized enriched gas phase near galaxies. We argue that of these three, the first scenario (enriched photoionized gas) can account for pixels with $\tau_{HI} \gtrsim 10$, while only the third explanation (the presence of hot, enriched gas) is plausible for pixels with $\tau_{HI} \lesssim 1$. Of course, it is important to note that every HI bin likely contains a mixture of pixels from different gas phases and ionization sources; the final behaviour is simply determined by the dominant phase.

3.4.1   Photoionization by the background radiation

The optical depth of HI is believed to be a good tracer of the photoionized gas density, even on an individual pixel basis (Aguirre et al., 2002). Hence, if the gas probed were pre-

dominantly photoionized and if the abundance of oxygen depended only on gas density, we would not expect to see any difference between the OVI(HI) relations of all pixels and those known to lie near galaxies in Fig. 3.1. Since a clear difference is observed, we postulate that this could be caused by an increase in the oxygen abundance near galaxies at fixed gas densities.

To test this idea, we turn to ionization modelling using CLOUDY (Ferland et al., 2013, version 13.03). Our setup involves a plane-parallel slab illuminated uniformly by an ionizing background, along a grid of varying temperatures and hydrogen densities, that covers both photoionization equilibrium (PIE) and collisional ionization equilibrium (CIE, discussed in § 3.4.3). For the fiducial case we use the ionizing background from Haardt & Madau (2001) including contributions from both quasars and galaxies, normalized to match the $z = 2.34$ metagalactic HI photoionization rate, $\Gamma = 0.74 \times 10^{-12}\,\text{s}^{-1}$, from Becker et al. (2007).[4] However, the shape and normalization of the background is subject to large uncertainties, and we explore the effect of varying them in Appendix 3.C.[5]

After obtaining individual ionization fractions from the above models as a function of density, n_{H}, and temperature, T, we can relate metallicity to optical depths using the following equation:

$$[\text{O/H}] = \log_{10} \frac{\tau_{\text{OVI}}}{\tau_{\text{HI}}} \frac{(f\lambda)_{\text{HI}}}{(f\lambda)_{\text{OVI}}} \frac{n_{\text{O}}}{n_{\text{OVI}}} \frac{n_{\text{HI}}}{n_{\text{H}}} - (\text{O/H})_\odot \qquad (3.3)$$

where f and λ are the oscillator strengths and rest wavelengths of the transitions, and we assume solar abundances from CLOUDY 13 (listed in Table 3.3). The resulting optical depth ratio contours, as a function of temperature and hydrogen number density and assuming solar metallicity, are shown in Fig. 3.6. At temperatures $T < 10^5$ K, photoionization dominates and the contours are only weakly dependent on temperature, while at higher temperatures and for sufficiently high densities collisional ionization dominates and the contours are independent of the density.

We would like to compare the observed optical depth ratios with those predicted from CLOUDY in order to estimate the gas metallicity. To compute the observed ratios, we begin with the τ_{OVI} points in the left panel Fig. 3.1. In order to correct for the presence of residual contamination from absorption by species other than OVI, we subtract the flat level (i.e. the asymptotic value of τ_{OVI} reached for small τ_{HI} and indicated by the horizontal, dashed line in Fig. 3.1) from all τ_{OVI} values. Following Schaye et al. (2003), to be conservative we added the error on the flat level linearly (rather than in quadrature) to the errors on τ_{OVI}, and finally we divide every τ_{OVI} point by its corresponding τ_{HI}. The results of this calculation are plotted in the left panel Fig. 3.7.

Next, since we are assuming that the gas is photoionized, we can transform the HI optical depths to gas densities, as was for example done in Rakic et al. (2012). The relation

---

[4] Measurements of Γ at $z = 2.4$ vary between $\Gamma = 0.5 \times 10^{-12}\,\text{s}^{-1}$ in Faucher-Giguère et al. (2008) up to $\Gamma = 1.0^{+0.40}_{-0.26} \times 10^{-12}\,\text{s}^{-1}$ in Becker & Bolton (2013). We choose the intermediate value of $0.74 \times 10^{-12}\,\text{s}^{-1}$ at $z = 2.34$ taken from the fitting formulas of Becker et al. (2007).

[5] We note that the assumption of PIE may break down as non-equilibrium effects become important in cooling gas at temperatures $< 10^6$ K. The presence of these effects causes collisional ionization to occur at lower temperatures compared to in equilibrium, although once an extragalactic background is included the impact of the effect of non-equilibrium cooling become less important (Oppenheimer & Schaye, 2013b).

Table 3.3: Solar abundances used in this work, taken from `CLOUDY` 13. References are 1. Allende Prieto et al. (2002); 2. Allende Prieto et al. (2001); 3. Holweger (2001).

Element	n_i/n_H	Ref.
H	1	
C	2.45×10^{-4}	1.
O	4.90×10^{-4}	2.
Si	3.47×10^{-5}	3.

between column density N and pixel optical depth at the line centre, τ_0, is:

$$
\begin{aligned}
\tau_0 &= \frac{\sqrt{\pi}e^2}{m_e c} \frac{Nf\lambda_0}{b_D} \\
&\approx \left(\frac{N}{3.43 \times 10^{13}\,\mathrm{cm}^{-2}} \right) \left(\frac{f}{0.4164} \right) \left(\frac{\lambda_0}{1215.67\,\text{Å}} \right) \\
&\quad \times \left(\frac{b_D}{26\,\mathrm{km\,s^{-1}}} \right)^{-1} .
\end{aligned}
\tag{3.4}
$$

Here, f is the oscillator strength, λ_0 is the rest-wavelength of the transition, and $b_D = \sqrt{2}v_{\mathrm{RMS}}$ is the Doppler line width, which we set to 26 km s^{-1}, the typical value measured by Rudie et al. (2012b). In order to apply this to our data, we must assume that the H$\textsc{i}$ pixel optical depths are close to the line centre $\tau_{\mathrm{H\textsc{i}}} = \tau_{0,\mathrm{Ly}\alpha}$. This is not a bad approximation, because the steepness of the H$\textsc{i}$ column density distribution function implies that it is more likely to be close to the maximum optical depth of a weaker absorber than it is to be in the wing of a stronger absorber. Indeed, Fig. 11 of Rakic et al. (2012) shows that the above methodology leads to very close agreement with the simulation result of Aguirre et al. (2002).

To convert $N_{\mathrm{H\textsc{i}}}$ to a hydrogen number density, we turn to Schaye (2001), who derive a relation between density and column density by assuming the absorbers are gravitationally confined gas clouds, which implies that they have sizes on the order of the local Jeans length. Combining their eq. 8 with eq. 3.4, we obtain:

$$
\begin{aligned}
n_{\mathrm{H}} &\approx 1.19 \times 10^{-5}\,\mathrm{cm}^{-3}\,\tau_{0,\mathrm{Ly}\alpha}^{2/3} \left(\frac{T}{2 \times 10^4\,\mathrm{K}} \right)^{0.17} \\
&\quad \times \left(\frac{\Gamma}{0.74 \times 10^{-12}\,\mathrm{s}^{-1}} \right)^{2/3} \left(\frac{f_{\mathrm{g}}}{0.0154} \right)^{-1/3} ,
\end{aligned}
\tag{3.5}
$$

where we have assumed the metagalactic photoionization rate to be $\Gamma = 0.74 \times 10^{-12}$ s^{-1}, the $z = 2.34$ value from Becker et al. (2007), and we have taken the temperature to be $T = 2 \times 10^4$ K, typical for a moderately overdense IGM region (e.g. Schaye et al., 2000b; Lidz et al., 2010; Becker et al., 2011; Rudie et al., 2012a). The result is insensitive to the precise value of the temperature, as long as the gas is predominantly photoionized, as assumed by Schaye (2001). We have also assumed a gas fraction close to the universal value of $f_{\mathrm{g}} = \Omega_{\mathrm{b}}/\Omega_{\mathrm{m}}$.

Thus, we can use eq. 3.5 to convert between H$\textsc{i}$ optical depth and hydrogen number density. Next, we consider the contour along a constant temperature of $T = 2 \times 10^4$ K in
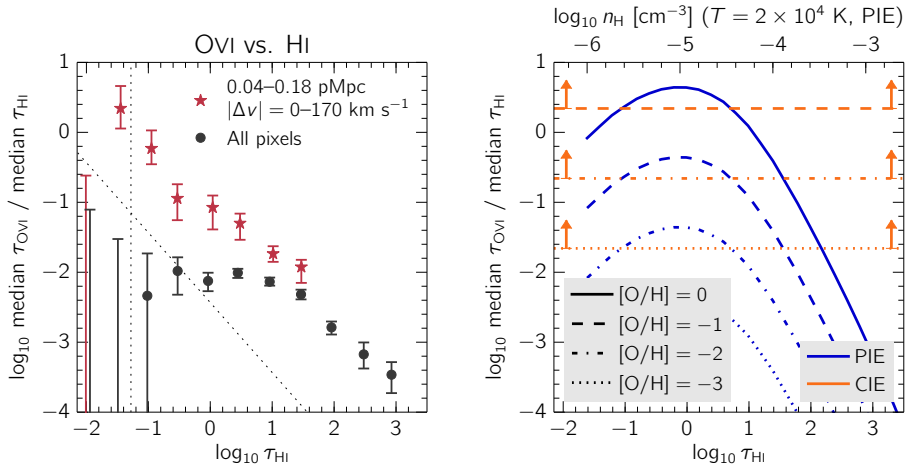
Figure 3.7: *Left panel:* The ratio of Ovi to Hi optical depths as a function of τ_{HI}. To compute these points, we used the data from Fig. 3.1. First, we subtracted the Ovi flat level from the median Ovi optical depths, in order to correct for contamination. After dividing the resulting values by their corresponding Hi optical depths, we obtain the points plotted here. The black vertical dotted line corresponds to the median value of all Hi pixel optical depths, while the diagonal line shows the median value of all Ovi pixel optical depths divided by the given value of τ_{HI} along the x-axis. *Right panel:* Theoretical ratios of Ovi to Hi as a function of τ_{HI} taken from CLOUDY modelling (see Fig 3.6). First, in the case of PIE, we assume that the gas has a temperature of 2×10^4 K, and convert Hi optical depths to a hydrogen number density using eq. 3.5 (the corresponding n_H values are shown on the upper y-axis). The blue curves show profiles taken along the vertical black dashed line in Fig. 3.6, where the different line styles demonstrate the effect of varying the metallicity. We also consider CIE, in which case cannot estimate the density from τ_{HI}. Instead, we can use the maximum theoretical ratio (indicated by the black circle at $T = 3 \times 10^5$ Fig. 3.6) to set a lower limit on the metallicity, and these are shown by the horizontal orange lines.

Fig. 3.6, from which we obtain theoretical optical depth ratios as a function of n_H. With eq. 3.5, we can convert the n_H dependence to corresponding values of τ_{HI}. The result of doing so is shown by the blue lines in Fig. 3.6, where the different line styles demonstrate the effect of varying the metallicity using eq. 3.3.

Hence, by interpolating between the blue curves in the right panel of Fig. 3.7, we can estimate a metallicity (assuming PIE) for each optical depth ratio τ_{OVI}/τ_{HI} in the left panel. The outcome of this procedure is plotted in the left panel of Fig. 3.8. To aid the interpretation, we indicate the baryon overdensity inferred from τ_{HI} along the upper x-axis (again, we can only convert HI optical depth to overdensity under the assumption of PIE).

Focusing first on the black points that correspond to the full pixel sample, we find that metallicity increases with overdensity Δ, and is in agreement with previous pixel optical depth studies (e.g. Schaye et al., 2003; Aguirre et al., 2008). Next, examining the values derived from pixels with small galactocentric distance (red stars), for pixels with $\tau_{HI} \gtrsim 10$ we infer the same metallicity-density relation as for the full pixel sample, but with metallicities that are ~ 0.5 dex higher. We conclude that for these HI optical depths, photoionized gas that is enriched with respect to random regions of the same density is consistent with our observations of OVI(HI) at small galactocentric distances.

However, turning to pixels with $\tau_{HI} \lesssim 1$, it is clear that the relation between metallicity and density is inverted. In this regime, the metallicity appears to increase with decreasing overdensity, with the highest metallicities found at the lowest overdensities, even reaching supersolar values. We do not consider this enrichment pattern to be physically plausible. Although some regions of relatively low density can be highly enriched, they usually arise in hot superbubbles. Furthermore, an underdense gas phase close to galaxies with $T \sim 10^4$ K and supersolar metallicities is not consistent with predictions from cosmological hydrodynamical simulations (e.g. Ford et al., 2013; Shen et al., 2013). The above suggests that one or more of our assumptions must be incorrect for the small galactocentric distance pixel sample.

3.4.2   Photoionization by stars in nearby galaxies

In this section, we test whether the enhancement of τ_{OVI} for a fixed τ_{HI} near galaxies can be explained by increased photoionization by radiation from the stars in the nearby galaxies. At sufficiently small galactocentric distances, we would expect the mean hydrogen ionization rate to be dominated by galactic radiation rather than by the metagalactic background radiation (e.g. Schaye, 2006; Rahmati et al., 2013b), which would reduce the HI optical depth at fixed density. Furthermore, since stars emit very little radiation with photon energies > 4 Ryd, we do not expect the OVI optical depth to be modified by local stellar sources, given that the ionization energy for OV is about 8.4 Ryd. Hence, if photoionization by nearby galaxies were important, we would expect the red stars in Fig. 3.1 to be shifted upwards relative to the black points and the red stars in Fig. 3.7 to be shifted towards the top-left relative to the black points. This is qualitatively consistent with the observations, which suggests that the difference between the two samples may be due to photoionization by local sources rather than due to the presence of hot, enriched gas. However, as we will show below, quantitatively this scenario does not work out.
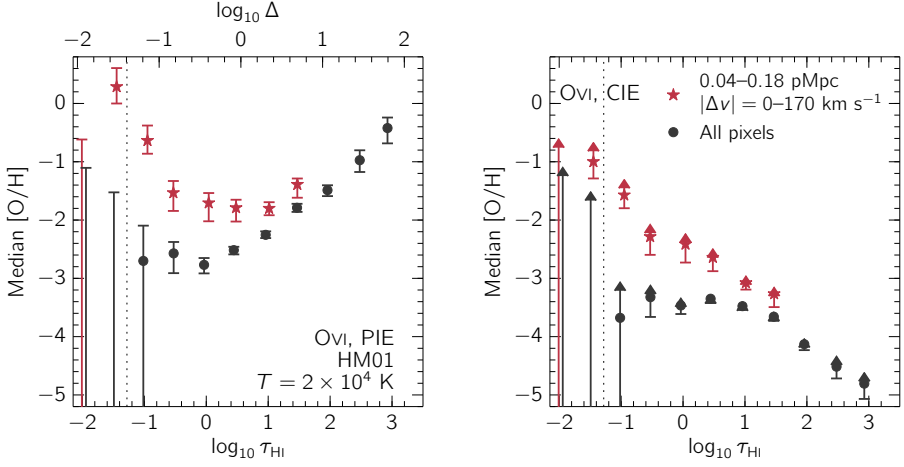
Figure 3.8: *Left panel:* Metallicity as a function of HI pixel optical depth. The metallicity was inferred from the ratio of τ_{OVI} to τ_{HI} (Fig. 3.7) assuming photoionization equilibrium (PIE, $T = 2 \times 10^4$ K) as described in the text. On the upper axis we show τ_{HI} converted to an overdensity Δ using the relation for photoionized gas that we assumed in the ionization models. Random regions (black circles) show a positive correlation between metallicity and density, while at small galactocentric distances (red stars) for $\tau_{\mathrm{HI}} \lesssim 1$ the metallicity increases inversely with density. Such an inverted metallicity-density relation is not physically expected and indicates that the assumption of PIE is probably incorrect. *Right panel:* Lower limits on the metallicity as a function τ_{HI}, inferred again from the measured optical depth ratios but now assuming collisional ionization equilibrium (CIE). The size of each arrow is proportional to the size of the error bar on the measured optical depth ratio. The inferred limits on the metallicity are lower than for PIE, but still imply that at least some of the gas near galaxies is substantially enriched.

We first need to evaluate the photoionization rate due to local sources, Γ_{ν_0}, at $\nu_0 = 1\,\mathrm{Ryd}$,

$$\Gamma_{\nu_0} = \int_{\nu_0}^{\infty} \frac{F(\nu)\sigma(\nu)}{h\nu}\, d\nu \qquad (3.6)$$

where h is the Planck constant, $F(\nu)$ is the incident flux, and $\sigma(\nu)$ is the photoionization cross section, taken to be $\sigma(\nu) = \sigma_0 (\nu/\nu_0)^{-3}$ where $\sigma_0 = 6.3 \times 10^{-18}\ \mathrm{cm}^{-2}$. To estimate the incident flux from a nearby galaxy, we assume that the galaxy is an isotropically emitting point source:

$$F(\nu) = f_{\mathrm{esc},\nu} \frac{L(\nu)}{4\pi R^2} \qquad (3.7)$$

where $L(\nu)$ is the galaxy luminosity, $f_{\mathrm{esc},\nu}$ is the escape fraction of photons at frequency ν, and R is the proper distance from the point source. For the luminosity, we use measurements of the KBSS galaxy luminosity function from Reddy & Steidel (2009), who obtained $M_{1700\text{Å},*} = -20.70$ mag. This corresponds to $L_{\nu,*} = 4.05 \times 10^{28}\, f_{\mathrm{esc},\lambda1700}^{-1}\, h_{0.7}^{-2}\ \mathrm{erg\ s^{-1}\ Hz^{-1}}$ at a rest wavelength of ~ 1700 Å, where $f_{\mathrm{esc},\lambda1700}$ is the escape fraction at this wavelength and $h_{0.7}$ is the Hubble constant in units of $70\ \mathrm{km\ s^{-1}\ Mpc^{-1}}$.

We then use the fact that spectral synthesis models corresponding to typical KBSS galaxy metallicities of $12 + \log(\mathrm{O/H}) = 8.4$ can be well-approximated by a blackbody curve
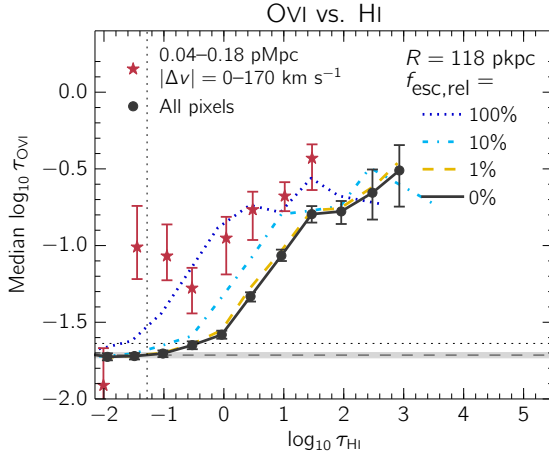
Figure 3.9: The data points are identical to those in the left panel of Fig. 3.1. The curves show the result for the full pixel sample (black circles) after dividing the H I optical depths by the boost factor in the H I photoionization rate expected due to ionizing radiation from the nearby galaxy for the relative escape fractions, $f_{\text{esc,rel}} \equiv f_{\text{esc},\lambda900}/f_{\text{esc},\lambda1500}$, indicated in the legend and for a distance to the source equal to the median impact parameter of the pixels in the small galactocentric distance sample. Even for $f_{\text{esc,rel}} = 100\%$, which is unrealistically high, the curve falls short of the red stars, implying that photoionization by radiation from the observed galaxies cannot explain the observed enhancement in O VI/H I near galaxies.

with $T_{\text{eff}} = 50000$ K (Steidel et al., 2014). Integrating this function numerically, we obtain:

$$\Gamma_{\nu_0} = 14.8 \times 10^{-12} \, \text{s}^{-1} \left(\frac{R}{118\,\text{pkpc}} \right)^{-2} \frac{f_{\text{esc},\lambda912}}{f_{\text{esc},\lambda1700}}. \tag{3.8}$$

where we take $R = 118$ pkpc because it is the median impact parameter of the galaxies that comprise our small galactocentric distance sample. Note that this choice is conservative since it assumes that the absorption within ±170 km s^{-1} of the galaxy arises in gas that is precisely at the distance of the galaxy. In reality, some of this gas will be in front or behind the galaxy and R will be greater than the impact parameter.

The remaining unknown in our estimate of the photoionization rate from local galaxies comes from the ratio of the escape fractions at 1 Ryd and at the observed wavelength of 1700 Å, $f_{\text{esc},\lambda912}/f_{\text{esc},\lambda1700}$. The literature contains many values for the escape fraction of Lyman continuum photons relative to that of non-ionizing UV continuum photons, $f_{\text{esc,rel}} \equiv f_{\text{esc},\lambda900}/f_{\text{esc},\lambda1500}$. Values range from $\sim 1\%$ to 83% (e.g. Steidel et al., 2001; Shapley et al., 2006; Iwata et al., 2009; Nestor et al., 2013; Mostardi et al., 2013; Cooke et al., 2014), although typical values are closer to the lower limit of this range.

Since we already expect $\Gamma_{\nu_0} = 0.74 \times 10^{-12}$ s^{-1} from the extragalactic background (Becker et al., 2007), adding a contribution from nearby galaxies would boost the H I photoionization rate by a factor of ~ 20 for an escape fraction $f_{\text{esc,rel}} = 100\%$ at the median impact parameter and would hence suppress the H I optical depths by the same amount. To test whether ionizing radiation from nearby galaxies can explain the difference between the O VI(H I) relations of the small galactocentric radii and the random pixel samples, we have

re-calculated the $O_{VI}(H_I)$ relation for random regions after dividing all the H_I pixel optical depths by the factor by which local sources boost the H_I ionization rate for various values of the relative escape fraction. The results are compared with the observed relation for the small galactocentric radii sample in Fig. 3.9. For $f_{esc,rel} \leq 10\%$ the effect of local sources is not strong enough to reproduce the observations. Even for the highly unrealistic case that $f_{esc,rel} = 100\%$, the boost in the H_I ionization rate is insufficient to completely account for the observed enhancement of O_{VI} small galactocentric distances for $\tau_{H_I} \lesssim 1$.

On the other hand, while for $\tau_{H_I} \gtrsim 10$ it appears that relative escape fractions of ~ 50% may be able to explain our observations, we reiterate that *average* observed relative escape fraction values are usually much lower than this for galaxies such as ours (e.g., Shapley et al., 2006). Furthermore, we note that by considering only the transverse rather than 3-dimensional distance to the galaxy, our estimate of the H_I photoionization rate boost is strictly an upper limit, and the true strength of the effect is almost certainly smaller.

As a final test, we have taken the blackbody spectrum used to approximate the local galaxy radiation and used it as input, along with the extragalactic background, into CLOUDY. We generated temperature-density planes showing optical depth ratios $\tau_{O_{VI}}/\tau_{H_I}$ (as in the right panel of Fig. 3.7), as well as $\tau_{O_{VI}}/\tau_{C_{IV}}$ and $\tau_{O_{VI}}/\tau_{Si_{IV}}$, and compared these with the output using only the extragalactic background. For the $O_{VI}(H_I)$ relation, we indeed found that the predicted ratios for photoionized gas at ~ 10^4 K were higher. However, as expected due to the fact that our assumed spectrum does not contain many photons with energies above 1 Ryd, for the observed ratio values there was almost no discernible difference between the $O_{VI}(C_{IV})$ and $O_{VI}(Si_{IV})$ relations derived with and without the contribution from nearby galaxies.[6] Hence, if local sources were responsible for the enhancement in $O_{VI}(H_I)$, we would not expect to see any difference between the small galactocentric distance and random pixel samples for the $O_{VI}(C_{IV})$ and $O_{VI}(Si_{IV})$ relations. This is not consistent with the fact that we find significantly enhanced O_{VI} for both fixed C_{IV} and fixed Si_{IV} much like we do for the $O_{VI}(H_I)$ relation (see the centre and right panels of Fig. 3.1). Thus, we conclude that enhanced photoionization due to the proximity of the observed galaxies cannot explain the enhancement of O_{VI} at fixed H_I that we observe for the small galactocentric distance pixel sample.

In the above scenario, we only consider photoionization by stars in the nearby galaxies because there is no evidence that our galaxies contain AGN. However, it was recently pointed out by Oppenheimer & Schaye (2013a) that because of the long recombination times for metals at densities typical of the circumgalactic medium, ions like O_{VI} may remain out of ionization equilibrium long after the AGN episode is over. In fact, for reasonable AGN duty cycles, the authors argue that much of the O_{VI} detected in quasar spectra resides in such fossil AGN proximity zones. On the other hand, in regions where the equilibrium neutral hydrogen fraction is low, H_I will equilibrate nearly instantaneously after the AGN turns off. Hence, in this scenario H_I would be photoionized and in equilibrium, while O_{VI} is out of equilibrium and enhanced because of the fossil AGN proximity effect. We would then expect the enhancement in O_{VI} to be strongest in regions of low H_I absorption, since such regions correspond to low densities and thus long recombination times. This is in qualitative agreement with our observations, although Oppenheimer &

---

[6]Invoking galaxy spectra with a soft X-ray component could potentially lead to more oxygen ionized to O_{VI} (e.g., Cantalupo, 2010), however these spectral models remain uncertain and we leave testing of this scenario to a future work.

Schaye (2013a) show that at very low density oxygen will become so highly ionized that OVI is suppressed, which would be inconsistent with our findings.

More generally, since (fossil) AGN proximity and higher gas temperatures both tend to increase the abundance of more highly ionized species relative to ions with lower ionization potentials, many of the predictions of these two scenarios will be qualitatively similar, although it remains to be seen whether the fossil proximity effect can work quantitatively. One important difference, however, is the expected widths of the absorption lines. If the oxygen is hot enough for OVI to be collisionally ionized, then the absorption lines will be broader than if the gas were photoionized. We intend to measure the widths of the metal absorption lines and to model the fossil AGN proximity effect in future work.

3.4.3   Collisionally ionized gas

It may be that at small galactocentric distances, much of the OVI absorption arises in collisionally ionized rather than photoionized gas. Indeed, the behaviour of the OVI(HI) relation for the near-galaxy pixels with $\tau_{\mathrm{HI}} \lesssim 1$ points to collisional ionization playing a role. In general, we would not expect to see very much HI associated with collisionally ionized OVI, as the HI fraction is very low at $T > 10^5$ K. The behaviour of the [O/H](Δ) relation that we inferred under the assumption of photoionization (Fig. 3.8) is rather suggestive, as the relation displays larger departures from the random regions with decreasing τ_{HI}.

If we are in fact probing collisionally ionized gas, then we cannot measure its metallicity as was done in § 3.4.1 – first because we are unable to estimate the gas density from the HI optical depth, and second because there is no natural equilibrium temperature. However, it is possible to put a lower limit on the metallicity by selecting the temperature and density that would maximize $\tau_{\mathrm{OVI}}/\tau_{\mathrm{HI}}$. In Fig. 3.6, we have marked the temperature and density where this theoretical maximum is reached by a small black circle. Then, in the right-hand panel of Fig. 3.7, the horizontal orange lines show the $\tau_{\mathrm{OVI}}/\tau_{\mathrm{HI}}$ ratio at this point for different metallicities.

Thus, irrespective of HI optical depth (which has no correspondence with density under the assumption of CIE) we can convert the observed optical depth ratios in the left-hand panel of Fig. 3.7 to lower-limits on the metallicity, and we show the result in the right panel of Fig. 3.8. As expected, the limits obtained are lower than the metallicities inferred when assuming photoionization. Nevertheless, some of the lower limits are sufficiently high to be interesting. The 1σ lower limit approaches [O/H] ~ −1 at the lowest bins in HI optical depth, where $\log_{10} \tau_{\mathrm{HI}} = -1.5$.

Given the reasonable metallicity limits in Fig. 3.8 combined with the fact that the previous two scenarios (photoionization by the extragalactic background or by local stellar radiation) cannot account for the OVI enhancement for $\tau_{\mathrm{HI}} \lesssim 1$, we conclude that collisional ionization is the dominant ionization source for a significant fraction of the small galactocentric distance pixels. We emphasize that in collisionally ionized gas, τ_{HI} is no longer a good estimator of density, and we could potentially be probing very high overdensities.

We also examined the OVI/CIV and OVI/SiIV ratios in Appendix 3.B. We conclude that OVI pixels near galaxies are more consistent with a hotter gas phase than the full pixel sample, and furthermore we find that the strength of this trend increases inversely with CIV and SiIV optical depths, as might be expected for collisionally ionized gas at ~ 3×10^5 K where these other ions are not abundant. However, since the results are not constraining,

the details are left to the Appendix.

3.5   Discussion and conclusions

We have used absorption by H I and metals to study the physical conditions near $z \sim 2.3$ star-forming galaxies in the fields of 15 hyper-luminous background QSOs that have been observed with Keck/HIRES as part of the Keck Baryonic Structure Survey (KBSS). We focused on 21 galaxies with impact parameters < 180 pkpc and isolated the pixels of the quasar spectra that are within ±170 km s^{-1} of the accurate galaxy redshifts provided by the KBSS. In Turner et al. (2014) we showed that the absorption by H I and various metal ions is strongly enhanced in these circumgalactic regions. The fact that both H I and the metals are enhanced raises the question whether the observed increase in the metal absorption merely reflects the presence of higher gas densities near galaxies or whether it implies that the gas near galaxies has a higher metallicity at fixed density or a different temperature from gas in random regions.

To address this question, we measured the pixel optical depths of O VI as a function of H I, C IV and Si IV, and compared the results for the pixels located at small galactocentric distances to the full pixel sample, which is representative of random regions. Our main result is the detection of a 0.3–0.7 dex enhancement (which reaches its maximum at $\log_{10} \tau_{\mathrm{H I}} \sim -1.5$) in the median optical depth of O VI at fixed $\tau_{\mathrm{H I}}$ for the small galactocentric distance sample when compared with the full pixel sample (Fig. 3.1). We verified that this enhancement, which we detected at 2–3σ confidence per logarithmic bin for $\tau_{\mathrm{H I}}$, $\tau_{\mathrm{C IV}}$, and $\tau_{\mathrm{Si IV}}$, is not due to differences in the redshift distribution or the quality of the quasar spectra between the small galactocentric distance and full pixel samples.

We proposed and tested three different hypotheses that may explain the observed enhancement of O VI(H I) near galaxies: (1) the gas is photoionized by the extragalactic background but has a higher metallicity at fixed density; (2) the gas is more highly ionized at fixed density by radiation from stars in the nearby galaxy; and (3) the enriched gas is hot and collisionally ionized.

To test scenario (1), we used CLOUDY ionization models and the relation between $\tau_{\mathrm{H I}}$ and density for photoionized, self-gravitating clouds from Schaye (2001) and Rakic et al. (2012) to convert the observed optical depth ratios into a metallicity-density relation, assuming $T \sim 10^4$ K, as expected for photoionized gas. We found that the full pixel sample gave a physically plausible metallicity-density relation that is consistent with previous studies which did not have information on the locations of galaxies. Furthermore, the same metallicity-density relation (but shifted up by $\sim$ 0.5 dex in metallicity) is also present for small galactocentric distance pixels that have $\tau_{\mathrm{H I}} \gtrsim 10$. Thus, for high H I optical depths, the enhancement of O VI at fixed $\tau_{\mathrm{H I}}$ is consistent with arising predominantly from enriched, photoionized gas. However, making this same assumption of PIE for $\tau_{\mathrm{H I}} \lesssim 1$ resulted in an [O/H] versus overdensity relation that cannot be easily explained, as [O/H] was found to increase strongly with decreasing overdensity, implying supersolar metallicities for underdense gas (left panel of Fig. 3.8). We therefore concluded that while photoionization by the background radiation is a plausible scenario for the random regions, it cannot account for the observed enhancement of O VI(H I) near galaxies.

In scenario (2) O VI is enhanced at fixed H I because radiation from stars in the nearby

galaxy suppresses H I, while leaving O VI unchanged. To test this explanation, we estimated the H I photoionization rate due to the galaxies. However, we found that only under the unrealistic assumptions that the relative escape fraction $f_{esc,\lambda900}/f_{esc,\lambda1500}$ is 100% and that the 3-D distance between the gas and the galaxy is equal to the impact parameter, can the flux of ionizing radiation from the galaxies explain the observed increase in τ_{OVI}/τ_{HI} near galaxies. Reducing the relative escape fraction to a still conservative value of 10% rules out this scenario as a dominant ionization source (Fig. 3.9). Furthermore, we found that such a galaxy proximity effect is predicted to have a much smaller effect on O VI(C IV) and O VI(Si IV) than on O VI(H I), which is inconsistent with our observations.

Contrary to photoionization by either the extragalactic background or local stellar radiation, scenario (3) can explain the enhancement in O VI(H I) near galaxies for pixels with $\tau_{HI} \lesssim 1$. If a substantial fraction of the enriched gas near galaxies is sufficiently hot for O VI to be collisionally ionized, i.e. $T > 10^5$ K, then we can account for the observations. By assuming the maximum O VI/H I ratio reached in collisional ionization equilibrium, we converted the observed optical depth ratios into lower limits on the metallicity, finding $[\text{O/H}] \gtrsim -1$ for gas with weak H I absorption (right panel of Fig. 3.8). Indeed, this measurement is supported by other characterizations of KBSS galaxy properties. Rudie et al. (2012b) found higher temperatures for fixed τ_{HI} near the KBSS galaxies, while Steidel et al. (2014) measured H II region metallicities of 0.4 $Z_\odot$, which could serve as a possible upper limit to the value presented here (although if metal-enriched winds drive most of the metals out of the star-forming regions, it is possible that the circumgalactic gas may have a higher metallicity than galactic H II regions). Furthermore, the inferred metallicities and temperatures of $T \gtrsim 10^5$ K are in agreement with the predictions of van de Voort & Schaye (2012) for galaxies with the masses and redshifts similar to ours.

In summary, we favour the conclusion that our galaxies are surrounded by hot ($T > 10^5$ K) gas of which a substantial fraction must have metallicity $\gtrsim 10^{-1}$ of solar. Furthermore, we find that this metal-enriched phase extends out to ~ 350 km s^{-1} of the galaxy positions (Fig. 3.2), which corresponds to $\gtrsim 1.5$ times the halo circular velocities. Because of the relatively high temperature that requires shock-heating, the large velocity range extending far outside the haloes, and high metallicity, we conclude that we have detected hot, metal-enriched outflowing gas. Future comparisons with hydrodynamical simulations, considering ion ratios as well as the kinematics and line widths, will provide strong constraints on models of galaxy formation and may provide further insight into the interpretation of our observations.

Acknowledgements

3.A   Correction of OVI contamination

Here we examine how modifying the Ovɪ contamination correction affects the resulting Ovɪ(Hɪ) relation. It is possible that the small galactocentric distance pixel sample suffers from more Hɪ contamination than the full pixel sample, given the larger on average Hɪ optical depth values (see the left panel of Fig. 3.3) and the proximity of Lyβ to Ovɪ (~ 1800 km s^{-1}). We postulate that if the enhancement of Ovɪ for fixed Hɪ optical depths at small galactocentric distances were largely due to uncorrected Hɪ Lyβ contamination, modification of the Ovɪ contamination would have a notable effect on this enhancement.

To test this, in Fig. 3.10 we show the Ovɪ(Hɪ) relation as in the left panel of Fig. 3.1, but with changes to the Ovɪ contamination correction. In the fiducial case, we subtract 5 orders of the Lyman series of Hɪ beginning with Lyβ, and then take the minimum of the Ovɪ doublet optical depths. In Fig. 3.10, we first show Ovɪ(Hɪ) after not subtracting any Hɪ but still taking the doublet minimum (left panel), not taking the doublet minimum but still subtracting Hɪ (centre panel), and not performing any correction at all (right panel). Although the absolute values of the apparent Ovɪ optical depths increase when fewer contamination corrections are performed, the significance of Ovɪ optical depth at fixed Hɪ for pixels at small galactocentric distance compared to the full pixel sample remains unchanged, indicating that our results are not sensitive to the Ovɪ contamination correction procedure.

Finally, we perform a simple calculation to demonstrate that the Hɪ Lyβ contamination is not predicted to have a large effect. To begin, we would like to estimate the typical Lyβ strength at a distance ~ 1800 km s^{-1} away from galaxies. For this, we use our measurement of the median optical depth as a function of distance along the galaxy LOS, as was done in the right panels of Fig. 6 from Turner et al. (2014), but extending out to ~ 1800 km s^{-1}. We find that the Hɪ Lyα optical depths asymptote to the median value of all pixels (0.051), and using the relative oscillator strengths of Lyα and Lyβ we can convert this to an expected median value of Hɪ Lyβ (0.0082). Adding this to the median value of all Ovɪ pixels (0.023), we obtain 0.031. This corresponds to ~ −1 in the left panel of Fig. 3.1, and is significantly less than the observed Ovɪ optical depth enhancement.

3.B   OVI(CIV) and OVI(SiIV)

In the centre and right panels of Fig. 3.1, we investigated whether the Ovɪ(Cɪv) and Ovɪ(Siɪv) relations depend on galactocentric distance. First, we note that we see similar behaviour for Ovɪ(Cɪv) and Ovɪ(Siɪv) as for Ovɪ(Hɪ) – that is, we find a higher τ_{OVI} at fixed τ_{X} for pix-
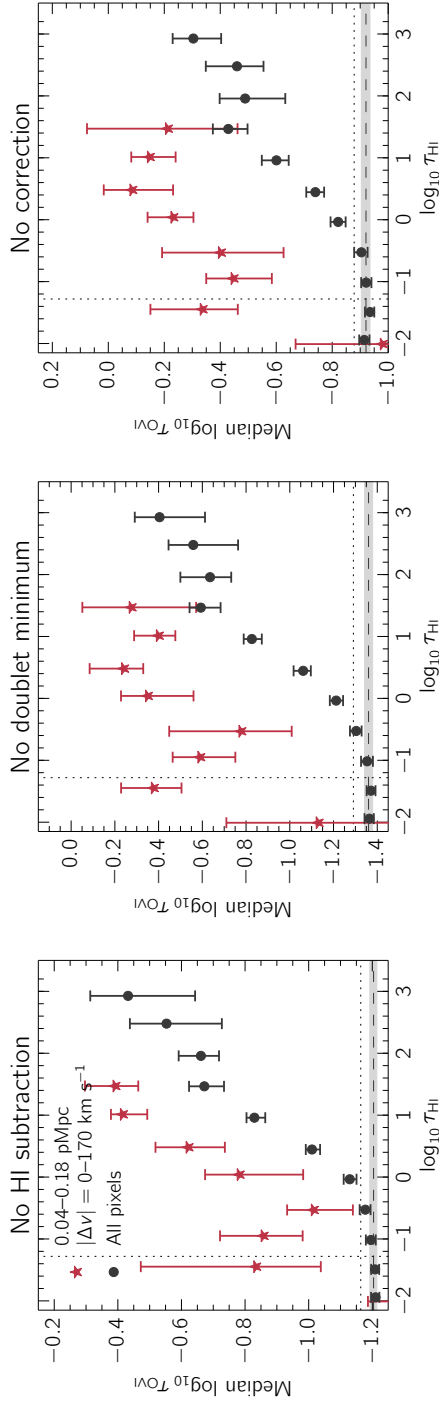
Figure 3.10: The same as the left panel Fig. 3.1, but varying the method of O VI contamination correction. The modifications shown here are the result of not subtracting any H I (left panel), not taking the doublet minimum (centre panel), and not performing any correction at all (right panel). This figure demonstrates that the qualitative behaviour of the enhancement of O VI optical depth at fixed H I for pixels at small galactocentric distance is entirely independent of the O VI contamination correction procedure.

els near galaxies compared to random locations, and the magnitude of this enhancement increases with decreasing τ_X.

As in § 3.3, we can use CLOUDY to model the optical depth ratios as a function of temperature and density. These temperature-density planes, along with the observed ratios, are shown in Fig. 3.11. We note that if we assume solar relative abundances, then the optical depth ratios determined from the CLOUDY models are fixed and do not depend on metallicity (unlike for optical depth ratios with τ_{HI} in the denominator).

Looking first at O VI(C IV), for $\log_{10} \tau_{CIV} \gtrsim -1$ pixels near galaxies and at random locations have similar optical depth ratios ranging from $\log_{10} \tau_{OVI}/\tau_{CIV} \sim -0.4$ to 0.5, which correspond to a maximum temperature of $T \sim 10^{5.4}$ K. On the other hand, at lower C IV optical depths, the ratios derived from pixels near galaxies are as high as $\log_{10} \tau_{OVI}/\tau_{CIV} \sim 1$, and are not inconsistent with the collisionally ionized region at $T \sim 3 \times 10^5$ K.

Similarly, for O VI(Si IV) the optical depth ratios derived from pixels with small galactocentric distances have higher values, and therefore higher temperature upper limits, than in the random regions. They reach values as high as $\log_{10} \tau_{OVI}/\tau_{SiIV} \sim 1.5$, which again corresponds to a maximum temperature of $T \sim 10^{5.4}$ K.

Taken together, the sample of pixels at small galactocentric distance show the same trend for O VI(C IV) and O VI(Si IV), discrepant from that of random locations: τ_{OVI}/τ_x *increases inversely* with τ_{CIV} and τ_{SiIV}. If the conditions at near galaxies are most favourable to the collisional ionization of O VI (i.e. temperatures $T = \sim \times 10^5$ K), then we would expect to find this oxygen in regions with less C IV and Si IV, and such a scenario is certainly not inconsistent with the above relations.

3.C   Ionization background

The spectral shape of the ionizing background radiation is a very large source of uncertainty for ionization modelling. In this section, we explore the impact that changing this background has on our results. We experiment with four different models, shown in Fig. 3.12, which have all been normalized to have the same H I photoionization rate, which we take from (Becker et al., 2007) to be $\Gamma = 0.74 \times 10^{-12}$ s^{-1} at $z = 2.34$. For our fiducial background, we use the Haardt & Madau (2001) quasar+galaxy model (HM01) and vary it in two ways. First, we use the quasar-only model, which increases the intensity above 1 Ryd (HM01 Q-only). We also invoke a model where the intensity above 4 Ryd is reduced by 1 dex, in order to simulate the absence of helium reionization (HM01 cut). Finally, we compare with the updated background from Haardt & Madau (2012, HM12).

As a first test, we examine the values of [O/H] derived when we assume PIE with $T = 2 \times 10^4$ K for the four different backgrounds in Fig. 3.13. We find that for the first three backgrounds (HM01, HM12, and Q-only) the results are in fairly good agreement. In general, the metallicity-density relation is steepest for HM01, and spans the largest range of [O/H] values.

Of the four backgrounds considered, the one salient outlier is the HM01 cut background (bottom-right panel). First, for the small galactocentric distance points, invoking this background produces reasonable (i.e. at least less than solar) metallicities for $\log_{10} \tau_{HI} < 1$. However, the qualitative behaviour of inferred [O/H] as density decreases is still present. Furthermore, for $\log_{10} \tau_{HI} > 1$, the inferred metallicities of the full pixel sample become un-
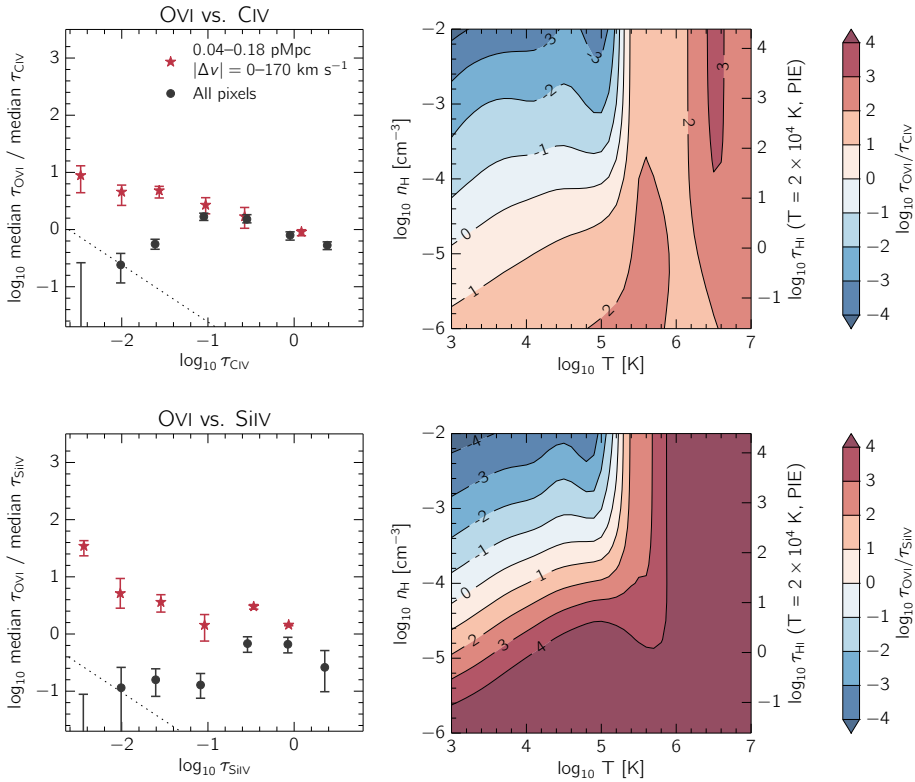
Figure 3.11: *Left column:* Median optical depth ratios derived from the Ovi(Civ) (top) and Ovi(Siiv) (bottom) relations in Fig. 3.1. The diagonal lines show the median value of all Ovi pixel optical depths divided by the given value of τ_{CIV} and τ_{SiIV} along the x-axis, and demarcates a conservative detection level. *Right column:* Predicted optical depth ratios from CLOUDY.
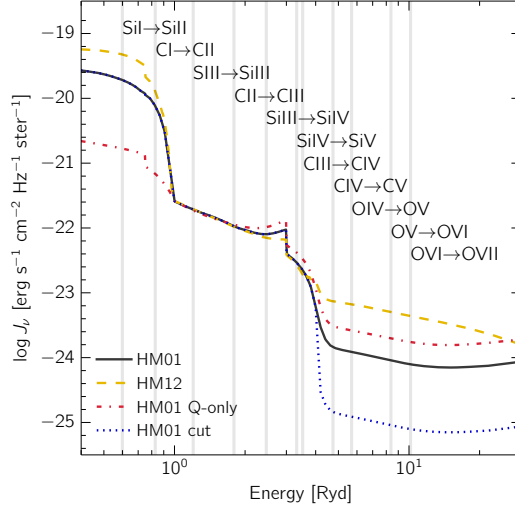
Figure 3.12: Comparison of different extragalactic ionization backgrounds.

realistically high (up to [O/H]$\sim$ 1, while Steidel et al. 2014 find $Z = 0.4\,Z_\odot$ for this galaxy sample), suggesting that this background is not a realistic choice.

Another significant change that would result from using the HM01 cut model is shown in Fig. 3.14, where we compare the the values of $\log_{10}\tau_{\rm OVI}/\tau_{\rm CIV}$ as a function of temperature and density for both the HM01 (solid black contours) and HM01 cut (dashed blue contours) backgrounds.

The observed ratios span values that range from $\sim 10^0$ to 10^1 for the small galactocentric distance sample. For the HM01 background, this corresponds to gas that has either $\log_{10} n_{\rm H} \sim -5$ to -4 cm^{-3} at $T \sim 2 \times 10^4$ K, or $\log_{10} n_{\rm H} \gtrsim -4.5$ cm^{-3} at $T \sim 10^{5.4}$ K. However, for HM01 cut, at the typical photoionized gas temperature of $T \sim 2 \times 10^4$ K, $\log_{10} n_{\rm H} \lesssim -5.2$ cm^{-3} for the range of observed optical depths, which corresponds to underdense values (i.e. $\Delta < 1$). Although the small galactocentric distance pixel sample could be reconciled with temperatures of $T \sim 10^{5.4}$ K, it is unlikely that the full pixel sample is typically probing such hot gas, or densities below the cosmic mean. We conclude that the HM01 cut background is in tension with ratios of $\tau_{\rm OVI}/\tau_{\rm CIV}$ derived from the full pixel sample.
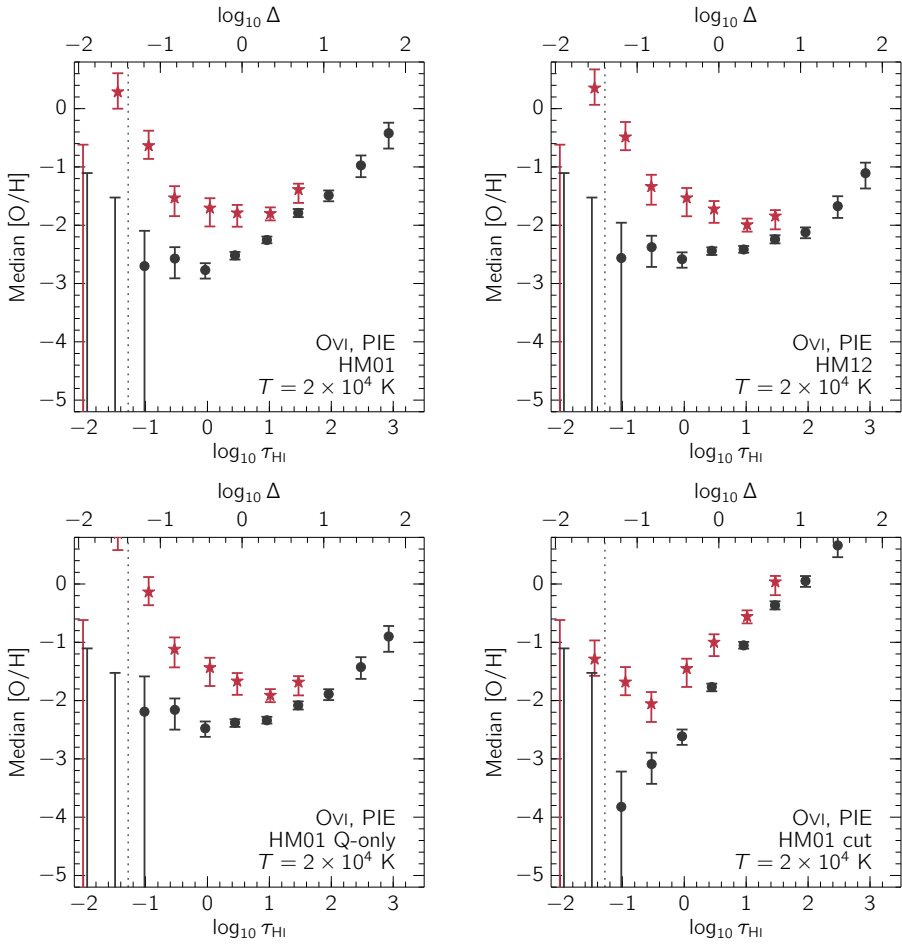
Figure 3.13: [O/H] derived from the Ovi(Hi) relation, for four different extragalactic backgrounds (as indicated in each panel), under the assumption of PIE.
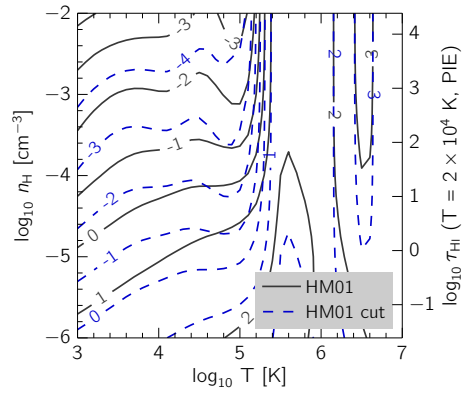
Figure 3.14: The predicted values of $\log_{10} \tau_{\mathrm{OVI}}/\tau_{\mathrm{CIV}}$ for the HM01 (black solid contours) and HM01 cut (blue dashed contours) backgrounds.

4 Absorption around $z \approx 2$ star-forming galaxies in the EAGLE simulations: HI, CIV and SiIV

We study HI and metal-line absorption around $z \approx 2$ star-forming galaxies by comparing observations from Turner et al. (2014) from the Keck Baryonic Structure Survey to the EAGLE cosmological, hydrodynamical simulations. We extract sightlines from the simulations and compare the properties of the absorption of HI, CIV and SiIV around simulated and observed galaxies using pixel optical depths, carefully mimicking the resolution, pixel size, and signal-to-noise ratio of the observations, as well as the distributions of impact parameters and galaxy redshift errors. We find that the observations are in excellent agreement with the EAGLE reference model. In particular, the simulation reproduces the high metal-line optical depths found at small galactocentric distances, the large-scale optical depth enhancement seen out to impact parameters of 2 pMpc, and the prominent redshift-space distortions, which we find are due to peculiar velocities rather than redshift errors. The agreement is best for halo masses ~ $10^{12.0}$ $M_\odot$, for which the predicted and observed stellar masses also agree. We also examine variations in the subgrid models for feedback and find that, for a fixed halo mass, HI and metal-line absorption is not strongly dependent on the choice of feedback model. From this we conclude that the observed redshift-space distortions are caused by infalling gas or virial motions rather than outflows.

Turner, Schaye et al.
In preparation

4.1   Introduction

Galaxy formation theory tells us that the flow of gas through galaxies, from accretion streams that feed star formation to the expulsion of gas by feedback from star formation and active galactic nuclei (AGN), is integral for setting galaxy properties. However, cosmological simulations are limited because of their inability to directly resolve the processes responsible for expelling gas from galaxies, forcing them to resort to subgrid models. As these subgrid feedback prescriptions are typically calibrated to reproduce properties of present-day galaxies, it is important to test the results against other observables.

In particular, the reservoir of gas around galaxies, known as the circumgalactic medium (CGM), lies in the region where inflowing and outflowing gas meets, making it an ideal

testing bed for simulations. Observations of intergalactic metals, which span wide ranges of ionization energies, can constrain the composition, kinematics and physical state of CGM. By directly comparing simulations and observations, we can gain insights into the physics of the gas flow in and around galaxies. Such studies can also help interpret the observations of the CGM.

Recent studies of simulations have encountered difficulties reproducing the observed H I covering fractions around massive galaxies at $z \sim 2$ (Fumagalli et al., 2014; Faucher-Giguère et al., 2015). However, Rahmati et al. (2015) demonstrated that the tension may be alleviated by better matching the simulated galaxy redshifts and masses to those of the observations, by measuring the absorption of the same velocity intervals, and by using simulations with efficient stellar and AGN feedback.

For metal line absorption, $z < 1$ O VI observations from Tumlinson et al. (2011) and Prochaska et al. (2011) have proven challenging to match, while the correspondence was better for low ions, perhaps due to a paucity of hot gas in the models (Hummels et al., 2013; Ford et al., 2015). In general, efficient feedback is required to find agreement with observations at large impact parameters (Stinson et al., 2012; Hummels et al., 2013). At higher redshift, Shen et al. (2013) were able to reproduce to the metal-line equivalent widths (EWs) from Steidel et al. (2010). Their simulations indicate that the extended absorption is mostly due to inflowing, rather than outflowing material, contrary to the model presented in Steidel et al. (2010). More recently, Suresh et al. (2015) compared to C IV observations from Turner et al. (2014), and found that even the most energetic wind model was unable to match the observations at 200–300 pkpc scales.

Here we will perform a comparison between the observations of absorption by H I, C IV, and Si IV around $z \sim 2$ galaxies of Turner et al. (2014, hereafter T14), and the Evolution and Assembly of Galaxies and their Environments (EAGLE) simulations (Schaye et al., 2015; Crain et al., 2015). EAGLE has been found to broadly reproduce a number of observables, including the present day galaxy stellar mass function, galaxy sizes and the Tully-Fisher relation (Schaye et al., 2015), galaxy colours (Trayford et al., 2015) and H_2 scaling relations (Lagos et al., 2015), the evolution of galaxy stellar masses (Furlong et al., 2015), and properties of H I absorption at $z \sim 2$–3 (Rahmati et al., 2015). The relatively high resolution and large cosmological volume $(100 \ \mathrm{cMpc})^3$ of EAGLE permits the study of massive haloes while still capturing the small scales that are vital for gas flows.

The observations of T14 are based on data from the Keck Baryonic Structure Survey (Rudie et al., 2012b; Steidel et al., 2014, KBSS), a galaxy redshift survey of 15 fields centred on hyper-luminous QSOs. T14 employed an approach known as the pixel optical depth method (Cowie & Songaila, 1998; Ellison et al., 2000; Schaye et al., 2000a; Aguirre et al., 2002; Schaye et al., 2003) to measure absorption in the QSO spectra for H I and five metal ions, making corrections for saturation and contamination. The redshifts and impact parameters from the KBSS survey were then used to characterize the statistical properties of the absorption around 854 $\langle z \rangle \approx 2.3$ galaxies. The pixel optical depth approach is particularly well-suited for comparison with simulations, as unlike fits to absorption lines, it can be applied quickly, automatically and uniformly to large numbers of (mock) spectra.

This work builds upon a previous study by Rakic et al. (2013), who also applied the pixel optical depth technique to the KBSS data in order to measure the median H I absorption around the galaxies, and compared the results with the OWLS simulations (Schaye et al., 2010). The authors measured a best-fit minimum halo mass of $\log_{10} M_{\mathrm{halo}}^{\mathrm{min}}/M_\odot = 11.6 \pm 0.2$

which agrees with independent measurements from clustering by Trainor & Steidel (2012, $\log_{10} M_{\text{halo}}^{\text{min}}/\text{M}_\odot$ = 11.7). They also determined that galaxy redshift errors and gas peculiar velocities were required to reproduce the observed redshift-space distortions. We expand upon the work of Rakic et al. (2013) by examining metal-line absorption by C IV and Si IV in addition to H I, and by comparing with the updated EAGLE simulations. The improvements provided by EAGLE compared to the OWLS simulations include a much better match to observations of galaxies, a substantially larger volume (100 cMpc instead of 25 cMpc) at a similar resolution, a cosmology consistent with current constraints, and a much improved hydrodynamics solver.

The structure of this paper is as follows. In § 4.2 we describe the simulations and our approach for generating mock spectra. In § 4.3.2 we present a direct comparison between the results from T14 and the simulations, while in § 4.4 we test the effect of varying our fiducial parameters such as the inclusion of redshift errors, gas peculiar velocities, and we assess the impact of modifying the simulation subgrid models. Our discussion and conclusions can be found in § 4.5. Finally, in Appendix 4.A we present resolution and box size tests. Throughout this work, we denote proper and comoving distances as pMpc and cMpc, respectively. Both simulations and observations use cosmological parameters determined from the Planck mission (Planck Collaboration et al., 2013), i.e. H_0 = 67.1 km s^{-1} Mpc^{-1}, Ω_m = 0.318, and Ω_Λ = 0.683.

4.2   Method

4.2.1   Simulations

We will compare the results of T14 to predictions from EAGLE, a suite of cosmological, hydrodynamical simulations. The EAGLE suite was run with a substantially modified version of the *N*-body TreePM smoothed particle hydrodynamics (SPH) code GADGET 3, last described in Springel (2005). In particular, the simulations employ the updated hydrodynamics solver "Anarchy" (Dalla Vecchia, in prep.; see also Appendix A of Schaye et al. 2015) which uses the pressure-entropy formulation of SPH from Hopkins (2013) and the time-step limiter from Durier & Dalla Vecchia (2012).

The simulations include subgrid models for the following physical processes: photoheating and radiative cooling via eleven elements (hydrogen, helium, carbon, nitrogen, oxygen, neon, magnesium, silicon, sulphur, calcium and iron) from Wiersma et al. (2009a) using a Haardt & Madau (2001) UV and X-ray background; star formation from Schaye & Dalla Vecchia (2008) with the metallicity-dependent gas density threshold of Schaye (2004); stellar evolution and enrichment from Wiersma et al. (2009b); black-hole seeding and growth from Springel et al. (2005); Rosas-Guevara et al. (2013) and Schaye et al. (2015). Stochastic, thermal stellar feedback from star formation is implemented as in Dalla Vecchia & Schaye (2012), where the injected energy depends on both the local metallicity and density. AGN feedback is also realized thermally as in Booth & Schaye (2009), but implemented stochastically (Schaye et al., 2015). The feedback in EAGLE has been calibrated to match observations of the *z* = 0 galaxy stellar mass function, the galaxy–black hole mass relation, and to give reasonable sizes of disk galaxies.

The EAGLE suite includes variations in box size, resolution, and subgrid physics. The largest run is the intermediate-resolution fiducial or reference ("Ref") model, which uses

Table 4.1: Characteristics of the EAGLE simulations. From left to right, the columns list the simulation identifiers, box size, number of particles, initial baryonic particle mass, dark matter particle mass, comoving (Plummer-equivalent) gravitational softening, maximum physical softening, and differences with respect to the reference run.

Simulation	L [cMpc]	N	m_b [M$_\odot$]	m_{dm} [M$_\odot$]	ε_{com} [ckpc]	ε_{prop} [pkpc]	Deviations from Ref.
Ref-L100N1504	100	2×1504^3	1.81×10^6	9.70×10^6	2.66	0.70	
Ref-L050N0752	50	2×752^3	1.81×10^6	9.70×10^6	2.66	0.70	
Ref-L025N0376	25	2×376^3	1.81×10^6	9.70×10^6	2.66	0.70	
Ref-L025N0752	25	2×752^3	2.26×10^5	1.21×10^6	1.33	0.35	Higher resolution
Recal-L025N0752	25	2×752^3	2.26×10^5	1.21×10^6	1.33	0.35	Higher resolution, recalibrated feedback
NoAGN	50	2×752^3	1.81×10^6	9.70×10^6	2.66	0.70	No AGN feedback
WeakFB	25	2×376^3	1.81×10^6	9.70×10^6	2.66	0.70	Weaker stellar feedback
StrongFB	25	2×376^3	1.81×10^6	9.70×10^6	2.66	0.70	Stronger stellar feedback

a 100 cMpc periodic box with 1504^3 of both dark matter and baryonic particles (denoted L100N1504). Information about the resolution and subgrid physics for each simulation used here can be found in Table 4.1. In § 4.3.2 we will focus on models with the reference subgrid physics, and we employ different box sizes and resolutions for convergence testing (Appendix 4.A), while in § 4.4 we compare with other subgrid models. We note that the high-resolution simulation (Ref-L025N0752) has also been run with subgrid physics recalibrated to better match the galaxy mass function (Recal-L025N0752). The alternative models that we consider are NoAGN, in which AGN feedback has not been implemented; and WeakFB and StrongFB, which employ half and twice as strong stellar feedback as the reference model, respectively. These subgrid variations are described in detail and compared with observations in Crain et al. (2015).

4.2.2 Generating mock spectra

To generate mock spectra, we use the z = 2.24 EAGLE snapshot, as it is closest to the median observed galaxy redshift of z = 2.34. We have tested using our runs at z = 2.0 and 2.5, and confirmed that when the intensity of the UV background is fixed such that the median neutral hydrogen optical depth in random regions agrees with the observations, the difference due to the use of different simulation redshifts is negligible for both H I and metal ions.

Dark matter halos are identified by first linking neighbouring dark matter particles using a friends-of-friends algorithm with a linking length of 0.2 times the mean separation. We then link each baryonic particle to its nearest dark matter particle, and invoke SubFind (Springel et al., 2001; Dolag et al., 2009) to identify bound structures. Here, we only consider central galaxies as we are selecting by halo mass, and leave the consideration of satellite galaxies to a future work.[1] The centre of each sub-halo is defined to be its centre of mass, and the mass M_{halo} is defined as the total mass within a radius where the density is 200 times the critical density of the Universe at the considered redshift. We note that although the measurement of M_{halo} is centred around the minimum gravitational potential of the most massive sub-halo, we find that our results are insensitive to whether we define the sub-halo centres using the centre of mass or the minimum gravitational potential.

The observations are magnitude limited ($\mathcal{R} \leq 25.5$ mag, Steidel et al. 2010) and will therefore to first order probe a minimum halo mass. We follow Rakic et al. (2013) and realize halo samples by drawing randomly (with replacement) from all halos in the snapshot with fixed minimum halo mass (M_{halo}^{min}) but without imposing a maximum halo mass. In practice, due to the steepness of the halo mass function, our results will be dominated by halos with masses close to M_{halo}^{min}. In this work, we present results for the range of minimum halo masses $\log_{10} M_{halo}^{min}/M_{\odot}$ = (10.5, 11.0, 11.5, 12.0, 12.5). This range is centred on the minimum halo mass measured by Rakic et al. (2013) ($\log_{10} M_{halo}^{min}/M_{\odot}$ = 11.6 ± 0.2) and Trainor & Steidel (2012) ($\log_{10} M_{halo}^{min}/M_{\odot}$ = 11.7). We give the median halo mass as well as the number of galaxies that corresponds to a given minimum halo mass for each simulation in Table 4.2.

For each minimum halo mass, we generated 12,000 spectra with impact parameters ranging from 35 pkpc (the smallest in the KBSS sample) to 5.64 pMpc. Although the KBSS

---

[1] The fraction of galaxies that are satellites in the fiducial Ref-L100N1504 simulation with stellar mass above $\log_{10} M_*/M_{\odot}$ = 10.2 (the median value of the observations) is 16%.

Table 4.2: The median halo mass and number of galaxies for the different $M_{\mathrm{halo}}^{\mathrm{min}}$, for each box size, resolution, subgrid variation and redshift.

| Simulation | z | Median $\log_{10} M_{\mathrm{halo}}/M_\odot$ | | | | | Number of galaxies | | | | |
$\log_{10} M_{\mathrm{halo}}^{\mathrm{min}}/M_\odot$		10.5	11.0	11.5	12.0	12.5	10.5	11.0	11.5	12.0	12.5
Ref-L100N1504	2.24	10.8	11.3	11.8	12.2	12.7	28812	9217	2729	689	111
Ref-L050N0752	2.24	10.8	11.3	11.8	12.2	12.6	3775	1242	348	78	8
Ref-L025N0376	2.24	10.8	11.3	11.7	12.1	…	470	161	46	10	0
Ref-L025N0752	2.24	10.8	11.3	11.7	12.1	…	521	167	47	10	0
Recal-L025N0752	2.24	10.8	11.3	11.7	12.1	…	521	165	48	10	0
NoAGN	2.24	10.8	11.3	11.7	12.2	12.6	3796	1236	349	80	11
WeakFB	2.24	10.8	11.3	11.7	12.1	…	500	162	48	10	0
StrongFB	2.24	10.8	11.3	11.7	12.1	…	460	156	47	10	0
Ref-L100N1504	2.01	10.8	11.3	11.8	12.2	12.7	29129	9873	3047	814	161
Ref-L100N1504	2.48	10.8	11.3	11.8	12.2	12.7	26771	8443	2402	540	87

data is only complete to impact parameters of 2 pMpc, we show the simulations to larger distances in order to explore some of the trends seen in the observations. As in T14, the impact parameter distribution is divided into twelve logarithmically spaced bins, and we generated 1000 spectra in each bin. The innermost bin is 0.55 dex in size, while the remaining eleven bins, starting at 0.13 pMpc, are all 0.15 dex wide. For the exact bin edge values please see Table 5 in T14.

Mock spectra were generated using the package SPECWIZARD written by Schaye, Booth, and Theuns, which is implemented as described in Appendix A4 of Theuns et al. (1998). The spectra were given the properties of the observed Keck/HIRES spectra: a resolution of FWHM ≈ 8.5 km s^{-1} and pixels of 2.8 km s^{-1} in size. We then added Gaussian noise with an S/N ratio equal to that measured in T14 (see their Table 4), which is about ~ 70 for H I and ~ 80 for C IV and Si IV. EAGLE imposes an effective equation of state on dense and cold particles representing the interstellar medium. Before generating mock spectra, we set the temperature of these particle to 10^4 K, but we found that this does not have a significant effect on our results because the cross section of such dense absorbers is very small.

There is significant uncertainty in the normalization and shape of the ionizing background radiation. Therefore, we follow standard practice and scale the strength of the ionizing background to match the observations. More specifically, before scaling the UV background, we generate a grid of 64×64 spectra covering the full 100 cMpc box, and measure the median optical depth of H I Lyα after convolving the spectra and adding noise. For each EAGLE simulation, the resulting median H I optical depth, which is representative of random regions and denoted $\tau_{\rm H I}^{\rm rnd}$, is given in the third column of Table 4.3. For subsequent runs, the spectra are synthesized with the normalization of the ionization background scaled such that $\tau_{\rm H I}^{\rm rnd}$ matches the observed value for the sample of T14 ($\log_{10} \tau_{\rm H I}^{\rm rnd} = -1.29$).

The median C IV and Si IV optical depths *after* scaling the ionization background are given in the fourth and fifth columns of Table 4.3. These are lower than the observed values by ~ 0.6 dex for C IV and by ~ 1.2 dex for Si IV. We have compared histograms of the optical depth distributions for the simulations and observations, and found that the dominant reason for this discrepancy is that the simulated spectra have more pixels with negative values. It is therefore likely that the observations contain (small) contributions from contamination due to the presence of other ions, atmospheric lines, and continuum fitting errors, which suppress the number of negative optical depth pixels and which are not present in the simulations. To account for these missing sources of contamination and noise, we calculate the difference between the observed and simulated $\tau_Z^{\rm rnd}$, and linearly add this difference to the optical depth of every pixel in the simulations. We have verified that this addition does not change the securely detected absorption. Rather, it serves to facilitate a comparison between observations and simulations for detections close to the noise level.

Finally, as the observed galaxy redshifts are measured with a finite precision, to perform a fair comparison we also add errors to the LOS positions of the simulated galaxies. As discussed in T14, the measurement uncertainty on the redshift of a galaxy depends on the manner in which it is measured and on the instrument used. T14 quote uncertainties of $\Delta v \approx 150$ km s^{-1} for LRIS, ≈ 60 km s^{-1} for NIRSPEC, and ≈ 18 km s^{-1} for MOSFIRE. Because the observations have focused on improving the redshift accuracy for the galaxies with smaller impact parameters, the errors are not uniform as a function of impact parameter. To capture this in the simulation, we have tabulated the fraction of galaxies with redshifts

Table 4.3: The median H$\textsc{i}$, C$\textsc{iv}$, and Si$\textsc{iv}$ optical depths for random regions from the observations (top row) and various EAGLE simulations (subsequent rows). The 1-σ errors on the median observed optical depths were calculated by bootstrap resampling (with replacement) the QSO spectra 1000 times. For the simulations, we present the median H$\textsc{i}$ optical depths *before* scaling the UV background, while for C$\textsc{iv}$ and Si$\textsc{iv}$ the results are derived after this adjustment had been performed.

Simulation	z	$\log_{10} \tau_{\mathrm{H\textsc{i}}}^{\mathrm{rnd}}$	$\log_{10} \tau_{\mathrm{C\textsc{iv}}}^{\mathrm{rnd}}$	$\log_{10} \tau_{\mathrm{Si\textsc{iv}}}^{\mathrm{rnd}}$
T04	2.34	$-1.29^{+0.02}_{-0.02}$	$-2.95^{+0.04}_{-0.04}$	$-3.16^{+0.06}_{-0.06}$
Ref-L100N1504	2.24	-1.43	-3.60	-4.37
Ref-L050N0752	2.24	-1.43	-3.60	-4.19
Ref-L025N0376	2.24	-1.38	-3.65	-4.37
Ref-L025N0752	2.24	-1.40	-3.64	-4.31
Recal-L025N0752	2.24	-1.39	-3.63	-4.36
NoAGN	2.24	-1.42	-3.59	-4.19
WeakFB	2.24	-1.39	-3.57	-4.29
StrongFB	2.24	-1.37	-3.85	-4.59
Ref-L100N1504	2.01	-1.56	-3.56	-4.33
Ref-L100N1504	2.48	-1.28	-3.64	-4.41

Table 4.4: The fraction of galaxies per impact parameter bin (with edges r_1 and r_2) with redshifts measured from observations taken using LRIS (LR, $\Delta v \approx 150$ km s^{-1}), NIRSPEC (NS, $\Delta v \approx 60$ km s^{-1}), and MOSFIRE (MF, $\Delta v \approx 18$ km s^{-1}).

Bin #	r_1 (pMpc)	r_2 (pMpc)	LR	NS	MF
1	0.04	0.13	0.23	0.15	0.62
2	0.13	0.18	0.18	0.00	0.82
3	0.18	0.25	0.36	0.09	0.55
4	0.25	0.36	0.28	0.03	0.69
5	0.36	0.50	0.34	0.07	0.59
6	0.50	0.71	0.52	0.07	0.41
7	0.71	1.00	0.48	0.03	0.49
8	1.00	1.42	0.56	0.04	0.40
9	1.42	2.00	0.71	0.05	0.24

measured from each instrument as a function of impact parameter (given in Table 4.4). Then, in the simulations, we apply redshift errors drawn from a Gaussian distribution with σ equal to the expected redshift error of the instrument, to the same fraction of galaxies as a function of impact parameter. For impact parameters larger than observed, we use the galaxy fractions from the final observed impact parameter bin.

4.3   Comparison with observations

4.3.1   The galaxy sample

We present the median stellar masses and median star formation rates (SFRs), for each $M_{\mathrm{halo}}^{\mathrm{min}}$ sample in Table 4.5. Note that for the observations, the median stellar mass is $\log_{10} M_*/\mathrm{M}_\odot =$

Table 4.5: Typical galaxy properties for the different M_{halo}^{min} considered, for each box size, resolution, subgrid variation and redshift. The quantities shown here are the median stellar mass and median SFR. The observed galaxies from T14 have a median stellar mass of $\log_{10} M_\star/M_\odot = 10.2$ and median SFRs of 30 $M_\odot$ yr^{-1}.

Simulation $\log_{10} M_{halo}^{min}/M_\odot$	z	Median $\log_{10} M_\star/M_\odot$					Median SFR [$M_\odot$ yr^{-1}]				
		10.5	11.0	11.5	12.0	12.5	10.5	11.0	11.5	12.0	12.5
Ref-L100N1504	2.24	8.3	9.1	9.8	10.4	10.7	0.2	1.3	6.5	15.3	19.4
Ref-L050N0752	2.24	8.3	9.0	9.8	10.3	10.5	0.2	1.4	6.0	10.4	11.2
Ref-L025N0376	2.24	8.3	9.1	9.8	10.2	…	0.2	1.7	6.9	18.4	…
Ref-L025N0752	2.24	8.3	9.2	9.7	10.1	…	0.3	2.1	4.6	9.1	…
Recal-L025N0752	2.24	8.2	9.1	9.7	10.1	…	0.2	1.4	4.1	15.9	…
NoAGN	2.24	8.3	9.0	9.8	10.7	11.0	0.2	1.3	9.2	39.7	103.8
WeakFB	2.24	8.8	9.5	10.1	10.3	…	0.5	2.8	7.7	14.3	…
StrongFB	2.24	7.7	8.4	9.1	9.6	…	0.0	0.3	1.3	5.8	…
Ref-L100N1504	2.01	8.3	9.1	9.9	10.4	10.7	0.2	1.3	6.0	13.8	18.1
Ref-L100N1504	2.48	8.3	9.0	9.8	10.4	10.7	0.2	1.4	7.0	17.2	28.0

10.2 and the median SFR is 30 $M_\odot$ yr^{-1}.[2] Furlong et al. (2015) found that observations of the evolution of the galaxy stellar mass function are reproduced remarkably well in EA-GLE. However, they noted that the normalisation of the specific SFR is 0.2–0.4 dex below observations at all lookback times.

To compare directly with our galaxy sample, in Fig. 4.1 we present probability distribution functions (PDFs) of the stellar masses and SFRs for different minimum halo masses taken from the Ref-L100N1504 simulation, as well as from the observations. We will focus on the range of $M_{\rm halo}^{\rm min} = 10^{11.5}$–$10^{12.0}$ $M_\odot$, which corresponds to median halo masses of $10^{11.8}$–$10^{12.2}$ (see Table 4.2) and agrees with the halo masses of the KBSS (Trainor & Steidel, 2012; Rakic et al., 2013). For this minimum halo mass range, we find very good agreement with the observed stellar masses. while the SFRs from the observations are systematically higher than in EAGLE (in agreement with the findings of Furlong et al. (2015)), although the medians only differ by a factor of ~ 2 for $M_{\rm halo}^{\rm min} = 10^{12.0}$. We conclude that performing the galaxy selection by stellar mass or SFR instead of halo mass would not significantly impact our results.

4.3.2   The circiumgalactic medium

The primary results of T14 can be summarized by their Fig. 4, where they presented the first 2-dimensional (2-D) maps of metal-line absorption around galaxies. These maps were constructed by using the galaxy redshifts to associate each galaxy with a region in the QSO spectrum. The recovered pixel optical depths for every galaxy were then binned by the impact parameter and LOS distance to the galaxy.

We reproduce the T14 maps of the median observed H I, C IV and Si IV optical depths in the leftmost column of Fig. 4.2. T14 noted the presence of a strong enhancement of the absorption near galaxies with respect to random regions that extends ~ 180 pkpc in the transverse direction and ~ ±240 km s^{-1} along the LOS. A second result was the detection of weak excess absorption out to a transverse distance of 2 pMpc, the maximum impact parameter probed, for H I and C IV.

The observations are compared with simulated samples with minimum halo masses of $10^{10.5}$, $10^{11.5}$, and $10^{12.5}$, shown respectively in columns 2–4 of Figure 4.2. Although we will explore the comparison more quantitatively in the subsequent figures, we can already glean some characteristic behaviours from the 2-D maps. Primarily, we find that the amount of absorption by metals and H I in the vicinity of galaxies increases with halo mass (from left to right), and that the effect is stronger for the metals. For C IV and Si IV, it appears that the $M_{\rm halo}^{\rm min} = 10^{11.0}$ $M_\odot$ model produces too little absorption while the $M_{\rm halo}^{\rm min} = 10^{12.0}$ $M_\odot$ produces too much, which suggests that the data agree most closely with a mass that lies within this range.

We would like to assess the goodness-of-fit of each of the models, however the χ^2 statistic cannot be used because the errors are non-Gaussian and correlated. Instead, we compute p-values for each $M_{\rm halo}^{\rm min}$ considered here in the following manner. For a given realization of the simulated data, we use 10,000 bootstrap realizations of the observations (performed by bootstrapping the galaxies in each transverse bin) and determine, for each

---

[2]The observational quantities are estimated using spectral energy distribution (SED) fits to 782 out of the 854 galaxies, while 180 of these 782 galaxies have their SFRs measured from Hα. See § 2.3 of Steidel et al. (2014) and references therein for more details.
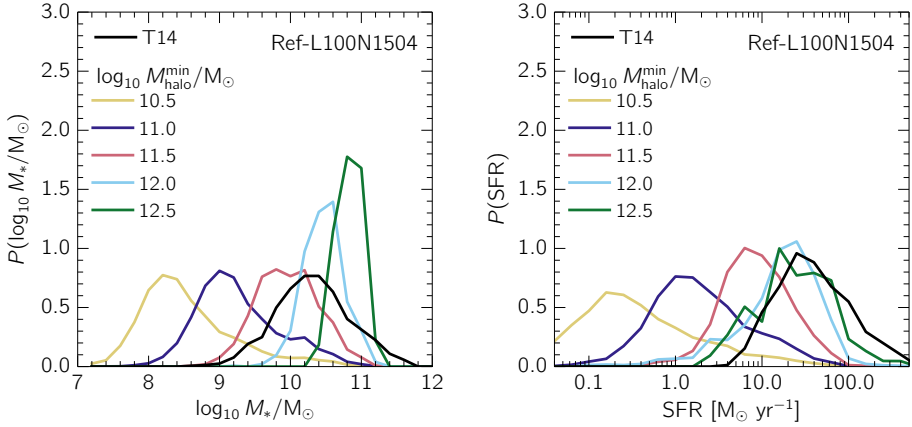
Figure 4.1: PDFs of galaxy stellar masses (left panel) and SFRs (right panel) for the KBSS galaxies in T14 (black lines), as well as for different $M_{\mathrm{halo}}^{\mathrm{min}}$ in the Ref-L100N1504 simulation (coloured lines). Previous measurements of the observed galaxy halo masses (Trainor & Steidel, 2012; Rakic et al., 2013) estimate $M_{\mathrm{halo}}^{\mathrm{min}}$ to be between $10^{11.5}$ and $10^{12.0}$ M$_\odot$ (represented by the red and cyan lines, respectively). The observed stellar masses agree very well with the simulations for these halo masses, while the observed SFRs are systematically somewhat higher than those of EAGLE by a factor of ~ 2.

Table 4.6: *p*-values (i.e. the probability that a model, with a given $M_{\mathrm{halo}}^{\mathrm{min}}$, is consistent with the observed un-smoothed data) from Fig. 4.2. We measure *p*-values using data from the full maps, and for the case of H I also for the same subset of bins used to measure halo mass as in Rakic et al. (2013). The data rule out all models with $M_{\mathrm{halo}}^{\mathrm{min}} \geq 10^{12.0}$ M$_\odot$, while all but the full map of C IV rule out $M_{\mathrm{halo}}^{\mathrm{min}} = 10^{10.5}$ M$_\odot$.

$\log_{10} M_{\mathrm{halo}}^{\mathrm{min}}/\mathrm{M}_\odot$	10.5	11.0	11.5	12.0	12.5
H I, full map	0.002	0.059	0.033	0.000	0.000
H I, LOS = 0.71–2.83 pMpc	0.003	0.085	0.340	0.034	0.000
C IV, full map	0.063	0.410	0.326	0.012	0.000
Si IV, full map	0.001	0.000	0.049	0.011	0.000

bin in the transverse and/or LOS direction, the percentile of the bootstrap realization that agrees with the simulations, where the percentiles are normalized to range from 0 to 50 (that is, if a percentile was > 50, it was subtracted from 100). Then, the percentiles corresponding to each LOS-impact parameter bin are divided by 100 and multiplied together to give a probability of the model. This procedure is also applied to all of the bootstrap realizations of the data, so that each realization has an associated probability. The *p*-values which we quote here are then given by the fraction of the realizations of the data that have a probability lower than that of the model. We note that if we pretend that the observations are the model, then this procedure yields *p*-values $\geqq 0.988$. We reject models with *p*-values < 0.05.

In Table 4.6, we present the *p*-values for each $M_{\mathrm{halo}}^{\mathrm{min}}$, for both the full (unsmoothed) map shown in Fig 4.2 as well as for distances along the LOS limited to the four bins within 170–670 km s^{-1} (or 0.71–2.83 pMpc for pure Hubble flow), as these bins were used in Rakic
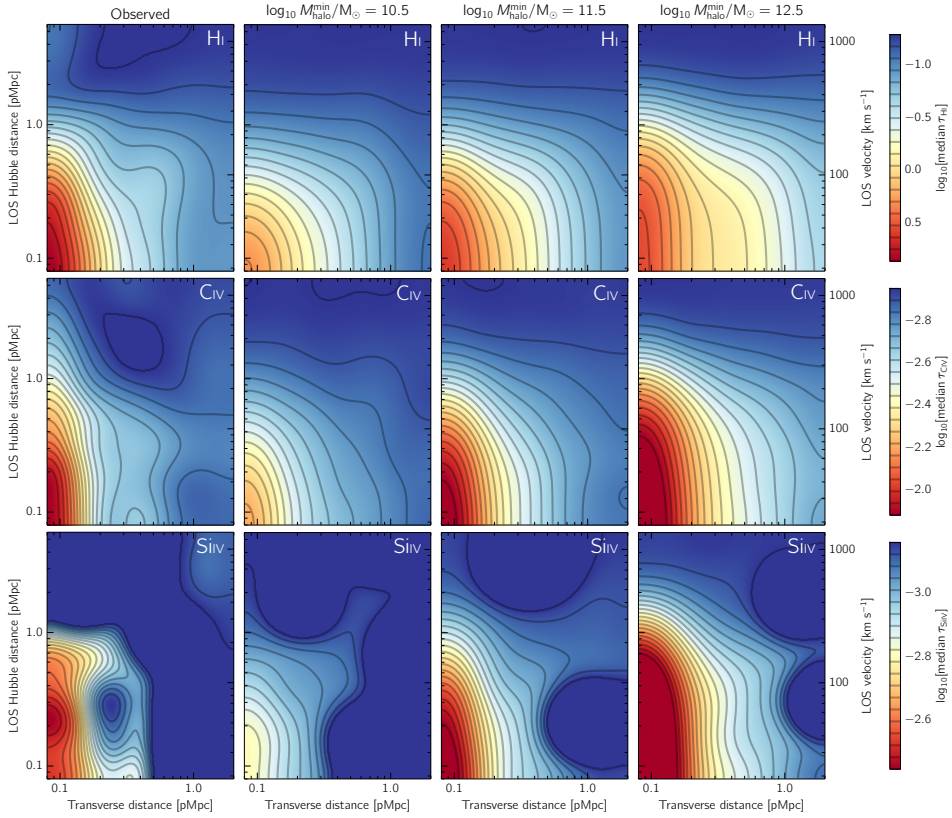
Figure 4.2: 2-D maps of median metal-line optical depth around galaxies, for H I (top row), C IV (centre row) and Si IV (bottom row). The leftmost column shows the KBSS observations from T14, while the following three columns display the results from the Ref-L100N1504 EAGLE simulations, with an increasing minimum halo mass of $M_{\mathrm{halo}}^{\mathrm{min}} = 10^{10.5}$, $10^{11.5}$, and $10^{12.5}$ $\mathrm{M}_{\odot}$ from left to right. The observations have been smoothed with a Gaussian that has a σ equal to the bin size (0.15 dex). The minimum optical depth values used in the colour scale are set to the median optical depth for random regions, which for each ion is by construction identical for the simulations and observations, while the maximum optical depth values are set by the maxima in the observations. The p-values, i.e. the probability that a model (with a given $M_{\mathrm{halo}}^{\mathrm{min}}$) is consistent with the observed unsmoothed data, are given in Table 4.6.

et al. (2013) to measure the halo mass from the HI data.[3] Rakic et al. (2013) chose this velocity range because there they found the HI absorption to be insensitive to variations in subgrid physics models. For HI, only the $M_{\mathrm{halo}}^{\min} = 10^{11.0}$ M$_\odot$ model is consistent with the full map, but the p-value for $10^{11.5}$ M$_\odot$ (0.033) is less than a a factor of two smaller than for $M_{\mathrm{halo}}^{\min} = 10^{11.0}$ (0.059). However, when using the restricted bin range of Rakic et al. (2013), the $M_{\mathrm{halo}}^{\min} = 10^{11.5}$ M$_\odot$ model is accepted with $p = 0.34$, in good agreement with Rakic et al. (2013).

Fitting to the full range of data points or the subset from Rakic et al. (2013) may, however, not be best approach for the metal-line absorption, where the detections are concentrated near the positions of galaxies, and most of the maps may be dominated by noise. For SiIV all models are formally ruled out by the data, although the disagreement is only marginal for $M_{\mathrm{halo}}^{\min} = 10^{11.5}$ M$_\odot$ ($p = 0.049$). On the other hand, CIV fares much better, most likely because the absorption above $\tau_{\mathrm{CIV}}^{\mathrm{rnd}}$ extends out to 2 pMpc so that the comparison between model and data is not dominated by regions consisting only of noise. For the full map, we find that models with $M_{\mathrm{halo}}^{\min} = 10^{10.5}$–$10^{12.0}$ M$_\odot$ are consistent with the data.

To avoid comparing noise with noise, we confront the simulations with the left parts of the 2-D maps (Fig. 6 from T14). In Fig. 4.3 we show a cut that runs along the LOS, where the inner two impact parameter bins (ranging from 35 to 180 pkpc) were combined. From let to right, the panels show the median optical depth as a function of LOS distance for HI, CIV and SiIV. Note that the y-axis range depends on the ion in question, and that the dynamic range is much larger for HI than for the metal ions. The observations are shown with black circles, while the coloured curves show the simulation results for halo masses ranging from $10^{10.5}$ to $10^{12.5}$ M$_\odot$, in intervals of 0.5 dex.

First examining HI in the left panel, we see that the HI optical depths are most sensitive to halo mass at intermediate velocities. For all minimum halo masses considered, the optical depths appear to be systematically lower than the ∼ 2 innermost points (out to 40 km s^{-1}). However, we emphasize that the errors along the LOS are correlated (to scales of ∼ 10^2 km s^{-1}, see Rakic et al. 2012) and that the model and data agree at the 1-σ level for all but the lowest halo masses, so this apparent discrepancy is not significant.

Turning next to the metals, we find that in contrast to HI, the median optical depths within 60 km s^{-1} of the galaxy positions are sensitive to halo mass. This holds for all velocities up to ∼ 600 km s^{-1} where all curves asymptote to τ_Z^{rnd}. Overall, we find that all the minimum halo masses considered here are consistent with the qualitative behaviour of the observations, which is that the metal-line absorption is strongly enhanced out to ∼ ±200 km s^{-1} along the LOS.

In Fig. 4.4 we examine cuts along the transverse direction, with a velocity width of ±170 km s^{-1}. The simulations again capture the qualitative behaviour of the data. The enhancement in the absorption decreases with the impact parameter and this gradient decreases with the distance to the galaxy. For all halo masses considered, the HI and CIV median optical depths show enhancement above τ_Z^{rnd} out to ∼ 5 pMpc. T14 postulated that the significant excess absorption observed at such large distances (i.e., many virial radii away from the host galaxy) is likely due to clustering effects. Support for this argument is given by Fig. 4.8, which shows that the median optical depths are not fully converged for box sizes < 50 cMpc, where clustering on ∼Mpc scales is not properly captured.

---

[3]The exact bin edge values differ slightly from Rakic et al. (2013), as the ones used here were chosen to be consistent with Rakic et al. (2012) and T14.
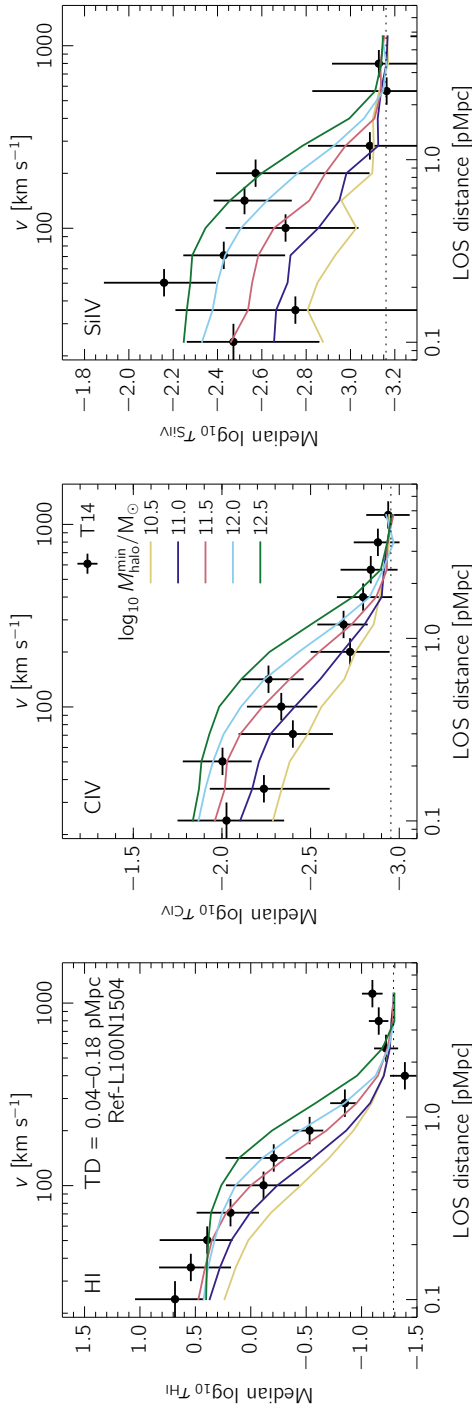
Figure 4.3: Cuts taken along the LOS through the maps from Fig. 4.2 (right column of Fig. 6 from T14). The size of the transverse bin, 0.04–0.18 pMpc, was chosen to include the strong absorption in both H I and metals. The observations from T14 are shown as black circles with 1-σ error bars, while the simulations are denoted by the lines where each colour represents a different minimum halo mass, and the horizontal dotted lines indicate τ_Z^{rnd}. The p-values for each halo mass model, based on the comparison shown here and on the cuts along the transverse direction shown in Fig. 4.4, are given in Table 4.7. Only the model with $\log_{10} M_{\mathrm{halo}}^{\mathrm{min}}/\mathrm{M}_\odot = 11.5$ is consistent with all of the data.
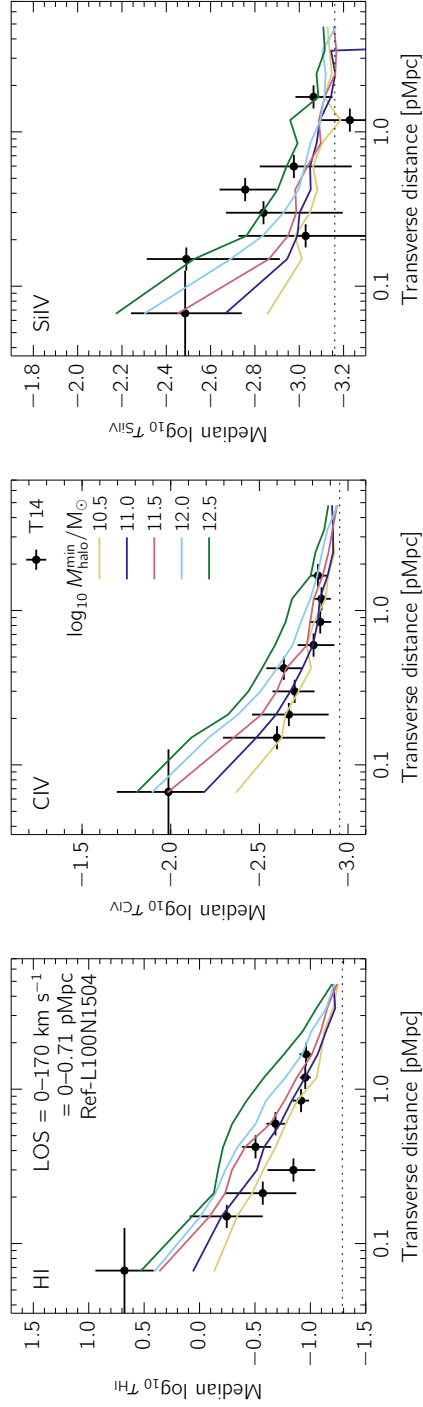
Figure 4.4: The same as Fig. 4.3, except taking a cut along the transverse direction of Fig. 4.2 with a size of ± 170 km s^{-1} (left-hand column of Fig. 6 in T14) The enhancement of H I and C IV absorption out to the maximum observed impact parameter of 2 pMpc is also seen in the simulations, and extends out to ~ 5 pMpc. The *p*-values resulting from a simultaneous comparison to this data plus that in Fig. 4.3 are given in Table 4.7.

Table 4.7: p-values for the models given the data shown in Figs. 4.3 and 4.4. Only the model with $M_{\mathrm{halo}}^{\mathrm{min}} = 10^{11.5}$ M$_\odot$ is consistent with all the data.

| $\log_{10} M_{\mathrm{halo}}^{\mathrm{min}}/\mathrm{M}_\odot$	10.5	11.0	11.5	12.0	12.5
H I	0.003	0.055	0.133	0.010	0.000
C IV	0.379	0.926	0.938	0.285	0.003
Si IV	0.023	0.035	0.099	0.068	0.030

Table 4.8: p-values for the models given the data shown in Fig. 4.5. While the H I data rule out all minimum halo masses except for $M_{\mathrm{halo}}^{\mathrm{min}} = 10^{11.5}$ M$_\odot$, the metal-line absorption data are less constraining.

| $\log_{10} M_{\mathrm{halo}}^{\mathrm{min}}/\mathrm{M}_\odot$	10.5	11.0	11.5	12.0	12.5
H I	0.003	0.026	0.109	0.027	0.000
C IV	0.100	0.484	0.835	0.474	0.074
Si IV	0.219	0.040	0.316	0.229	0.143

Finally, in Table 4.7 we present the p-values of simultaneous comparisons to the data from Figs. 4.3 and 4.4. The H I data are consistent with $M_{\mathrm{halo}}^{\mathrm{min}}$ between $10^{11.0}$ and $10^{11.5}$ M$_\odot$. While the C IV data only exclude the highest minimum halo mass model, $10^{12.5}$ M$_\odot$, the Si IV data are consistent with $M_{\mathrm{halo}}^{\mathrm{min}} = 10^{11.5}$–$10^{12.0}$ M$_\odot$. Therefore, only the model with $M_{\mathrm{halo}}^{\mathrm{min}} = 10^{11.5}$ is consistent with all of the data.

In Fig. 4.5 we examine redshift-space distortions, i.e., how the absorption along the LOS differs from that of the transverse direction (Fig. 5 from T14). We have plotted the median optical depths from the innermost bin along the LOS (solid lines, filled squares for the observations) and the transverse direction (dashed lines, open circles for the observations). The data and models show strong and comparable redshift-space distortions. The p-values for the comparisons are given in Table 4.8. The H I data rule out all models except for $M_{\mathrm{halo}}^{\mathrm{min}} = 10^{11.5}$ M$_\odot$, but the metal data is not very constraining. Although a simple "chi-by-eye" would eliminate the lowest-mass models, the errors are non-Gaussian and along the LOS they are correlated.

The results for H I in Fig. 4.5 can be directly contrasted with the top left panels of Fig. 7 (for points along the LOS) and Fig. 8 (for points in the transverse direction) in Rakic et al. (2013). In these figures, the authors examined the same optical depth profiles from the KBSS observations as are shown here, but using an older version of the data with larger redshift errors, and compared the results to the OWLS simulations. They found that in the smallest transverse distance bin, the OWLS simulations significantly underestimated the highest observed H I optical depths. The relative success of the EAGLE simulations compared to those presented in Rakic et al. (2013) can be partly attributed to the smaller redshift errors in the latest KBSS data, however even after removing redshift errors the H I optical depths in Rakic et al. (2013) were still well below those from the observations. We conclude that the EAGLE simulations provide a much better agreement to observations of H I in absorption than was found in OWLS.
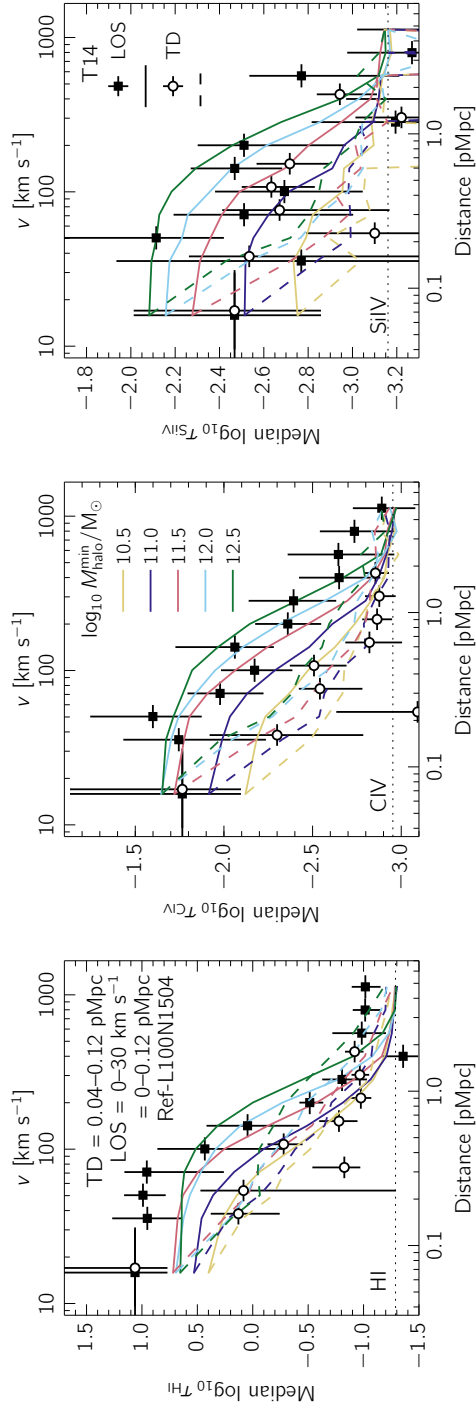
Figure 4.5: The median optical depth from cuts of equal size taken in the transverse direction and along the LOS, in order to study the redshift-space distortions (Fig. 5 in T14). The observed medians and 1-σ errors are indicated in black, while the coloured lines show simulations using different $M_{\mathrm{halo}}^{\mathrm{min}}$. The filled squares and solid lines denote the median optical depths along the LOS, while the open circles and dashed lines indicate the transverse direction. The p-values for the models are given in Table 4.8.
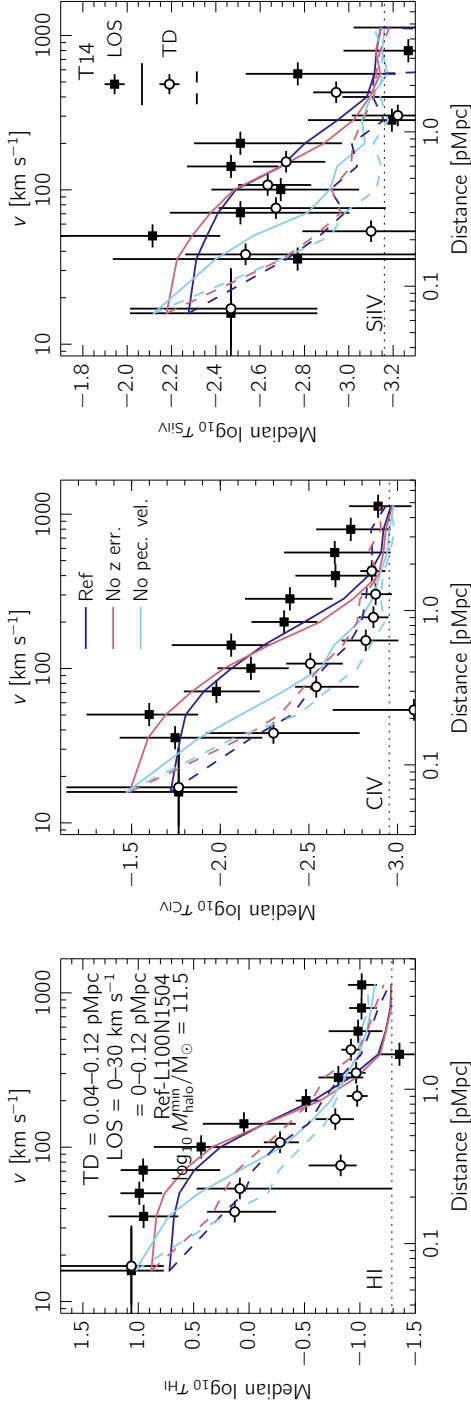
Figure 4.6: The same as Fig. 4.5, but only presenting $M_{halo}^{min} = 10^{11.5}\ M_\odot$, and comparing to models without redshift errors (red line) and without peculiar velocities (cyan line). Without redshift errors, the median optical depths decrease more steeply along the LOS, and there is also more absorption along the transverse direction for the velocity bin shown (0–30 km s^{-1}). Without peculiar velocities, the median optical depths along the LOS and transverse directions are almost identical, with the former still being slightly smoothed by the redshift errors. Peculiar velocity differences are required to obtain the large observed redshift space distortions.

Table 4.9: p-values for the top row of Fig. 4.7. While the H I data rule out all models except for $M_{\mathrm{halo}}^{\mathrm{min}} = 10^{12}$ M$_\odot$ for Ref and StrongFB, the observed metal-line absorption is consistent with most models. Note that for Ref, the p-values differ from Table 4.8 because those values were for a box size of 100 cMpc whereas here we use a 25 cMpc box to facilitate a fair comparison with the StrongFB and WeakFB models.

	H I			C IV			Si IV		
$\log_{10} M_{\mathrm{halo}}^{\mathrm{min}}/\mathrm{M}_\odot$	11.0	11.5	12.0	11.0	11.5	12.0	11.0	11.5	12.0
Ref	0.000	0.025	0.095	0.245	0.614	0.600	0.035	0.067	0.035
StrongFB	0.000	0.013	0.075	0.040	0.258	0.497	0.161	0.064	0.025
WeakFB	0.000	0.003	0.015	0.442	0.769	0.812	0.160	0.151	0.226

Table 4.10: p-values from the bottom row of Fig. 4.7. We note that in order to compare with the NoAGN mode, we use a 50 cMpc box for Ref, and thus the p-values differ from those presented in Table 4.8.

	H I			C IV			Si IV		
$\log_{10} M_{\mathrm{halo}}^{\mathrm{min}}/\mathrm{M}_\odot$	11.0	11.5	12.0	11.0	11.5	12.0	11.0	11.5	12.0
Ref	0.060	0.072	0.098	0.611	0.747	0.582	0.223	0.060	0.267
NoAGN	0.028	0.093	0.018	0.419	0.743	0.858	0.181	0.273	0.228

4.4 Model variations

In this section we will examine the effects of varying some of our fiducial parameters. The analysis presented so far has included impact parameter dependent galaxy redshifts errors. In Fig. 4.6, we show the same redshift-space distortions as in Fig. 4.5, but we have now added a simulation without any redshift errors. As demonstrated previously in Rakic et al. (2013), we find that the removal of redshift errors increases the median optical depths at small galactocentric distances, both in the transverse direction and along the LOS. However, the effect is modest because the KBSS redshift errors are small for most galaxies (see § 4.2.2).

We are also interested in the effects of peculiar velocities, i.e. how much of the elongation along the LOS is due to differences between the peculiar velocities of the galaxy and the surrounding gas (rather than redshift errors). We have run SPECWIZARD with galaxy and gas peculiar velocities set to zero, and plot the result as the cyan lines in Fig. 4.6. The redshift-space distortions for the cyan lines are strongly suppressed compared to the other cases, i.e., the solid and dashed lines are much closer together, with the remaining difference due to redshift errors. Turning off peculiar velocities decreases the median optical depths along the LOS, except for the innermost bin. Without peculiar velocity differences, the redshift space distortions are much smaller than observed.

Fig. 4.7 shows the result of varying the subgrid feedback relative to the reference EA-GLE run. In the top row, we compare the median optical depths from Ref-L025N0376 to the WeakFB and StrongFB runs, which use respectively half and twice as efficient stellar feedback as the reference model. Note that all of these models use a 25 cMpc box, so at large transverse distances the results will not be converged with the size of the simulation volume. In Table 4.5, we can see that for a fixed halo mass, the median stellar mass of a simulated galaxy from the StrongFB model is 0.6–0.7 dex lower than for Ref, and for WeakFB
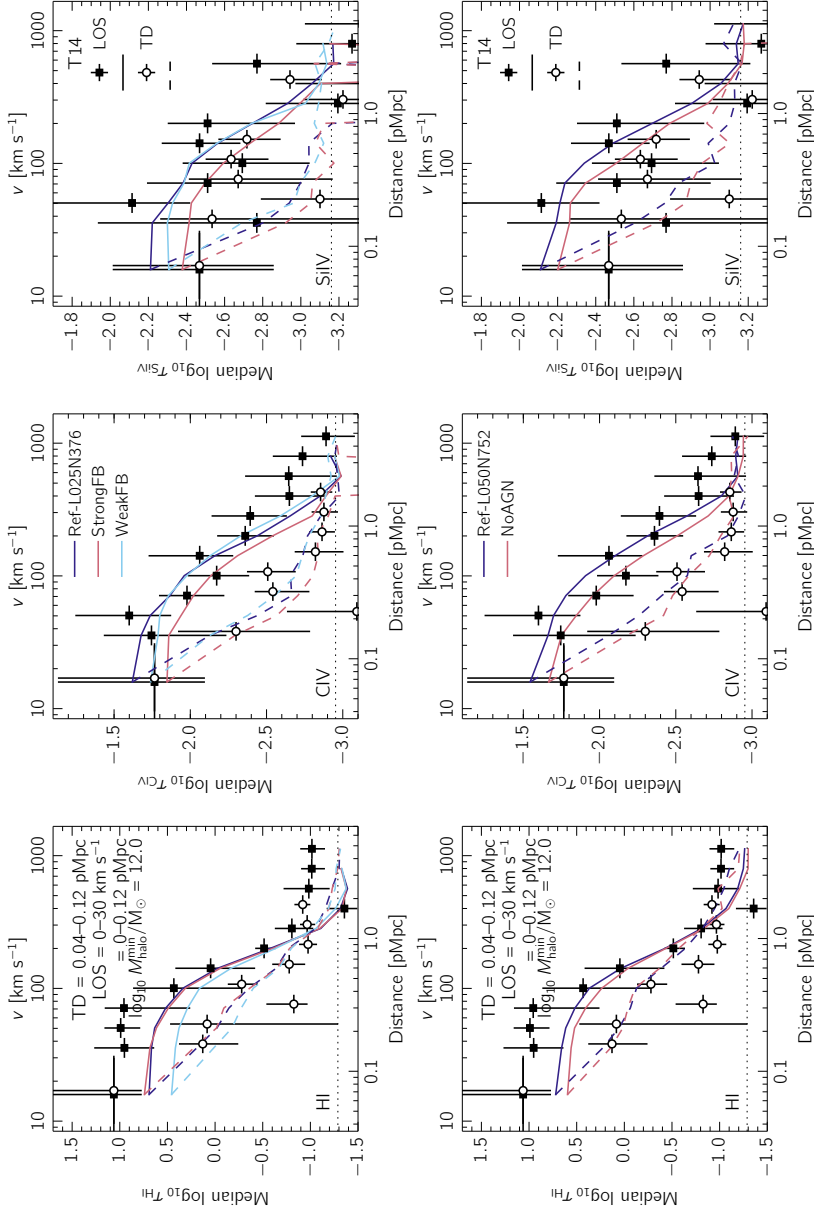
Figure 4.7: As Fig. 4.5, but for different EAGLE feedback prescriptions. In the top row, we show the reference model, as well as results from the WeakFB and StrongFB runs, all using a 25 cMpc box. We display $M_{\rm halo}^{\rm min} = 10^{12.0}$ M$_\odot$ because it is the only minimum halo mass model not ruled out by the H I data for this small box size (see Table 4.9 for p-values). In the bottom row, we present the reference and NoAGN model, both using a 50 cMpc box, also for $M_{\rm halo}^{\rm min} = 10^{12}$ M$_\odot$. The p-values for these models are given in Table 4.10. At fixed halo mass, the metal-line absorption around our galaxies is not a good discriminator between feedback models. This indicates that these observed redshift-space distortions are likely not dominated by outflows, but rather by infall or virial motions.

it will be higher by up to 0.5 dex (although this difference decreases with increasing halo mass). Indeed, Crain et al. (2015) demonstrated that while the galaxy stellar mass function is systematically overestimated by the WeakFB model, the converse is true for the StrongFB model. This point is import to keep in mind because in this work we are selecting galaxies at fixed halo mass, which will correspond to different stellar masses that depend on the subgrid physics model. Only the reference model matches the observed halo masses of galaxies with stellar masses and redshifts equal to those of the KBSS observations.

In Table 4.9, we present the p-values for the different models. The HI data rule out all models except for $M_{\mathrm{halo}}^{\mathrm{min}} = 10^{12}$ $M_\odot$ for Ref and StrongFB. This result appears to be in tension with the fiducial model where lower minimum halo masses are preferred (Table 4.8). This discrepancy comes from the lack of enhanced optical depths at large distances, which are due to clustering, in the 25 cMpc box relative to our fiducial 100 cMpc box.

In spite of the stark differences in galaxy properties, we find that the CIV absorption data are unable to rule out any of the models (except for $M_{\mathrm{halo}}^{\mathrm{min}} = 10^{11.0}$ $M_\odot$ for the StrongFB simulation). Furthermore, for SiIV, while only $M_{\mathrm{halo}}^{\mathrm{min}} = 10^{11.5}$ $M_\odot$ from the reference model is consistent with the data, all but one of the subgrid variation models cannot be excluded.

The bottom row of Fig. 4.7 compares the median optical depths from the NoAGN run to the 50 cMpc reference model, Ref-L050N752, and the corresponding p-values are listed in Table 4.10. Fig. 4.7 presents results for $M_{\mathrm{halo}}^{\mathrm{min}} = 10^{12.0}$ $M_\odot$, as we do not expect the exclusion of AGN to have a strong effect below this halo mass. While the HI data exclude the $M_{\mathrm{halo}}^{\mathrm{min}} = 10^{11.0}$ and $10^{12.0}$ $M_\odot$ NoAGN models, the metal-line absorption results are consistent with all models.

The results from Fig. 4.7 have an important implication for the interpretation of the observations of T14. As mentioned previously, T14 found that the HI and metal-line absorption is enhanced along the LOS with respect to the transverse distance for velocities up to $\sim \pm 240$ km s^{-1}. Given the small galaxy redshift errors, this was interpreted as being caused by gas motions from infall, outflows, or virial motions. However, because the measured velocity scale is close to the that of the expected galaxy circular velocities (≈ 217 km s^{-1}), it was not possible to differentiate between the different scenarios.

Since outflows are thought to be driven by energetic feedback from star formation and AGN, if the observed redshift-space distortions were dominated by outflowing gas, one would expect a significant difference between models with substantially different feedback physics. As demonstrated in Fig. 4.7, for a fixed sample of haloes we find almost no differences in the metal-line absorption properties after varying the subgrid models for feedback. This implies that, at least according to the simulations, the observed redshift-space anisotropies are dominated by virial motions and/or inflows, rather than by outflowing gas.

4.5 Discussion and conclusions

We have compared the circumgalactic HI and metal-line absorption in the EAGLE cosmological hydrodynamical simulations with observations. EAGLE includes subgrid prescriptions for both stellar and AGN feedback, that have been calibrated to match observations of the $z \sim 0$ galaxy stellar mass function, the black hole-galaxy mass relation, and galaxy disk sizes. The fiducial EAGLE model has been run with a relatively high resolution (1504^3 particles) in a cosmologically representative box size (100 cMpc).

In this work we compare the results from EAGLE to observations from T14. The authors used data from the KBSS, a spectroscopic galaxy survey in 15 QSO fields, to study the properties of the gas around 854 star-forming galaxies at $z \approx 2$. T14 applied the pixel optical depth technique to the QSO spectra and combined the absorption information with the positions and redshifts of the galaxies in the field to construct the first 2-D maps of metal-line absorption around galaxies.

We have used the simulations to generate mock spectra that were designed to mimic the properties of the QSO spectra from the KBSS. The galaxy impact parameter distribution and redshift errors were also matched to those of the observations. We compared the simulated and observed optical depths of H I, C IV and Si IV as a function of transverse and LOS separation from galaxies. Our main conclusions are:

- The galaxy stellar masses from EAGLE are in very good agreement with the observations for $M_{\rm halo}^{\rm min} = 10^{11.5}$–$10^{12.0}$ $M_\odot$ (corresponding to median halo masses of $10^{11.8}$–$10^{12.2}$), which is the halo mass range inferred from observations (Trainor & Steidel, 2012; Rakic et al., 2013). The SFRs also show broad agreement, especially for $M_{\rm halo}^{\rm min} = 10^{12.0}$, which matches the observed SFR PDF closely and has a median SFR only a factor of two below that of the observations (Fig. 4.1).

- The EAGLE simulations reproduce the observed H I, C IV and Si IV absorption around galaxies in detail, including the redshift-space distortions. The observations are most consistent with a minimum halo mass of $10^{11.5}$ $M_\odot$, in agreement with Rakic et al. (2013) (Figs. 4.2, 4.3, 4.4).

- T14 detected enhanced median optical depths above $\tau_Z^{\rm rnd}$ for H I and C IV in the transverse direction out to impact parameters of 2 pMpc (the maximum in their sample). The simulations are consistent with this result, and find that this enhancement extends to ~ 5 pMpc. This enhancement is not seen in the 25 cMpc simulation box, and we conclude that its origin is due to clustering (Fig. 4.4).

- Although redshift errors smooth optical depths along the LOS and reduce them slightly in the transverse direction, with MOSFIRE the almost negligible redshift errors (≈ 18 km s^{-1}) have only a small effect on the results (Fig. 4.6).

- Gas peculiar velocities are required to obtain the significantly higher median optical depths along the LOS compared to the transverse direction (Fig. 4.6).

- Increasing or decreasing the supernova feedback strength by a factor of two or removing AGN feedback does not substantially alter the results for C IV and Si IV at fixed halo mass, in spite of large differences in galaxy stellar masses. It is therefore likely that the enhancement of optical depths along the LOS compared to the transverse direction is not caused by outflows, but rather by infalling gas or virial motions. (Fig. 4.7).

For future work, we are interested in examining the origin of the redshift-space distortions more closely. From Fig. 4.6, we know that the relative enhancement of optical depths along the LOS with respect to the transverse directions is due to gas peculiar velocities. However, from the data alone we are unable to tell whether the motions are dominated by

inflows, outflows, or virial motions. By generating simulated spectra using a subset of gas particles with different velocities relative to the nearest host galaxy, we can use the simulations to make more detailed predictions about the velocity of the gas. Furthermore, particularly for the study of different feedback models, we would also like to examine galaxies with the same minimum *stellar* mass, which will likely lead to strong discrepancies between the different feedback models.

Lastly, we would like to study OVI in the simulations. This is a particularly interesting transition, as Turner et al. (2015) concluded from a study of optical depth ratios in the KBSS data that OVI traces hot, collisionally ionized outflowing gas. However, OVI is not as straightforward to analyse in the simulations as the ions studied in this work, as it is located in the Lyβ forest and therefore suffers from strong contamination from HI Lyman series lines. This contamination must be modelled using large numbers of realistic "long spectra", i.e. spectra constructed by stitching together sightlines from different snapshot redshifts, and and the mock spectra have absorption spanning a large redshift path similar to observed QSO spectra. We leave this task for future work.

4.A   Resolution and box size tests

We examine the effects of varying the simulation box size in Fig. 4.8, where we plot the same cuts along the LOS (top row) and transverse distance (bottom row) as were shown in Figs. 4.3 and 4.4. We show results from the fiducial model Ref-L100N1504, as well as from the reference run in the 50 and 25 cMpc boxes with the same resolution. The median optical depth profiles for the 50 and 100 cMpc runs are converged, while for the 25 cMpc box the optical depths tend to be lower.

To test the effects of varying resolution, we turn to the 25 cMpc box which has been realized with resolutions higher than the fiducial one used in this work. The L025N0752 simulation includes a version that has been run using the subgrid physics of the reference model (Ref-) and one that has been recalibrated to better match the $z \approx 0$ galaxy stellar mass function (Recal-). In Fig. 4.9 we plot the median optical depths along the LOS (top row) and transverse distance (bottom row) for these high-resolution runs as well as for our fiducial resolution (376^3 particles in the 25 cMpc box) and finally a lower resolution of 188^3 particles.

We find that for all ions and halo masses, the optical depth profiles from the fiducial and high-resolution runs are in agreement, while those from the low-resolution runs are systematically lower. We can therefore conclude that our fiducial simulation is converged.
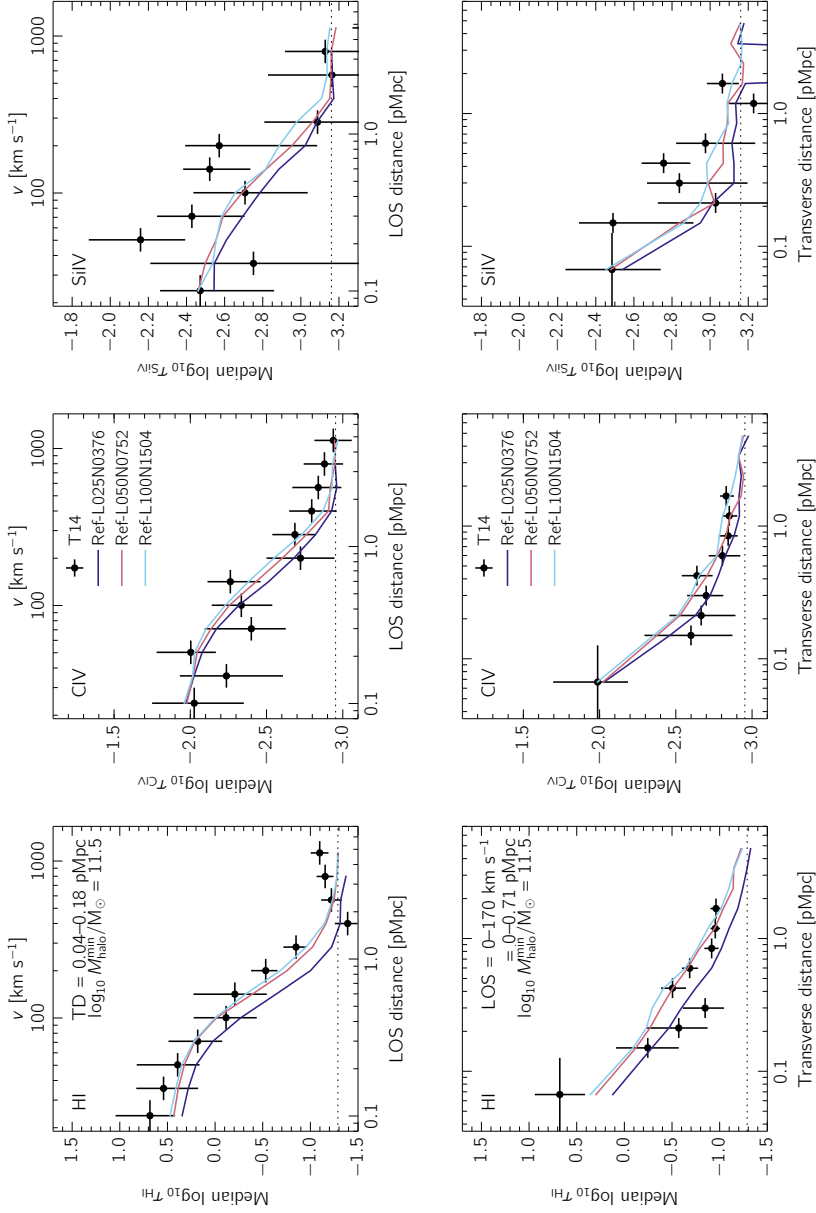
Figure 4.8: Convergence with respect to simulation box size, where we plot the median optical depths as a function of distance from galaxies along the LOS (top row) and in the transverse direction (bottom row). From left to right we show H I, C IV, and Si IV for $M_{\mathrm{halo}}^{\mathrm{min}} = 10^{11.5}$ $M_\odot$. While the optical depths from the 25 cMpc box are systematically lower than for the other runs, our fiducial simulation is converged.
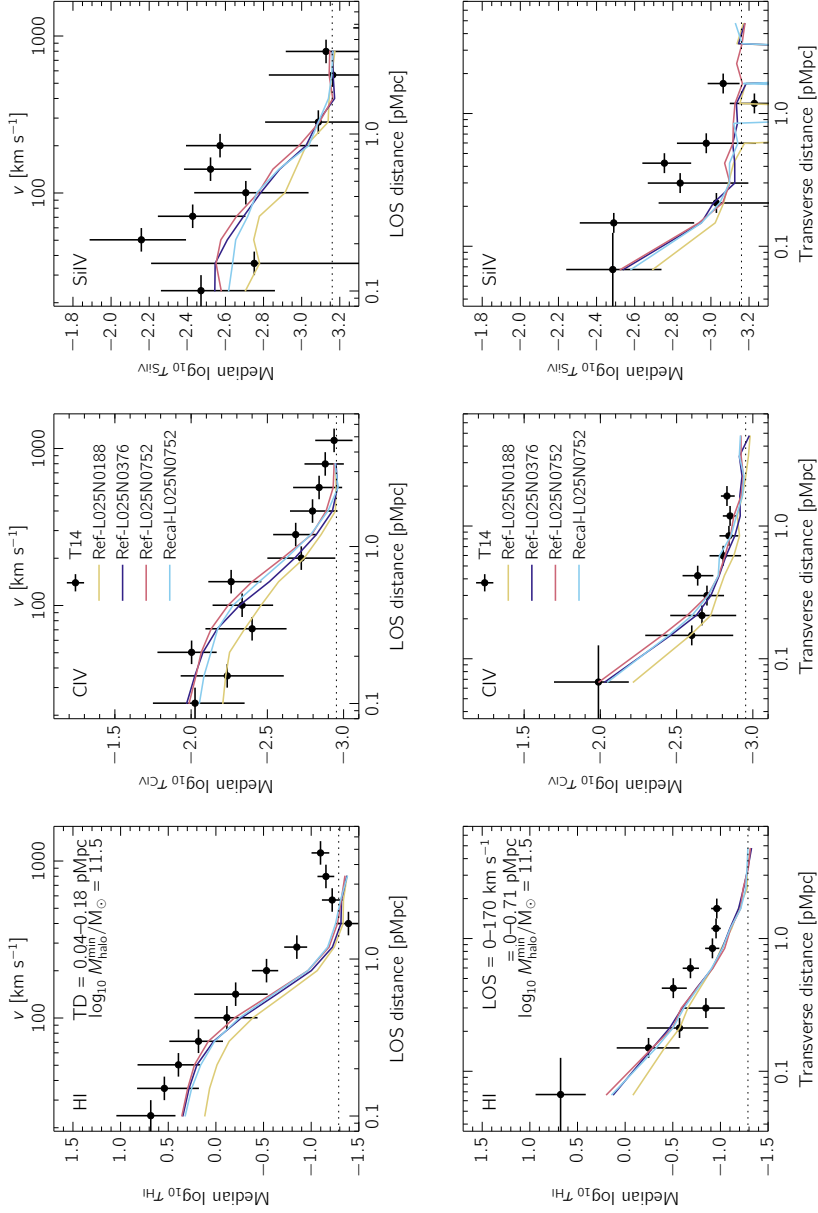
Figure 4.9: The same as Fig. 4.8, but instead presenting convergence with respect to the numerical resolution. We use the 25 cMpc box simulations showing the reference model for 188^3, 376^3 and 752^3 particles, in addition to the recalibrated L025N0752 run. The lowest-resolution run, Ref-L025N0188, has lower median optical depths in the innermost LOS and transverse distance bins compared to realizations with higher resolutions, but the fiducial intermediate- and high- resolution runs agree, indicating that the fiducial simulation is converged.

5 Observations of the $z \sim 3.5$ intergalactic medium and comparison to the EAGLE simulations

We study the $z \sim 3.5$ intergalactic medium (IGM) by comparing new, high-quality absorption spectra of eight QSOs with $\langle z_{\text{QSO}} \rangle$ = 3.75 to the EAGLE cosmological hydrodynamical simulations. We employ the pixel optical depth method to study how the absorption of one ion varies as a function of another, and uncover strong correlations between CIV, SiIV, OVI and HI, between CIII and CIV, and between SiIII and SiIV. Mock spectra were generated from the EAGLE simulations and given properties designed to mimic the observations. We find good agreement between the simulated and observed optical depth relations $\tau_{\text{OVI}}(\tau_{\text{HI}})$, $\tau_{\text{CIII}}(\tau_{\text{CIV}})$ and $\tau_{\text{SiIII}}(\tau_{\text{SiIV}})$. However, for $\tau_{\text{CIV}}(\tau_{\text{HI}})$ and $\tau_{\text{SiIV}}(\tau_{\text{HI}})$, the observed $\tau_{\text{CIV}}^{\text{med}}$ and $\tau_{\text{SiIV}}^{\text{med}}$ are higher than those measured from the simulations. The discrepancy increases from up to $\sim$ 0.1 dex at τ_{HI} = 1 to $\sim$ 1 dex at τ_{HI} = 10^2, where we are likely probing dense regions at small galactocentric distances. Invoking different models for the ionizing background radiation, including models softened above 4 Ryd to account for delayed completion of HeII reionization, can bring the observations and simulations into agreement for $\tau_{\text{HI}} \lesssim 10$. Using simulations run at a higher resolution also helps to relieve the tension, although not enough to fully explain the observed difference. The consideration of radiation from local sources could be important for ionizing HI at small galactocentric distances, and would increase the strength of simulated metal-line absorption at fixed τ_{HI}. Finally, the good agreement with the observed OVI(HI) relation, which likely probes a hot, collisionally ionized gas phase, indicates that the simulations are not in tension with the hot phase of the IGM, and suggests that the outflows responsible for the enrichment of the IGM may have insufficient cold gas.

Turner, Schaye et al.
In preparation

5.1 Introduction

It is now well established the the high redshift intergalactic medium (IGM) is enriched with heavy metals to metallicites of 10^{-3} to 10^{-2} solar (e.g., Cowie et al., 1995; Schaye et al., 2003; Simcoe et al., 2004; Aguirre et al., 2008). While metals only constitute a fraction of the total baryon budget, they play an integral role in our understanding of galaxy formation and evolution by providing a fossil record of star formation, and by impacting cooling-rates which can alter structure on many scales (e.g., Haas et al., 2013a).

Because metals are synthesized and released from stars located in very overdense environments, that they need to travel large distances to reach the diffuse IGM, and this transport is likely driven by feedback from star formation and active galactic nuclei (AGN). Although the need for inclusion of these processes in simulations is clear, the mechanisms responsible are not resolved even in state-of-the-art cosmological simulations, making their implementation uncertain. By comparing observed and theoretical metal-line absorption in the IGM, we may be able to constrain enrichment mechanisms such as outflows.

Models and simulations of the IGM have been used to make predictions about sources of metal pollution. Booth et al. (2012) determined that the observations of (Schaye et al., 2003) of Civ associated with weak Hi at $z \sim 3$ can only be explained if the low-density IGM has been enriched primarily by low-mass galaxies ($M_{halo} \leq 10^{10} M_\odot$) that drive outflows to distances of $\sim 10^2$ proper kiloparsecs (pkpc). They calculated that $> 10\%$ of the simulated volume and $> 50\%$ of the baryonic mass in their successful model was polluted by metals. The simulations studied in Wiersma et al. (2010) predicted that at least half of the metals found in the $z = 2$ IGM were ejected from galaxies at $z \geq 3$, and that these galaxies had masses less than $M_{halo} = 10^{11} M_\odot$. This picture is consistent with observations by Simcoe et al. (2004), who estimate that half of all baryons are enriched to metallities $> 10^{-3.5} Z_\odot$ by $z \sim 2.5$.

Studies of the IGM using the direct detection of individual metal lines can typically only probe highly overdense gas, which constitutes a very small volume fraction of the Universe. In this work, we employ an approach known as the pixel optical depth method (Cowie & Songaila, 1998; Ellison et al., 2000; Schaye et al., 2000a; Aguirre et al., 2002; Schaye et al., 2003). This technique is a valuable tool for studying the IGM, as it allows us to detect metals statistically even in low-density gas. At the redshifts studied in this work, direct detection of metal-line absorption in regions of the spectrum contaminated by Hi is nearly impossible due to the density of the forest. Instead, by using the pixel optical depth method we can correct for contamination and derive statistical properties of absorption by metals in this region. Another advantage of this technique is that it is fast and objective, and thus can be applied uniformly to both observations and simulations.

We apply the pixel optical depth method to both observations and simulations. Our observational sample consists of new spectra of eight $3.62 \leq z \leq 3.922$ QSOs with uniform coverage and high signal-to-noise (S/N). We compare the results to the Evolution and Assembly of Galaxies and their Environments (EAGLE) cosmological hydrodynamical simulations (Schaye et al., 2015; Crain et al., 2015). The EAGLE simulations are ideal for studying metal-line absorption in the IGM, as they have been run at high resolution in a cosmologically representative volume (2×1504^3 particles in a 100 cMpc box). EAGLE has been demonstrated to be in good agreement with a number of relevent observables, including the properties of Hi absorption at $z \sim 2$–3 (Rahmati et al., 2015) and Ovi and Civ column density distribution functions at $z \sim 0$ (Schaye et al., 2015). Furthermore, the simulations reproduce the present-day galaxy stellar mass function, galaxy sizes and the Tully Fisher relation (Schaye et al., 2015), and have been found to match observations of galaxy colours (Trayford et al., 2015) and the evolution of galaxy stellar masses (Furlong et al., 2015).

This paper is structured as follows. In § 5.2, we describe the observations and simulations. We also summarize the pixel optical depth method, and how it is applied. The results are presented in § 5.3, and we give a discussion and conclusions in § 5.4 and 5.5, re-

spectively. Throughout this work, we denote proper and comoving distances as pMpc and cMpc, respectively. Both simulations and observations use cosmological parameters determined from the Planck mission (Planck Collaboration et al., 2013), i.e. $H_0 = 67.1\,\mathrm{km\,s^{-1}\,Mpc^{-1}}$, $\Omega_m = 0.318$, and $\Omega_\Lambda = 0.683$.

5.2 Method

5.2.1 Observations

We analyze a sample of eight QSOs with $3.62 \leq z_{QSO} \leq 3.922$. They were selected based on their redshift and the existence of substantial, high S/N data taken with VLT/UVES. Initially, there were already 76.0 hours of UVES data, excluding overheads, of the QSOs. Follow-up observations to fill in the gaps and improve S/N were completed in 62.7 hours of on-source time in programmes 091.A-0833(A), 092.A-0011(A) and 093.A-0575(A) (P.I. Schaye). We note that for Q1422+23, the gaps in the UVES data were filled using archival observations with Keck/HIRES of comparable S/N and resolution (which is $\approx 8.5\,\mathrm{km\,s^{-1}}$). The properties of the QSOs and the S/N of the spectra are summarized in Table 5.1.

The reduction of the UVES data was performed using the `UVES-headsort` and `UVES-popler` software by Michael T. Murphy, and binned to have a uniform velocity dispersion of $1.3\,\mathrm{km\,s^{-1}}$. The HIRES data was reduced using T. Barlow's MAKEE package, and binned on to $2.8\,\mathrm{km\,s^{-1}}$ pixels. The continuum fits for the spectra were performed by hand. Any DLAs or Lyman break regions (i.e., due to strong absorbers in H I) were masked out, with the exception of DLAs in the Lyα forest, which were unmasked when recovering the H I to be used for subtraction of contaminating absorption by higher-order Lyman series lines from O VI and C III optical depths.

To homogenize the continuum fitting errors, we implemented the automated continuum fitting procedure of Schaye et al. (2003) at wavelengths greater than that of the QSO's Lyα emission, which was applied to both the observed and simulated spectra. The spectrum is divided into rest-frame bins of $\Delta\lambda = 20$ Å, which have central wavelength λ_i and median flux $\bar{f}_i$. A B-spline is then interpolated through $\bar{f}_k$, and pixels with flux $N_\sigma^{cf} \times \sigma$ below the interpolated values are discarded, where σ is the normalized noise array. We then recalculate $\bar{f}_k$ without the discarded pixels, and repeat the procedure until convergence is reached. We use $N_\sigma^{cf} = 2$, which has been shown to be optimal in the C IV region for spectra with a quality similar to ours, as it induces errors that are smaller than the noise by at least an order of magnitude (Schaye et al., 2003).

5.2.2 Simulations

We compare the observations to predictions from the EAGLE cosmological hydrodynamical simulations. EAGLE was run with a substantially modified version of the *N*-body TreePM smoothed particle hydrodynamics (SPH) code `GADGET 3` (last described in Springel 2005). EAGLE uses the hydrodynamics algorithm "Anarchy" (Dalla Vecchia, in prep.; see Appendix A1 of Schaye et al. 2015) which invokes the pressure-entropy formulation of SPH from Hopkins (2013) and the time-step limiter from Durier & Dalla Vecchia (2012). The fiducial EAGLE model is run in a 100 cMpc periodic box with 1504^3 of both dark matter

Table 5.1: Properties of the QSOs used in this work, and the median S/N in the Hɪ Lyα and Cɪv recovery regions. The columns list, from left to right, name, R.A., Dec, redshift, magnitude from Véron-Cetty & Véron (2010), and S/N in the Lyα forest region and Cɪv region, respectively (see § 5.2.3 for the definition of these regions).

| Name	R.A.	Dec	z_{QSO}	Mag	S/N$_{Lyα}$	S/N$_{CIV}$
Q1422+23	14:24:38	+22:56:01	3.620	16.5	87	82
Q0055−269	00:57:58	−26:43:14	3.655	17.47	60	79
Q1317−0507	13:20:30	−18:36:25	3.700	16.54	59	90
Q1621−0042	16:21:17	−23:17:10	3.709	17.23	78	92
QB2000−330	20:03:24	−32:51:44	3.773	18.4	105	83
PKS1937−101	19:39:57	−13:57:19	3.787	19.0	96	64
J0124+0044	01:24:03	+00:44:32	3.834	17.90	48	59
BRI1108−07	11:11:13	−15:55:58	3.922	18.10	29	29

and baryonic particles, and is denoted Ref-L1001504. To test convergence with resolution and box size, runs varying the number of particles and box size were also completed, and are listed in Table 5.2.

The stellar feedback in EAGLE is implemented as in Dalla Vecchia & Schaye (2012), where thermal energy is imparted stochastically. While the temperature of heated particles is always increased by $10^{7.5}$ K, the probability varies with the local metallicity and density (Schaye et al., 2015; Crain et al., 2015). The simulations include thermal AGN feedback (Booth & Schaye, 2009), also implemented stochastically (Schaye et al., 2015). Both stellar and AGN feedback have been calibrated such that the simulations match the observed $z \sim 0$ stellar mass function and galaxy–black hole mass relation, and give sensible disk-galaxy sizes. We note that of the two highest-resolution runs, Ref-L025N072 has been realized with the same subgrid parameters used in the fiducial model, while for the Recal-L025N072 the subgrid parameters were re-calibrated to better match the observed galaxy stellar mass function.

EAGLE also includes a subgrid model for photo-heating and radiative cooling via eleven elements: hydrogen, helium, carbon, nitrogen, oxygen, neon, magnesium, silicon, sulphur, calcium and iron (Wiersma et al., 2009a), assuming a Haardt & Madau (2001) UV and X-ray background. Star formation is implemented with a gas metallicity-dependent density threshold (Schaye, 2004) as described in Schaye & Dalla Vecchia (2008), followed by stellar evolution and enrichment from Wiersma et al. (2009b). Finally, details of the subgrid model for black-hole seeding and growth can be found in Springel et al. (2005); Rosas-Guevara et al. (2013) and Schaye et al. (2015).

For each of our eight observed QSOs, we synthesize 100 corresponding mock spectra using the SPECWIZARD package by Schaye, Booth, and Theuns (implemented as described in Appendix A4 of Theuns et al. 1998). To create mock spectra that resemble the observed QSOs and whose absorption features span a large redshift range, we follow Schaye et al. (2003) and stitch together the physical state of the gas taken from uncorrelated sightlines from snapshots with different redshifts. The ionization balance of each gas particle is estimated using interpolation tables generated from Cloudy (Ferland et al., 2013, version 13.03) assuming uniform illumination by a QSO+galaxy Haardt & Madau (2001) ultra-violet background (UVB). Self-shielding for Hɪ was included by modifying the ionization fraction using the fitting functions of Rahmati et al. (2013a). The normalization of the UVB
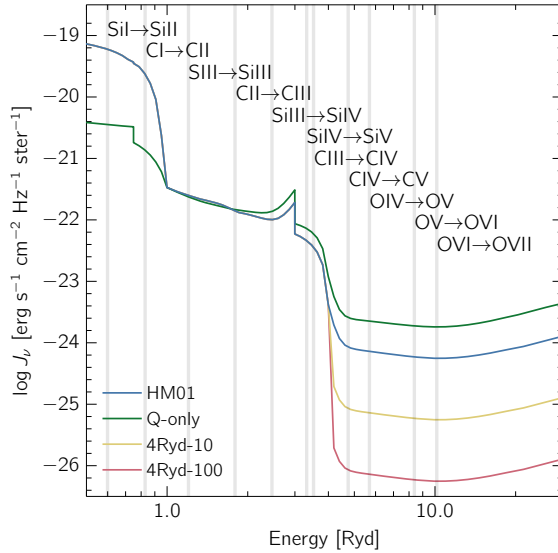
Figure 5.1: The intensity as a function of energy for the different UVB models. The different models are: HM01 QSO+galaxy (Haardt & Madau, 2001), which is our fiducial model; Q-only, which is also by Haardt & Madau (2001) but only considers an ionizing contribution from QSOs; and 4Ryd-10 (4Ryd-100), the same as the fiducial model except that the intensity is reduced by a factor of 10 (100) above 4 Ryd. The vertical light grey lines indicate the ionization energies of ions of interest. All of the UVBs have been normalized to have the same intensity as HM01 at 1 Ryd.

is set such that the median recovered H I Lyα optical depth of the simulated QSOs agrees with that of the observations. In the EAGLE simulations, the dense particles that represent the multiphase interstellar medium are not allowed to cool below an effective equation of state. We set their temperatures to 10^4 K when generating the mock spectra, although we note that due to the small cross section of such dense absorbers the effect of including them is negligible.

We set the simulated QSO redshifts to be identical to those of the observed sample, and we we consider absorption ranging from $1.5 < z < z_{QSO}$ in every case. We include contributions from from 31 H I Lyman series transitions beginning with Lyα, and metal-line absorption from C II, C III, C IV, Fe II, N V, O VI, Si II, Si III, and Si IV. To match the observations, the simulated spectra are convolved with a Gaussian with a FWHM=6.6 km s^{-1}, and resampled on to pixels of 1.3 km s^{-1}. For each observed QSO, we have measured the noise as a function of wavelength and normalized flux, and generated random Gaussian noise with the same variance, which is applied to the simulations.

In addition to using a QSO+galaxy Haardt & Madau (2001) UVB (which we denoted as "HM01"), we examine alternatives to the fiducial model, and have plotted their intensity as a function of energy at $z = 3.5$ in Fig. 5.1. We also consider the Haardt & Madau (2001) background using quasars only ("Q-only"), which which is much harder than the fiducial

Table 5.2: Characteristics of the EAGLE simulations. From left to right, the columns list the simulation name, box size, number of particles, initial baryonic particle mass, dark matter particle mass, comoving (Plummer-equivalent) gravitational softening, and maximum physical softening.

Simulation	L	N	m_{b}	m_{dm}	$\varepsilon_{\mathrm{com}}$	$\varepsilon_{\mathrm{prop}}$
	[cMpc]		[$M_\odot$]	[$M_\odot$]	[ckpc]	[pkpc]
Ref-L100N1504	100	2×1504^3	1.81×10^6	9.70×10^6	2.66	0.70
Ref-L050N0752	50	2×752^3	1.81×10^6	9.70×10^6	2.66	0.70
Ref-L025N0376	25	2×376^3	1.81×10^6	9.70×10^6	2.66	0.70
Ref-L025N0752	25	2×752^3	2.26×10^5	1.21×10^6	1.33	0.35
Recal-L025N0752	25	2×752^3	2.26×10^5	1.21×10^6	1.33	0.35

model above ~ 4 Ryd. Furthermore, to explore the possible effects of a delayed He II reionization, we consider UVBs that are significantly softer above 4 Ryd. To implement this, we use the QSO+galaxy model and reduce the intensity above 4 Ryd by a factor of 10 (100), which we denote as "4Ryd-10" ("4Ryd-100").

5.2.3   Redshift range

The first step for the pixel optical depth recovery involves choosing optimal redshift limits. The fiducial redshift range is selected to lie in the Lyα forest, defined to be:

$$(1 + z_{\mathrm{qso}})\frac{\lambda_{\mathrm{Ly}\beta}}{\lambda_{\mathrm{Ly}\alpha}} - 1 \leq z \leq z_{\mathrm{qso}} - (1 + z_{\mathrm{qso}})\frac{3000\,\mathrm{km\,s}^{-1}}{c} \qquad (5.1)$$

where $\lambda_{\mathrm{Ly}\alpha} = 1215.7$ Å and $\lambda_{\mathrm{Ly}\beta} = 1025.7$ Å are the H I Lyα and Lyβ rest wavelengths, respectively. The lower limit was chosen to avoid the Lyβ forest and corresponds to the Lyβ transition at the redshift of the QSO, while the upper limit is 3000 km s^{-1} bluewards of the QSO redshift to avoid any proximity effects.

For H I, C IV ($\lambda_{\mathrm{rest}} = [1548.2, 1550.8]$ Å) and C III ($\lambda_{\mathrm{rest}} = 977.0$ Å) we use the above redshift limits. For the remaining ions, we make slight modifications, listed below, in order to homogenize the contamination. We use the notation $\lambda_{Z,k}$ which represents the rest wavelength of multiplet component k of the ion Z.

1. O VI ($\lambda_{\mathrm{rest}} = [1031.9, 1037.6]$ Å): We limit the recovery to where O VI overlaps with the Lyβ forest and place a cut-off at the Lyα forest region, which leads to $z_{\mathrm{max}} = (1 + z_{\mathrm{qso}})\lambda_{\mathrm{H I, Ly}\beta}/\lambda_{\mathrm{O VI},2} - 1$

2. Si III ($\lambda_{\mathrm{rest}} = 1206.6$ Å): We constrain the recovered optical depth region to not extend outside of the Lyα forest. For Si III, which extends slightly bluewards into the Lyβ forest, we set $z_{\mathrm{min}} = (1 + z_{\mathrm{qso}})\lambda_{\mathrm{Ly}\beta}/\lambda_{\mathrm{Si III}}$.

3. Si IV ($\lambda_{\mathrm{rest}} = [1393.8, 1402.8]$ Å): To avoid contamination by the Lyα forest, we limit the blue end of the Si IV recovery by setting $z_{\mathrm{min}} = (1 + z_{\mathrm{qso}})\lambda_{\mathrm{Ly}\alpha}/\lambda_{\mathrm{Si IV},1} - 1$.

5.2.4   Pixel optical depth method

We employ the pixel optical depth method, which we use to study absorption on an individual pixel basis rather than by fitting Voigt profiles to individual lines. The goal is to

obtain statistics on absorption by HI and various metal ions in the IGM, and on how their absorption relates to one another. Our implementation is close to that of Aguirre et al. (2002), but with the improvements of Turner et al. (2014). The exact methodology is described in full detail in Appendix A of Turner et al. (2014), and we summarize it here.

After restricting the redshift range, the first step is to convert the flux of every pixel of ion Z and multiplet component k to an optical depth $\tau_{Z,k}(z) = -\ln(F)$, where $F(\lambda)$ is the normalised flux at $\lambda = \lambda_k(1 + z)$. Then, depending on the ion, corrections are made for saturation or contamination, as described below.

1. For HI Lyα, while there is very little contamination in the Lyα forest, the absorption in many of the pixels will be saturated, and we use the higher order Lyman series transitions to correct for this. Specifically, if we consider a Lyα pixel to be saturated, we look to $N = 16$ higher-order Lyman lines (beginning with HI Lyβ), and take the minimum optical depth, scaled to that of Lyα, of all unsaturated pixels at the same redshift (if any). If we are unable to correct the pixel due to saturation of the higher-order transitions, we set it to a flag value of 10^4. Finally, we search for and discard any contaminated pixels, by checking that higher-order transitions do not have optical depth values significantly below what would be expected from the scaled HI Lyα optical depth.

2. For OVI and CIII, we can use the corrected HI Lyα optical depths to estimate and subtract contamination by HI. We do so beginning with HI Lyβ ($N = 2$) and use higher-order Lyman series orders up to $N = 5$. For saturated OVI and CIII pixels, the optical depth is not well defined and therefore the above subtraction is not performed. Instead, we leave the pixel uncorrected, unless the saturation can be attributed to HI, in which case the pixel is discarded.

3. SiIV and OVI are both closely-spaced doublets, and we can use this fact to correct for contamination. To do so, we scale the optical depth of the weak component to match that of the strong component, and take the minimum of the two components modulo noise. We only take the scaled optical depth of the weaker component if it is significantly lower (when taking into account the noise array) than the stronger component.

4. For CIV, which is a strong transition redward of the Lyα forest, the largest source of contamination is by its own doublet. To correct for this, we perform an iterative self-contamination correction. We first discard any pixels determined to be contaminated by other ions, by checking whether the optical depth of a pixel is too high to be explained by half of the associated stronger component combined with twice the associated weaker component. We then subtract the estimated contribution of the weaker component from each pixel, iterating until convergence is reached.

5.2.5 Analysis

For the analysis, we would like to see how the absorption from one ion varies with that from another. The procedures used here are also described in § 3.4 and 4.2 of Aguirre et al.
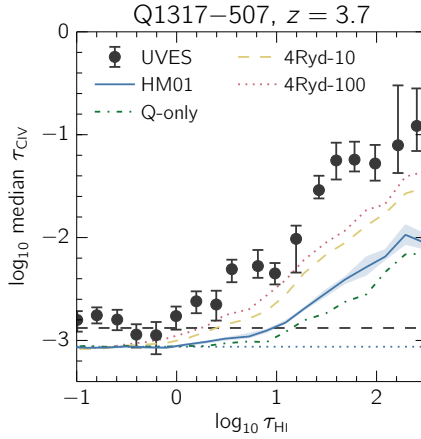
Figure 5.2: Example analysis of the CIV(HI) relation for Q1317−507. The observations are shown by the points and the simulations by the solid curves, with the different colours representing variations in the UVB. 1σ errors are indicated by the bars (shaded region) for the observations (fiducial simulation), and were determined by bootstrap resampling spectral chunks (mock spectra). We indicate $\tau_{\min}$ by the horizontal dashed and dotted lines for the observations and simulations, respectively.

(2004). As an illustrative example, we will consider the ions CIV and HI. For a single observed QSO, we use the recovered pixel optical depths to construct a set of pixel pairs where each pair shares the same redshift. We then divide the ions into bins of $\log \tau_{\rm HI}$, and take the median $\tau_{\rm HI}$ and $\tau_{\rm CIV}$ in each bin, to obtain $\tau_{\rm CIV}^{\rm med}(\tau_{\rm HI})$, which from this point forward we will denote as CIV(HI). The result of this procedure applied to one of our QSOs is shown in Fig. 5.2, and we briefly describe the characteristics here.

We make note of two different regimes within the CIV(HI) relation. The first is on the right-hand side of Fig. 5.2, where $\tau_{HI} \gtrsim 1$. Here, the median CIV optical depth increases with HI, which indicates that the pixels are probing gas enriched by CIV. The value of $\tau_{\rm CIV}^{\rm med}$ constrains the number density ratio of CIV to HI. Next, we turn to the region with $\tau_{HI} \lesssim 1$, where $\tau_{\rm CIV}^{\rm med}$ is approximately constant. This behaviour arises because the median CIV optical depths reach values below the flat level $\tau_{\min}$, which is essentially a detection limit set by noise, contamination, and/or continuum fitting errors. An important caveat to keep in mind throughout this work is that the median recovered metal-line optical depth is not necessarily representative of *typical* intrinsic pixel optical depths for a given HI bin. In particular, as the metal-line optical depths approach the flat level, it is likely that many individual pixels in a given HI bin have intrinsic metal optical depths at or below the flat level itself. In this case, the median recovered metal optical depth will be determined by the fraction of pixels that have optical depths above the flat level.

To construct the CIV(HI) relation for the observed spectra, HI bins containing fewer than 25 pixels total, are discarded. Furthermore, we divide each spectrum into chunks of 5 Å, and discard any bins containing fewer than 5 unique chunks. To measure errors on $\tau_{\rm CIV}^{\rm med}$, we create new spectra by bootstrap resampling the chunks 1000 times with replace-

ment. We then measure CIV(HI) for each bootstrap realization of the spectrum and take the error in each τ_{HI} bin to be the 1σ confidence interval of all realizations.

For the simulated spectra, we measure CIV(HI) for each mock spectrum, and require that each τ_{HI} bin have at least 5 pixels in total. Next, we combine the results for all 100 mock spectra associated with a single observed QSO by measuring the median CIV optical depth in each τ_{HI} bin for all spectra, and we discard any bin containing contributions from fewer than 5 spectra. Errors are calculated by bootstrap resampling the spectra 1000 times.

Next, we compute the flat levels τ_{min}, by taking the median of all pixels that have $\tau < \tau_c$, and take $\tau_c = 0.1$ when binning in HI, and 0.01 when binning in CIV and SiIV. To estimate the error on τ_{min}, for the observations we again divide the spectrum into 5 Å chunks, measure τ_{min} for 1000 bootstrap realizations, and take the 1σ confidence interval. For the simulations, we calculate τ_{min} for each spectrum, and take the final value to be the median value from all 100 spectra.

Finally, we would like to combine the results from the different QSOs. Because our sample is uniform in terms of S/N, we simply combine the binned data points directly without subtracting τ_{min}. However, because the implementation of the noise, continuum fitting errors and contamination in simulations is not completely accurate, the flat levels differ from the observations. To account for this offset, we linearly add the difference between flat levels ($\tau_{\mathrm{min}}^{\mathrm{obs}} - \tau_{\mathrm{min}}^{\mathrm{sims}}$) to the median optical depths in the simulations. We have verified that performing this step before the QSOs are combined does not modify the results. Next, to measure the combined median values, we perform χ^2 fitting of a single value of $\tau_{\mathrm{CIV}}^{\mathrm{med}}$ to all points in the bin, which is plotted against the central value of each HI bin (in contrast to the results from individual QSOs, which are plotted against the median of all HI pixel optical depths in each bin). We discard any data points that have contributions from fewer than four QSOs, and the 1σ errors are estimated by bootstrap resampling the QSOs. The combined results for CIV(HI) can be seen in the left panel of Fig. 5.3.

5.3 Results

We begin by examining relations involving metal-line optical depths against HI in Fig. 5.3, where we have plotted CIV(HI), SiIV(HI) and OVI(HI) from left to right. The grey points with error bars represent the observations, while the curves show results from simulations, with different colours indicating variations in the UVB model. The data from the observations is presented in Table 5.3.

These relations can potentially probe gas metallicity as a function of density, as explained below using CIV as an illustrative example. The equation for metallicity can be written as follows:

$$[\mathrm{C/H}] = \log_{10} \frac{\tau_{\mathrm{CIV}}}{\tau_{\mathrm{HI}}} \frac{(f\lambda)_{\mathrm{HI}}}{(f\lambda)_{\mathrm{CIV}}} \frac{n_{\mathrm{C}}}{n_{\mathrm{CIV}}} \frac{n_{\mathrm{HI}}}{n_{\mathrm{H}}} - (\mathrm{C/H})_\odot, \tag{5.2}$$

where f and λ are the oscillator strength and rest wavelength. While $\tau_{\mathrm{CIV}}/\tau_{\mathrm{HI}}$ can be measured from the data, $n_{\mathrm{C}}/n_{\mathrm{CIV}}$ and $n_{\mathrm{HI}}/n_{\mathrm{H}}$ need to be estimated. If the gas being probed is photoionized, which has been found to be a reasonable assumption for CIV and SiIV (Schaye et al., 2003; Aguirre et al., 2004), then HI is considered a good tracer of the density (Schaye, 2001), even on an individual pixel basis (Aguirre et al., 2002). Thus, fixing the gas
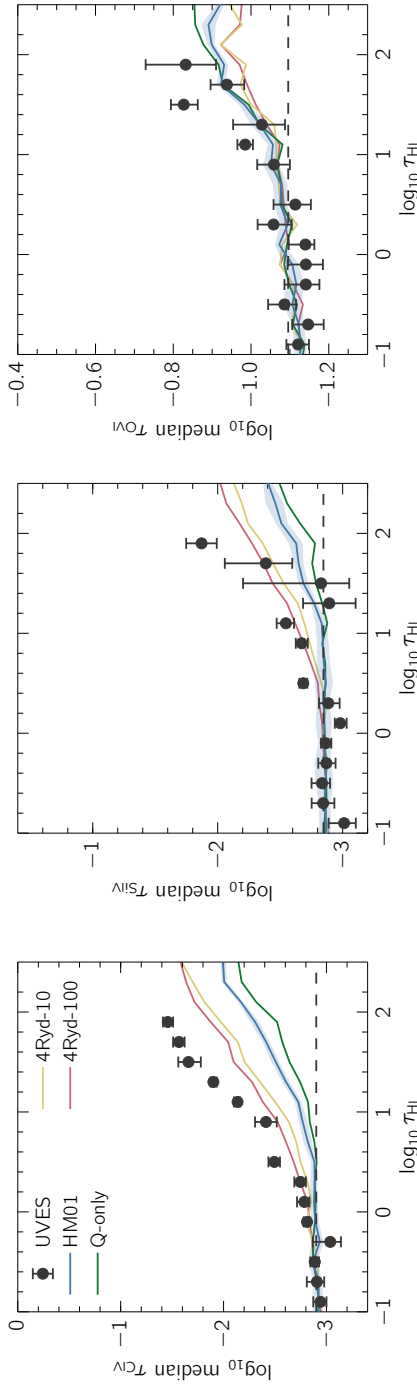
Figure 5.3: Median recovered pixel optical depths binned by H I for C IV (right), Si IV (centre) and O VI (right). The data from eight QSOs have been combined, and the 1σ error bars are measured by bootstrap resampling the QSOs. The black circles show the data, while the curves denote the results from simulations, where different colours represent variations in the UVB and we show the 1σ error region around the fiducial HM01 model. The median τ_{min}, which is the same for the observations and simulations by construction, is indicated by the dashed horizontal line. The data from the observations is provided in Table 5.3. We find that the simulation run with the fiducial UVB systematically underpredicts the median C IV and Si IV optical depths. The discrepancy is lessened by invoking a softer UVB (4Ryd-10 and 4Ryd-100), although the metal optical depths associated with the strongest H I absorption is still underestimated by ~ 0.5 dex. In contrast, the predicted O VI(H I) relation (right panel) is insensitive to the UVB models, and in good agreement with the observations.

Table 5.3: Observational data shown in Fig. 5.3. The left column indicates the central $\log_{10} \tau_{\rm HI}$ value of each bin, and the next three columns list the $\log_{10}$ median recovered optical depths for the $C_{IV}(H_I)$, $Si_{IV}(H_I)$, and $O_{VI}(H_I)$ relations, respectively, along with the 1σ errors. We also show the median $\log_{10} \tau_{\rm min}$ of the eight QSOs in the row where $\log_{10} \tau_{\rm bin} = -9.0$.

$\log_{10} \tau_{\rm bin}$	$C_{IV}(H_I)$	$Si_{IV}(H_I)$	$O_{VI}(H_I)$
-9.00	-2.90	-2.85	-1.10
-0.90	$-2.94^{+0.07}_{-0.06}$	$-3.01^{+0.12}_{-0.09}$	$-1.12^{+0.03}_{-0.03}$
-0.70	$-2.91^{+0.10}_{-0.07}$	$-2.84^{+0.09}_{-0.09}$	$-1.15^{+0.04}_{-0.04}$
-0.50	$-2.89^{+0.04}_{-0.04}$	$-2.83^{+0.08}_{-0.06}$	$-1.09^{+0.04}_{-0.03}$
-0.30	$-3.04^{+0.17}_{-0.10}$	$-2.87^{+0.07}_{-0.07}$	$-1.14^{+0.06}_{-0.04}$
-0.10	$-2.81^{+0.03}_{-0.03}$	$-2.87^{+0.04}_{-0.04}$	$-1.14^{+0.05}_{-0.04}$
0.10	$-2.79^{+0.07}_{-0.05}$	$-2.98^{+0.04}_{-0.05}$	$-1.14^{+0.04}_{-0.02}$
0.30	$-2.75^{+0.06}_{-0.05}$	$-2.88^{+0.07}_{-0.09}$	$-1.06^{+0.04}_{-0.04}$
0.50	$-2.49^{+0.06}_{-0.05}$	$-2.69^{+0.03}_{-0.03}$	$-1.11^{+0.06}_{-0.04}$
0.70	…	…	…
0.90	$-2.41^{+0.11}_{-0.10}$	$-2.67^{+0.05}_{-0.05}$	$-1.06^{+0.04}_{-0.04}$
1.10	$-2.14^{+0.04}_{-0.03}$	$-2.55^{+0.07}_{-0.07}$	$-0.98^{+0.02}_{-0.02}$
1.30	$-1.90^{+0.03}_{-0.03}$	$-2.89^{+0.21}_{-0.21}$	$-1.03^{+0.07}_{-0.06}$
1.50	$-1.66^{+0.10}_{-0.12}$	$-2.83^{+0.62}_{-0.22}$	$-0.83^{+0.03}_{-0.04}$
1.70	$-1.57^{+0.06}_{-0.05}$	$-2.38^{+0.33}_{-0.21}$	$-0.94^{+0.04}_{-0.04}$
1.90	$-1.46^{+0.05}_{-0.05}$	$-1.87^{+0.12}_{-0.12}$	$-0.83^{+0.10}_{-0.08}$

temperature at 2×10^4 K (typical for a moderately overdense IGM region, e.g. Schaye et al. 2000b; Lidz et al. 2010; Becker et al. 2011), we can estimate the gas density from $\tau_{\rm HI}$ using equation 5 of Turner et al. (2015).

With the density and temperature fixed, the the ionization fractions of H_I and C_{IV} can be predicted from `Cloudy` ionization modelling. Therefore, equation 5.2 illustrates that at fixed $\tau_{\rm HI}$, the metallicity will only depend on $\log_{10} \tau_{\rm CIV}$ under these assumptions. Thus, in the left panel of Fig. 5.3 where we examine the $C_{IV}(H_I)$ relation, if our assumption of photoionization equilibrium holds then a higher C_{IV} at fixed H_I will correspond to a higher metallicity at fixed density.

In the following analysis, we will consider the results in two different regimes, separated by $\tau_{\rm HI} \sim 10$. The reasons for this are: (1) if the gas being probed is mainly in photoionization equilibrium, then higher H_I optical depths will be probing dense regions closer to galaxies, rather than the diffuse IGM, and (2) in this regime the H_I pixel optical depths will be highly saturated, and even though this is corrected for in our recovery procedure, the final values still suffer from large uncertainties compared to their unsaturated counterparts

With the above in mind, we can interpret the results of Fig. 5.3. First focusing on the left panel, we find that at fixed H_I, the observed median C_{IV} optical depths are significantly higher than in the fiducial UVB simulations. The discrepancy increases from ~ 0.1 dex at $\tau_{\rm HI} = 1$ to ~ 0.5 dex at $\tau_{\rm HI} = 10$ and ~ 1 dex at $\tau_{\rm HI} = 10^2$. This suggests that at a given gas overdensity, the carbon abundance in the simulations could be lower than that of the observations by up to ~ 0.5 dex (~ 1.0 dex) for $\tau_{\rm HI} \lesssim 10$ ($\tau_{\rm HI} \gtrsim 10$). Next, we examine different UVB models. While the harder Q-only background provides a worse match to the observations, 4Ryd-10 and 4Ryd-100 fare much better. Although these models still fall short of the observed $\tau_{\rm CIV}^{\rm med}$ by about ~ 0.5 dex in the highest $\tau_{\rm HI}$ bin, the softest background

is nearly fully consistent with the observations for $\tau_{\rm HI} \lesssim 10$.

In the centre panel of Fig. 5.3, we show SiIV(HI), and find results that are qualitatively similar to those for CIV(HI), but with overall better agreement between the simulations and observations. While for $\tau_{\rm HI} \gtrsim 10$ the SiIV optical depths are underestimated by the fiducial UVB simulations by a factor ranging from ~ 0.2 dex at $\tau_{\rm HI} = 10$ up to ~ 0.8 dex at $\tau_{\rm HI} = 10^2$, below this threshold the discrepancy only reaches ~ 0.1 dex. Invoking the softest UVB model leads to near agreement for all but the highest HI optical depth.

Next, we consider the OVI(HI) relation in the right panel of Fig. 5.3. While CIV and SiIV are expected to mainly probe cool photoionized gas, OVI reaches its peak ionization fraction of 0.2 at $T = 3 \times 10^5$ K, which is close to temperatures expected of shocks associated with accretion events or winds. Simulations predict that OVI around massive galaxies resides primarily in collisionally ionized gas (e.g. Stinson et al., 2012; Ford et al., 2013; Shen et al., 2013). Applying ionization modelling to observations also provides evidence that OVI near strong HI can probe this hot gas phase (e.g, Aguirre et al., 2008; Danforth & Shull, 2008; Savage et al., 2014; Turner et al., 2015).

Indeed, the results from the right panel of Fig. 5.3 differ considerably from the previous two relations. Firstly, the simulation realized with the fiducial UVB is almost fully consistent with the observations, with any discrepant points offset by a maximum of 0.2 dex (note the smaller dynamic range of the y-axis compared to the previous panels). Furthermore, while the alternate UVBs have slightly lower $\tau_{\rm OVI}$ than the fiducial model, overall we do not find significant differences between the models. This suggests that in EAGLE the OVI(HI) relation may be probing a primarily collisionally ionized gas phase, where variations in the ionization background do not have a significant impact on the results. We note that if the pixel optical depths do not originate predominantly from photoionized gas, then $\tau_{\rm HI}$ can no longer be used as a measure of the density.

While metal ions as a function of $\tau_{\rm HI}$ can probe the metallicity-density relation, examining different ionization states of a single element can the physical properties of the gas, because the ionization fractions that set the relative optical depths will only depend on the temperature, the density, and the UV radiation field (but not on the metallicity). These optical depth ratios have previously been used to determine that the gas probed by CIV and SiIV is consistent with being in photoionization equilibrium (Schaye et al., 2003; Aguirre et al., 2004).

Fig. 5.4 examines CIII(CIV) and SiIII(SiIV), and the observational data is provided in Table 5.4. Looking first at CIII(CIV), we find that HM01 is consistent with all of the CIV bins, while the remaining models fall short of the highest point. We also see that for this relation, the harder Q-only background is favoured compared to the softer variations. The 4Ryd-100 model does particularly poorly, and differs from the observations by up to 0.4 dex. Next, we find the SiIII(SiIV) relation to be somewhat less constraining. While the HM01 model presents the largest discrepancy with the data, the difference is not more than ~ 0.1 dex when the errors are considered, and is only seen in the highest SiIV bins. Indeed, SiIII overlaps mainly with the Lyα forest and we do not perform any contamination correction, so we consider it more uncertain than CIII. Thus, we find good agreement between the data and the fiducial UVB model for both relations, which suggests that the temperature and density of the gas probed by CIV and SiIV pixels is consistent between the observations and simulations.

In Fig. 5.5 we examine relations between different metal ions, which trace relative abun-
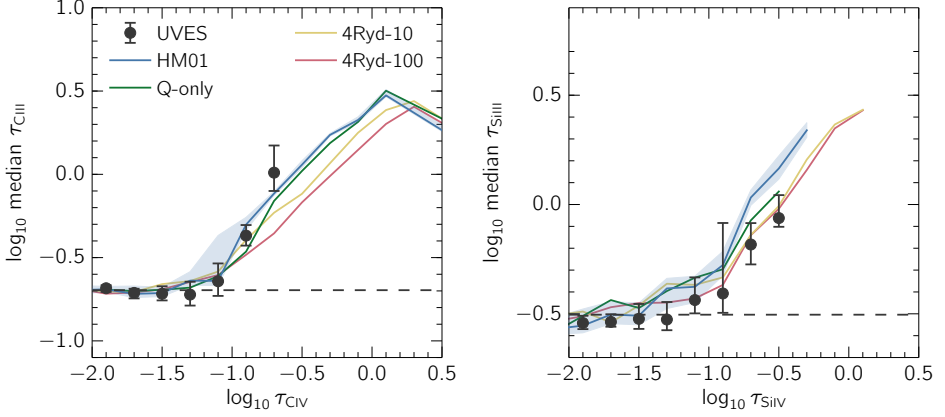
Figure 5.4: The same as Fig. 5.3, but showing CIII(CIV) and SiIII(SiIV), and with the data from observations presented in Table 5.4. Unlike for relations binned by HI, different ionization states of the same element are not sensitive to the metallicity of the gas. We find that for CIII(CIV), the simulations and data are in good agreement for the fiducial ionizing background, and the observations particularly disfavour the softest UVBs. The SiIII(SiIV) relation is somewhat less constraining, and while the median SiIII optical depths from HM01 model are slightly above the observed values, the discrepancy is no more than 0.1 dex and only seen in the highest SiIV bins. This indicates that the temperature and density of the gas probed by pixels with detected CIV and and SiIV is well captured by the simulations, without needing to invoke modifications to the ionizing background.

Table 5.4: Observational data from Figs. 5.4 and 5.5. The format is the same as Table 5.3, but here we present relations binned by either CIV or SiIV optical depths. The left column indicates the central value of the CIV or SiIV bin, and the subsequent columns list the median recovered optical depths for the relation denoted in the top row. The row where $\log_{10} \tau_{bin} = -9$ provides the median $\log_{10} \tau_{min}$ of the eight QSOs.

$\log_{10} \tau_{bin}$	CIII(CIV)	SiIII(SiIV)	SiIV(CIV)	OVI(CIV)	OVI(SiIV)
−9.00	−0.70	−0.50	−2.78	−1.06	−1.10
−1.90	$-0.68^{+0.02}_{-0.02}$	$-0.54^{+0.03}_{-0.03}$	$-2.84^{+0.03}_{-0.03}$	$-1.17^{+0.08}_{-0.05}$	$-1.12^{+0.03}_{-0.04}$
−1.70	$-0.71^{+0.03}_{-0.03}$	$-0.54^{+0.04}_{-0.02}$	$-2.82^{+0.05}_{-0.06}$	$-1.07^{+0.03}_{-0.03}$	$-1.10^{+0.03}_{-0.02}$
−1.50	$-0.72^{+0.04}_{-0.04}$	$-0.52^{+0.07}_{-0.05}$	$-2.64^{+0.05}_{-0.04}$	$-1.02^{+0.02}_{-0.02}$	$-1.08^{+0.04}_{-0.04}$
−1.30	$-0.72^{+0.08}_{-0.07}$	$-0.53^{+0.08}_{-0.05}$	$-2.45^{+0.05}_{-0.05}$	$-1.05^{+0.04}_{-0.04}$	$-0.99^{+0.03}_{-0.05}$
−1.10	$-0.64^{+0.11}_{-0.09}$	$-0.44^{+0.10}_{-0.06}$	$-2.21^{+0.05}_{-0.05}$	$-0.95^{+0.02}_{-0.02}$	$-0.99^{+0.05}_{-0.04}$
−0.90	$-0.37^{+0.06}_{-0.06}$	$-0.41^{+0.32}_{-0.09}$	$-1.98^{+0.07}_{-0.05}$	$-1.00^{+0.15}_{-0.09}$	$-0.86^{+0.04}_{-0.03}$
−0.70	$0.01^{+0.16}_{-0.11}$	$-0.18^{+0.10}_{-0.09}$	$-1.57^{+0.18}_{-0.10}$	$-0.66^{+0.08}_{-0.07}$	$-0.81^{+0.29}_{-0.09}$
−0.50	...	$-0.06^{+0.10}_{-0.04}$	$-1.07^{+0.19}_{-0.20}$	$-0.43^{+0.03}_{-0.04}$	$-0.90^{+0.54}_{-0.15}$
−0.30	...	...	$-1.87^{+0.36}_{-0.17}$	$-0.82^{+0.31}_{-0.09}$	...
−0.10	...	...	$-0.82^{+0.34}_{-0.01}$	$-0.40^{+0.04}_{-0.00}$	...
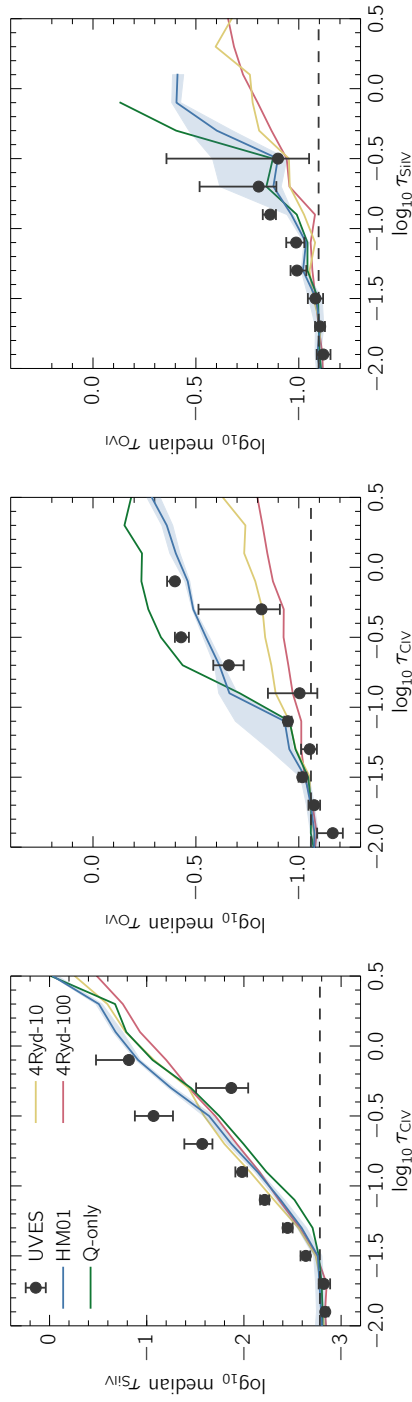
Figure 5.5: The same as Fig. 5.3, except showing Siɪv(Cɪv), Ovɪ(Cɪv) and Ovɪ(Siɪv) from left to right, which probe relative abundances. The data from the observations is given in Table 5.4. In the left panel, we find that $\tau_{\mathrm{SiIV}}^{\mathrm{med}}$ is underestimated by the simulations, and is insensitive to the choice of UVB. Next, for Ovɪ(Cɪv) and Ovɪ(Siɪv) we observe a stronger sensitivity to different ionizing background models compared to Ovɪ(Hɪ). For these relations, we observe a better match between the fiducial and hardest UVB models (HM01 and Q-only), in tension with the results from Cɪv(Hɪ) and Siɪv(Hɪ) relations, where we find a strong preference for the softer ionization backgrounds (see Fig. 5.3).

dances and physical conditions. The data for this figure is provided in Table 5.4. For example, Si/C, which can be estimated using the Si IV(C IV) relation, has been found to be greater than solar by a factor of a few (e.g., Songaila, 2001; Boksenberg et al., 2003; Aguirre et al., 2004). In the left panel of Fig. 5.5, we plot the median Si IV optical depth against C IV. While the results are not very sensitive to the choice of ionizing background, all UVB models present a paucity of Si IV with respect to the observations. Since [Si/C] is not fixed in the simulations, this may indicate that at $z \sim 3.5$ they have lower [Si/C] than observed.

We briefly draw attention to the bin centred at $\log_{10} \tau_{\mathrm{C IV}} = -0.3$, where the median Si IV optical depth deviates starkly from the rest of the points. The same behaviour is also seen in the central panel of Fig. 5.5, in which we examine O VI(C IV). To find the origin of this inconsistency, we turn to the relations of individual QSOs, in Figs. 5.13 and 5.14. In the case of Q1317−507 (the upper right panel of both figures), the median Si IV and O VI optical depths are unusually low in this C IV bin, while having relatively small error bars (the median optical depths of different QSOs are combined in linear space). We conclude that these points from Q1317−507, likely the result of small number statistics, are responsible for the anomaly in the Si IV(H I) and C IV(H I) relations.

The centre panel of Fig. 5.5 shows $\tau_{\mathrm{O VI}}^{\mathrm{med}}$ binned by $\tau_{\mathrm{C IV}}$. In contrast to the O VI(H I) relation (Fig. 5.3, right panel), it is apparent that the median O VI(C IV) optical depth depends strongly on the choice of UVB. This is consistent with the picture that C IV primarily traces photoionized gas, which will be sensitive to the ionizing background. We find that the fiducial HM01 model is most consistent with the data for this relation, even when including the bin centred at $\log_{10} \tau_{\mathrm{C IV}} = -0.3$. Finally, in the right panel of Fig. 5.5 we show O VI(Si IV). Except for $\log_{10} \tau_{\mathrm{Si IV}} \gtrsim -0.5$, we observe a much weaker sensitivity to UVB compared to O VI(C IV), but we still find that the fiducial model provides the best match to the data.

5.4   Discussion

In the previous section, we compared observations of pixel optical depth relations to the EAGLE simulations. We considered a fiducial QSO+galaxy HM01 UVB (Haardt & Madau, 2001), as well a harder QSO-only model, and two softer UVBs with reduced intensity above 4-Ryd by factors of 10 and 100, respectively. For O VI(H I), we found an insensitivity to the ionizing background model, and saw good agreement between the simulations and the data. However, the observed median optical depths from the C IV(H I) and Si IV(H I) relations were measured to be systematically higher than those derived from the simulations using the fiducial UVB. The discrepancy is found to be up to ~ 0.5 dex below $\tau_{\mathrm{H I}} = 10$ and up to 1 dex for H I bins above this threshold. For Si IV(H I), invoking the softest UVB (4Ryd-100) fully alleviates the tension, while for C IV(H I) we still find this model fall short of the data, but only for $\tau_{\mathrm{H I}} \gtrsim 10$. In this section, we would like to discuss possible reasons for this observed mismatch.

Can the discrepancies between the observations and simulations be attributed to differences in the UVB? We have indeed found better agreement with the observed C IV(H I) and Si IV(H I) relations using our softest UVBs, 4Ryd-10 and 4Ryd-100. The reduced intensity above 4 Ryd disfavours ionization to higher states, increasing the abundances of Si IV and C IV. The Haardt & Madau (2001) models take He II reionization into account, and predicts that the He III fraction already reaches 50% at $z \sim 6$. However, recent studies

suggest that the reionization process is patchy, with HeII optical depths still high above $z \gtrsim 3$ (e.g., Shull et al., 2010; Worseck et al., 2011). Thus, the work presented here probes the epoch where the observed gas may be subject to a heavily fluctuating UVB above 4 Ryd. The much better match of the 4Ryd-10 and 4Ryd-100 UVBs suggest that HeII reionization could be complete too early in the simulations. Turning to other optical depth relations, we find that CIII(CIV) and SiIII(SiIV) do not strongly rule out the 4Ryd-10 and 4Ryd-100 models. While these soft UVBs are inconsistent with OVI(CIV), it is only for bins where $\log_{10} \tau_{\mathrm{CIV}} \gtrsim -0.7$, which are higher than relevant for Fig. 5.3.

An alternative effect could be the presence of ionization due to stellar light from nearby galaxies, which is thought to be important for absorbers are rare as Lyman limit systems (Schaye, 2006; Rahmati et al., 2013b). The strength of the ionizing radiation emitted by galaxies drops sharply above 4 Ryd, but could strongly ionize HI, lowering the typical optical depths. If HI optical depths are lower, than at a fixed HI the metal line optical depths will be higher. This could explain the larger discrepancy seen at $\tau_{\mathrm{HI}} \gtrsim 10$, where the pixel optical depths are probing denser gas at small galactocentric distances compared to lower HI optical depths. However, since it is difficult to estimate the shape and normalization of this ionizing radiation (and it likely should not be applied uniformly), we leave testing of this explanation to a future work.

Another possibility is that the metallicity in the simulations is too low, and/or that the metals are not getting out far enough in the IGM. A too low metallicity or volume filling fraction of enriched gas could occur if the simulations are not resolving the low-mass galaxies thought to be important for metal pollution (e.g., Wiersma et al., 2010; Booth et al., 2012). In Appendix 5.A, we examined results from simulations with higher resolutions than our fiducial model (the Ref- and Recal-L025N0752 runs). These simulations can resolve galaxies (containing at least 100 star particles) with $M_\star = 2.3 \times 10^7$ M$_\odot$, almost an order of magnitude below that of our fiducial model, where a 100 star particle galaxy would have stellar mass of 1.8×10^8 M$_\odot$. Indeed, we find that relations involving CIV are not fully converged at our fiducial resolution, and invoking the highest-resolution model for CIV(HI) results in an increase in $\tau_{\mathrm{CIV}}^{\mathrm{med}}$ of up to ~ 0.3 dex in the highest HI bins. This result suggests that our fiducial simulation may be missing metals ejected from galaxies with stellar masses below $\sim 1.8 \times 10^8$ M$_\odot$. However, while a higher resolution should certainly bring the observations and simulations closer to agreement, the effect does not appear to be strong enough to fully explain the differences seen in the CIV(HI) relation, and furthermore the SiIV(HI) relation shows almost no change when the resolution is increased. Therefore, we believe that other effects may be at play.

An important piece of information to consider is the good agreement between the observed and simulated OVI(HI) relations. The insensitivity of the different UVB models to $\tau_{\mathrm{OVI}}^{\mathrm{med}}$ (when binned by HI) suggests that the gas is primarily collisionally ionized, and hence that OVI(HI) is probing a hotter gas phase than CIV(HI) and SiIV(HI). From this, we can conclude that the simulations correctly capture the *hot* gas in the IGM at $z \sim 3.5$. The lack of CIV and SiIV, on the other hand, may not be due to a too low metallicity or volume filling fraction, but rather to an incorrect gas phase. If too much of the enriched gas is excessively hot, then too much carbon and silicon will be ionized to states above CIV and SiIV, reducing the number of pixels with detectable CIV and SiIV absorption.

Aguirre et al. (2005) found an even more severe underestimation of simulated median CIV optical depths, with the tension also being alleviated by invoking a softer UVB. In con-

trast to EAGLE, the simulations in Aguirre et al. (2005) did not include metal-line cooling, and the study found that most of the metals resided in a too-hot gas phase ($10^5 \lesssim T \lesssim 10^7$ K). The authors speculated that the simulations could be brought into agreement with the observations by implementing metal-line cooling, but here we have shown that this is not the case. However, the inclusion of metal-line cooling may have aided in resolving other issues. While we find good agreement between our observations and simulations of the CIII(CIV) relation, Aguirre et al. (2005) measured a far too low $\tau_{\mathrm{CIII}}^{\mathrm{med}}$, indicating a much stronger mismatch in the temperature and/or density of the gas in their simulations.

It may be that the temperature of the gas in our simulations is sensitive to the details of the implementation of stellar feedback implementation. The stellar feedback in EAGLE is implemented thermally, using a stochastic prescription in which the initial temperature of the heated is gas is guaranteed to exeed $10^{7.5}$ K (Dalla Vecchia & Schaye, 2012). The probability of heating events was calibrated to observations of galaxy stellar masses and disk sizes at $z \sim 0$, but observations of the CGM were not considered. Our results suggest that at $z \sim 3.5$, the outflows driven by stellar feedback may not contain enough cold gas. While Furlong et al. (2015) found that galaxy star formation rate densities and stellar masses are in good agreement with observations for $z \sim 3$–4, the work presented here suggests that other indicators may be needed to fully test the feedback implementation at these redshifts.

To conclude the discussion, we draw a connection between this work and Chapter 4, where we compared observations of the circumgalactic medium around $z \sim 2.5$ galaxies to the EAGLE simulations. In contrast to this work, there we found excellent agreement between observed and simulated CIV and SiIV optical depths. There are at least two possible reasons for this difference. First, the galaxies in Chatper 4 were relatively massive ($M_{\mathrm{halo}} \sim 10^{12}$ M$_\odot$), while most the IGM is thought to have been enriched by galaxies with much lower masses (e.g., Booth et al., 2012). Second, in Chapter 4 we only studied the gas around galaxies at impact parameters larger than 35 kpc. In this work, we may be going to smaller galactocentric distances since the maximum median HI optical depth found in Chapter 4 is $\tau_{\mathrm{HI}} \sim 10$, and we encounter the largest discrepancy between the observations and simulations above this value. Thus, while in Chapter 4 we found good agreement between EAGLE and gas around massive galaxies, in this study the tension between observations and simulations presents itself due to our sensitivity to outflows from lower-mass galaxies, as well as the possibility that we are probing smaller galactocentric distances at the highest HI optical depths.

5.5 Conclusion

In this work we used pixel optical depth relations to study the $z \sim 3.5$ IGM, taking data from a sample of eight $\langle z_{\mathrm{QSO}} \rangle$ = 3.7 QSOs, and compared our results with the EAGLE simulations. The QSOs were observed with VLT/UVES, and their spectra are uniform in their S/N and coverage. We employed the pixel optical depth technique to obtain HI and metal-line absorption partially corrected for the effects of noise, contamination, and saturation. The resulting pixel optical depth relations were compared to those derived from mock spectra generated from the EAGLE simulations. The mock spectra were synthesized to have a resolution, pixel size, S/N and wavelength coverage closely matched to the observations. We have considered a fiducial QSO+galaxy UVB (Haardt & Madau, 2001), as well

as a harder QSO-only model and models with reduced intensity above 4 Ryd by factors of 10 and 100, respectively. The fiducial EAGLE model has been run in a cosmologically representative box size (100 cMpc) at a relatively high resolution (2×1504^3 particles), and the supernova and AGN feedback has been calibrated to reproduce the $z \sim 0$ galaxy stellar mass function, galaxy-black hole mass relation, and galaxy disk sizes. Our conclusions are listed below.

- We have detected strong correlations for the observed CIV(HI), SiIV(HI), OVI(HI) relations, as well as for CIII(CIV) and SiIII(SiIV) (Figs. 5.3 and 5.4).

- We find that for the CIV(HI) and SiIV(HI) relations, the observed metal-line optical depths are higher than the simulations run with the fiducial HM01 UVB. For CIV(HI), we find a discrepancy of up to ~ 0.1 dex at $\tau_{\mathrm{HI}} = 1$, ~ 0.5 dex at $\tau_{\mathrm{HI}} = 10$, and ~ 1 dex at $\tau_{\mathrm{HI}} = 10^2$, where we believe we are probing gas at high densities and small galactocentric distances. For SiIV(HI) the agreement is slightly better, and we find that the observed data points are higher by up to ~ 0.2 dex at $\tau_{\mathrm{HI}} = 10$ up to ~ 0.8 dex at $\tau_{\mathrm{HI}} = 10^2$. In contrast, OVI(HI), which likely probes a hotter gas phase, provides good agreement with the data (Fig. 5.3).

- We consider UVBs that differ from the fiducial HM01 model, including a harder quasar-only background (Q-only) and softer backgrounds with 10 and 100 times reduced intensity above 4 Ryd (4Ryd-10 and -100). The softer models, which may be more realistic than our fiducial background if HeII is still partially ionized at $z \sim 3.5$, are a better match to the CIV(HI) and SiIV(HI) relations, and can nearly reproduce the observations for $\tau_{\mathrm{HI}} \lesssim 10$. The results of the OVI(HI) relation are insensitive to the change in UVB, which suggests that OVI is tracing predominantly collisionally ionized gas (Fig. 5.3).

- Examining relations that investigate different ionization states of the same element, CIII(CIV) and SiIII(SiIV), we find good agreement between the observations and simulations for both the fiducial UVB and softer models (Fig. 5.4).

- Unlike OVI(HI), the OVI(CIV) and OVI(SiIV) relations demonstrate sensitivity to the UVB for $\tau_{\mathrm{CIV}} \gg 10^{-1}$ and $\tau_{\mathrm{SiIV}} \gtrsim 1$, and we find OVI(CIV) is best described by the hardest models (the fiducial HM01 and Q-only). The dependence on the ionizing background suggests that OVI pixels with associated strong CIV and SiIV reside in a cooler, photoionized gas phase compared to the gas probed by OVI(HI) (Fig. 5.5).

- We discuss possible reasons why CIV and SiIV optical depths with associated HI are underestimated by the fiducial simulations, and we consider a combination of four explanations to be the most likely.

  1. Ionization by local sources may be important to include in the simulations. Since the strength of the radiation emitted by stars typically falls sharply above 4 Ryd, this would ionize HI while having a much smaller effect on the metals, which would increase the median metal-line absorption for a fixed HI. This explanation is particularly viable for $\tau_{\mathrm{HI}} \gtrsim 10$, where we may be probing small galactocentric distances.

2. The completion of He II reionization in the HM01 simulations may arrive too early, or it may be too uniform, since the observations indicate that it could be quite patchy around $z \sim 3.5$ (e.g., Shull et al., 2010; Worseck et al., 2011). This explanation is supported by the better agreement with the 4Ryd-10 and 4Ryd-100 models to the C IV(H I) and Si IV(H I) observations. However, even the 4Ryd-100 model cannot fully explain the C IV(H I) observations for $\tau_{\mathrm{H\,I}} \gtrsim 10$.

3. The simulations may not be resolving the low-mass galaxies required to pollute the diffuse IGM. We find that invoking the highest-resolution simulations, Ref- and Recal-L025N0752, improves the agreement with the observed C IV(H I) relation by ~ 0.3 dex at $\tau_{\mathrm{H\,I}} \sim 10^2$. While resolution likely plays a role, the magnitude of the effect is not large enough to fully explain the discrepancy, particularly for the Si IV(H I) relation, which we find to be almost insensitive to the resolution increase.

4. The stellar feedback in the simulations may be driving outflows that contain insufficient cold gas. The agreement between the observed and simulated O VI(H I) relation, which probably traces collisionally ionized gas, indicates that the simulations correctly capture this hotter gas phase, and that it contains enough metals. However, if the gas is overall too hot with respect to the observations, then more C IV and Si IV will be ionized to higher energy levels, leading to a paucity of pixels with detected $\tau_{\mathrm{C\,IV}}$ and $\tau_{\mathrm{Si\,IV}}$.

Thus, the combination of a too hard UVB, and energetic stellar feedback creating outflows without enough cool gas, are likely the cause of the disparity we find between the observed and simulated C IV(H I) and Si IV(H I) relations.

For future work, we would like to use the simulations to pinpoint which galaxies are responsible for the IGM pollution. We can generate spectra using subsets of the gas particles in the simulations. By only including (or excluding) gas particles around galaxies of specific halo masses, we can determine the most important contributors to IGM enrichment. Furthermore, we plan to measure the scatter in the simulations, in order to compare with the results of Aguirre et al. (2005), who found that the metal distribution in their simulations was less homogeneous than observed. On the observational side, we are currently obtaining data using the VLT/MUSE integral field unit (Bacon et al., 2010), to perform a blind galaxy survey (through Lyα emission) in the QSO fields. We will be able to combine the galaxy redshifts and impact parameters with QSO absorption information to study the H I and metal-line absorption of the circumgalactic medium of faint Lyα emitters. By comparing these results to observations, we may be able to better identify the source of the remaining discrepancy between EAGLE and the $z \sim 3.5$ IGM.

5.A   Resolution tests

In this appendix, we test the numerical convergence of the EAGLE simulations. We first examine the effects of varying the simulation box size. In Fig. 5.6, where we show optical depth relations derived from the fiducial Ref-L100N1504 simulation, as well as from the reference runs in 50 and 25 cMpc volumes with the same resolution. To create these optical

depth relations (which in this case are not designed to mimic observations of any particular QSO), we have generated 100 spectra with z_{QSO} = 3.94, chosen such that the redshift of the Lyα forest is centred around the z = 3.53 EAGLE snapshot. The S/N was set to be 75 throughout each spectrum, and the UVB was the default Haardt & Madau (2001) model. We find that the optical depth relations in Fig. 5.6 are converged for the two largest box sizes (50 and 100 cMpc).

Next, in Fig. 5.7 we explore the effects of the numerical resolution, to both test for convergence and to investigate whether pushing to lower galaxy masses may impact the enrichment of the IGM. For this, we use the 25 cMpc box, for which simulations have been run with resolutions higher than the fiducial one used in this work. There are two versions of the highest-resolution simulation L025N0752: one that has been run using the subgrid physics of the reference model (Ref-) and one that has been recalibrated to better match the $z \approx 0$ galaxy stellar mass function (Recal-). We present the optical depth relations for the above high-resolution runs, as well as for our fiducial resolution (2×376^3 particles in the 25 cMpc box) and finally a lower-resolution of 188^3 particles.

In the upper left panel of Fig. 5.7, we examine CIV(HI) and find sensitivity to resolution in the highest HI bins ($\tau_{HI} \gtrsim 10^2$). For the lowest-resolution run, the median CIV optical depth is ≈ 0.5 dex lower than for the fiducial model, while points from the highest-resolution simulations are up to ≈ 0.3 dex above those of the fiducial run. For the remaining optical depths relations, the differences are very small ($\lesssim 0.1$ dex).

These results primarily indicate that our fiducial resolution is nearly converged. However, we do find some sensitivity to resolution in relations involving CIV. The suggests that a higher resolution results in more carbon and/or temperature conditions that favour triply-ionized carbon. However, we note that the effect is not large enough to completely resolve the discrepancy with observations found in Fig. 5.3. Furthermore, SiIV(HI) shows very little sensitivity to resolution.

5.B   Results from single QSOs

In this appendix, we present the pixel optical depth relations derived from individual QSOs, which were combined to obtain the relations shown in Figs. 5.3, 5.4, and 5.5. Here we display the optical depth relations in the same order as they appear in the paper: CIV(HI) (Fig. 5.8), SiIV(HI) (Fig. 5.9), OVI(HI) (Fig. 5.10), CIII(CIV) (Fig. 5.11), SiIII(SiIV) (Fig. 5.12), SiIV(CIV) (Fig. 5.13), OVI(CIV) (Fig. 5.14), and OVI(SiIV) (Fig. 5.15).
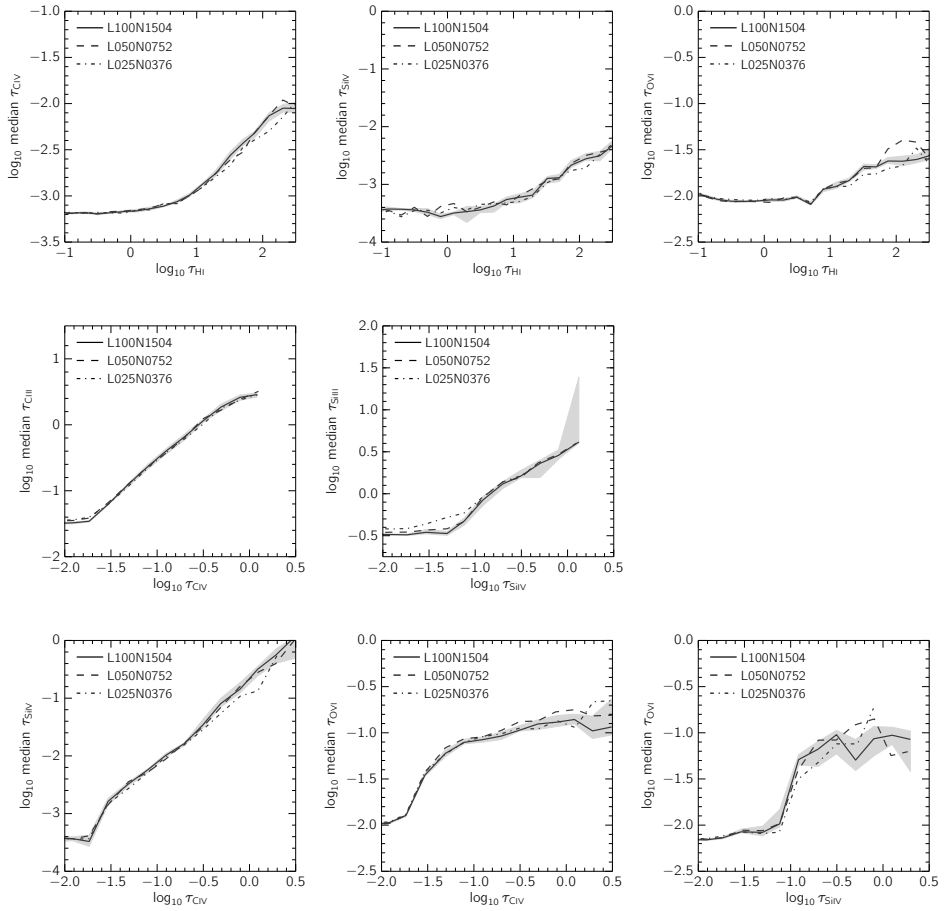
Figure 5.6: Convergence with respect to simulation box size, where we plot the same optical depth relations as were presented in Figs. 5.3, 5.4, and 5.5, but without combining different QSOs. For clarity, we only show the error region around the fiducial model (L100N1504), which was determined by bootstrap resampling the mock spectra. We find that our fiducial simulation is converged.
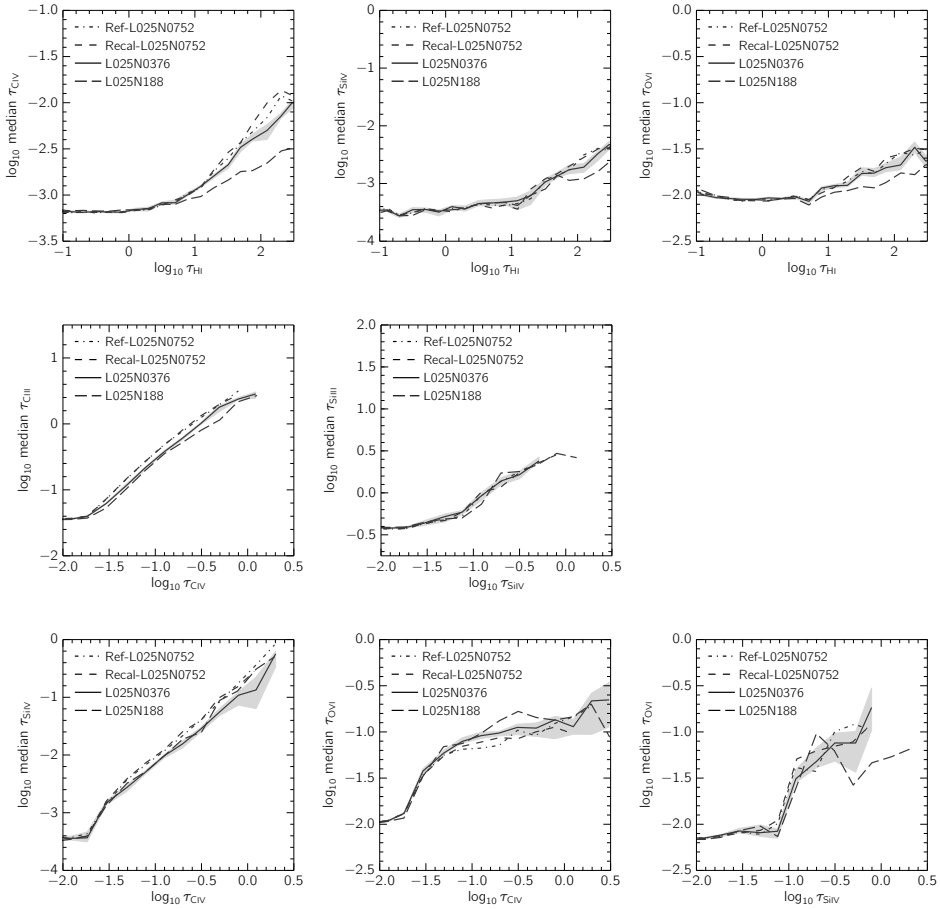
Figure 5.7: The same as Fig. 5.6, but showing convergence with respect to the numerical resolution and using a 25 cMpc box. Our fiducial resolution is given by the L025N0376 run, and indicated by the solid line and shaded error region. While the lowest-resolution run, Ref-L025N0188, deviates significantly from the others (especially for the CIV(HI) relation), we find mostly good agreement between the fiducial intermediate- and high- resolution runs, which demonstrates that the fiducial resolution is nearly converged. However, the higher-resolution runs predict about 0.3 dex higher $\tau_{\mathrm{CIV}}^{\mathrm{med}}$ at $\tau_{\mathrm{HI}} \sim 10^2$, indicating the the CIV associated with these rare, strong absorbers has not yet converged.
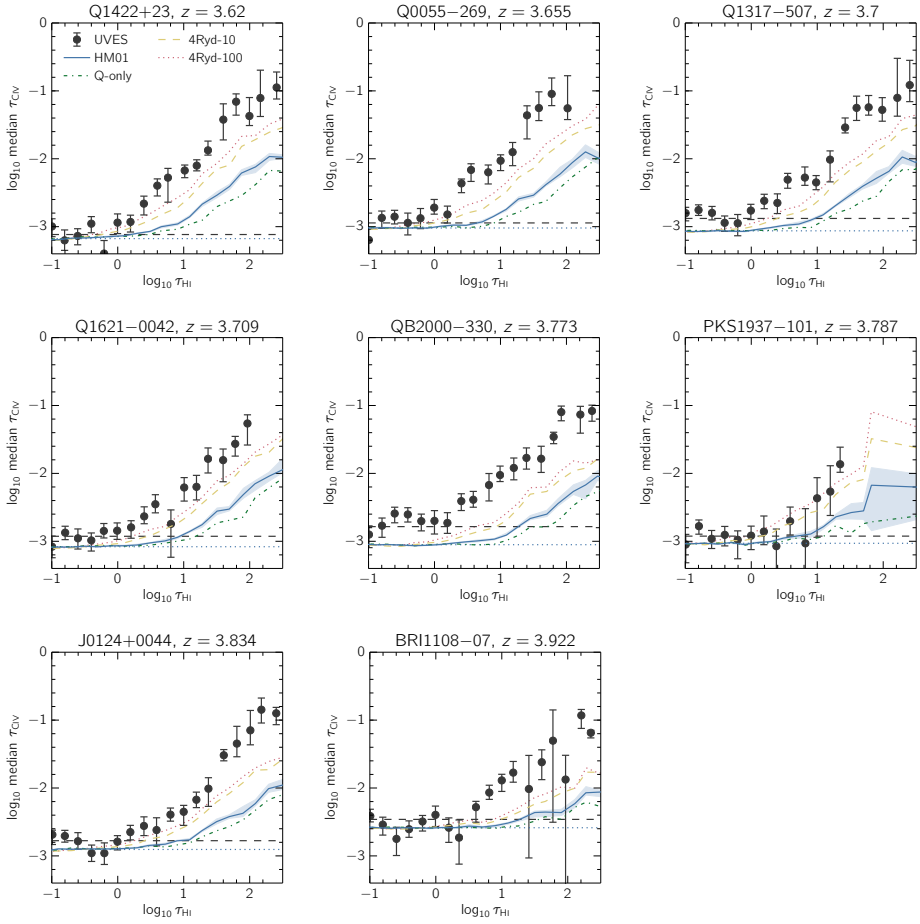
Figure 5.8: Median C IV optical depth in bins of τ_{HI} for all eight QSOs. The black points represent the observed data, while the curves show results from simulated spectra created using different UVB models. The 1σ error bars on the observations were estimated by bootstrap resampling chunks of the spectrum, while the error regions shown for the fiducial simulation were calculated by bootstrap resampling the 100 mock spectra used to generate the data. The value of τ_{min} is indicated by the dashed line for the observations, and the dotted lines for the simulations.
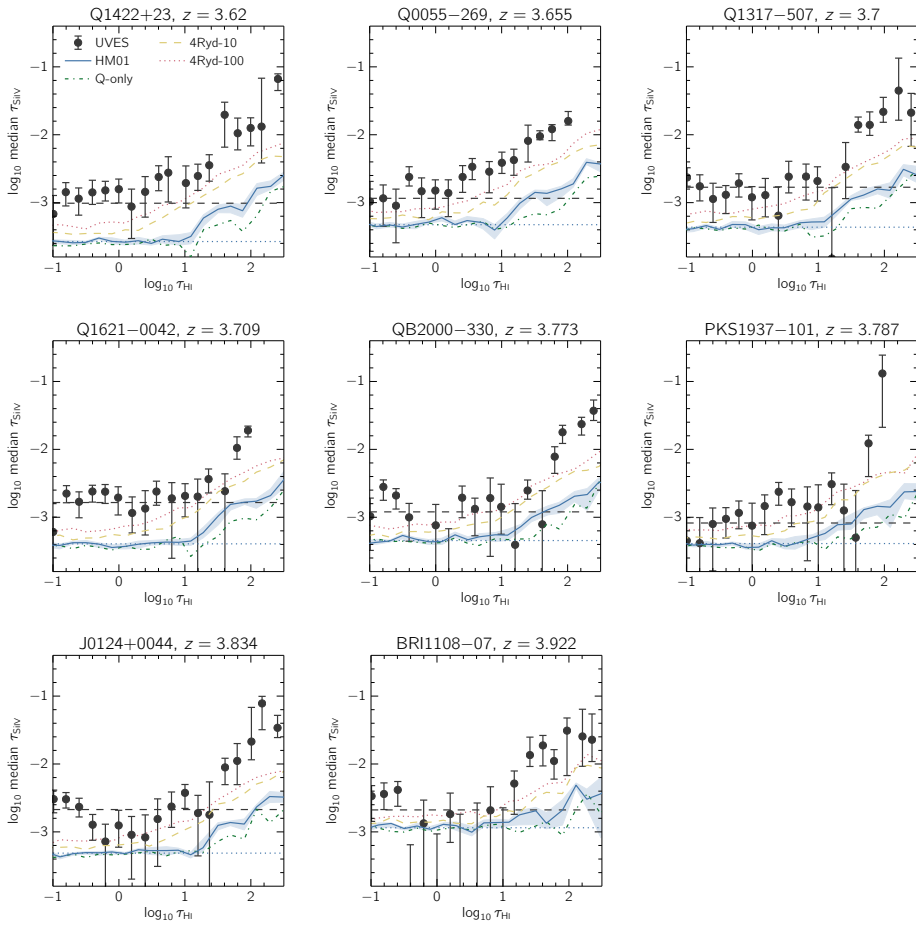
Figure 5.9: Same as Fig. 5.8, but for Si IV (H I).
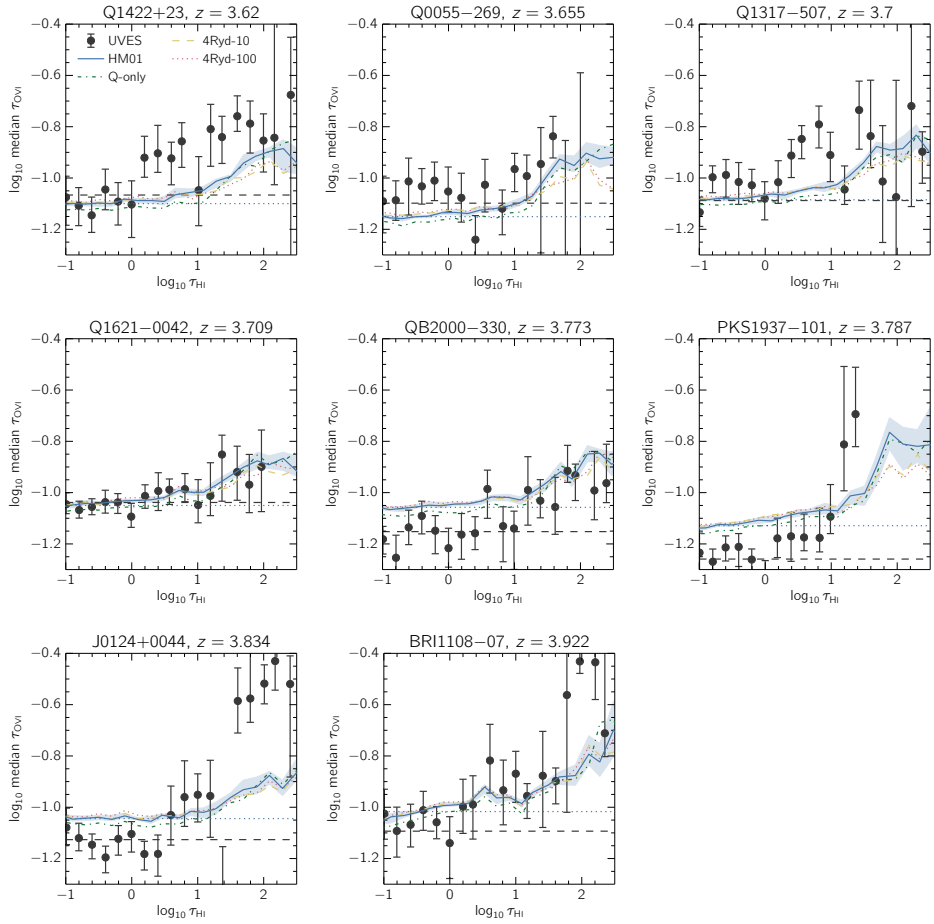
Figure 5.10: Same as Fig. 5.8, but for Ovi(Hi).

Figure 5.11: Same as Fig. 5.8, but for CIII(CIV).

Figure 5.12: Same as Fig. 5.8, but for Si III(Si IV).

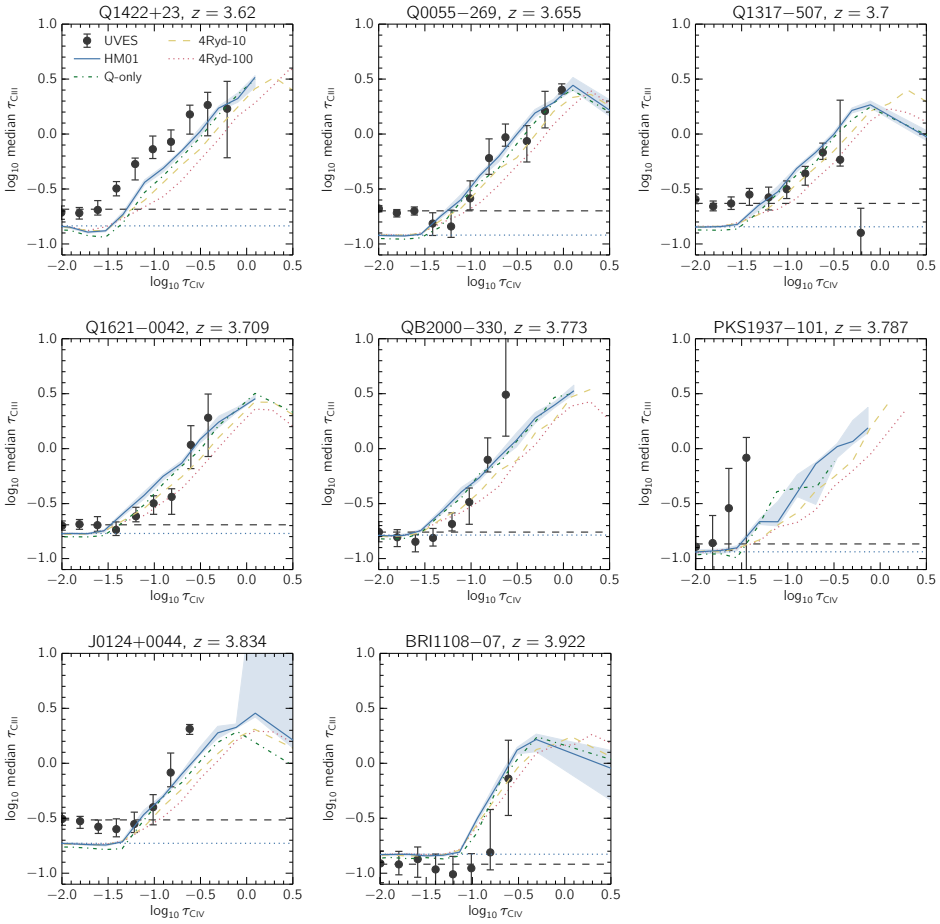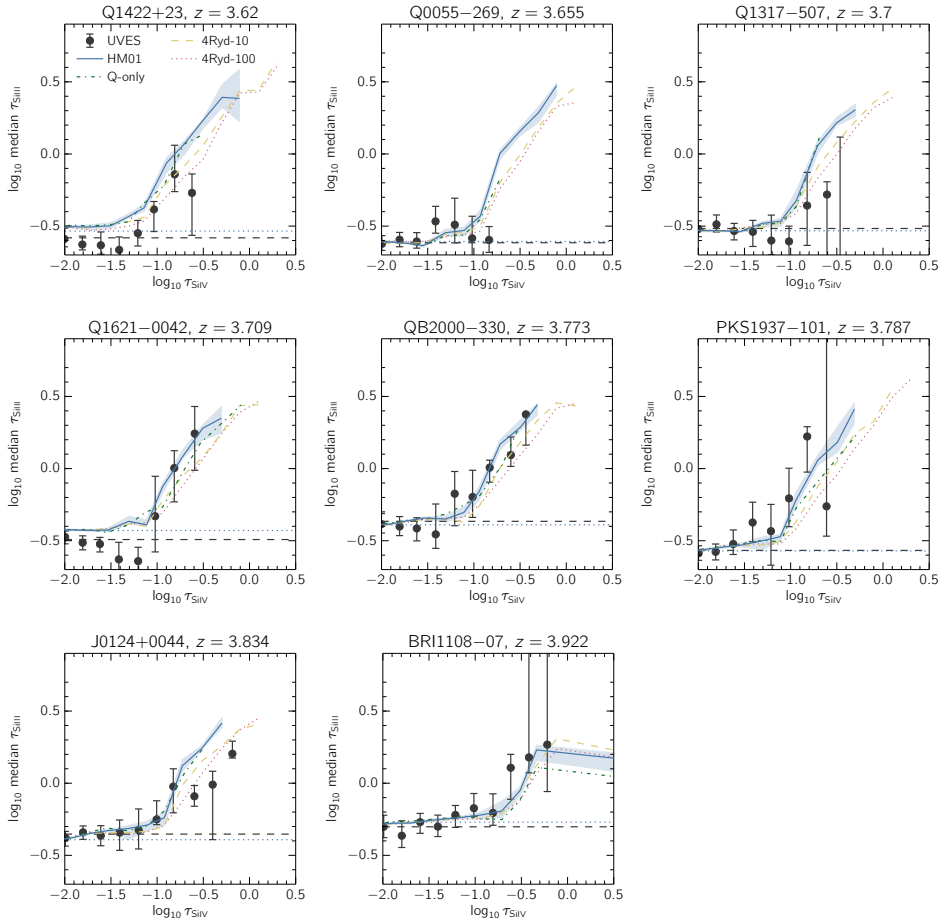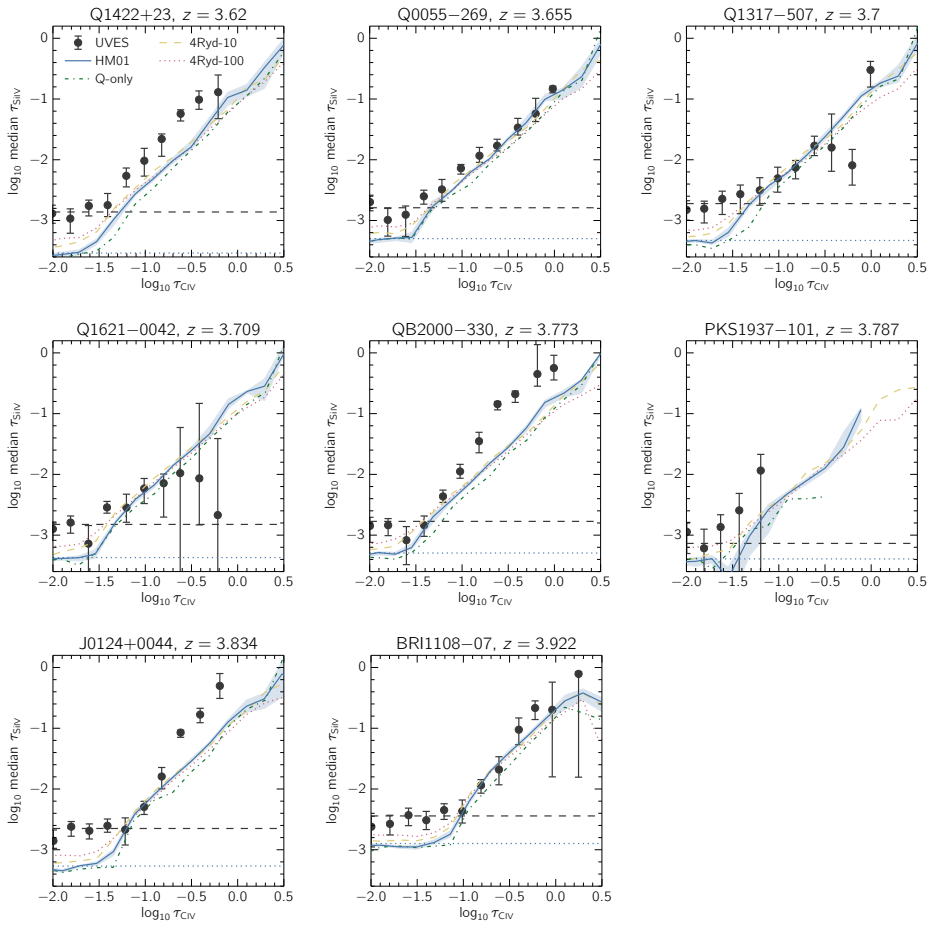**Figure 5.13:** Same as Fig. 5.8, but for Siiv(Civ).
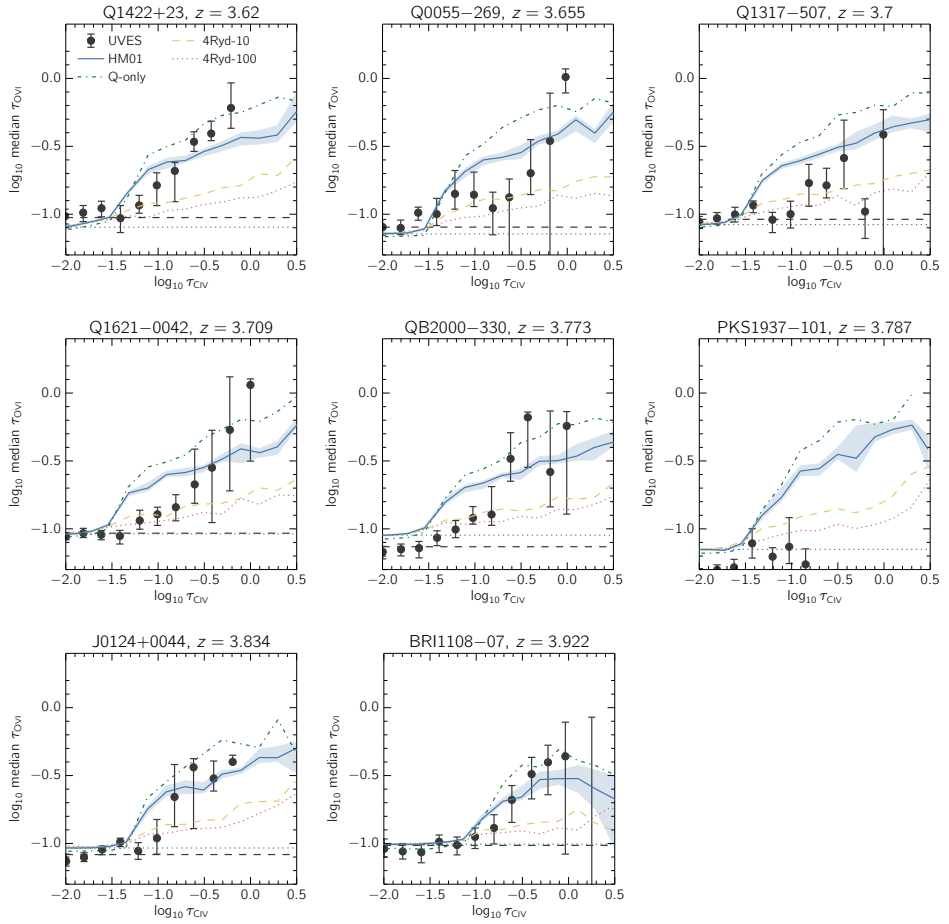
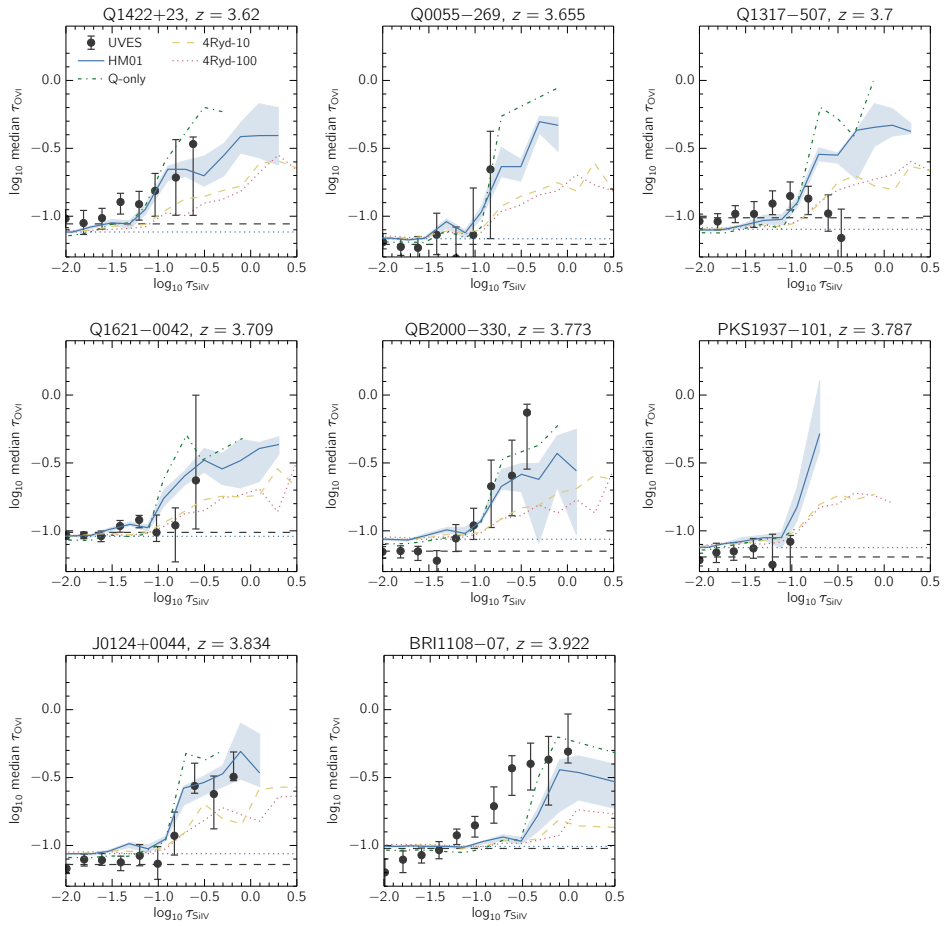**Figure 5.14:** Same as Fig. 5.8, but for O$\textsc{vi}$(C$\textsc{iv}$).

Figure 5.15: Same as Fig. 5.8, but for OvI(SiIV).

References

Adams, J. J., Uson, J. M., Hill, G. J., & MacQueen, P. J. 2011, ApJ, 728, 107

Adelberger, K. L., Shapley, A. E., Steidel, C. C., et al. 2005a, ApJ, 629, 636

Adelberger, K. L., Steidel, C. C., Pettini, M., et al. 2005b, ApJ, 619, 697

Adelberger, K. L., Steidel, C. C., Shapley, A. E., et al. 2004, ApJ, 607, 226

Adelberger, K. L., Steidel, C. C., Shapley, A. E., & Pettini, M. 2003, ApJ, 584, 45

Aguirre, A., Dow-Hygelund, C., Schaye, J., & Theuns, T. 2008, ApJ, 689, 851

Aguirre, A., Hernquist, L., Schaye, J., et al. 2001, ApJ, 560, 599

Aguirre, A., Schaye, J., Hernquist, L., et al. 2005, ApJ, 620, L13

Aguirre, A., Schaye, J., Kim, T.-S., et al. 2004, ApJ, 602, 38

Aguirre, A., Schaye, J., & Theuns, T. 2002, ApJ, 576, 1

Ajiki, M., Taniguchi, Y., Murayama, T., et al. 2002, ApJ, 576, L25

Allende Prieto, C., Lambert, D. L., & Asplund, M. 2001, ApJ, 556, L63

—. 2002, ApJ, 573, L137

Aracil, B., Petitjean, P., Pichon, C., & Bergeron, J. 2004, A&A, 419, 811

Bacon, R., Accardo, M., Adjali, L., et al. 2010, in Society of Photo-Optical Instrumentation Engineers (SPIE) Conference Series, Vol. 7735, Society of Photo-Optical Instrumentation Engineers (SPIE) Conference Series, 8

Bahcall, J. N., & Spitzer, Jr., L. 1969, ApJ, 156, L63

Bechtold, J., Weymann, R. J., Lin, Z., & Malkan, M. A. 1987, ApJ, 315, 180

Becker, G. D., & Bolton, J. S. 2013, MNRAS, 436, 1023

Becker, G. D., Bolton, J. S., Haehnelt, M. G., & Sargent, W. L. W. 2011, MNRAS, 410, 1096

Becker, G. D., Rauch, M., & Sargent, W. L. W. 2007, ApJ, 662, 72

Bergeron, J., Aracil, B., Petitjean, P., & Pichon, C. 2002, A&A, 396, L11

Bergeron, J., & Boissé, P. 1991, A&A, 243, 344

Bergeron, J., Cristiani, S., & Shaver, P. A. 1992, A&A, 257, 417

Bi, H. 1993, ApJ, 405, 479

Bi, H., & Davidsen, A. F. 1997, ApJ, 479, 523

Bi, H. G., Boerner, G., & Chu, Y. 1992, A&A, 266, 1

Bland, J., & Tully, B. 1988, Nature, 334, 43

Boksenberg, A., Sargent, W. L. W., & Rauch, M. 2003, ArXiv Astrophysics e-prints, astro-ph/0307557

Booth, C. M., & Schaye, J. 2009, MNRAS, 398, 53

Booth, C. M., Schaye, J., Delgado, J. D., & Dalla Vecchia, C. 2012, MNRAS, 420, 1053

Bordoloi, R., Tumlinson, J., Werk, J. K., et al. 2014, ApJ, 796, 136

Cantalupo, S. 2010, MNRAS, 403, L16

Carswell, B., Schaye, J., & Kim, T.-S. 2002, ApJ, 578, 43

Cen, R., Miralda-Escudé, J., Ostriker, J. P., & Rauch, M. 1994, ApJ, 437, L9

Chen, H.-W., Lanzetta, K. M., & Webb, J. K. 2001, ApJ, 556, 158

Chen, H.-W., & Mulchaey, J. S. 2009, ApJ, 701, 1219

Conroy, C., Shapley, A. E., Tinker, J. L., Santos, M. R., & Lemson, G. 2008, ApJ, 679, 1192

Cooke, J., Ryan-Weber, E. V., Garel, T., & Díaz, C. G. 2014, MNRAS, 441, 837

Cowie, L. L., & Songaila, A. 1998, Nature, 394, 44

Cowie, L. L., Songaila, A., Kim, T.-S., & Hu, E. M. 1995, AJ, 109, 1522

Crain, R. A., Schaye, J., Bower, R. G., et al. 2015, ArXiv e-prints, arXiv:1501.01311

Dalla Vecchia, C., & Schaye, J. 2012, MNRAS, 426, 140

Danforth, C. W., & Shull, J. M. 2008, ApJ, 679, 194

Dekel, A., Birnboim, Y., Engel, G., et al. 2009, Nature, 457, 451

Dolag, K., Borgani, S., Murante, G., & Springel, V. 2009, MNRAS, 399, 497

Durier, F., & Dalla Vecchia, C. 2012, MNRAS, 419, 465

Ellison, S. L., Songaila, A., Schaye, J., & Pettini, M. 2000, AJ, 120, 1175

Erb, D. K., Shapley, A. E., Pettini, M., et al. 2006a, ApJ, 644, 813

Erb, D. K., Steidel, C. C., Shapley, A. E., et al. 2006b, ApJ, 647, 128

—. 2006c, ApJ, 646, 107

Fabian, A. C. 2012, ARA&A, 50, 455

Faucher-Giguère, C.-A., Hopkins, P. F., Kereš, D., et al. 2015, MNRAS, 449, 987

Faucher-Giguère, C.-A., Kereš, D., & Ma, C.-P. 2011, MNRAS, 417, 2982

Faucher-Giguère, C.-A., Lidz, A., Hernquist, L., & Zaldarriaga, M. 2008, ApJ, 688, 85

Faucher-Giguère, C.-A., Lidz, A., Zaldarriaga, M., & Hernquist, L. 2009, ApJ, 703, 1416

Ferland, G. J., Porter, R. L., van Hoof, P. A. M., et al. 2013, Rev. Mexicana Astron. Astrofis., 49, 137

Ford, A. B., Oppenheimer, B. D., Davé, R., et al. 2013, MNRAS, 432, 89

Ford, A. B., Werk, J. K., Dave, R., et al. 2015, ArXiv e-prints, arXiv:1503.02084

Fox, A. J., Bergeron, J., & Petitjean, P. 2008, MNRAS, 388, 1557

Franx, M., Illingworth, G. D., Kelson, D. D., van Dokkum, P. G., & Tran, K.-V. 1997, ApJ, 486, L75

Fumagalli, M., Hennawi, J. F., Prochaska, J. X., et al. 2014, ApJ, 780, 74

Furlong, M., Bower, R. G., Theuns, T., et al. 2015, MNRAS, 450, 4486

Haardt, F., & Madau, P. 2001, in Clusters of Galaxies and the High Redshift Universe Observed in X-rays, ed. D. M. Neumann & J. T. V. Tran

Haardt, F., & Madau, P. 2012, ApJ, 746, 125

Haas, M. R., Schaye, J., Booth, C. M., et al. 2013a, MNRAS, 435, 2931

—. 2013b, MNRAS, 435, 2955

Heckman, T. M., Armus, L., & Miley, G. K. 1990, ApJS, 74, 833

Heckman, T. M., Lehnert, M. D., Strickland, D. K., & Armus, L. 2000, ApJS, 129, 493

Hernquist, L., Katz, N., Weinberg, D. H., & Miralda-Escudé, J. 1996, ApJ, 457, L51

Holweger, H. 2001, in American Institute of Physics Conference Series, Vol. 598,

Joint SOHO/ACE workshop "Solar and Galactic Composition", ed. R. F. Wimmer-Schweingruber, 23–30

Hopkins, P. F. 2013, MNRAS, 428, 2840

Hummels, C. B., Bryan, G. L., Smith, B. D., & Turk, M. J. 2013, MNRAS, 430, 1548

Iwata, I., Inoue, A. K., Matsuda, Y., et al. 2009, ApJ, 692, 1287

Jones, T., Stark, D. P., & Ellis, R. S. 2012, ApJ, 751, 51

Kaiser, N. 1987, MNRAS, 227, 1

Kereš, D., Katz, N., Weinberg, D. H., & Davé, R. 2005, MNRAS, 363, 2

Lagos, C. d. P., Crain, R. A., Schaye, J., et al. 2015, ArXiv e-prints, arXiv:1503.04807

Lehnert, M. D., Heckman, T. M., & Weaver, K. A. 1999, ApJ, 523, 575

Liang, C. J., Kravtsov, A. V., & Agertz, O. 2015, ArXiv e-prints, arXiv:1507.07002

Lidz, A., Faucher-Giguère, C.-A., Dall'Aglio, A., et al. 2010, ApJ, 718, 199

Lopez, S., Ellison, S., D'Odorico, S., & Kim, T.-S. 2007, A&A, 469, 61

Mac Low, M.-M., & Ferrara, A. 1999, ApJ, 513, 142

Madau, P., Ferguson, H. C., Dickinson, M. E., et al. 1996, MNRAS, 283, 1388

Martin, C. L. 2005, ApJ, 621, 227

McLean, I. S., Steidel, C. C., Epps, H. W., et al. 2012, in Society of Photo-Optical Instrumentation Engineers (SPIE) Conference Series, Vol. 8446, Society of Photo-Optical Instrumentation Engineers (SPIE) Conference Series

Miralda-Escudé, J., Cen, R., Ostriker, J. P., & Rauch, M. 1996, ApJ, 471, 582

Mostardi, R. E., Shapley, A. E., Nestor, D. B., et al. 2013, ApJ, 779, 65

Nestor, D. B., Shapley, A. E., Kornei, K. A., Steidel, C. C., & Siana, B. 2013, ApJ, 765, 47

Nielsen, N. M., Churchill, C. W., Kacprzak, G. G., & Murphy, M. T. 2013, ApJ, 776, 114

Oppenheimer, B. D., & Davé, R. 2008, MNRAS, 387, 577

Oppenheimer, B. D., Davé, R., Katz, N., Kollmeier, J. A., & Weinberg, D. H. 2012, MNRAS, 420, 829

Oppenheimer, B. D., Davé, R., Kereš, D., et al. 2010, MNRAS, 406, 2325

Oppenheimer, B. D., & Schaye, J. 2013a, MNRAS, 434, 1063

—. 2013b, MNRAS, 434, 1043

Pettini, M., Steidel, C. C., Adelberger, K. L., Dickinson, M., & Giavalisco, M. 2000, ApJ, 528, 96

Pieri, M. M., Frank, S., Mathur, S., et al. 2010, ApJ, 716, 1084

Pieri, M. M., Schaye, J., & Aguirre, A. 2006, ApJ, 638, 45

Pieri, M. M., Mortonson, M. J., Frank, S., et al. 2014, MNRAS, 441, 1718

Planck Collaboration, Ade, P. A. R., Aghanim, N., et al. 2013, ArXiv e-prints, arXiv:1303.5076

Prochaska, J. X., Weiner, B., Chen, H.-W., Mulchaey, J., & Cooksey, K. 2011, ApJ, 740, 91

Quider, A. M., Pettini, M., Shapley, A. E., & Steidel, C. C. 2009, MNRAS, 398, 1263

Rahmati, A., Pawlik, A. H., Raičevic M., & Schaye, J. 2013a, MNRAS, 430, 2427

Rahmati, A., & Schaye, J. 2014, MNRAS, 438, 529

Rahmati, A., Schaye, J., Bower, R. G., et al. 2015, ArXiv e-prints, arXiv:1503.05553

Rahmati, A., Schaye, J., Pawlik, A. H., & Raicevic, M. 2013b, MNRAS, 431, 2261

Rakic, O., Schaye, J., Steidel, C. C., et al. 2013, MNRAS, 433, 3103

Rakic, O., Schaye, J., Steidel, C. C., & Rudie, G. C. 2011, MNRAS, 414, 3265

—. 2012, ApJ, 751, 94

Reddy, N. A., & Steidel, C. C. 2009, ApJ, 692, 778

Reddy, N. A., Steidel, C. C., Pettini, M., et al. 2008, ApJS, 175, 48

Rosas-Guevara, Y. M., Bower, R. G., Schaye, J., et al. 2013, ArXiv e-prints, arXiv:1312.0598

Rudie, G. C., Steidel, C. C., & Pettini, M. 2012a, ApJ, 757, L30

Rudie, G. C., Steidel, C. C., Shapley, A. E., & Pettini, M. 2013, ApJ, 769, 146

Rudie, G. C., Steidel, C. C., Trainor, R. F., et al. 2012b, ApJ, 750, 67

Rupke, D. S., Veilleux, S., & Sanders, D. B. 2005, ApJS, 160, 115

Savage, B. D., Kim, T.-S., Wakker, B. P., et al. 2014, ApJS, 212, 8

Savage, B. D., & Sembach, K. R. 1991, ApJ, 379, 245

Schaye, J. 2001, ApJ, 559, 507

—. 2004, ApJ, 609, 667

—. 2006, ApJ, 643, 59

Schaye, J., Aguirre, A., Kim, T.-S., et al. 2003, ApJ, 596, 768

Schaye, J., Carswell, R. F., & Kim, T.-S. 2007, MNRAS, 379, 1169

Schaye, J., & Dalla Vecchia, C. 2008, MNRAS, 383, 1210

Schaye, J., Rauch, M., Sargent, W. L. W., & Kim, T.-S. 2000a, ApJ, 541, L1

Schaye, J., Theuns, T., Rauch, M., Efstathiou, G., & Sargent, W. L. W. 2000b, MNRAS, 318, 817

Schaye, J., Dalla Vecchia, C., Booth, C. M., et al. 2010, MNRAS, 402, 1536

Schaye, J., Crain, R. A., Bower, R. G., et al. 2015, MNRAS, 446, 521

Schechter, P. 1976, ApJ, 203, 297

Shapley, A. E., Steidel, C. C., Pettini, M., & Adelberger, K. L. 2003, ApJ, 588, 65

Shapley, A. E., Steidel, C. C., Pettini, M., Adelberger, K. L., & Erb, D. K. 2006, ApJ, 651, 688

Shen, S., Madau, P., Guedes, J., et al. 2013, ApJ, 765, 89

Shull, J. M., France, K., Danforth, C. W., Smith, B., & Tumlinson, J. 2010, ApJ, 722, 1312

Shull, J. M., Smith, B. D., & Danforth, C. W. 2012, ApJ, 759, 23

Sicmoe, R. A. 2011, ApJ, 738, 159

Simcoe, R. A., Sargent, W. L. W., & Rauch, M. 2002, ApJ, 578, 737

—. 2004, ApJ, 606, 92

Simcoe, R. A., Sargent, W. L. W., Rauch, M., & Becker, G. 2006, ApJ, 637, 648

Songaila, A. 1998, AJ, 115, 2184

—. 2001, ApJ, 561, L153

Springel, V. 2005, MNRAS, 364, 1105

Springel, V., Di Matteo, T., & Hernquist, L. 2005, MNRAS, 361, 776

Springel, V., White, S. D. M., Tormen, G., & Kauffmann, G. 2001, MNRAS, 328, 726

Steidel, C. C., Adelberger, K. L., Giavalisco, M., Dickinson, M., & Pettini, M. 1999, ApJ, 519, 1

Steidel, C. C., Adelberger, K. L., Shapley, A. E., et al. 2003, ApJ, 592, 728

Steidel, C. C., Erb, D. K., Shapley, A. E., et al. 2010, ApJ, 717, 289

Steidel, C. C., Giavalisco, M., Pettini, M., Dickinson, M., & Adelberger, K. L. 1996, ApJ, 462, L17

Steidel, C. C., Pettini, M., & Adelberger, K. L. 2001, ApJ, 546, 665

Steidel, C. C., Shapley, A. E., Pettini, M., et al. 2004, ApJ, 604, 534

Steidel, C. C., Rudie, G. C., Strom, A. L., et al. 2014, ArXiv e-prints, arXiv:1405.5473

Stinson, G. S., Brook, C., Prochaska, J. X., et al. 2012, MNRAS, 425, 1270

Stocke, J. T., Penton, S. V., Danforth, C. W., et al. 2006, ApJ, 641, 217

Suresh, J., Bird, S., Vogelsberger, M., et al. 2015, MNRAS, 448, 895

Tepper-García, T., Richter, P., Schaye, J., et al. 2011, MNRAS, 413, 190

Theuns, T., Leonard, A., Efstathiou, G., Pearce, F. R., & Thomas, P. A. 1998, MNRAS, 301, 478

Trainor, R. F., & Steidel, C. C. 2012, ApJ, 752, 39

Trayford, J. W., Theuns, T., Bower, R. G., et al. 2015, ArXiv e-prints, arXiv:1504.04374

Tremonti, C. A., Moustakas, J., & Diamond-Stanic, A. M. 2007, ApJ, 663, L77

Tripp, T. M., Sembach, K. R., Bowen, D. V., et al. 2008, ApJS, 177, 39

Tumlinson, J., Thom, C., Werk, J. K., et al. 2011, Science, 334, 948

Tummuangpak, P., Bielby, R. M., Shanks, T., et al. 2014, MNRAS, 442, 2094

Turner, M. L., Schaye, J., Steidel, C. C., Rudie, G. C., & Strom, A. L. 2014, MNRAS, 445, 794

—. 2015, MNRAS, 450, 2067

Tytler, D. 1987, ApJ, 321, 49

van de Voort, F., & Schaye, J. 2012, MNRAS, 423, 2991

van de Voort, F., Schaye, J., Booth, C. M., Haas, M. R., & Dalla Vecchia, C. 2011, MNRAS, 414, 2458

Véron-Cetty, M.-P., & Véron, P. 2010, A&A, 518, A10

Weaver, R., McCray, R., Castor, J., Shapiro, P., & Moore, R. 1977, ApJ, 218, 377

Weiner, B. J., Coil, A. L., Prochaska, J. X., et al. 2009, ApJ, 692, 187

Werk, J. K., Prochaska, J. X., Thom, C., et al. 2013, ApJS, 204, 17

Werk, J. K., Prochaska, J. X., Tumlinson, J., et al. 2014, ApJ, 792, 8

Wiersma, R. P. C., Schaye, J., Dalla Vecchia, C., et al. 2010, MNRAS, 409, 132

Wiersma, R. P. C., Schaye, J., & Smith, B. D. 2009a, MNRAS, 393, 99

Wiersma, R. P. C., Schaye, J., & Theuns, T. 2011, MNRAS, 415, 353

Wiersma, R. P. C., Schaye, J., Theuns, T., Dalla Vecchia, C., & Tornatore, L. 2009b, MNRAS, 399, 574

Worseck, G., Prochaska, J. X., McQuinn, M., et al. 2011, ApJ, 733, L24

Zhu, G., Ménard, B., Bizyaev, D., et al. 2014, MNRAS, arXiv:1309.7660

Zibetti, S., Ménard, B., Nestor, D., & Turnshek, D. 2005, ApJ, 631, L105

Samenvatting

Gewoonlijk denkt men dat een sterrelstelsel met name uit sterren bestaat. Dit beeld mist echter een belangrijke component, namelijk het gas dat zich tussen de sterren en rondom sterrenstelsels bevindt en dat de bouwstof voor nieuwe sterren levert. Dit gas is te difuus om waargenomen te worden door emissie, zodat we het alleen waar kunnen nemen als absorptie tegenover heldere lichtbronnen in de achtergrond. Hiervoor worden gewoonlijk quasars gebruikt, waarvan het licht wordt uitgezonden door materiaal dat in het super massieve zwarte gat valt.

Een enkel spectrum van een quasar kan honderden absorptielijnen bevatten, die veroorzaakt worden door het gas rondom sterrenstelsels en in het inter galactisch medium (IGM). Deze absorptielijnen komen voornamelijk door neutraal waterstof, dat veel in het Heelal voorkomt, maar ook door andere elementen zoals koolstof, zuurstof en silicium. Een gangbare methode voor het karakteriseren van de eigenschappen van de absorptie bestaat uit het fitten van individuele lijn-profielen. Deze aanpak kan echter zeer lastig zijn voor quasars in het vroege Heelal, simpelweg vanwege het hoge aantal absorptielijnen in een spectrum. Daarom definiëren we een kleiner gebied van het spectrum waar we een lijn van een bepaald ion verwachten, in plaats van het bestuderen van individuele lijnen over het hele spectrum. Vervolgens karakteriseren we de absorptie-sterkte over het volledige gebied door de reductie in flux over elke pixel te meten.

Een andere belangrijke uitdaging aan het bestuderen van gas in absorptie ligt in het vinden van de sterrenstelsels die verantwoordelijk zijn voor de absorptie. In deze thesis gebruiken we data van het baanbrekende Keck Baryonic Structure Survey (KBSS), dat zich richt op sterrenstelsels in de buurt van 15 quasars. Elk sterrenstelsel in dit onderzoeksproject is spectroscopisch waargenomen, zodat het mogelijk is om emissie-lijnen van elk sterrenstelsel te associëren met absorptielijnen in het quasar-spectrum.

Hoewel waarnemingen ons veel leren over sterrenstelsels, hebben we cosmologische simulaties nodig om de resultaten te interpreteren en in context te plaatsen met de theorie over de vorming van sterrenstelsels. Hoewel theoretische modellen in staat zijn veel waargenomen eigenschappen van sterrenstelsels te reproduceren, is er grote onzekerheid over de implementatie van de fysieke processen die gas uit sterrenstelsels drijven, bekend als 'energetische feedback'. Deze processen zijn bijvoorbeeld explosies van supernovae, stralingsdruk van jonge sterren, en stralingsdruk en jets van actieve super massieve zwarte gaten. Het voornaamste probleem is dat de fysieke processen zich op schalen afspelen die veel kleiner zijn dan de typische resolutie van moderne cosmologische simulaties. Het is daarom niet mogelijk de input parameters van deze processen a priori vast te stellen. Dit probleem is met name prangend omdat kleine wijzigingen in de input parameters grote

gevolgen hebben voor de eigenschappen van gesimuleerde sterrenstelsels.

De moeilijkheid om realtistische energetische feedback te simuleren blijft voorlopig een van de grootste puzzels van de theorie over de vorming van sterrenstelsels. Een belangrijke stap voorwaarts is om de resultaten van simulaties te vergelijken met waarnemingen. Het gas rondom sterrenstelsels in het bijzonder biedt een belangrijk laboratorium waar we de gevolgen van feedback kunnen testen. Deze regio representeert het samenspel van invallend ongerept gas met de uitdrijvende galactische winden, die verrijkt zijn door zware elemten ontstaan in supernovae. Het is daarom zeer sensitief voor details in de implementatie van energetische feedback. De sterkte van absorptielijnen van verschillende ionisatie-toestanden van zware elementen, die een grote diversiteit hebben, kan belangrijke aanwijzingen tot de compositie en toestand van het gas bevatten.

Thesis inhoud

In deze thesis bestuderen we de absorptie van neutraal waterstof en zware elementen toen het Heelal slechts 2 miljard jaar oud was. We gebruiken zowel waarnemingen van het eerdergenoemde KBSS project, als gearchiveerde data en nieuwe waarnemingen van de UVES spectrograaf op de Very Large Telescope (VLT). Dit tijdperk is in het bijzonder interessant omdat het de mogelijkheid biedt het Heelal waar te nemen in de tijd waarin het meest actief was en de meeste sterren gevormd zijn. Bovendien zijn emissielijnen door de expansie van het Heelal roodverschoven naar golflengten waarop ze waarneembaar zijn met instrumenten op telescopen op aarde. Met behulp van de pixel optische diepte methode hebben we de unieke mogelijkheid om het gas rondom sterrenstelsels in dit cruciale tijdperk te bestuderen.

In Hoofdstuk 2 gebruiken we data van het KBSS project om de absorptielijn-eigenschappen te bestuderen van absorptie door waterstof en zware elementen rondom 854 sterrenstelsels. Met behulp van de optische diepte methode meten we de absorptie rondom elk sterrenstelsel en gebruiken deze informatie om voor het eerst een twee-dimensionale kaart te maken van absorptie door zware elementen rondom sterrenstelsels. We ondervinden dat de absorptie versterkt is in de buurt van sterrenstelsels en dat een kleine versterking waarneembaar is tot op de maximale afstand die we kunnen meten. De absorptie van het quasar-spectrum bevat ook informatie over de snelheid van het gas, waaruit we concluderen dat het gas rond de waargenomen sterrenstelsels in beweging is doordat het ofwel in of uit het sterrenstelsel gedreven wordt, of omdat het erom roteert.

In Hoofdstuk 3 gebruiken we wederom data van het KBSS project om de fysieke toestand van het gas rondom sterrenstelsels te bestuderen. In plaats van het individueel bestuderen van de absorptie van waterstof of zware elementen, onderzoeken we de absorptie varieert van ion tot ion. Deze meting van de verhoudingen van ionen kan vervolgens vergeleken worden met de uitkomsten van modellen die ionisatie-toestanden simuleren, die aanwijzingen geven over de dichtheid en temperatuur van het gas. We bestuderen de absorptie van zuurstof in vergelijking met waterstof, zowel in de nabijheid van sterrenstelsels als op lukraak gekozen gebieden in het IGM. Het gas in het IGM is meestal gefoto-ioniseerd en heeft een temperatuur van $\sim 10^4$ K. Dichterbij sterrenstelsels vinden we een grotere verhouding van zware elementen ten opzichte van waterstof dan in het IGM. Bovendien vinden we bewijs voor een hete gas-component ($T \sim 10^{5.5}$K) dat verhit is door botsingen van

atomen en waarschijnlijk via galactische wind met hoge snelheid uit sterrenstelsels wordt geblazen.

In Hoofdstuk 4 vergelijken we de resultaten van Hoofdstuk 2 met de cosmologische simulaties van het EAGLE project. We doen metingen aan gezichtslijnen door de simulatie waarvan de eigenschappen gekozen zijn zodat ze overeenkomen met de waarnemingen. We vinden een excellente overeenkomst tussen waarneming en simulatie, voor zowel de hoge versterking in de nabijheid van sterrenstelsels, als de aanhoudende versterking tot verre afstanden. Bovendien vinden we dat het gas rondom de sterrenstelsels echt in beweging is. We onderzoeken hoe verschillende methoden van de implementatie van feedback, waar we de sterkte van de stellaire feedback met een factor twee verhogen en verlagen, onze resultaten veranderen. Het resultaat is echter dat er geen significante verschillen zijn. Dit duidt erop dat de belangrijkste contributie aan de beweging van gas van invallend gas of rotatie komt, in plaats van gas dat uit sterrenstelsels gedreven wordt.

In Hoofdstuk 5 richten we onze blik op het IGM. We passen de pixel optische diepte techniek toe op nieuwe, hoge kwaliteit spectra van acht quasars die waargenomen zijn met VLT/UVES. Net als in Hoofdstuk 3 bestuderen we how de absorptie verschilt tussen verschillende ionen, en we vergelijken dit met de EAGLE simulaties. De simulaties vertonen overeenkomst met zowel de waarnemingen van de relaties tussen zuurstof en waterstof als met de relaties tussen verschillende ionisatie-toestanden van koolstof en silicium. Voor een vaste hoeveelheid waterstof absorptie hebben de simulaties echter te weinig koolstof of silicium. Deze discrepantie is het grootst voor de hoogste waterstof kolomdichtheden, die wellicht representatief zijn de regios nabij sterrenstelsels. De overeenkomst tussen waarneming en simulatie wordt verbeterd wanneer de resolutie van de simulatie verhoogd wordt, zodat sterrenstelsels met lagere massa nauwkeuriger berekend worden, die mogelijk een belangrijke bijdrage leveren aan de verrijking van zware elementen in het IGM. We merken eveneens op dat de relatie tussen zuurstof en waterstof (waarin de simulatie en waarneming overeenstemmen) waarschijnlijk ontstaat door gas dat door botsingen van atomen wordt verhit, terwijl de bestudeerde ionisatie-toestanden van koolstof en silicum voorkomen in koeler, gefoto-ioniseerd gas. Dit betekent de chemische verrijking van zware elementen in heet gas in de simulaties nauwkeurig is, terwijl de overeenkomst tussen het koelere gas in de simulaties en waargenomen koolstof en silicium onvoldoende nauwkeurig is.

List of publications

1. **Turner, M. L.**, Schaye, J., Steidel, C. C., Rudie, G. C., Strom, A. L. 2015, *Detection of hot, metal-enriched outflowing gas around z ≈ 2.3 star-forming galaxies*, MNRAS, 450, 2067.

2. **Turner, M. L.**, Schaye, J., Steidel, C. C., Rudie, G. C., Strom, A. L. 2014, *Metal-line absorption around z ≈ 2.4 star-forming galaxies in the Keck Baryonic Structure Survey*, MNRAS, 445, 794.

3. **Turner, M. L.**, Côté, P., Ferrarese, L., Jordàn, A., Blakeslee, J .P., Mei, S., Peng, E., & West, M. J. 2012, *The ACS Fornax Cluster Survey: The Nuclei of Early-Type Galaxies*, ApJS, 203, 5.

4. **Turner, M. L.**, Rutledge, R. E., Letcavage, R., Shevchuk, A. S. H., Fox, D. B. 2010, *A Limit on the Number of Isolated Neutron Stars Detected in the ROSAT All-Sky-Survey Bright Source Catalog*, ApJ, 714, 1424.

5. Richard, J., Patricio, V., Martinez, J.,Bacon, R., Clement, B., Weilbacher, P., Soto, K., Wisotzki, L., Vernet, J., Pello, R., Schaye, J., **Turner, M.**, Martinsson, T. 2015, *MUSE observations of the lensing cluster SMACSJ2031.8-4036: new constraints on the mass distribution in the cluster core*, MNRAS, 446, L16.

6. Steidel, C. C., Rudie, G. C., Strom, A. L., Pettini, M., Reddy, N. A., Shapley, A. E., Trainor, R. F., Erb, D. K., **Turner, M. L.**, Konidaris, N. P., Kulas, K. R., Mace, G., Matthews, K., McLean, I. S. 2014, *Strong Nebular Line Ratios in the Spectra of z ~ 2–3 Star-forming Galaxies: First Results from KBSS-MOSFIRE*, ApJ, 795, 165.

7. Haakonsen, C. B., **Turner, M. L.**, Tacik, N. A., Rutledge, R. E. 2012, *The McGill Planar Hydrogen Atmosphere Code (McPHAC)*, ApJ, 749, 52.

Curriculum Vitae

I was born on June the 17th, 1987 in Oakville, Canada, and grew up in the neighbouring city of Burlington, where I attended elementary and high school.

In 2005 I began studying physics at McGill University in Montréal. For my honours research project, I worked with Prof. J. Nadeau studying quantum dots. During the summer of 2008, I worked for Prof. R. Rutledge, where I assisted with writing a program to solve radiative transfer in a hydrogen atmosphere. I also began a project with Prof. Rutledge searching for isolated neutron stars using archival data. I graduated from McGill in 2009 with first class honours. Later that year, I began a master's at the University of Victoria, under the supervision of Prof. P. Côté at the Herzberg Institute of Astrophysics. The topic of my thesis was nuclear star clusters in the centres of galaxies in the Virgo and Fornax clusters. I graduated with a Master's in Science in 2011.

In the autumn of 2011 I began my PhD at Leiden Observatory, working with Prof. J. Schaye and Prof. C. Steidel (Caltech). My research focused on both observations and simulations of the gas around galaxies. During my PhD, I visited Caltech in Pasadena, USA, and had the opportunity to go observing with the William Herschel Telescope at La Palma, Keck/HIRES in Hawaii, USA, and MUSE on the Very Large Telescope in Chile. I also presented my work at international conferences in the Netherlands, France, Germany, Italy, the UK, and the USA.

In October 2015, I will begin a postdoctoral position with Prof. R. Simcoe at MIT in Boston, USA.

Acknowledgements

I would like to thank the many people who have helped and supported me throughout the years.

My beginnings in research wouldn't have been possible without my undergraduate supervisors Jay Nadeau and Bob Rutledge, and my master's supervisor Patrick Côté. I thank you for always encouraging and believing in me!

In Leiden I had the chance to be part of Joop's research group, which has always been an incredibly great bunch of people! Freeke, Milan, and Marcel, group meeting wouldn't have been the same without you guys. Olivera, thanks for patiently answering my many questions. Ali, although we may disagree on optimal office temperature, it's great to see you around at conferences. Rob, I think the group efficiency dropped by 200% after your departure. Jorryt, thanks so much for translating my summary into Dutch! Joki, I am exponentially cooler just by knowing someone from Iceland. Alex North, I can only hope my future officemates are as considerate as you. Chris, I trust you will keep the Canadian spirit going. Sylvia, I will certainly miss our lunches together! Lorrie, I'm so happy that you joined the MUSE team, and I wish we could have had more girls nights. Marijke, you are an awesome academic little sister, and furthermore a great colour palette twin! Let me know if you ever modify your lunch menu.

I am really grateful for all the amazing friends I made in Leiden, you really made the years fly by! Marco, thanks for being an awesome officemate, group mate, roommate and travel buddy. I owe the completion of my thesis to the high oxygen levels in the office thanks to your plants, and I will definitely be keeping in touch to stay on top of the latest restaurant, movie and tablet game reviews. Alex South, I like how you are such an easy going guy, although this can be a problem if the two of us are ever tasked with a decision. I really enjoyed our conversations about internet memes, and I definitely plan on visiting New Zealand one day. And special thanks to Marco and Alex South for agreeing to be my paranymphs, which involved a lot of legwork for them due to my absence! Tiffany, you are such a kind and supportive friend. You really helped pull me through my last year, and I am so excited to see you and Tom in the US. Andra, although it was difficult to catch you around the Sterrewacht, the time we did spend together was always great. It meant a lot to share the job application ordeal together, and I hope to see you and Viktor next summer. Mattia, you are a hilarious guy, and let me know if you ever want to start that "fashion" blog (I will try my best not be featured in there). Going to Jordan was really a blast, and of course I was so happy to be at your wedding! Anna, I'm very glad that you are now stuck with Mattia. It was great to get to know you these past years, and I will definitely be seeing you in NYC. Marissa, in addition to being a great driving force behind

the Leiden social life, I can't thank you enough for introducing me to Insanity during our epic Berlin trip. You are single-handedly responsible for my final proposition. Caroline and Heather, I'm so glad you rescued me from my horrible first apartment, I really had fun living together on Fitterstraat. I also have many others to thank for making all the lunches, dinners, coffees, borrels and parties truly awesome throughout the years: Alex West, Allison, Ben, Bram, David, Jeroen, Jesse, Francisco, Gaby, Irene, Maryam, Matteo, Mayuresh, Renske, Sebastian, Shannon, Thanja, and Willem.

During my PhD, I had the chance to visit my collaborators at Caltech. Gwen, you have always been incredibly kind and supportive, and overall an amazing mentor. I am very lucky to have had your advice and guidance! Allison, we had some great (and not so great) observing runs, and I really enjoyed our trip around the Big Island.

To my mom, dad, Babi and Dêda, thank you for always unconditionally supporting and encouraging me throughout all of my studies. I truly couldn't have done it without you! To my "little" brother Dave, thanks for keeping me cool, and I'm very proud of you! To my older sisters Helen and Christina, you have always been such amazing role models for me. Uncle John, Aunt Jenny, Michelle and Nick, thanks for all of your support. I would also like to thank my Italian side of the family, Maria, Bernardo, and Eve, for being so welcoming and providing a perfect escape from the Dutch weather. Finally, Bennie, I am thankful every day that "operation maple syrup" was a success. You are my luck and I'm so excited for our future adventures together in America!